Investigation of Wear Mechanisms in Abradable-Blade Contacts

The University Of Sheffield.

Eldar Rahimov

Department of Mechanical Engineering
The University of Sheffield

This dissertation is submitted for the degree of
Doctor of Philosophy

November 2022

Acknowledgements

I would like to thank my supervisor Matthew Marshall for his continuous support throughout this project. His technical expertise, positive attitude and willingness to help have immensely helped me. I would also like to thank my second supervisor Charles Lord for his advice during this project.

I would like to express my gratitude to my industrial supervisors Glen Pattinson and Lloyd Pallett and other Rolls-Royce plc. staff, especially Mike Keenan, Simon Read, Dan Everington and Matthew Hancock for their help with obtaining samples for experiments, technical advise and general research discussions that helped to identify the optimal direction for this project.

Next, I would to thank all the members of university technical staff, especially, Oliver Cooper, Jamie Booth and Mathew Hall for helping with the rigs in the Swift laboratory, Dave Butcher, Luke Callaghan, Gareth Barker, Dave Webster and Geoffrey Hibberd for helping with the manufacture of components for the experimental work and Christopher Todd and Mike Herbert for their help with electrical components and rig control. Their input was invaluable for making this project happen.

Lastly, I would like to thank my PhD colleagues and friends - Julián García Panizo, Alvaro Parody, Allan Liu, Andreas Hadjisoteriou, Boxiu Zhang, Aleena James and Aaron Baillieu for helping through the challenges of doing the PhD research and going through the pandemic, and making these 4 years fun.

Abstract

Abradable materials are thermally sprayed on the inside of casings in aero-engines to provide a seal between rotating blades and a casing. The use of such materials in aero engines have been an area of research interest over the past few decades as small reductions in clearances between stationary and rotating parts can lead to large increases in engine efficiency. The tight requirements for abradable coatings and increase in compressor temperature from stage to stage have led to the development of abradable materials specific for different compressor stages. In this thesis wear mechanisms observed in two types of contacts were investigated: between the Ti(6Al4V) blades and AlSi-polyester abradable used in lower temperature compressor stages and between the Inconel 718 blades and NiCrAl-bentonite abradable used in higher temperature compressor stages.

This was accomplished through commissioning a new high-speed testing rig with a capability to achieve speed up to 280m/s and instrumenting it with a front-on stroboscopic imaging system. The new imaging system allowed new insights into adhesion and abrasion mechanisms observed in tests with AlSi-polyester abradable samples. For adhesions, it was shown that the combination of bulk temperature and flash temperature concepts was able to explain most of the observations in this work. It was shown that the likelihood of adhesions formation increased with contact forces and decreased with blade tip thickness.

For contacts with NiCrAl-bentonite abradable two distinct contact modes were identified. These contact modes were then explained through the balance between the incursion rate and the rate of abradable fracture. It was shown in this work, that blade length plays a significant role in the effectiveness of abradable surface fracture, with very long (low stiffness) blades leading to inefficient fracture.

The effect of angled blades was investigated with short (stiff) blades and compared their effectiveness when they were introduced to long blades in previous research. It was shown that with short blades, angles did not offer the same increase in abradable fracture effectiveness. It was then suggested that both an increase in stiffness and introduction of an angle to long (less stiff) blades improve abradable fracture in a similar manner, and with stiff blades angles do not offer further performance improvements.

The difference in blade wear performance between flat and angled blades was explained through the presence of low temperature abrasive wear and thermally driven abrasive wear. The low temperature abrasive wear rate was low and no wear was observed with flat blades. With angled blades, however, some wear occurred due to the very low thickness at the sharp blade tip. The thermally driven wear occurred for tests that transitioned to the high-force contact mode. This type of wear occurred earlier during a test and the wear rate was higher for flat blades than for angled blades.

Finally, the effects of such simplifications such as using blades with a fixed rather than a variable chord thickness and performing tests at a single rather than a variable incursion rate were investigated. It was shown that both these simplifications can have an influence on test outcomes and that the effect of simplifications used on scaled test rigs needs to be accounted for when considering the applicability of results from such rigs to actual aero-engines.

Table of contents

List of figures

List of tables

Nomenclature

I incursion rate in m/pass

n_r revolution number

$n_{rcurrent}$ current revolution number

Other Symbols

θ angle of deviation of the blade position on an image from the vertical

b_b blade thickness

b_d length of the flat section at the edge of the disk

F_s dynamometer sampling frequency in Hz

i_{rate} incursion rate in m/pass

l_b combined radial length of the disk and blade edge (i.e. the blade edge length from the disk's centre, equivalent to r_{tip})

l_d radial length of the disk (i.e. disk edge length from the centre of the disk)

l_{rtotal} current rub length in m

P_b the perpendicular projection length of the blade's edge from the disk's centre

P_d perpendicular projection length of the disk edge from the centre of the disk

R_{de} radius of disk edge curvature

rpm_{max} maximum rotational speed in revolutions/minute (rpm)

r_{tip} blade tip radius in m

v_{linear} stage linear incursion speed in m/s

V_{test} voltage corresponding to the necessary spindle rotational speed in V

v_{tip} blade tip speed in m/s

Chapter 1

Introduction

Both the International Air Transport Association (IATA) and Flightpath 2050 (Europe's vision for Aviation) have defined the significant reduction in aviation's CO_2 emissions as one of their long term goals [1]. The IATA has suggested creating more efficient aircrafts and engines, weight savings in current aircraft fleet, streamlining aircraft routes and a global market-based measure to fill any remaining emissions gap as key pillars of addressing the CO_2 emissions goal [2].

Overall aircraft engine efficiency can be improved with advancements in aircraft components efficiency, propulsive efficiency, modified and new engine cycles [3]. Improved overall engine efficiency also leads to lower fuel consumption and, hence, offers additional economic benefits. Focusing on components efficiency, tip leakage between rotating blades and a casing is one of the primary loss sources in axial compressors used in turbofan aero-engines [4].

1.1 Abradable materials

To understand the benefits of using abradables, it is important to understand the mechanism of clearance formation in aero-engine compressors. The mismatch of thermal expansion rates of blades and a compressor casing as well as centrifugal forces acting on the blades can lead to contacts between the blades and the casing. Without a sacrificial layer on the casing surface, contact between a blade and the casing would result in blade wear and an increase in clearance between rotating blades and a casing as seen in Fig. 1.1a. With abradable materials, the clearance between the blades and the casing can be designed in such a way that even if contact occurs due to thermal expansion or centrifugal loads, a seal would be created by the blades cutting a path in an abradable material. The presence of an abradable materials also allows one to manage a periodic contact risk due to manoeuvres leading to high shaft loading and movement, and thus, create a seal for all operating conditions. Even

if a blade is returned to the original radial position, the gap created is less detrimental to the aerodynamic performance as this gap is still sufficiently sealed by the abradable material to both sides of a blade as demonstrated in Fig. 1.1b resulting in reduction in tip leakage losses. Another important consideration for using abradables is that lower forces are needed in cutting abradables (abradable wear) as compared to forces needed to cause blade wear, resulting in a decrease in danger of a significant damage to the blades, shaft and casing. This is important for increasing the safety and reliability of aero-engine compressors.

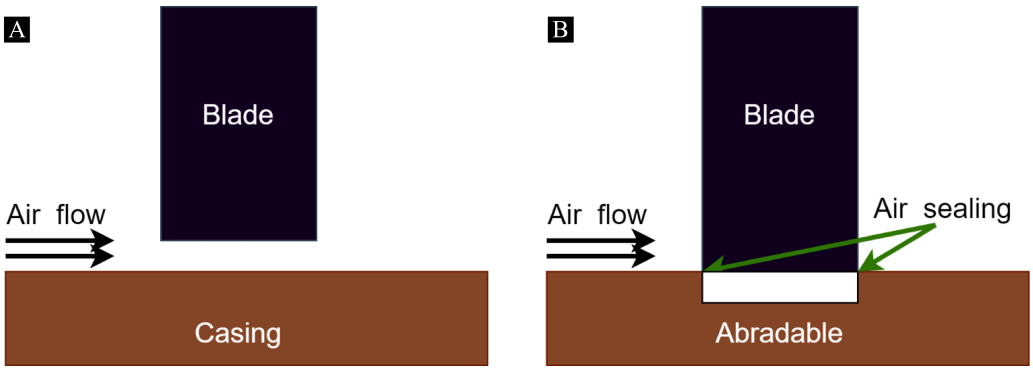

Fig. 1.1 a) The clearance created by blade wear due to a blade interaction with casing b) the trench created in an abradable due to a blade interaction with abradable.

1.2 Abradables overview

Abradable materials used in aero-engines need to provide sufficient sealing between them and rotating blades. To ensure sealing, they need to be effectively abraded when a contact with a blade occurs. A number of materials such as polymers and low shear strength metals such as aluminium or bronze and copper alloys could fulfil such requirement, however, the use of such materials was limited by the engine temperature limitation to low temperature engine stages as these materials can usually be used only till the temperature of 250°C [5].

Such limitation was addressed by the use of thermally sprayed materials that could combine the shearability of polymeric materials with higher strength of metal alloys such as AlSi. For even higher temperature applications, a different type of abradable materials was developed, where individual particles were bonded together only to some degree with a coarse macro-porous microstructure with spherical particles instead of a typical lamellar microstructure [5]. The abradable materials specific to different compressor stages due to changes in a stage temperature are summarised in Fig. 1.2. In the following sections the two abradables materials (AlSi-polyester and NiCrAl-bentonite) used in this work will be further reviewed.

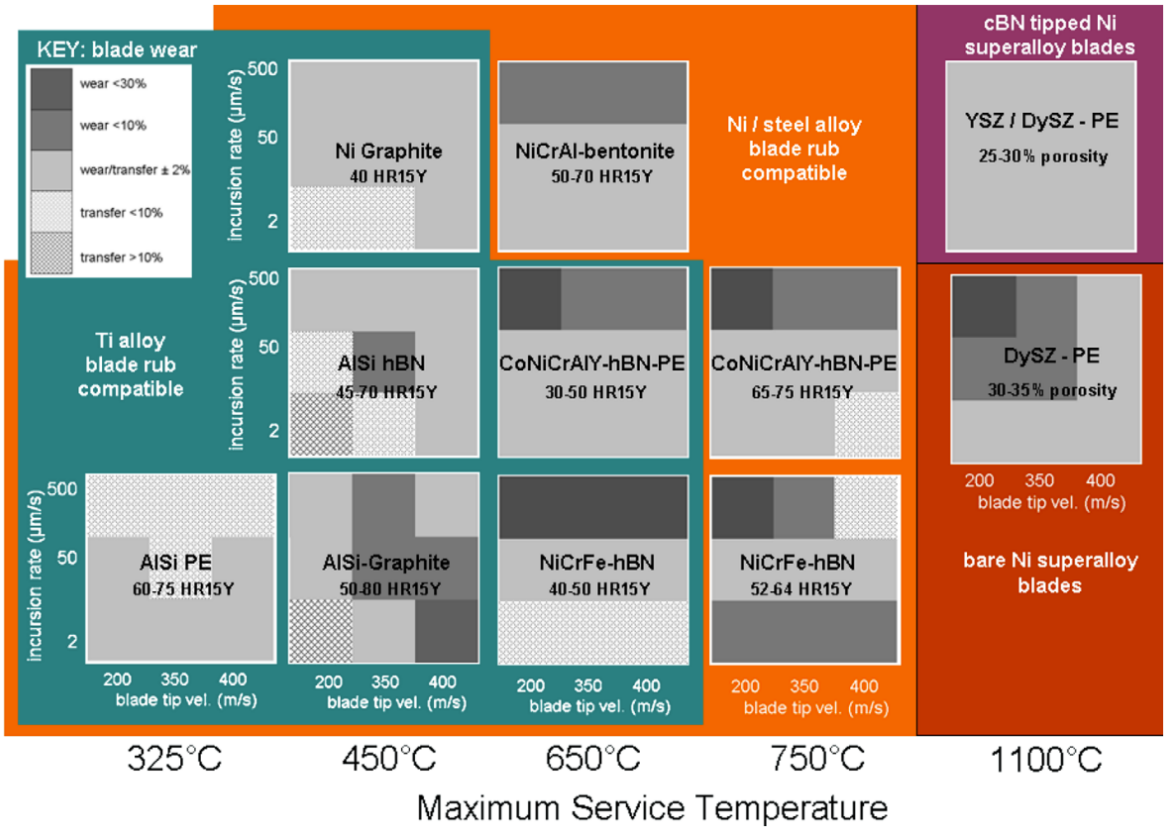

Fig. 1.2 Abradable materials used in aero-engines [5].

1.3 AlSi-polyester abradable

AlSi-polyester abradable is deposited using an atmospheric plasma spraying (APS) method. It is designed to combine shearable and heat-resistant properties of polyester with high strength mechanical properties of AlSi alloy [5]. The chemical composition consists of 53%Al, 7%Si, and 40% polyester by weight. This abradable is typically used in lower compressor stages up to the temperature of 325-350°C with polyester maximum operating temperature being the limiting factor. This coating is typically sprayed to the hardness of 60-75 on the HR15Y Superficial Rockwell hardness scale and can be used against titanium alloy, nickel alloy or steel blades. High energy heat input of APS allows a high degree of microstructure control [5]. A SEM image of a AlSi-polyester abradable coating showing its microstructure is given in Fig. 1.3.

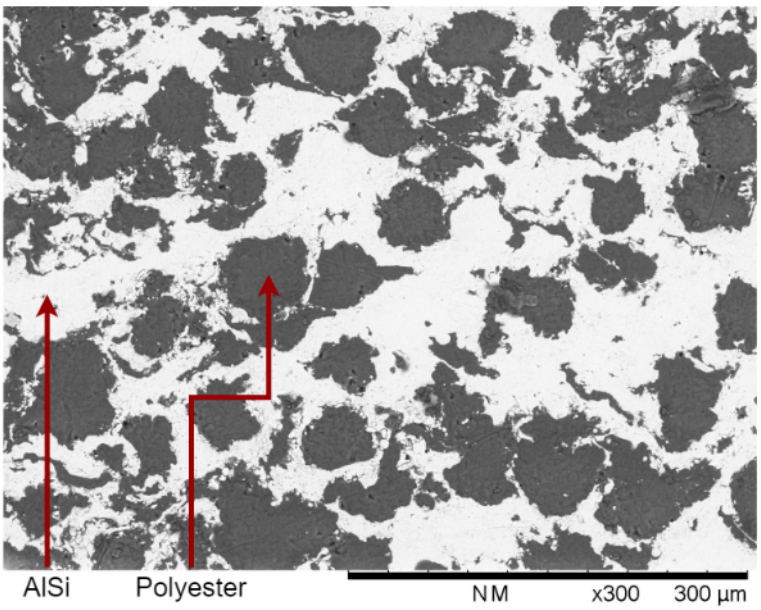

Fig. 1.3 An example SEM image of AlSi-polyester abradable microstructure [6].

1.4 NiCrAl-bentonite abradable

In contrast to the AlSi-polyester abradable, the NiCrAl-bentonite abradable is deposited using a flame (combustion) spraying method. It is typically used in the temperature range of 450°C and 650°C against steel or nickel alloy blades. This coating is sprayed using a cermet powder consisting of the bentonite core encapsulated by the NiCrAl alloy. The chemical composition consists of 71%Ni, 4%Cr, 4%Al, and 21% bentonite by weight [7]. This coating is typically sprayed to the hardness of 30-60 on the HR15Y Superficial Rockwell hardness scale, however, it was previously shown to harden with time at elevated temperatures. In flame spraying particle sizes are kept coarse resulting in deposition of fairly spherical particles instead of lamellar microstructure resulting in macro-porous coating architecture. A SEM image of a NiCrAl-bentonite abradable coating showing its microstructure is given in Fig. 1.4.

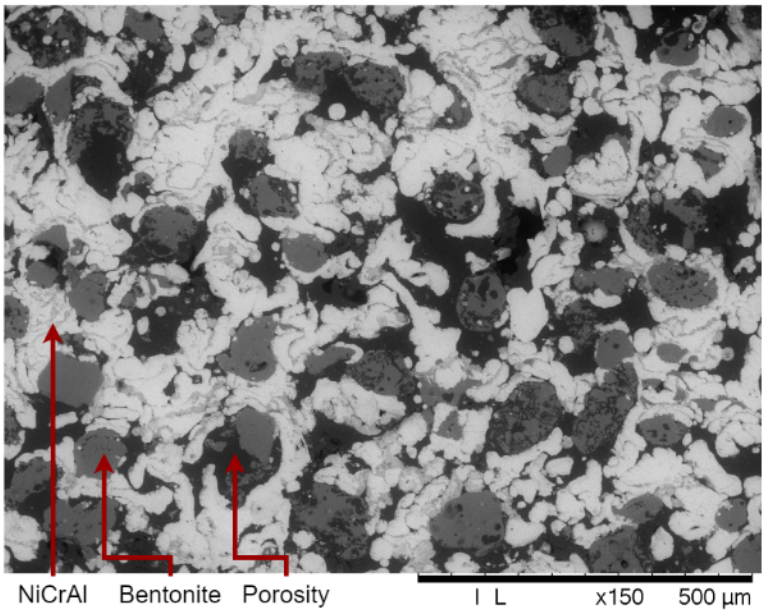

Fig. 1.4 An example SEM image of NiCrAl-bentonite abradable microstructure [6].

1.5 Aim and objectives

The primary aim of this thesis is to advance the current understanding of the wear mechanisms encountered in contacts with abradable materials and the understanding of how these wear mechanisms could be improved through the investigation of two types of contacts: AlSi-polyester abradable – Ti(6Al4V) blades and NiCrAl-bentonite abradable – Inconel 718 blades. This aim will be achieved through accomplishing the following objectives:

- Develop a front-on stroboscopic imaging system for the new high-speed testing rig at the University of Sheffield. This rig will allow to perform tests up to the speed of 280m/s with the front-on imaging allowing to track blade length changes along an entire blade width throughout each test.
- Develop image processing methods for blade images captured using the new stroboscopic imaging system. These methods include tools for analysis of individual adhesion and wear events and calculation of average values of adhesion rates and peak heights.
- Investigate wear mechanisms observed in contacts between AlSi-polyester abradable samples and Ti(6Al4V) blades with the help of the new stroboscopic imaging system and developed image processing methods.

- Investigate wear mechanisms observed in contacts between NiCrAl-bentonite abradable samples and Inconel 718 blades using the existing 200m/s testing rig at the University of Sheffield and the new 280m/s high-speed rig.
- Perform high-speed tests of angled Inconel 718 blades against NiCrAl-bentonite abradable samples. This will further investigate the benefits of angled blades in contacts with NiCrAl-bentonite abradable that were identified in the previous research at the University of Sheffield [8].
- Perform tests aimed at a closer representation of real-life engine condition. The first set will include tests with blades of varying chord thickness to identify localised effects with the help of the new stroboscopic imaging system. The second set will include tests with two incursion rates included within a single test to investigate how different incursion rates experienced by an abradable in the past can impact the present abradable-blade contact.

1.6 Thesis layout

Chapter 1 describes the motivations for the use of abradable materials in the aero-engines and provides an overview of the abradables that are currently used in aero-engine compressors. The aim and objectives of this PhD thesis are also outlined. In chapter 2 a summary of the current state of research on the abradables used in aero-engine compressors is given. Main gaps in the current research and how this work will attempt to address them are discussed. Chapter 3 gives a detailed overview of the new 280m/s high speed rig and its instrumentation. Additional methods used for post-test analysis of blades and abradable samples such as Alicona for surface measurements and SEM for microstructure imaging are also discussed. In chapter 4, processing methods developed for the analysis of data obtained using instrumentation installed on the 280m/s rig as well as data from the additional tools used for post-test analysis of blade and abradable samples are given.

In chapter 5 – the first experimental chapter, results from the tests investigating contacts between AlSi-polyester abradable samples and Ti(6Al4V) blades are presented. The effects of abradable hardness, blade tip speed and incursion rate on wear mechanisms are identified and the importance of these results is discussed.

In chapter 6 results from the tests aimed at investigating the factors influencing wear mechanisms in contacts between NiCrAl-bentonite abradable samples and Inconel 718 blades are given. The effects of test repeatability, blade tip speed, incursion rate, blade length and rig stiffness are considered and the importance of these results is discussed.

In chapter 7 results from the high-speed tests performed with angled Inconel 718 blades and NiCrAl-bentonite abradable samples are presented. The main focus of this chapter is on the effect of different angles on results and the comparison of positive and negative blade tip angles (having the longest edge as the trailing or leading edge). The comparison of the effectiveness of angled blades at different speeds is also presented.

Chapter 8 focuses on tests with an improved representation of real-life engine conditions. In the first part, localised effects due to variations in the blade thickness along its chord are investigated with the help of stroboscopic imaging. The second part of the chapter focuses on the discussion of results from the tests aimed at understanding how incursion rate history in a given abradable-blade contact impacts current contact conditions.

In chapter 9 the main findings of the tests performed as part of this PhD are discussed in the context of the general body of research into abradable materials. The findings of this PhD are then summarised in chapter 10 and suggestions for future work are given in chapter 11.

Chapter 2

Literature review

For abradable materials used in compressor stages of aero engines the research can be primarily divided into research into material science and research into tribological properties of contacts between aero-engine blades and such materials. Both areas are important for optimising the efficiency of aero-engine compressors. Better abradable linings properties such as erosion resistance can reduce wear of the linings due to environmental factors; and better rub behaviour between a lining and a blade ensures reduced blade abrasive and adhesive wear.

Abradable linings research methods can also be subdivided into several categories including modelling of the abradables and abradable-blade contacts, experimental testing of abradable properties and abradable-blade contacts and full scale engine tests of abradable materials performance.

In this chapter, first, the research methods used for investigation of abradable materials properties are going to be covered. Then, modelling and experimental studies focused on abradable-blade interaction will be discussed, followed by a detailed overview of work focused on wear mechanisms in AlSi-based and NiCrAl-bentonite abradables that are considered in this thesis. At the end, the gaps in current research are highlighted.

2.1 Abradable materials properties

The key performance criteria for abradable materials used in turbomachinery equipment such as aero-engines were outlined by Wilson [5]. These are:

- Coating cohesive strength.
- Oxidation resistance at elevated temperatures.
- Corrosion resistance in aqueous or chemical fluids and gases.

- High temperature corrosive attack e.g. silicates.
- (CMAS), chlorides, sulphides.
- Sintering resistance at elevated temperatures.
- Thermal shock / cycle resistance.
- Resistance to solid particle erosion.

The requirement for abradable materials to comply with the criteria outlined above has guided the majority of the material science research on abradables. Their ability to resist heat, hardness, resistance to abrasion and erosion were explored through modelling and experimental testing.

2.1.1 Modelling methods

The modelling work has primarily focused on mechanical and thermal properties of abradables. Wang et al. [9] made one of the first attempts to model abradable mechanical and thermal properties of ceramic abradables. Two approaches (small-angle neutron scattering (SANS) measurements based approach and an approach based on using thresholded SEM images for mesh generation with the object oriented finite (OOF) element method) were used for estimation of properties of porous coatings fabricated with four different types of zirconia feed powder. It was found that finite element analysis results based on either approach underestimated drop in mechanical and thermal conductivity values due to pores in the material for as sprayed coatings. Both approaches were a lot more accurate for coatings where splat boundaries were removed by thermally cycling the coatings. It was also found that an image based approach was able to simulate anisotropy in coatings' elastic modulus results more accurately than the SANS approach. This study showed the importance of intersplat boundaries in reduction of thermal and mechanical properties and the potential use of the finite element approach for studying mechanical properties of thermal barrier coatings.

Faraoun et al. [10, 11] have attempted to model abradable mechanical properties based on analysis of SEM images of AlSi-hBN and NiCrAl-bentonite abradable samples. Different structural elements such as, for example, metal, bentonite and porosity phases for a NiCrAl-bentonite abradable were separated using thresholds based on grey levels of each phase on images. Equivalent images based on using ellipses to represent individual hBN particles for AlSi-hBN abradable and individual bentonite particles and areas of porosity for NiCrAl-bentonite abradable were then constructed for the calculation of mechanical properties of both abradable types. However, no discussion on the accuracy of representation of individual

particles in abradable structure as ellipses was given. Also, there has been no experimental data to confirm the results of the simulations.

The work on modelling the thermal and mechanical properties of AlSi-based coatings based on segmentation of SEM images was continued by Bolot et al. [12, 13] and Watson et al. [14]. In these studies, it was shown that such methods could be used to effectively estimate properties of abradable materials. In the work by Watson et al. [14] it was shown that modelling results gave a good prediction of density and specific heat capacity for both AlSi-polyester and AlSi-hBN abradable materials. Additionally, a good agreement between modelled and experimentally measured results was observed for thermal conductivity of the AlSi-polyester abradable, but poor correlation between such results was seen for the AlSi-hBN abradable, where the modelling approach significantly overestimated the thermal conductivity. This was likely due to binder isolating hBN from the metal matrix resulting in hBN acting as the thermal flow barrier. When the thermal conductivity of the hBN phase was reduced to the value of the binder, the modelled thermal conductivity for the abradable material agreed with the experimentally measured values supporting that suggestion.

2.1.2 Experimental testing methods

In experimental testing, the most commonly measured property is the abradable hardness on the HR15Y Superficial Rockwell hardness scale as abradable materials are sprayed to a designated hardness range [5]. Additionally, mechanical properties such as microhardness and ultimate tensile strength [15], erosion resistance [16] and thermal properties such as specific heat capacity and thermal conductivity [14] were previously measured. Some research was also initiated by Skiba [17, 18] on mechanical behaviour of coatings under high strain rates at a variety of temperatures.

While the measurements of mechanical properties were shown to be useful for improved understanding of abradable materials and how the properties of sprayed materials are different from their individual constituents, they could provide only limited insights into contacts between aero-engine blades and such materials. Such contacts required more factors to be considered such as effects of blade tip speed, incursion rate of a blade into an abradable material, abradable phase distributions, temperatures and fracture mechanisms observed during contacts.

To improve the representativeness of contacts occurring in aero-engines while maintaining the simplicity and low-cost of mechanical testing procedures, some attempts were made to relate sliding wear volume [19] and scratch testing results [20, 15] to in-service abradable performance.

Yi el al. [19] evaluated the abradability of materials using sliding wear volume. In this work it was shown that for a given abradable type, abradability decreased with an increase

in hardness. However, it was also shown that the abradability of different types of materials could not be compared by their hardness values, as even if the hardness values were close, the abradability results were very different. This highlighted that hardness measurements on their own could not be used to compare different types of abradable materials.

In a later work by Ma et al. [20, 15], an attempt was made to assess the performance of abradables by the means of a standard low-speed scratch test. The progressive abradability hardness, PAH, which was defined as the work done per abraded material volume was used as a measure of abradability of a material. It was shown that PAH correlated well with such mechanical parameters as hardness, elastic modulus and ultimate tensile strength. The PAH results were compared to findings from industrial engine tests from datasheets by Sulzer Metco Ltd (Oerlikon Metco). It was found that the materials claimed to have better erosion resistance and lower abradability, had higher PAH values when scratch tested. That suggested that PAH could be used as an inexpensive and effective way to characterise abradability of a material.

Despite some new insights into performance of abradable materials, the sliding volume and scratch testing methods had limitations similar to other mechanical properties testing methods, as they failed to reproduce contact conditions observed within aero-engine compressors and could not be used on their own to explain the wear mechanisms of blades and abradable materials observed in aero-engines. Therefore, contacts between blades and abradable materials have been further evaluated through more representative investigation methods.

2.2 Abradable-blade interaction research

Similarly to research into abradable materials properties, the interactions between aero-engine blades and abradable materials have been investigated using both modelling and experimental approaches.

2.2.1 Modelling methods

The abradable-blade contact simulations have primarily focused on understanding the blade dynamics in the abradable-blade contacts and the effect of non-linearity on such contacts [21, 22]. Some attempts were also made to simulate common wear mechanisms [23] and predict blade wear based on contact temperatures [24].

In the earlier work by Wang [24], contact temperatures of a titanium blade rubbed against the NiCrAl-silicate and AlSi seals were modelled. This work had several interesting findings. Firstly, it was shown that the temperature reached a steady-state value only after 500 revolutions for rubs against both types of seals despite an initial sharp rise in temperatures. This result was

later used by multiple researchers to justify performing scaled rig tests at ambient rather than engine representative temperatures. The temperature results in this work were used to predict elastic modulus of the contacting materials showing that for contacts against the NiCrAl-silicate seal the blade modulus dropped below that of the seal and for contacts against the AlSi seal the blade modulus always remained above that of the seal as shown in Fig. 2.1. This result successfully explained the experimental finding where for the contact with the NiCrAl-silicate seal a significant amount of blade wear was observed, while for the contact with the AlSi seal almost no blade wear was seen.

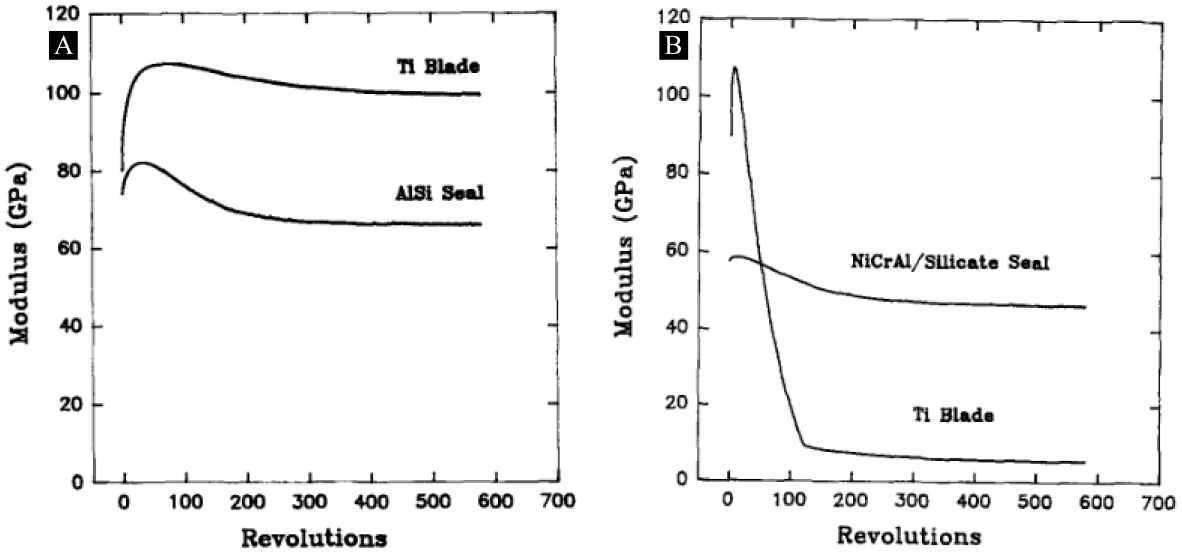

Fig. 2.1 a) Elastic modulus changes for the titanium blade – NiCrAl-silicate seal contact showing that the modulus of the seal is higher than that of the blade at the later rubbing stages, b) elastic modulus changes for the titanium blade – AlSi seal contact showing that the modulus of the blade is higher than that of the seal during the entire rubbing stage [24].

However, this work had a number of limitations. It only considered a single test condition while in aero-engines a variety of incursion conditions can occur. For that condition, the performed analysis was applicable as the rubbing contact occurred followed by the abrasive wear mechanism. However, previous research has shown that a variety of wear mechanisms can occur in such contacts including abrasive wear observed in this study, but also cutting, adhesive transfer and tribo-oxidation [25].

One of the early attempts to simulate the dynamics of the abradable-blade interaction was performed by Batailly et al. [26] using a numerical simulation. It was found that the wear pattern observed was dependent on the blade first bending mode frequency. It was shown that the simulated blade dynamics matched well with experimental results and the simulation was able to predict the wear pattern correctly. It was also suggested that the jumps in vibrations

amplitude could be related to desynchranisation of the blade due to alteration of abradable mechanical properties.

In the work by Legrand et al. [27] the numerical algorithm was shown to be an effective tool for applications such as detection of severe operating conditions and critical rotational velocities. It was also suggested that the numerical tools could be used for optimisation of blade designs for making them more robust to the contact conditions.

Later work by Batailly et al. [28, 29] and Nyssen et al. [30] has further explored the impact of different testing parameters on wear profiles observed in abradable materials. It was shown that both bending and torsional blade vibration modes have an impact on the final wear profile. It was demonstrated that wear profiles could be significantly different at locations corresponding to different parts of a blade (leading edge, middle of chord, trailing edge) as shown in Fig. 2.2. Additionally, it was shown in the work by Nyssen et al. [30] that the initial clearance played a significant role on the dynamics of the contact and with decreases in clearance unexpected interactions could occur highlighting the importance of performing the dynamical analysis when a reduction in clearance is desirable.

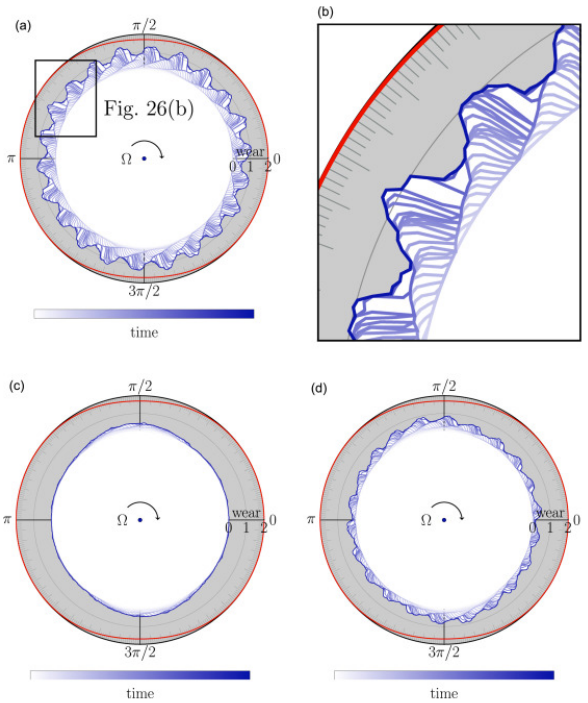

Fig. 2.2 Evolution of the wear profiles (blue) at different locations of the casing superimposed with the overall casing deformation (red), (a) leading edge, (b) zoom for the leading edge, (c) middle of chord, (d) trailing edge [29].

In the work by Berthoul al. [23] a simulation of an actual incursion test was attempted. The blade in that simulation was modelled using 3D elements, with blade material calibrated such that its first eigenfrequencies matched the ones measured experimentally. The modelled experimental set-up consisted of a fixed blade with a spinning cylinder coated with abradable into which the blade was incurring. The work attempted to model wear of an abradable coating by modelling a combination of individual wear mechanisms previously identified by Schmid [31] and understanding the influence of wear mechanisms on blade dynamics. Each wear mechanism was described through analytical equations, however, the applicability of these equations to contacts with abradable materials was not experimentally verified. Additionally, the results of simulations depended on the correct identification of wear mechanism for a given contact condition, which is still an area requiring further research. While such modelling route showed a good potential for linking wear mechanisms to blade dynamics, better understanding of wear mechanisms and their effect on contact forces is required to increase the fidelity of such models.

The modelling approaches were shown to be a powerful tool for understanding how blade and abradable vibrations could lead to varying contact incursion rates and properties. They highlighted that understanding the dynamics of a system is of fundamental importance for predicting the worst-case contact conditions and for understanding what tools are available for decreasing the severity of such conditions for abradable-blade contacts.

However, as of now, they showed only limited applicability for understanding the blade and abradable surface wear properties. This is due to a number of reasons, primarily the very complex uneven microstructure of abradable materials, which is usually significantly simplified for modelling purposes. The models themselves were usually formed based on simplified wear mechanism formulations, largely due to the lack of well-established understanding of such mechanisms in the current body of abradable research as will be discussed in later sections.

2.2.2 Experimental research using scaled and full-scale rigs

Similarly to general research in tribology, the representativeness of contact conditions in abradable testing differed in complexity from simple wear testing approaches discussed in section 2.1.2 to more realistic conditions achieved through testing on experimental scaled and full-scale rigs. The testing on such rigs was found to be important for better understanding of contacts between blades and abradable material due to complex contact conditions (high contact speeds and temperatures) and abradable microstructure. The developed rigs aim to reproduce conditions observed in aero-engines, and could be classified as scaled or full-scale depending on how closely these conditions are represented. These rigs also differ in the complexity of the installed instrumentation.

Some of the experimental rigs were developed for improved understanding of blade dynamics in contacts with abradable materials such as in the works by Baiz et al. [32] and Mandard et al. [33]. The majority of the experimental rigs, however, were developed with a focus on improvements in understanding of wear mechanisms in abradable-blade contacts.

One of the full-scale testing rigs was developed by Oerlikon Metco, the manufacturer of the abradable coatings commonly used in aero-engines and was used for investigation of such coatings by a number of researchers [25, 31, 34]. The schematic of this rig is given in Fig. 2.3. This rig is stated to be capable of reaching blade tip speed of up to 500m/s. Incursion speed is stated to be 1-2000µm/s, however, as the radius of the rotating disk is unknown, the incursion rates per pass are unknown. This rig additionally allows testing at temperatures between 20 and 1200ºC by heating the shroud and specimen contact area with high velocity gas stream from high velocity flame generator, closely recreating conditions observed in the aero engine abradable-blade contacts. Based on the rig diagram in Fig. 2.3, it appears that this rig is instrumented with a force transducer to measure captured forces and a thermocouple to measure abradable sample temperatures. Post-test blade weight measurements were used for wear maps in the work by Borel et al. [25] and post-test blade height change measurements were used for wear maps in the article by Wilson [5].

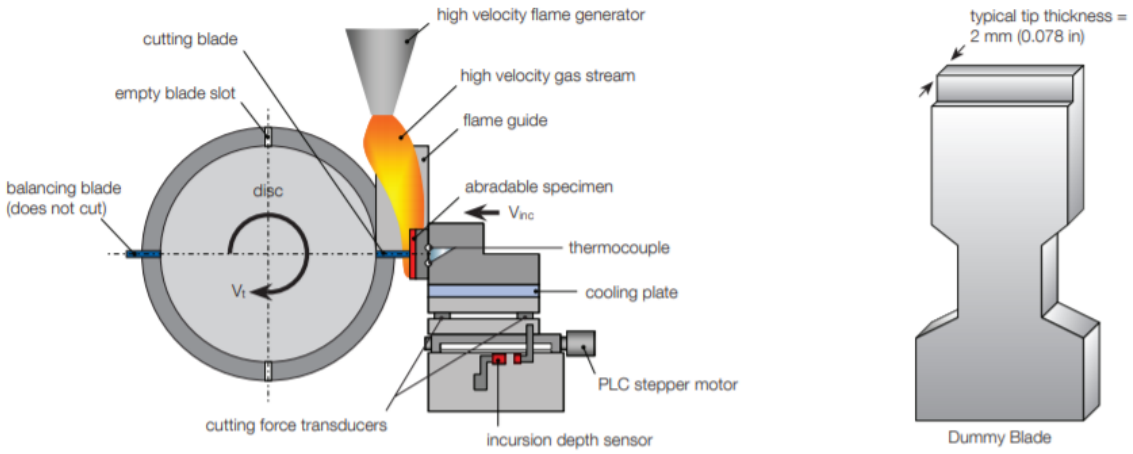

Fig. 2.3 The Oerlikon Metco rig schematic [35].

Another rig capable of reaching engine representative speeds was constructed by the National Research Council Canada [36, 37]. An image of the rig is shown in Fig. 2.4. This rig is capable of reaching the blade tip speed of 425m/s and incursion speed from 2.5µm/s to 760µm/s. The rig is capable of heating an abradable sample up to a temperature of 600ºC with a wire-wound resistor located at the back of a tested sample, meaning that only the abradable, but not the rotating blade is heated. Based on the diagram, it is possible to perform both axial

and radial incursions using this rig. It is also instrumented with a pyrometer for temperature measurements and a load cell for force measurements. In the work by Dadouche et al. [36] blade material loss measured in mm^3 as well as post-test images of abradable rub tracks were used for comparing results of different tests.

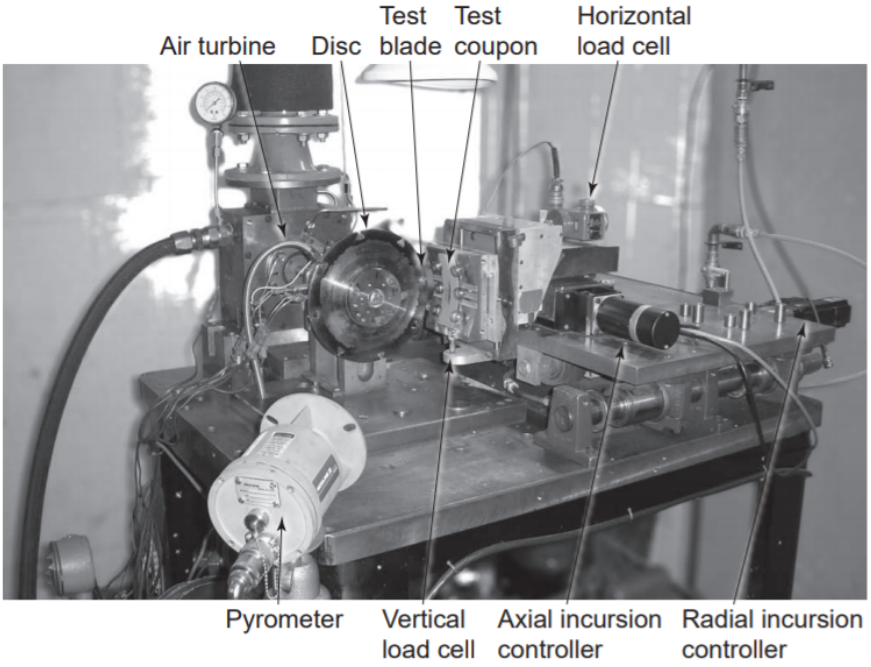

Fig. 2.4 The Gas Turbine Laboratory rig [36].

The rig developed in Zhejiang University [38, 39] can also reach engine representative speeds. The rig is powered by a 45kW DC motor with the disk assembly being on a flexible shaft, which is connected to the disk by a pulley. Schematic of the rig is shown in Fig. 2.5. According to the specifications, the rig is capable of producing the maximum blade tip speed of 520m/s. The stated incursion speed is 5-2000µm/s and the maximum heating temperature is 1200ºC, which makes it very similar in specifications to the Oerlikon Metco rig. This rig is additionally instrumented with a piezoelectric dynamometer and an infrared thermometer, suggesting that force and temperature data can be collected by this rig. There is also a capability for collecting wear debris. Post-test measurements of blades and abradable samples sample weight changes were also recorded for the tests performed using this rig.

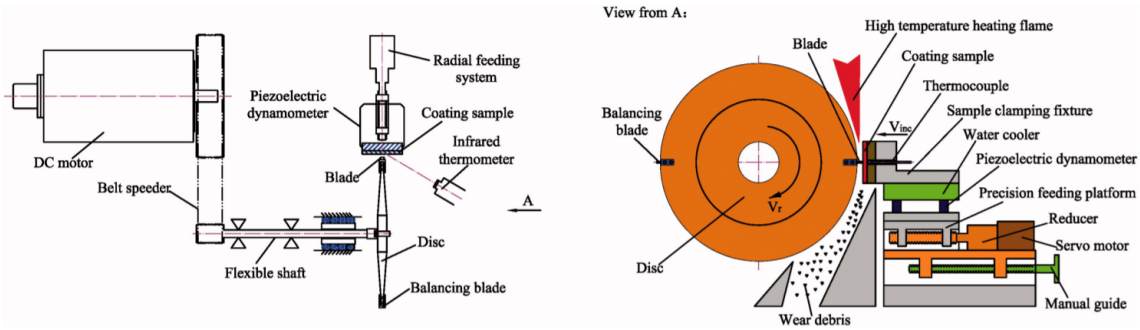

Fig. 2.5 Zhejiang University rig schematic [38].

One of the scaled rigs, which can't reach the engine representative speeds of 380-400m/s was developed at the University of Sheffield. This rig is later referred in this report as the low-speed rig and can reach speeds up to 200m/s [40]. The diagram of the rig is shown in Fig. 2.6. The rig can achieve incursion rates between 0.1 and 1000µm/s. It is instrumented with a pyrometer for measuring the abradable surface temperature during a test, a force dynamometer capable of collecting force data in 3 dimensions, a holder for collection of wear debris and a stroboscopic imaging system, allowing to monitor the maximum length of a blade from the side during an entire performed test. Despite being limited to a lower speed than the rigs mentioned above, the stroboscopic imaging system installed on this rig allowed to track changes in blade maximum length in-situ for the first time as shown in the work by Fois et al. [41], being an improvement to commonly used post-test blade length and weight measurements.

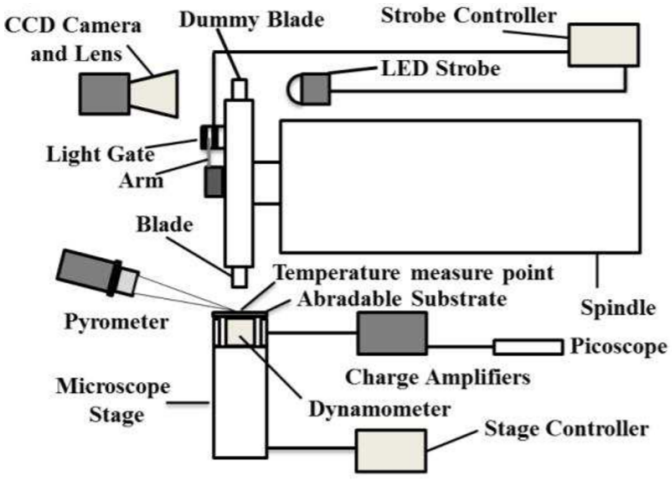

Fig. 2.6 The University of Sheffield rig [42].

Another rig with a similar design was developed at Chinese Academy of Sciences [43, 44]. Its schematic is given in Fig. 2.7. This rig is capable of reaching speed of up to 300m/s and uses a 2000W xenon lamp to heat up the abradable sample suggesting only the sample and not the blade is heated. The incursion speed range is stated to be 2-5000µm/s. This rig is instrumented with a dynamometer for monitoring forces during a test. Post-test measurements of blade length and weight changes were recorded for tests performed using this rig. Additionally, SEM and profilometry were used for a more detailed post-test analysis of blade and abradable wear patterns.

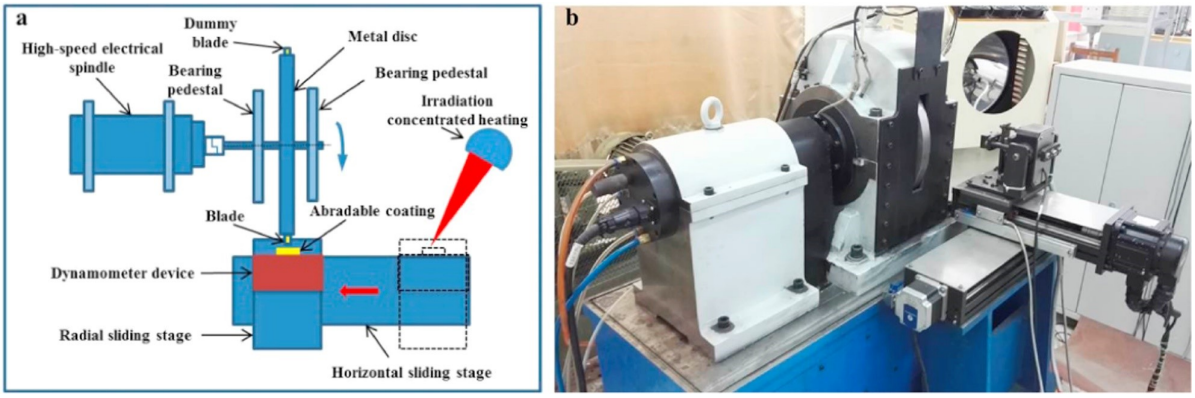

Fig. 2.7 The Chinese Academy of Sciences rig [44].

Latterly, a rig was developed at Technische Universität Dresden with a novel capability to test blades of engine representative geometry and ability to vary the number of abradable segments from 1 to 20 as presented by Nitschke et al. [45]. The rig picture is shown in Fig. 2.8. However, the blade tip speed and incursion rate capabilities are unknown from the literature and only limited data is currently available from the tests performed using this rig.

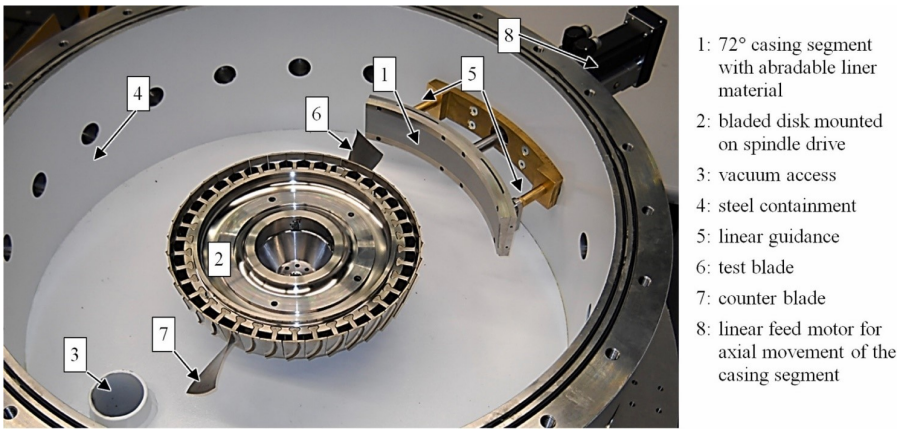

Fig. 2.8 The Technische Universität Dresden rig [45].

Table 2.1 Summary of experimental abradables testing rigs.

Rig	Engine Speed	Engine Temperature	Blade Geometry	Force data	Temperature data	In-situ Blade length
Oerkilon Metco	x	x		x	x	
Zhejiang University	x	x		x	x	
NRCC	x	x (only abradable)		x	x	
University of Sheffield				x	x	x
Shenyang		x (only abradable)		x	x	
Dresden	?		x	x	x	

Table 2.1 summarises the instrumentation available on different rigs that were discussed above, x indicates that this feature is included in the rig, ? denotes places where insufficient information is available. All the rigs attempt to measure forces observed during abradable-blade contacts as they are a good indicator of abradable material removal effectiveness. Most of the rigs capture abradable temperature during a test as it can provide further insight into wear mechanisms. Most researchers have also used post-test measurements of blades weight or length change to guide their discussion of wear mechanisms observed during tests. Recently, some advancements were made in this area as using such tools as SEM and profilometry for a more detailed post-test analysis of wear conditions on the blade [44] and using stroboscopic system for measuring blade maximum length changes throughout a test [41].

2.2.3 Wear mechanisms in tests with the AlSi-based abradables

Most of the research on experimental test rigs was performed on understanding the wear mechanisms of AlSi-based materials, primarily AlSi-polyester and AlSi-hBN. Borel et al. [25] produced the first comprehensive list of wear mechanisms commonly seen in aeroengines compressors through examinations of in-service worn AlSi-plastic and nickel-graphite coatings

from compressor stages. The following wear mechanisms were identified: erosion, corrosion and oxidation of an abradable coating, cutting, deformation of an abradable coating when it was plastically deformed by a blade tip resulting in coating compaction, adhesive transfer from an abradable to a blade and vice versa, melting of materials at the rubbing interface and tribo-oxidation in labyrinth segments.

Despite no information of what rubbing conditions, for example, incursion speeds, have produced such wear mechanisms, these findings had a significant importance for abradable research as they were commonly used by researchers as a benchmark for results from experimental work. The comparisons were made to ensure that rub conditions (such as blade tip speed and incursion speed) used during laboratory tests were representative of engine conditions, i.e. produced realistic wear mechanisms that are observed in aero-engines. Experimental rigs were then used to try to identify conditions, which lead to the above-mentioned wear mechanisms in an attempt to understand what rub conditions would allow to minimise occurrence of the unfavourable wear mechanisms.

In the same article, Borel et al. [25] presented results obtained by using the Oerlikon-Metco rig for AlSi-plastic type abradables in the form of wear maps shown in Fig. 2.9. These maps have shown that for an AlSi-plastic coating with a filler material molten at this temperature, adhesive transfer to the blade has occurred for most of the tested conditions, except for very high blade tip speeds, where blade tip melting wear occurred, likely due to excessive frictional heating in a contact. For an AlSi-plastic coating with a filler material solid at the testing temperature, for low speeds, adhesive transfer to the blade tip occurred at low incursion speeds, smearing for medium incursion speeds, and adhesive transfer from the blade tip to the coating at high incursion speeds; for high speeds, cutting wear mechanism was observed. Although not specified in the article, it is believed by the author that the AlSi-plastic coating with a molten filler was the AlSi-polyester type abradable and the AlSi-plastic coating with a solid filler was the AlSi-hBN type abradable.

These wear maps were useful for understanding the operating regimes (combinations of blade tip and incursion speeds) leading to favourable and unfavourable wear mechanisms in abradables, however only two factors (blade tip speed and incursion speed) were considered and only a limited number of data points were obtained. That limited the applicability of such maps to only a very specific set of testing conditions.

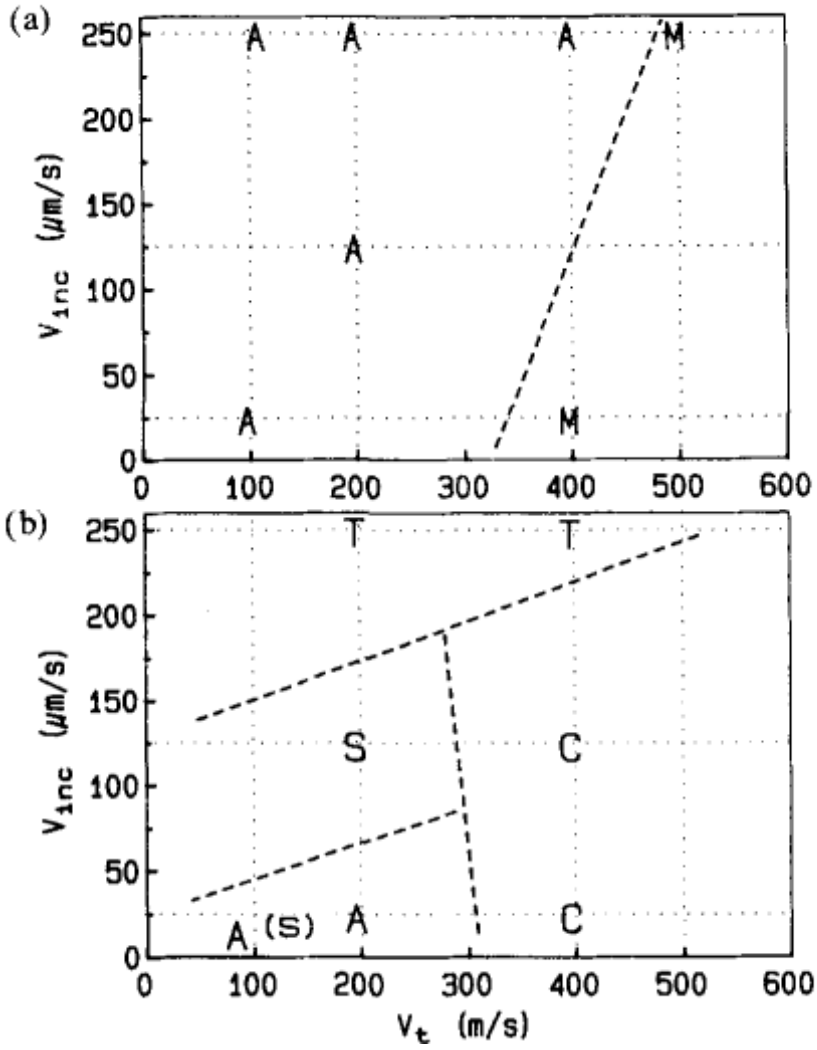

Fig. 2.9 Wear mechanism maps o£ two different AlSi-plastic coatings tested at T = 350°C. a, Coating with low-melting-plastic (molten at 350 °C); b, coating with higher-melting-plastic (solid at 350 °C). The letters show where tests were run and which mechanism occurred: A, adhesive transfer from the coating to the blades; M, melting wear of blade tip; S, smearing; C, cutting; T, adhesive titanium transfer from the blade to the coating [25].

Following on, Bounazef et al. [46] has performed characterization of AlSi-hBN abradables of 60.74 hardness on the HR15Y Superficial Rockwell hardness scale using the Oerlikon Metco rig and found that high blade tip speeds and incursion rates led to reduced material transfer to the blade as can be seen in Fig. 2.10. Cutting was suggested as the key mechanism for higher incursion speeds of 60μm/s and 550μm/s. Adhesive transfer from an abradable to a blade was seen at the lowest incursion speed of 10μm/s. Additionally, in the work by Bounazef et al. [46]

the fracture of adhesions from a blade was observed suggesting that post-test analysis of blades might not be sufficient for classifying the severity of adhesive wear.

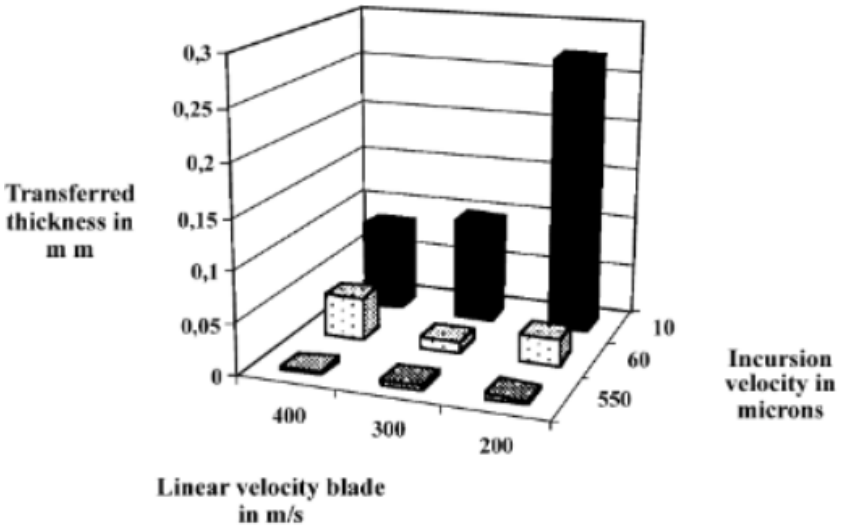

Fig. 2.10 Three-dimensional wear map [46].

In order to better understand the wear mechanisms, a scaled 200m/s rig was used at the University of Sheffield by Stringer et al. [40] and Fois et al. [41, 47, 42]. In the work by Stringer et al. [40], it was identified that mixed wear modes could occur at different blade width locations within a single test. This finding has demonstrated the limitation of using the weight change and the maximum post-test blade length for wear mechanism classification.

The results obtained by Fois et al. [41] using the stroboscopic imaging system allowed to track the progression of a wear mechanism throughout a test for the first time. The fracture of adhesions during a test was confirmed from the imaging results as shown in Fig. 2.11 highlighting that post-test analysis of blades might not be sufficient for classifying the severity of adhesive wear.

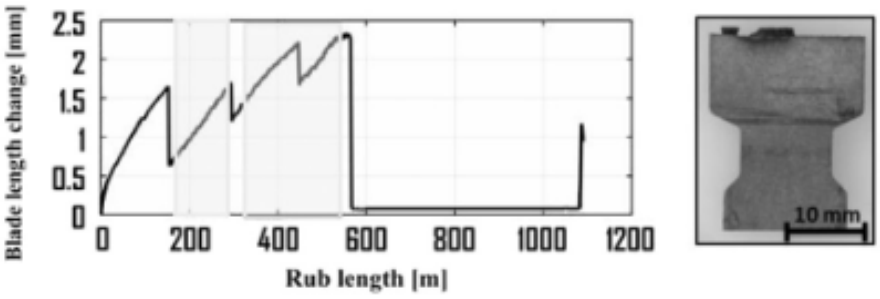

Fig. 2.11 Blade length change as a function of rub length for blade velocity 150m/s, and an incursion rate of 0.02µm/pass [41].

By combining measurements obtained using the stroboscopic imaging system and dynamometer, Fois [48] created a more detailed wear map for the AlSi-hBN abradable material shown in Fig. 2.12. The general trend in results was similar to observations by Bounazef et al. [46] with increases in blade tip speed and incursion rate leading to the cutting wear mechanism with low formation of adhesions and similarly, at low incursion rates adhesions were observed. However, the results by Fois [48] showed that different test outcomes could occur with abradable samples of different sprayed hardness with all the other testing parameters being the same. This result showed that testing an abradable material batch of a single hardness is insufficient to fully classify the performance of an abradable material and tests should be performed with the entire range of spraying hardnesses for a given material (for example, the commonly used spraying range for the AlSi-hBN abradable material is 45-70 on the HR15Y Superficial Rockwell hardness scale [5]).

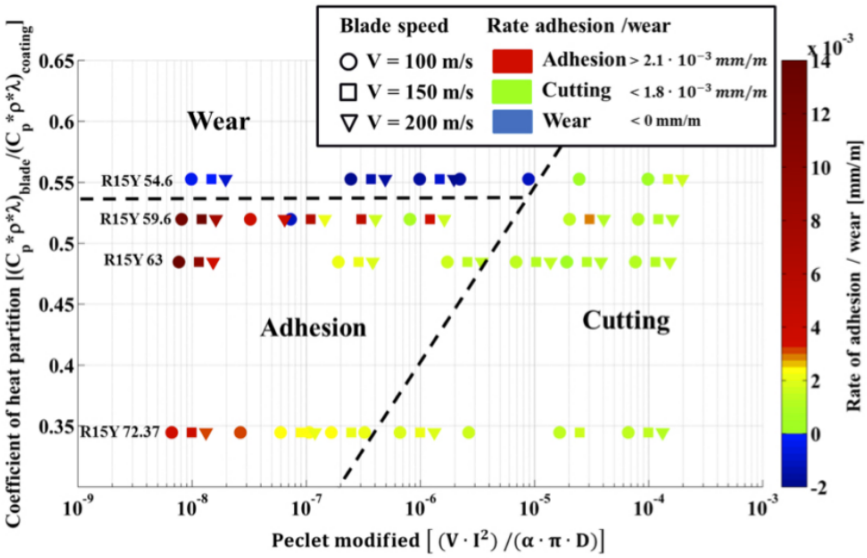

Fig. 2.12 Wear map of the AlSi-hBN material based on coefficient of heat partition and Peclet number [48].

Xue et al. also investigated AlSi-hBN abradables – titanium blades contacts using a rig developed at the Chinese Academy of Sciences [43, 49, 50, 44] and found a similar strong effect of both speed and incursion rate on the observed wear mechanisms. Based on the post-test analysis they concluded that a high blade speed and low incursion rate were the requirements for the increased abradable transfer to a blade. There was also evidence blade wear and adhesive transfer to the blade co-occurred for the test at 0.085µm/pass incursion rate and 90m/s blade speed further supporting previous findings that mixed wear mechanisms could occur in tests with abradable materials.

Additionally, in the work by Xue et al. [44] the effects of blade materials characteristics on wear mechanisms in contacts with AlSi-hBN abradable were investigated. Blades of three different titanium alloys (Ti(6Al4V), Ti(8Al1Mo1V), and Ti(5Al2Sn2Zr4Cr4Mo)) were tested at three different incursion speeds 5µm/s, 50µm/s, and 500µm/s). It was found that for the tests with Ti(6Al4V) blades, the adhesions were the most severe, the Ti(8Al1Mo1V) blades had fewer adhesions and the Ti(5Al2Sn2Zr4Cr4Mo) blades had the fewest adhesions as shown in Fig. 2.13. It was suggested that the differences observed between blades of different compositions were primarily due to differences in thermal properties with the Ti(5Al2Sn2Zr4Cr4Mo) blades having the minimal amount of adhesions due to the high thermal conductivity and high molybdenum content. The results in this work demonstrated that not only the abradable composition but also blade composition is important in determining what wear mechanisms occur in abradable-blade contacts.

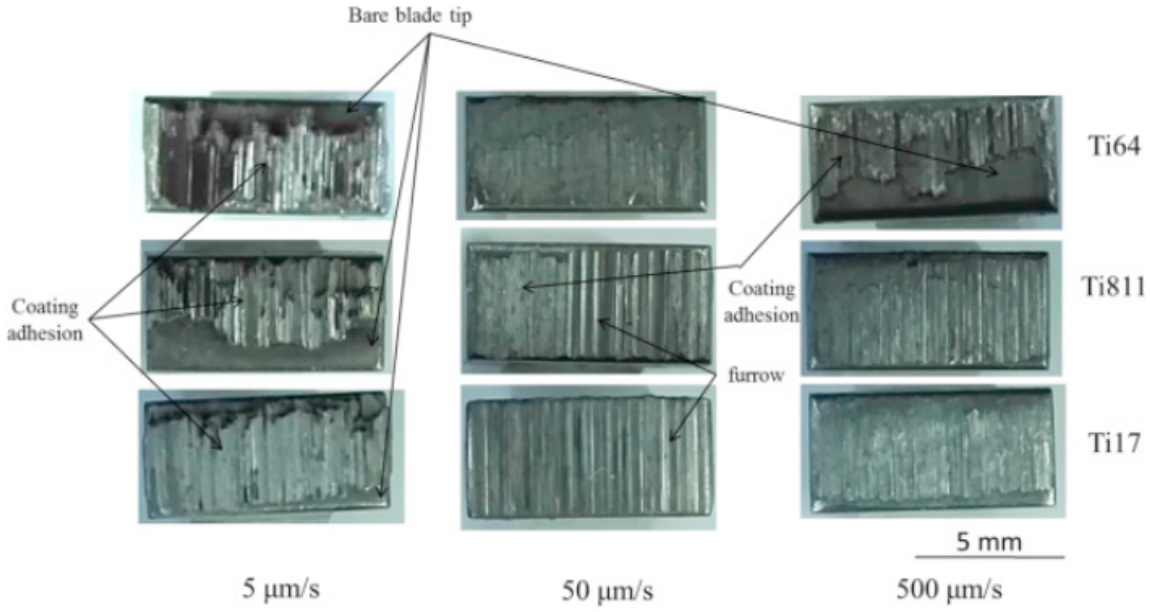

Fig. 2.13 Macro-morphologies of the wear scars of the rubbed blade tips [44].

Latterly, contacts with AlSi-polyester abradable were investigated on the the University of Sheffield scaled 200m/s rig by Watson et al. [6, 51] and Hadjisoteriou [52]. In the work by Watson [6], incursion tests were performed with Ti(6Al4V) blades rubbed against AlSI-polyester abradables of 3 hardnesses (55, 63 and 79 on the HR15Y Superficial Rockwell hardness scale) at 3 speeds (100m/s, 150m/s and 200m/s) and 3 incursion rates (0.02µm/pass, 0.2µm/pass and 2µm/pass). The results from these tests were used to created a statistical model relating contact forces, temperatures and blade wear to testing parameters through equations defined by suggested wear mechanisms. Adhesive and abrasive wear was suggested for low

incursion rates (0.02µm/pass and 0.2µm/pass) and cutting for high incursion rates (2µm/pass) as shown in Fig. 2.14. It was shown that the model for forces provided a good fit to test results at low incursion rates, but not at the 2µm/pass incursion rate. While the suggested mechanisms could not fully explain the test results at 2µm/pass and were not able to explain why under some conditions blade wear and under other adhesions occurred for the adhesive and abrasive wear mechanism, they managed to relate the contact mechanics principles to the wear mechanisms observed in contacts with AlSi-polyester abradable and provided a good starting point for further investigations of wear mechanisms in such contacts.

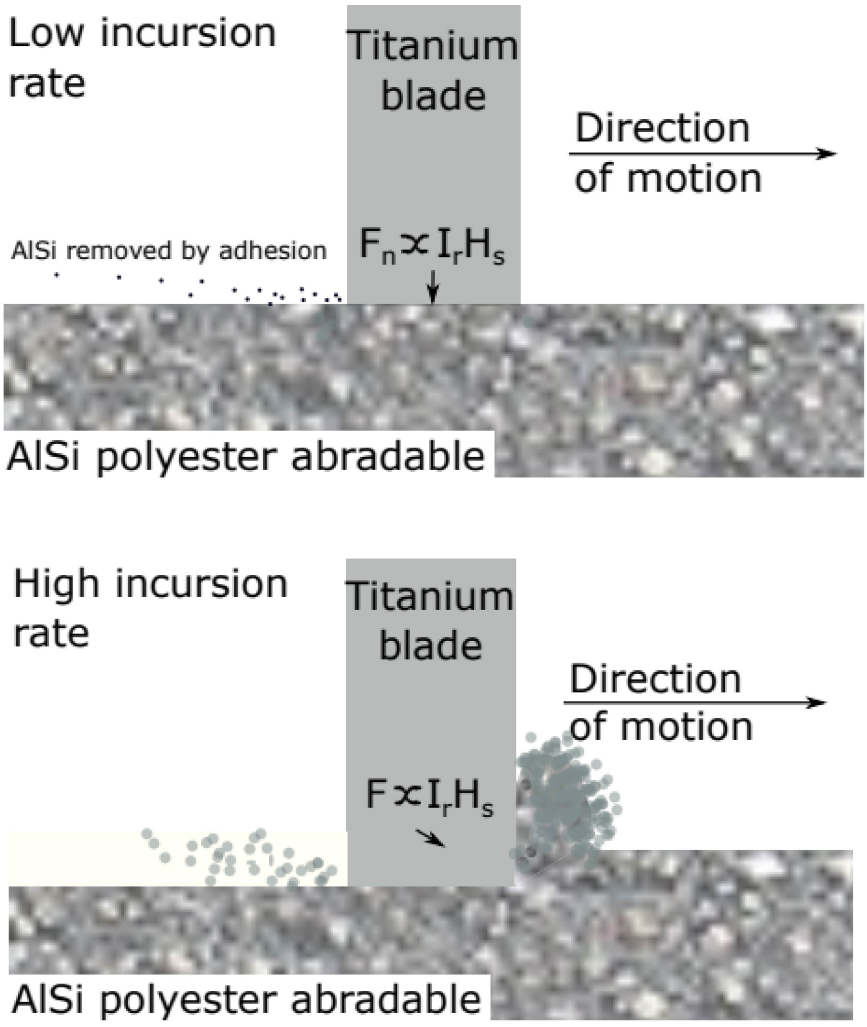

Fig. 2.14 The wear mechanisms hypothesised for the AlSi-polyester abradable [6].

In the work by Hadjisoteriou [52] contacts with AlSi-polyester and AlSi-hBN abradables were further explored through a number of improved in-situ measurement techniques such as measurements of wear debris ejection direction with a side-on camera focused on an

abradable sample rather than a blade. The results shown in Table 2.2 showed that the way incursion rate affected ejection direction is similar for both materials with higher incursion rate promoting more material ejection at the front of a blade. However, despite some improvement, a significant amount of material was still removed from the back of a blade for both materials, particularly for the AlSi-polyester material, where at the most favourable conditions (H55 hardness, 2µm/pass) only 57% was removed from the front. Additionally, with an increase in hardness, the improvement with incursion rate significantly decreased, with H82 samples having a similar amount of material removed from the front at all incursion conditions. This might offer an explanation to why the statistical model based on the cutting mechanism suggested by Watson [6] for tests at high incursion rates with AlSi-polyester abradable samples did not provide a good fit to test results as rubbing could still be significant at such incursion rates.

Table 2.2 The results from material ejection analysis showing the total percentage of material removed from each direction, M601 is the AlSi-polyester abradable and M320 is the AlSi-hBN abradable [52].

Test No.	**Abradable Material**	**Hardness (RY15)**	**Incurssion Rate (micros/pass)**	**Front of Blade (%)**	**Back of Blade (%)**
1	M601	55	2	56.54	43.46
2	M601	55	0.2	47.638	52.362
3	M601	55	0.02	38.987	61.013
***4**	M601	70	2	55.789	44.211
5	M601	70	0.2	48.954	51.046
6	M601	70	0.02	39.578	60.422
***7**	M601	82	2	34.221	65.779
8	M601	82	0.2	37.651	62.349
9	M601	82	0.02	35.155	64.845
10	M320	58	2	59.456	40.544
11	M320	58	0.2	47.692	52.308
12	M320	58	0.02	32.452	67.548
****13**	M320	64	2	62.145	37.855
14	M320	64	0.2	52.975	47.025
15	M320	64	0.02	38.114	61.886
****16**	M320	70	2	70.454	29.546
17	M320	70	0.2	58.486	41.514
18	M320	70	0.02	48.958	51.042

Note: * Indicates observation of excessive sparks during the test, ** Indicates observation of very high angle of ejection during the test

It was shown that a different trend with hardness was seen for the AlSi-hBN material, where the proportion of material ejected from the front of a blade increased with an increase in hardness. This result agreed with the previous findings by Fois et al. [42] where it was shown that test outcomes improved at all incursion conditions with an increase in AlSi-hBN abradable hardness. Interestingly, it can also be seen in Table 2.2 that not all of the AlSi-hBN abradable material was removed from the front of a blade for tests even at 2µm/pass, suggesting that cutting commonly used to describe contacts with AlSi-hBN abradable at high incursion rates could be an incomplete description of the contact mechanism for this type of abradable too, and some rubbing could still be occurring.

2.2.4 Wear mechanisms in tests with the NiCrAl-bentonite abradable

Significantly less experimental work has been performed on understanding the wear mechanisms in contacts with the NiCrAl-bentonite abradable used in higher temperature stages of compressors in comparison to AlSi-based abradable materials discussed in the previous section, with works by only two authors identified in this area: Taylor et al. [53] and Watson et al. [8, 6, 51].

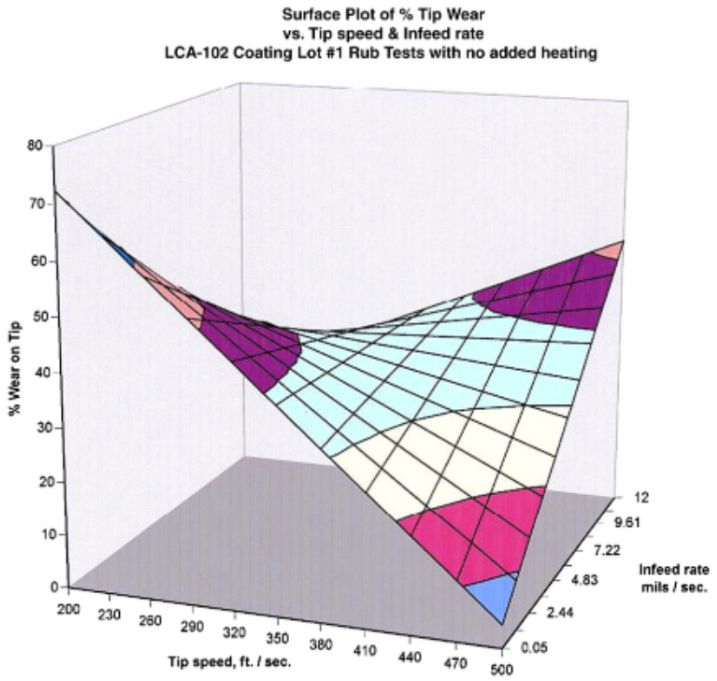

Fig. 2.15 Surface plot of % tip wear resulting from multiple correlation to tip speed and infeed rate test variables. Non-heated tests [53].

In the work by Taylor et al. [53], a range of blade tip speeds(200-500ft/s or 61-152m/s) and incursion speeds was considered (0.05-12mils/s or 1.27-305µm/s, the converted incursion rates were 0.4-244µm/pass). In that study the lowest blade tip wear was seen for the test condition at the highest blade speed and the lowest incursion speed. As can be seen in Fig. 2.15, an interesting interaction was observed where the percentage of blade wear decreased with an increase in incursion speed at the lowest speed of 200ft/s and increased with an increase in incursion speed at the highest speed of 500ft/s. While such behaviour was noted, no explanation of it was provided in that work.

The work by Taylor et al. [53] provided a good initial overview of the wear mechanisms in contacts with NiCrAl-bentonite abradable, however, it had a few limitations such as considering samples from only a batch of a single nominal hardness and considering only one type of blade tip alloy. Some of these limitations were addressed in a later study by Watson et al. [51], where abradable samples from batches of different hardnesses were considered.

In that work, it was found that abradable hardness and incursion rate had the largest influence on the wear mechanisms in contacts with NiCrAl-bentonite abradable. Both the increase in hardness and incursion rate increased contact forces and led to more blade wear. An increase in the blade tip speed was shown to improve test outcomes, but the impact of this parameter was lower than that of the hardness and incursion rate. Interestingly, no interaction between the blade tip speed and incursion rate was observed in this work and the effects of both incursion rate and blade tip speed were consistent at different incursion conditions.

It is important to note, however, that the upper bound of incursion rates considered in the work by Watson et al. [51] was considerably lower than in the work by Taylor et al. [53] (2µm/pass vs 244µm/pass). Additionally, tests up till the incursion rate of 97µm/pass in the work by Taylor et al. [53] were following a similar trend to results by Watson et al. [51] with an increase in incursion rate leading to an increase in blade wear. The difference occurred only for the test at 244µm/pass, where a significant improvement in blade wear occurred. This could have been caused by a transition to a different abradable removal mechanism, likely cutting, creating this non-linearity in the results by Taylor et al. [53]. It is also important to note that based on the data available on contacts with abradable materials in aero-engines, the incursion rates are unlikely to significantly exceed 2µm/pass suggesting that this non-linearity occurs only at incursion rates outside of the interest range for aero-engine applications and that abradable removal mechanism in aero-engines is consistent with what was observed in tests by Watson et al. [51] and the lower end of considered incursion rates in tests by Taylor et al. [53].

Based on the results obtained from tests at different speeds and incursion rates and with abradable samples of different hardnesses Watson suggested the sub-surface damage and release

mechanism illustrated in Fig. 2.16 as the primary abradable removal mechanism for tests with the NiCrAl-bentonite abradable.

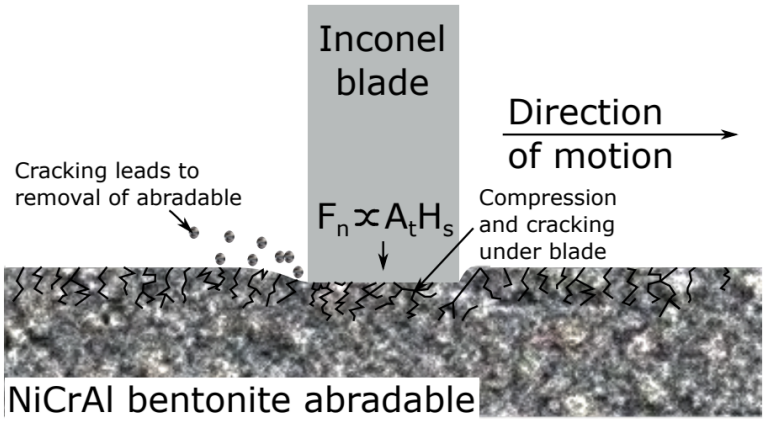

Figure 4.16: The sub-surface damage mechanism hypothesised for the NiCrAl bentonite abradable

Fig. 2.16 The sub-surface damage mechanism hypothesised for the NiCrAl-bentonite abradable [6].

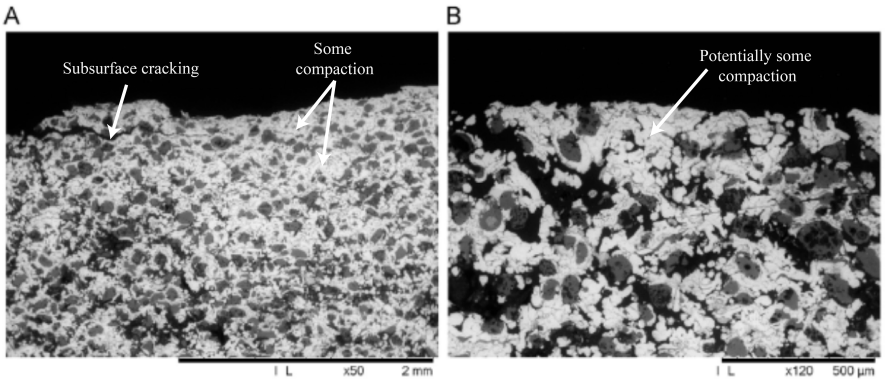

Fig. 2.17 a) A micrograph of the abradable from a test against batch B at 2µm/pass showing severe compaction and subsurface cracking and b) a micrograph of the abradable from a test against batch A at 0.02µm/pass showing local compaction at the surface [51].

The effect of incursion rate on wear mechanisms was then explained through this suggested abradable removal mechanisms. At low incursion rates, sub-surface damage to the abradable was able to keep up with incursion rate and blade wear was low. With an increase in incursion rate, it was suggested that the mechanism remained the same but increase in forces and temperatures led to consistent blade wear throughout the test. At the highest tested incursion rate (2µm/pass) damage to the abradable surface could not be accommodated quickly enough

and abradable compaction occurred. A significant amount of abradable compaction was confirmed through SEM measurements of abradable surface. Additionally, a small amount of local surface compaction was seen for a test even at the lowest incursion rate of 0.02µm/pass as shown in Fig. 2.17. This agreed with the results by Taylor et al. [53] where abradable compaction was also seen for tests at high incursion rates up to 97µm/pass (no significant compaction was observed for the previously discussed test at 244µm/pass).

Following the initial set of results, potential blade tip modifications were explored in the work by Watson [8] to improve test outcomes at unfavourable test conditions for tests with the NiCrAl-bentonite abradable (high incursion rates with samples of high hardness). The used modifications were the addition of grits of different sizes on blade tips, using a Cr(Al)N coating on standard blades and using blades with an angled tip and a Cr(Al)N coating as shown in Fig. 2.18.

Out of all the tested modifications, blades with an angled geometry and Cr(Al)N coating showed that largest potential for improving test outcomes. Additionally, in further work [6] it was shown that the improvement in performance was primarily due to the addition of an angled tip geometry rather than the use of the Cr(Al)N coating.

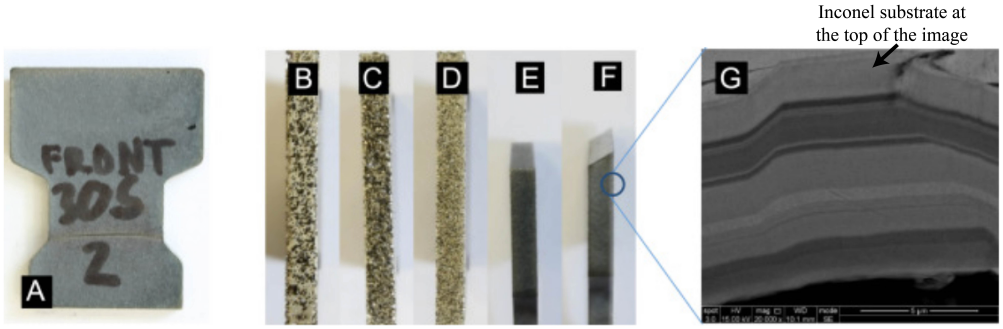

Fig. 2.18 a) The shape of the blade samples, tips of blades prepared with b) large, c) medium and d) small grits, e) the flat and f) chamfered tip morphologies of the Cr(Al)N blades used and g) a secondary electron image of the Cr(Al)N coating, with the Inconel 718 substrate the top of the image respectively. Blades are 20 mm wide and 2 mm thick [8].

With further testing, the addition of an angled geometry was identified as potentially simple modification for blade tips to improve test outcomes in terms of blade wear at low incursion rates (0.02µm/pass). It was also shown that a larger angle led to a larger amount of improvement up to the tested angle of 20 degree (Fig. 2.19). At medium and high incursion rates (0.2-2µm/pass), angled blades showed no benefit or detriment in performance in comparison to the standard blades with a flat tip.

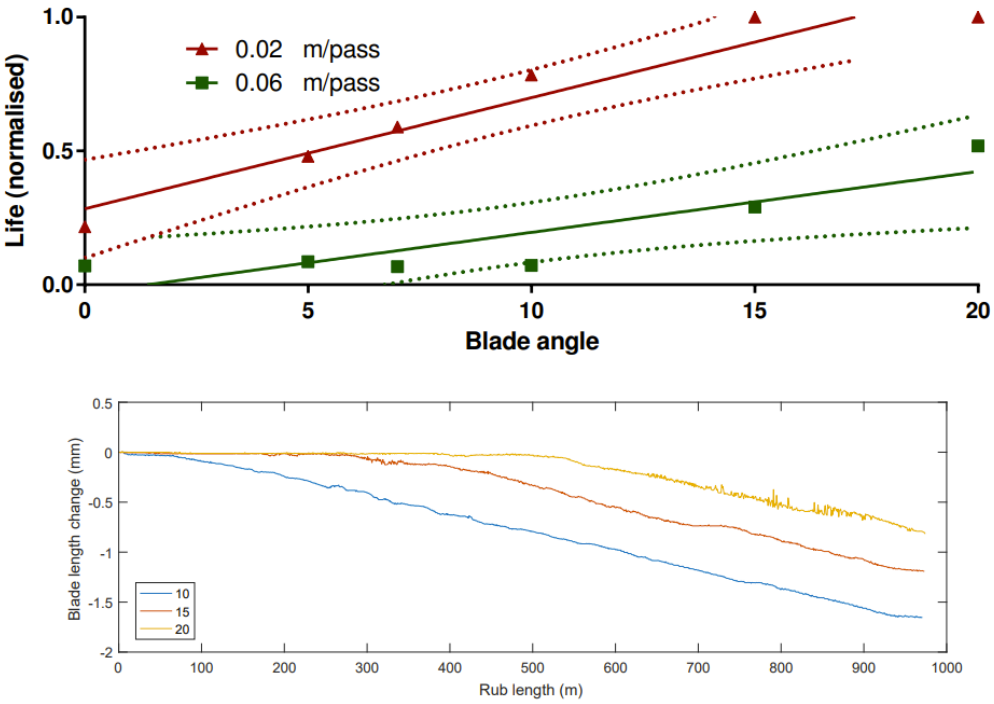

Fig. 2.19 The life of the blades from tests at 0.02µm/pass and 0.06µm/pass with tip angles from 0 - 20 degrees with lines of best fit and 95% confidence bounds normalised by the total expected test rub length (top plot) and full blade length results from tests at 0.06µm/pass (bottom plot) [6].

The improvement in performance at low incursion rates was explained by reductions in contact forces and temperatures, however, this proposed mechanism could not explain why no benefit was seen at higher incursion rates. Further research is required to identify how angled blades improve blade wear performance before they could be implemented in aero-engines.

2.2.5 Summary

The research on abradable materials could be largely subdivided into research into material properties and research into abradable-blade contact mechanics with both performed through either modelling or experimental approaches.

The research into material properties of abradables allowed to better understand how spraying parameters could affect mechanical and thermal properties and gave insights into the microstructure of abradable materials. However, material properties on their own were insufficient to predict the wear mechanisms observed in contacts with abradable materials and most of the research on wear mechanisms observed in such contacts was performed using scaled and full-scale experimental rigs.

The knowledge base on wear mechanisms in contacts with abradable materials was expanded over the years by multiple researchers. The main wear mechanisms were identified to be abradable cutting, blade wear, adhesion formation, abradable removal through sub-surface damage and abradable compaction. Abradable cutting was characterised by an effective abradable surface removal resulting in smooth abradable surface and little to no damage to a blade. This mechanism occurred in contacts with AlSi-hBN abradable at high speed and incursion rate testing conditions as was demonstrated by Bounazef et al. [46] and Fois [41].

The blade wear mechanisms occurred as a result of two body abrasion between a blade and an abradable. When this mechanism occurred, blade surface was frequently visibly thermally damaged. This mechanism was observed in contacts with AlSi-polyester and AlSi-hBN abradables at low incursion rates [51, 41] and with NiCrAl-bentonite abradable at most of the considered incursion rates [51].

Adhesion formation was characterised by the transfer of abradable material onto blade tip resulting in an increase in blade length. This mechanism occurred in contacts with AlSi-polyester and AlSi-hBN abradables at the lower end of incursion rates (0.02-0.2µm/pass) [51, 41]. For the tests, where adhesions occurred, post-test blade tips usually had non-uniform length and abradable samples were grooved.

The sub-surface damage mechanism was explained by repeated blade strikes leading to crack growth in the top layer of abradable surface and causing subsequent fracture of small particles from an abradable surface. It was suggested as the primary abradable removal mechanism in contacts with the NiCrAl-bentonite abradable [51].

Finally, compaction (densification of the top layer) of an abradable has occurred during some of the tests with NiCrAl-bentonite abradable at high incursion rates [51] and AlSi-hBN abradable at low incursion rates [48].

A large part of experimental work has focused on classifying which of these wear mechanisms occur depending on testing conditions for different combinations of blade and abradable materials. Such testing parameters as incursion rate, blade tip speed, abradable hardness (particularly for the AlSi-hBN abradable), and blade tip alloy materials were identified as important in determining the outcome of an incursion test. However, there are still some gaps in current understanding of contacts with abradable materials.

These gaps for example include the classification of a wear mechanism under certain testing conditions. For example, for tests with the AlSi-polyester abradable at high incursion rates, cutting was previously assumed to be the abradable removal mechanism, while a model based on the cutting mechanism in the work by Watson et al. [6] was not able to explain the test outcomes and later results by Hadjisoteriou [52] showed that a significant amount of abradable

is still released behind a blade at such testing conditions indicating that rubbing could be important.

Furthermore, for tests at low incursion rates (0.02µm/pass) a mixed wear mechanism with both blade wear and adhesions present was previously observed with both AlSi-polyester and AlSi-hBN abradables. This mixed mechanism was explained by the presence of localities on abradable sample surfaces due to the randomness of the spraying process, however, a complete explanation of which material properties lead to blade wear and which lead to adhesions was not given. In the work by Xue et al. [44] it was suggested that blade thermal properties such as thermal conductivity played an important role in determining whether adhesions occur or not, but further research is required in the area of explaining adhesive transfer and blade wear mechanisms.

The research into these mechanisms was complicated by the limitations of blade length measurements techniques. In the past research these wear mechanisms were commonly assessed by post-test investigation of blades and abradable samples or by using a side-on stroboscopic imaging technique. The limitations of using blade length and weight change measurements for wear mechanism classification have been shown by Stringer et al [40] for the cases where simultaneous blade wear and adhesive mechanisms occurred within a single test. Additionally, in the works by Bounazef et al. [46] and Fois et al. [41] fracture of adhesions from a blade was observed suggesting that post-test analysis of blades might not be sufficient for classifying the severity of adhesive wear. In the work by Fois et al. [41] using a side-on stroboscopic imaging allowed measurements of the maximum blade length throughout an entire test. However, by measuring from the side, it wasn't possible to tell at what exact position along the blade width adhesions occurred, what was the size of an adhesion in terms of its width and if there were only one or multiple different adhesions on a blade along its width at any given time. In this work, a front-on stroboscopic imaging system is developed for the new test rig, where the entire blade width is seen to address the limitations of using the side-on imaging and post-test blade length measurements for wear mechanisms classification. Details about the design and operation of the rig and the front-on stroboscopic imaging system are given in chapter 3.

For NiCrAl-bentonite abradable, only limited experimental results have been published. The works by Taylor et al. [53] and Watson et al. [8, 6, 51] allowed to establish relationships between testing parameters such as incursion rate, blade tip speed and abradable surface hardness and the amount of blade wear and abradable compaction observed during tests. In the work by Watson et al. [51] subsurface damage and release was identified as the abradable removal mechanism.

However, several limitations have been identified in the current knowledge of contacts with the NiCrAl-bentonite abradable. In the published works, the maximum testing blade tip

speed was 200m/s [51]. As speed was identified as an important parameter in determining the severity of blade wear, it will be necessary to conduct tests at higher speeds to understand if the trends seen in previous research hold up at engine representative speeds. This limitation will be partially addressed in this thesis by performing tests at up to 280m/s blade tip speed on the newly commissioned test rig.

In the work by Watson [6], an addition of the angled geometry to the blade tip allowed to improve test outcomes at low incursion rates(0.02-0.06µm/pass) in terms of blade wear. In this work, the effectiveness of introducing an angled geometry will be further investigated in an attempt to improve the understanding of the mechanism that leads to improved outcomes, which is required before such modification could be implemented in aero-engines.

Finally, no experimental studies have been identified which investigated the effects of simplifications used on experimental test rigs on test outcomes. In this work, the effect of two such simplifications will be investigated to improve the understanding of how results obtained using test rigs could be translated to incursion event outcomes in aero-engines.

Chapter 3

Materials and methodology

This chapter covers the materials and equipment used in this thesis. First, standard blades and abradable samples used for incursion tests are described. Then, two rigs used to perform incursion tests are presented, with the main focus given to the newly commissioned high-speed rig. This chapter ends with a description of all the equipment used for the pre and post-test analysis of blades and abradable samples.

3.1 Blades

The standard blades used throughout this thesis are a simplified version of the blades used in aero-engine compressors with features such as a twist, lean, camber and variable chord thickness ignored for simplicity of manufacture. They have a flat cutting face, as shown in Fig. 3.1(b,d). The design is shown in Fig. 3.1(a,b) for short blades and Fig. 3.1(c,d) for long blades. The long blade is the original design used by the Sheffield research group; the short blade is the new design with an increased resistance to bending failure when excessive tangential forces occur during a test.

The blades differed by material and design. Two materials were used: Ti(6Al4V) blades for tests against the AlSi-polyester abradable and Inconel 718 blades for tests against the NiCrAl-bentonite abradable. The blade designs can be split into two categories: standard and modified. Only the standard blade designs are presented here; when a modified blade design is used, such design will be presented in detail in a relevant experimental chapter.

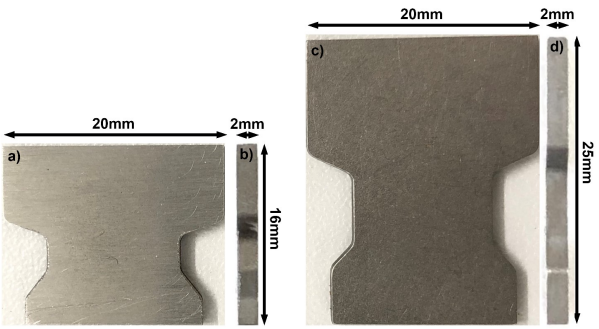

Fig. 3.1 Standard short blade design, a) front view, b) side view; standard long blade design, c) front view, d) side view.

3.2 Abradable samples

Two types of abradable materials were used: AlSi-polyester and NiCrAl-bentonite. All abradable materials were sprayed onto identical stainless steel sample backing plates (80mm x 80mm) to an area of 60mm x 60mm. A standard coating thickness was around 4mm but could be different depending on the batch of samples and could be between 3mm and 5mm. An example of a standard abradable sample is given in Fig. 3.2.

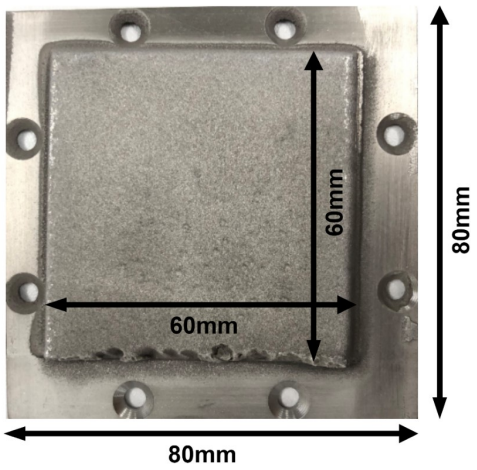

Fig. 3.2 A standard AlSi-polyester abradable sample. The 8 holes are for mounting a sample on the sample holder.

3.2.1 Age hardening

Previous data from Rolls-Royce plc. have shown that NiCrAl-bentonite abradables undergo age hardening at their operating temperature (Fig. 3.3). The hardness values were stable after

3000 minutes (50 hours) for samples hardened under all temperature conditions. To account for the worst-case operating conditions, all the NiCrAl-bentonite samples used in this thesis were aged at 750°C for 100 hours in a box furnace (Elite Thermal Systems Ltd, BCF11/8). AlSi-polyester samples were not aged.

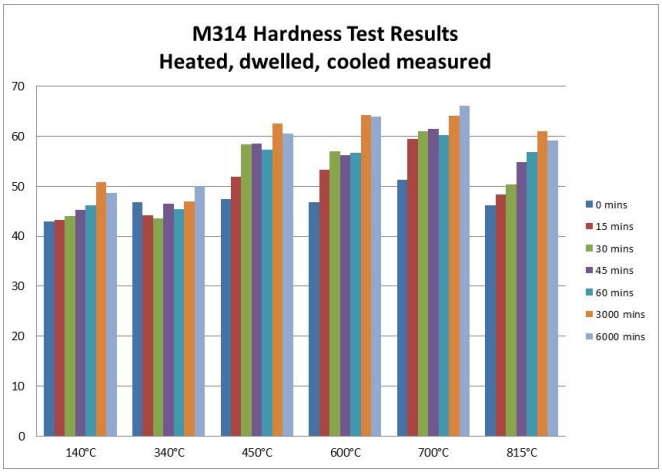

Fig. 3.3 The NiCrAl-bentonite abradable age-hardening results [54].

3.3 Test rigs

Two test rigs have been used for the incursion tests in this thesis: the low-speed rig previously used by multiple researchers [48, 6, 52] and the newly commissioned high-speed rig. Both rigs operate using a similar principle, with a rotating blade incurring into an abradable sample mounted on a moving stage. Both rigs are instrumented with a dynamometer, a pyrometer and a secondary camera for spark detection. The front-on strobe is installed on the high-speed rig, while the side-on strobe is installed on the low-speed rig. A diagram giving a summary of the rigs' instrumentation is shown in Fig. 3.4.

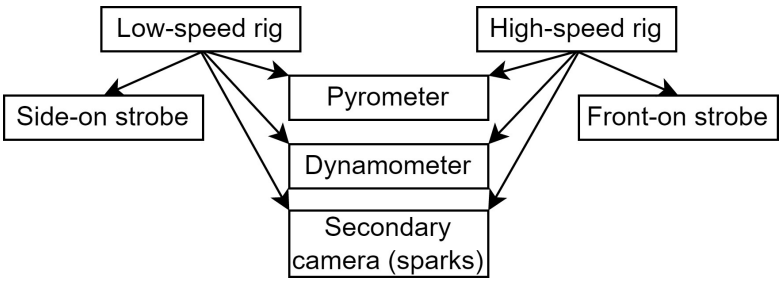

Fig. 3.4 The summary of the rigs' instrumentation.

The high-speed rig is going to be described first and in more detail as this rig was primarily used for the tests for this thesis. The low-speed rig is similar in concept and operation to the high-speed rig, and will be covered subsequently.

3.3.1 High-speed rig

This test rig consists of the following components shown in Fig. 3.5 and 3.6: a spindle, a stage, bearing supports, a disk, which is supported in between the front and the back bearings and a rig containment, which is built out of steel plates and steel blocks, which are filled with concrete on the inside. The spindle (GMN HSP170s - 30000/19) is controlled by the inverter (Emerson SK4401). The spindle is cooled by the water chiller (Hyfra Chilly 45) and lubricated by an oil-air lubricating unit. Gaps in the spindle's casing are purged by a pressurised air supply [6].

The disk is connected to the spindle through a flexible coupling. The cutting and dummy (for disk balancing) blades are inserted into the disk slots located 180 degrees from each other. The cutting tip radius is 163mm with short blades, and the maximum achievable blade tip speed is 300m/s. It is limited by the balance between available spindle power and total (primarily aerodynamic) drag in the system.

The stage consists of a front plate, which allows for attaching the force dynamometer and test samples on it, a ball screw (HD30406-MF-M-U2-20-C20B High Precision Linear Actuator Ball screw driven), a system of gearboxes resulting in a total gear ratio of 600:1 and a servo motor (KEB, 24.SM200-42B0), which is controlled by the rig computer through a stage inverter (KEB combivert F5 servo) [6]. The maximum linear stage speed is 2200µm/s. The practical minimum linear speed is 1µm/s, with the limit imposed by the ability of the servo motor inverter to maintain a constant low speed.

It should also be noted, that during this PhD a new containment was designed [55] and installed for the high-speed, which allowed easier assembly and disassembly of the containment if required and better access to the rig. The image of the new containment is given in Fig. 3.7.

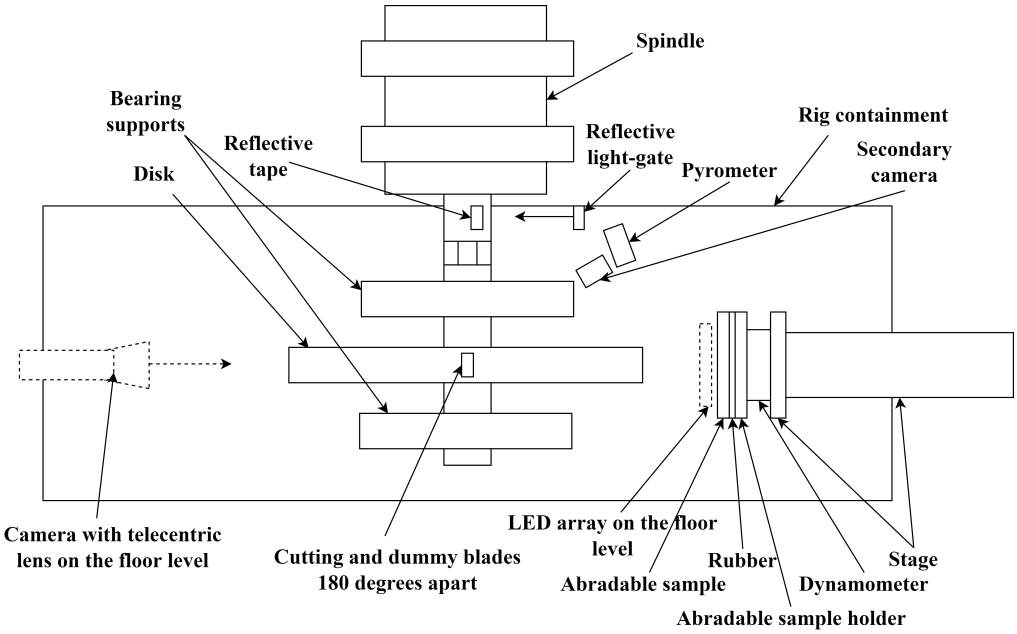

Fig. 3.5 The high-speed rig diagram, top view.

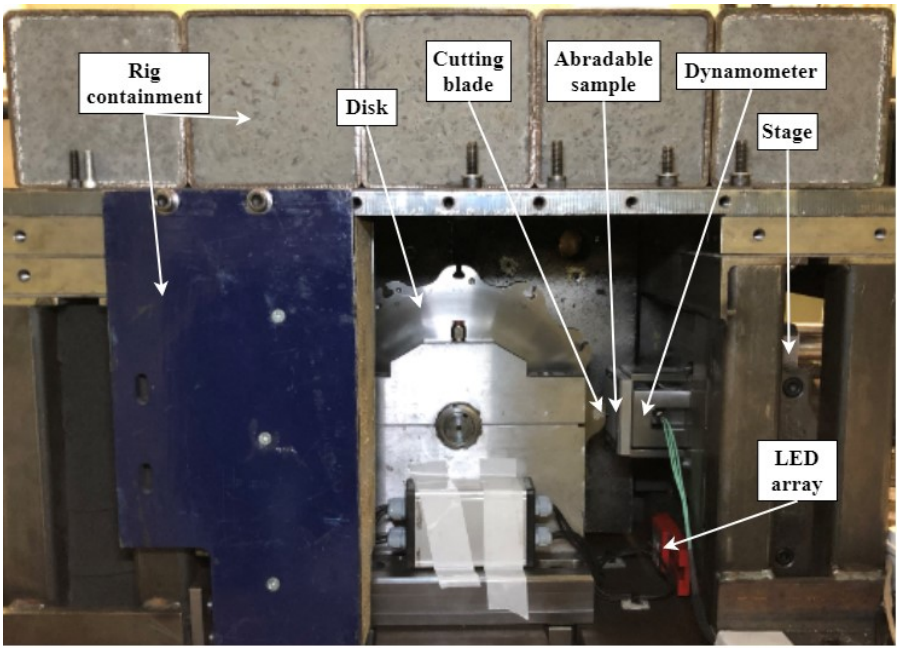

Fig. 3.6 The high-speed rig image, side view.

Fig. 3.7 The new containment for the high-speed rig, top view.

3.3.1.1 Front-on imaging system

The stroboscopic system allows an image of the blade to appear stationary, as light is only on when the blade is in a position best suited for imaging it. The system on the high-speed rig consists of the following parts: a reflective tape mounted on the shaft, a reflective fibre sensor (Omron SensorE32-D21R), an amplifier (Omron E3NX-FA41), a LED strobe controller (Gardasoft PP880) fitted with a signal delay board, LEDs (SHARP GW5BTJ50K03 LED Module, MINI ZENIGATA Series, Cool White, 5000K, 690lm) and a camera (Basler ace - acA1300-60gm, 1.3M resolution, 5.3µm x 5.3µm pixel size) fitted with a telecentric lens (Edmund Optics 0.25X SilverTL™, a combination of the camera and the lens leads to an image pixel size of 21.2µm x 21.2µm). LEDs are positioned directly opposite to the camera from the other side of the blade so that for the captured image, the blade is positioned on a line between the LED array and the camera. The set-up is illustrated in Fig. 3.5.

The system works based on the following principle: the reflective sensor has an emitter (shining light on the shaft) and a receiver (measuring the amount of reflection). When the sensor faces the shaft section with no reflective tape, no reflection is received, and when the sensor faces the shaft section with reflective tape, maximum reflection is received. A threshold is then set on the sensor amplifier between these two values.

During a shaft rotation, the sensor sees the reflective tape once per revolution of the shaft and sends a signal to the strobe controller once the reflection value passes the set threshold

as illustrated in Fig. 3.8. The strobe then turns on the LEDs with a pre-defined delay for a specified pulse width duration. The required delay is based on two factors: the angular position of the reflective tape on the shaft with respect to the cutting blade position and the rotational speed of the shaft and disk assembly. The pulse width and delay times can be controlled from the rig computer using an RS232 communication interface through the Termite software.

The delay can be specified between 5.85µs and 13.1ms with a step of 0.05µs which corresponds to a rotation of 0.00528 degrees at the maximum rotational speed of 17600rpm (the worst-case scenario in terms of uncertainty). That means that almost no uncertainty is introduced by the fact that delays can only be selected as discrete values. However, the human error of selecting a correct delay time was still present.

The pulse width time can be specified between 0.1 and 5µs with a step of 0.1µs. The maximum pulse width of 5µs corresponds to LEDs being on for 0.528 degrees at the maximum rotational speed of 17600rpm, leading to an insignificant amount of blurring on an image due to blade rotation, which had no effect on the quality of data from the images.

The stroboscopic imaging technique is currently operational up to the speed of 300m/s, and the camera records at 60frames/s, capturing approximately one image every five revolutions of the disk at this speed. The image exposure was set as three revolutions of the disk for most tests to increase the total amount of light on the images. Such image capturing settings (capturing images at a lower frame rate than the disk rotational frequency with each image averaged over three revolutions of the disk due to exposure) were acceptable as a difference in blade edge geometry between consecutive revolutions was very small except for the cases where an adhesion delaminated from a blade edge. Significant differences in blade edge geometries occurred on much larger timescales during a test. An example image produced by the stroboscopic imaging system when the camera was exposed over three revolutions of a blade is shown in Fig. 3.9.

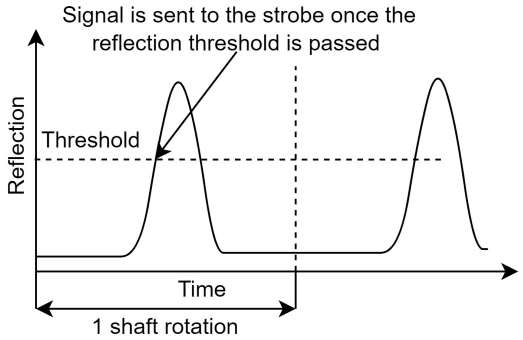

Fig. 3.8 The reflective sensor working principle.

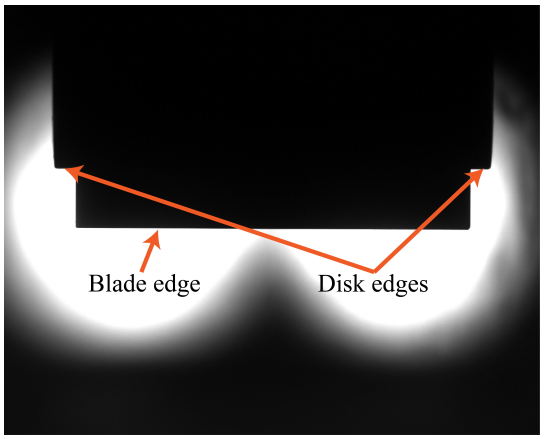

Fig. 3.9 The image of a spinning blade (at 16400 rpm) exposed over three revolutions of a blade.

3.3.1.2 Secondary camera

A secondary camera is installed on the high-speed rig for monitoring the level of sparking during a test. The components include a camera (Edmund Optics EO-1312M Monochrome USB) and a lens (Edmund Optics 25mm C VIS-NIR Series Fixed Focal Length Lens). An example image from the secondary camera is given in Fig. 3.10.

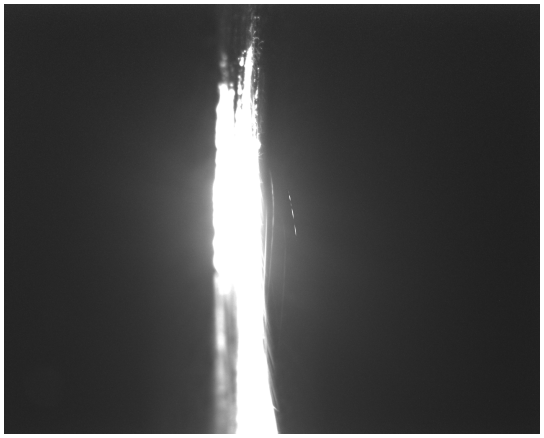

Fig. 3.10 An example image from the secondary camera focused on the contact area between a blade and an abradable sample showing sparking in the contact

3.3.1.3 Dynamometer

A 3-axis dynamometer (Kistler Type 9347C) is installed on the high-speed rig. It is used to measure contact forces between a rotating blade and a stationary abradable sample during

incursion tests. It is connected to the rig computer through a charge amplifier (Kistler Type 5070A) and a digital oscilloscope (PicoScope 3000 or PicoScope 5000), as shown in Fig. 3.11.

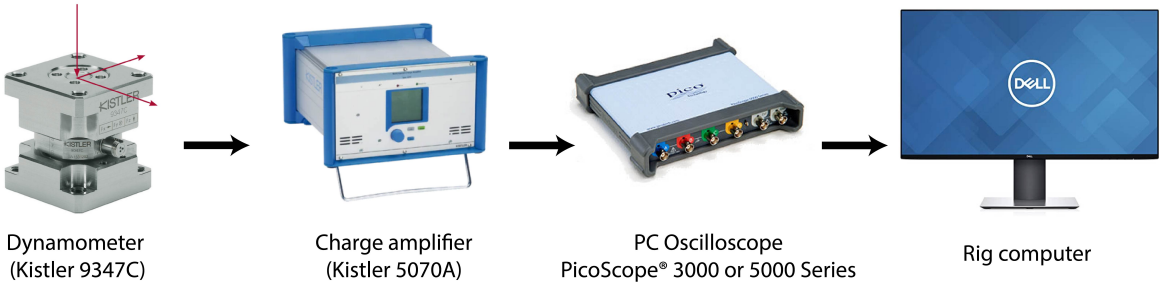

Fig. 3.11 The dynamometer connection from the sensor to the rig computer.

The dynamometer is positioned between the stage front plate and an abradable sample holding plate, as shown in Fig. 3.12. Conventions for force directions used throughout this thesis are the following: normal force is in the direction perpendicular to the direction of blade rotation, and tangential force is in the direction of blade rotation.

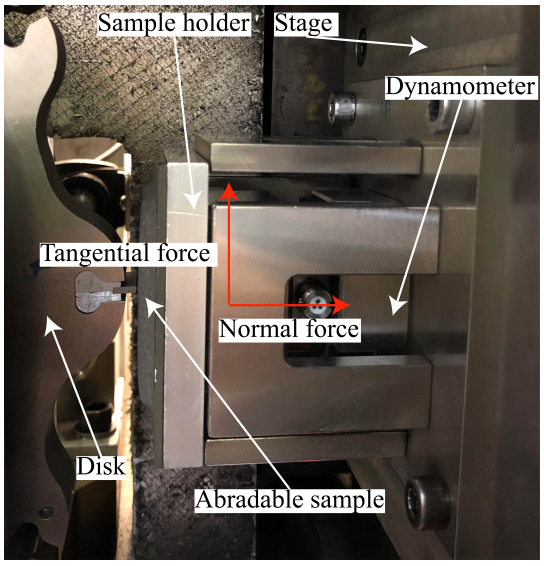

Fig. 3.12 The dynamometer assembly with red arrows indicating force conventions used throughout this thesis.

Data from the dynamometer could be affected by vibrations, which could originate from two sources: excitation from the spinning disk (even when there is no contact between the disk and an abradable) and the dynamometer vibrations following a blade strike.

Vibrations due to the spinning disk occurred when the 12th multiple of the disk rotational frequency (due to 12 slots in the disk) coincided with the dynamometer's natural frequency

in the direction of normal forces. An example of such vibrations is shown in Fig. 3.13 – half-amplitude of vibrations was 300N with no ability to identify individual blade strikes.

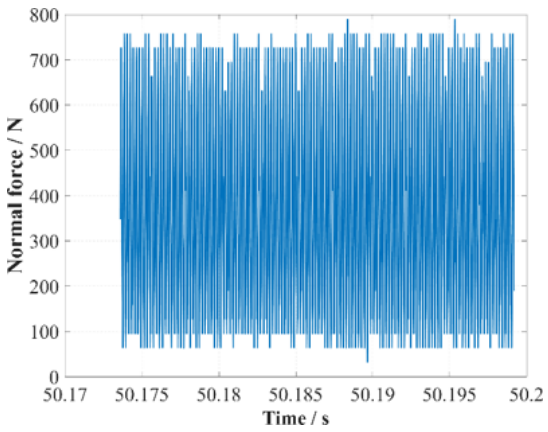

Fig. 3.13 The dynamometer response without the rubber between a sample and the sample holder for the test with short flat Inconel 718 blade and H55 M314 abradable sample (heat-treated for 1h) at 200m/s speed and 0.06µm/pass incursion rate.

Vibrations following blade strikes occurred due to system response being underdamped. Such response is normal, however, it was desirable that force damped down to 0N before the next blade strike occurs – so that vibration from a previous blade strike does not interfere with a new blade strike.

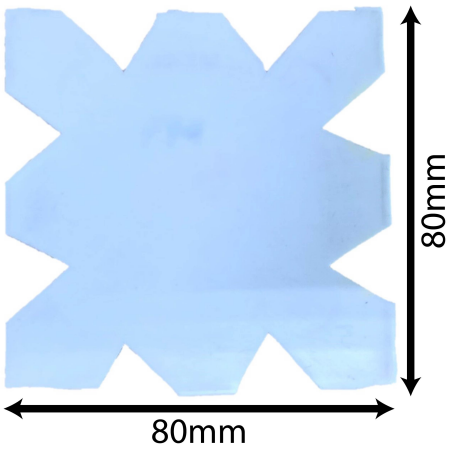

Fig. 3.14 The rubber sheet placed between an abradable sample and the sample holder.

The rubber sheet shown in Fig. 3.14 was installed between an abradable sample and a sample holding plate (the rubber sheet is not present in Fig. 3.12, but was installed for all of the incursion tests on the high-speed rig) to reduce vibrations of the dynamometer during an incursion test. It matches the dimensions of the sample plate (80x80mm) with cut-outs made

for bolts that secure an abradable sample to the sample holder. Installation of the rubber sheet has allowed reducing both the vibrations from the spinning disk and improved damping in response to blade strikes. This improvement in force signal can be seen in Fig. 3.15, where individual blade strikes are clearly seen.

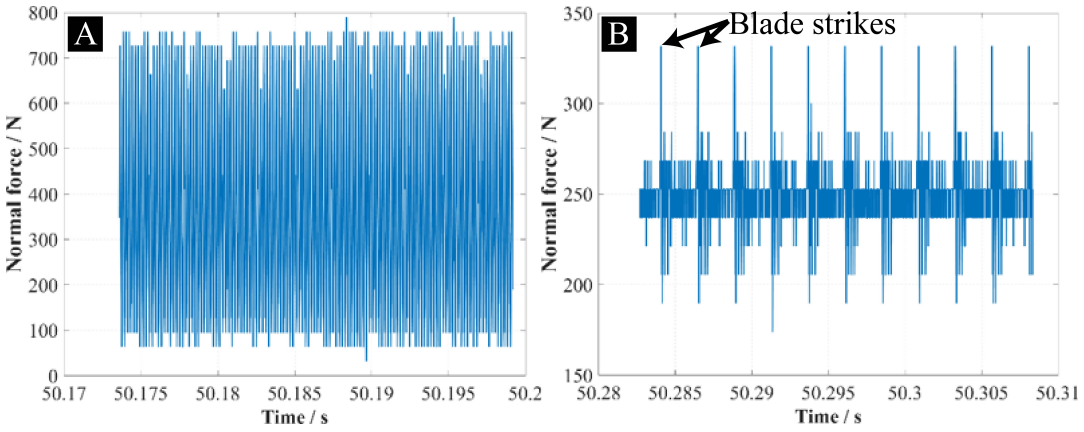

Fig. 3.15 The dynamometer response a) without the rubber between a sample and the sample holder, b) with rubber added; both responses are for tests with short flat Inconel 718 blades and H55 M314 abradable samples (heat-treated for 1h) at 200m/s speed and 0.06µm/pass incursion rate.

3.3.1.4 Pyrometer

The high-speed rig is fitted with an infrared pyrometer (Micro Epsilon CTLM-3H1CF3, 0.7mm focus at 200mm focus distance). It can record temperatures between 150°C and 1000°C and is pointed at the blade-abradable contact area. The sampling frequency is 50Hz, the system accuracy is ±(0.3% T of reading +2C) [56].

3.3.2 Low-speed rig

The low-speed rig consists of the following components: a spindle (GMN HSP120g - 21000/9), a microscope stage (SIGMA KOKI SGSP80-20ZF, can reach linear speeds of 0.1 - 2000µm/s with a step of 0.1µm/s), a disk, which is connected to the spindle with an HSK-C40 coupling, and a rig containment, built out of wood and supporting aluminium plates as shown in Fig. 3.16 and 3.17. The spindle is controlled by the inverter (Emerson SK3403) and is cooled by the water chiller (Hyfra Chilly 45). Similarly to the high-speed rig, the cutting and dummy (for disk balancing) blades are inserted into the disk slots located 180 degrees from each other. With short blades, the cutting tip radius is 96mm, and the maximum achievable blade tip speed is

200m/s. It is limited by the spindle maximum rotational speed. The design of the low-speed rig is described in more detail in [48].

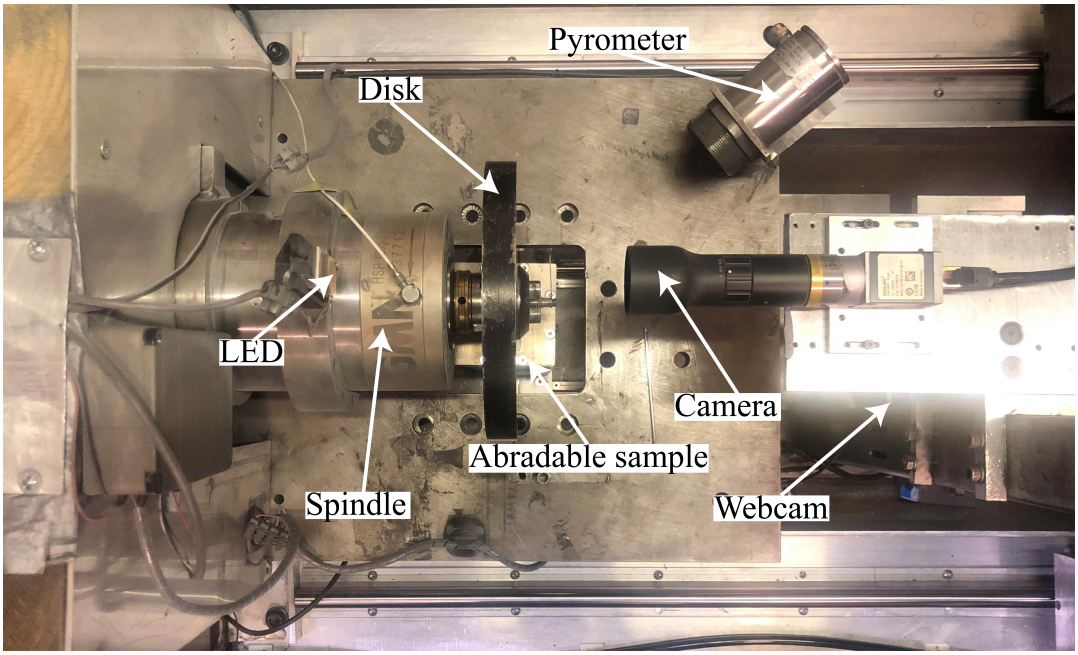

Fig. 3.16 The low-speed rig image, top view.

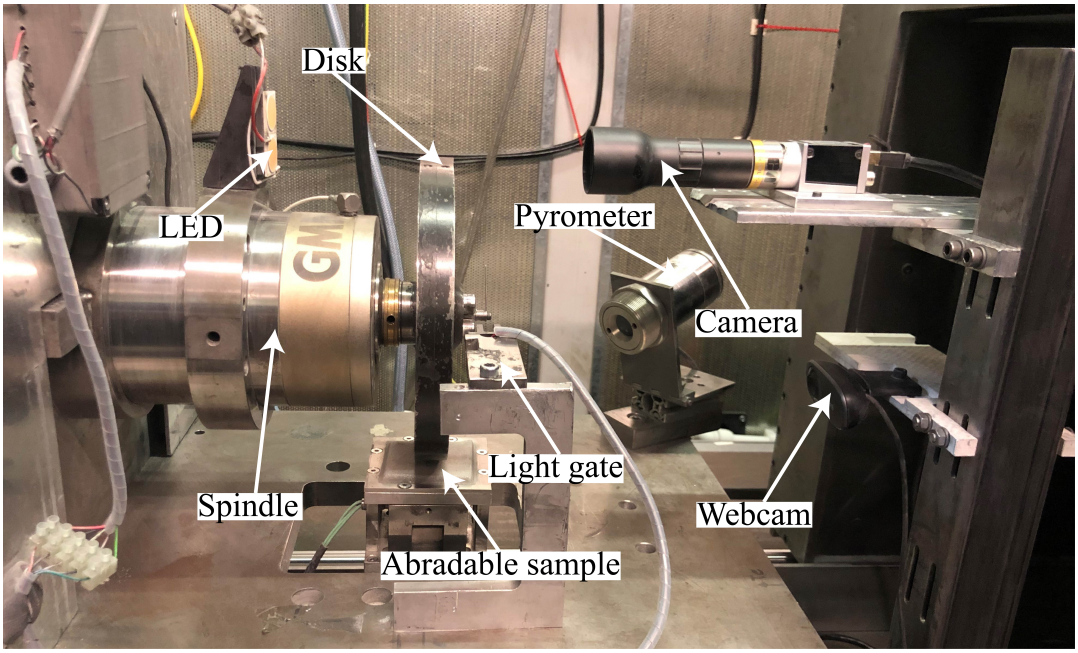

Fig. 3.17 The low-speed rig image, side view.

3.3.2.1 Side-on imaging system

The stroboscopic imaging system installed on the low-speed rig is similar in principle to the one installed on the high-speed rig. It allows capturing an image of a blade from the side rather than from the front. The system consists of the following components: an interruptive sensor (Optek OPB916B), a LED strobe controller (Gardasoft RT200F-20), an LED (Cree CXA2530 LED) and a camera (Basler Ace acA1600-60gm Monochrome GigE, 2M resolution, 4.5µm x 4.5µm pixel size) fitted with a telecentric lens (Edmund Optics 1X SilverTL™, a combination of the camera and the lens leads to an image pixel size of 4.5µm x 4.5µm). The strobe delay can be specified between 3µs and 999ms in steps of 1µs/100µs depending on the value selected for delay. The pulse width can be specified between 1µs and 999ms in steps of 1µs/100µs depending on the value selected for pulse width. An example image obtained using the low-speed rig system is given in Fig. 3.18.

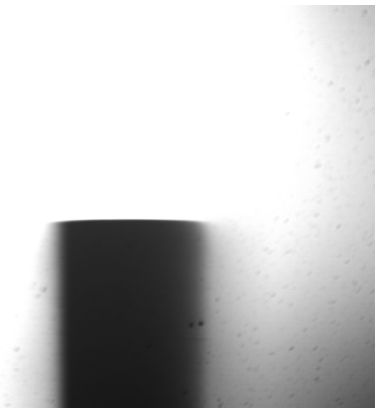

Fig. 3.18 An example image obtained using the low-speed rig stroboscopic imaging system.

3.3.2.2 Secondary camera

The low-speed rig is instrumented with a secondary camera (Logitech C310 HD WEBCAM) to monitor the level of sparking during a test.

3.3.2.3 Dynamometer and pyrometer

The dynamometer and pyrometer systems installed on the low-speed rig are identical to the ones on the high-speed rig described in sections 3.3.1.3 and 3.3.1.4 respectively.

3.3.3 Test procedure

Both rigs are operated using a similar test procedure. Before the start of a test, an abradable sample is mounted on the sample holder plate on the dynamometer, and cutting and dummy blades are secured in the disk using removable blade holders. The stage position, where a blade just touches an abradable is determined setting a zero point on the abradable surface. The stage is then retracted by 500µm from the determined location to allow spin-up of the disk with no contact between a blade and an abradable sample. The rig containment and test cell are closed prior to the disk spin-up as a safety measure.

After the test cell is locked, each rig is controlled through their respective LabVIEW programme. The following test conditions can be defined in a programme: blade tip speed, cutting tip radius (distance from the centre of the disk to the tip of a cutting blade), incursion rate and incursion depth. Test parameters are then used to calculate voltage corresponding to the necessary spindle rotational speed and stage linear speed as follows:

$$V_{test} = 10\frac{v_{tip}}{2\pi r_{tip} rpm_{max}} \tag{3.1}$$

where V_{test} is voltage corresponding to the necessary spindle rotational speed in V, v_{tip} is blade tip speed in m/s, r_{tip} is blade tip radius in m and rpm_{max} is the maximum rotational speed in revolutions/minute (rpm) defined on the spindle inverter.

$$v_{linear} = i_{rate}\frac{v_{tip}}{2\pi r_{tip}} \tag{3.2}$$

where, v_{linear} is stage linear incursion speed in m/s and i_{rate} is incursion rate in m/pass.

After the parameters are defined in the programme, spindle can be spun up to speed – by using a mechanical dial control for the low-speed rig or by pressing a button in LabVIEW for the high-speed rig. Once a spindle is up to the necessary speed, an incursion can be started by pressing the respective button in the programme. Data from all the installed sensors are collected automatically by the programme during a test. Once a test is complete, the programme automatically sends a signal to retract the stage back to the pre-test position (500µm away from the original abradable-blade contact location). Spindle is then turned off by using a mechanical dial for the low-speed rig or automatically by the LabVIEW programme for the high-speed rig.

The testing parameters for performed incursion tests (blade type, abradable material, blade tip speed, incursion rate, rub depth) will be given in relevant experimental chapters.

3.4 Materials characterisation techniques

Several techniques have been used for pre and post-test characterisation of blade and abradable samples. These include surface profile measurements using Alicona SL, SEM images using Desktop SEM TM3030 and hardness measurements on the HR15Y Superficial Rockwell hardness scale.

3.4.1 Alicona SL

Post-test, surface images were recorded for some of the tested abradable samples using the Alicona SL (Bruker Alicona) equipment. The 5x AX lens was used, which had a vertical resolution of 460nm. The measurement area was about 27mm across the cutting direction and 20mm along the cutting direction. An example area used for measurements is shown in Fig. 3.19.

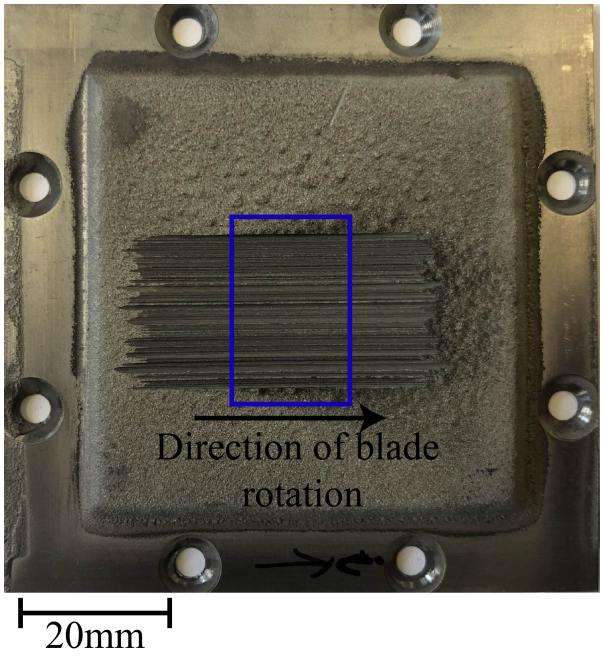

Fig. 3.19 The area selected for the Alicona analysis is shown in blue.

3.4.2 SEM measurements

Back-scattered SEM images of the tested blades and abradable samples were collected using the Desktop SEM TM3030 equipment for further analysis of blade adhesions and wear. The magnifications between x40 and x120 were used. An example of a SEM image of a blade is

given in Fig. 3.20a and of a tested AlSi-polyester abradable surface sectioned across the cutting direction in Fig. 3.20b.

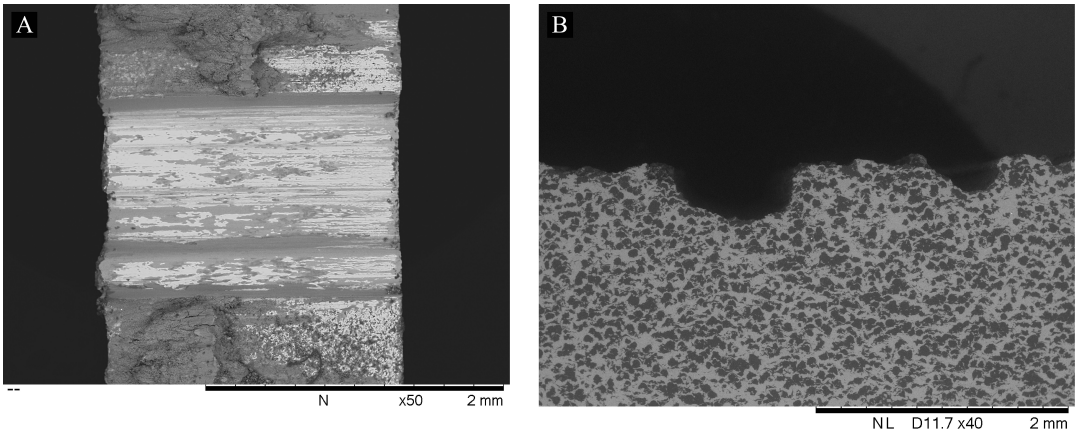

Fig. 3.20 a) a SEM image of a tested Ti(6Al4V) blade, b) a SEM image of a tested AlSi-polyester abradable sample sectioned across the cutting direction.

3.4.3 Rockwell hardness measurements

Abradable materials are sprayed to a target hardness on the HR15Y Superficial Rockwell hardness scale. Some of the abradable samples were hardness tested according to the ASTM E18-15 to validate that they were within the targeted range. The hardness of an abradable sample can vary in different sample locations due to differences in a local material composition. Therefore, hardness was tested in multiple locations for each sample (between 6 and 9) and average hardness value was recorded. The hardness measurements were outsourced. It is important to note that later in this thesis when the hardness value is given in the format of "Hxx", "xx" is the hardness value on HR15Y Superficial Rockwell hardness scale.

3.4.4 Summary

In this chapter, experimental rigs used to perform incursion tests were presented together with an overview of instrumentation installed on these rigs and the equipment used for post-test analysis of blades and abradable samples. In the next chapter, analysis methods developed for data captured during incursion tests and post-test analysis of blades and abradable samples will be presented.

Chapter 4

Data processing

This chapter covers the methods used to analyse data captured during incursion tests and post-test measurements of abradable samples using Alicona. All the processing is shown on the example of data from the test at 200m/s blade tip speed, 0.2µm/pass incursion rate, and 1000µm incursion depth with the Ti(6Al4V) blade rubbed against the AlSi-polyester H69 hardness abradable sample.

4.1 Dynamometer

The dynamometer data processing is presented first, as this data is used to identify test start and end times. The processing is accomplished through the following steps:

First, both tangential and normal force data are imported into MATLAB R2019b. A complete dataset of normal forces is plotted, and test start and end times are selected, as shown in Fig. 4.1a. Tangential and normal force data and a vector of time values are trimmed using the indices of test start and end times. The time values are datumed to the point of test start. For example, if the start time is 8.2s, all time values are subtracted by 8.2 so that the first point of the trimmed dataset corresponds to a time value of 0s. An example of a trimmed normal force dataset plotted against datumed time values is shown in Fig. 4.1b. The time when force data capture is started, and test start and end times are recorded for trimming data from other installed sensors.

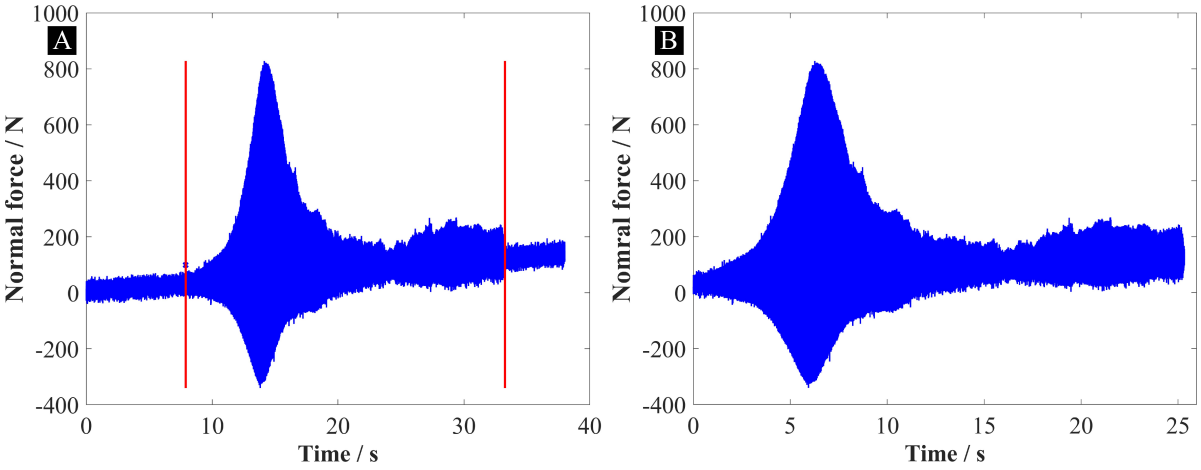

Fig. 4.1 a) A full dataset of normal forces with red lines showing selected test start and end times b) a trimmed dataset of normal forces with time values datumed to the point of time start.

The trimmed tangential and normal force data are then divided into segments. Each segment has a length corresponding to one disk revolution. The length of segments for a given test is determined using the equation below:

$$SegmentLength = F_s \frac{2\pi r_{tip}}{v_{tip}} \tag{4.1}$$

where F_s is the dynamometer sampling frequency.

For each data segment, the maximum value of force is selected. This value corresponds to a single blade strike, as the peak force occurs when a cutting blade strikes an abradable once per disk revolution. A single segment of force data is shown in Fig. 4.2, with the blade strike location highlighted.

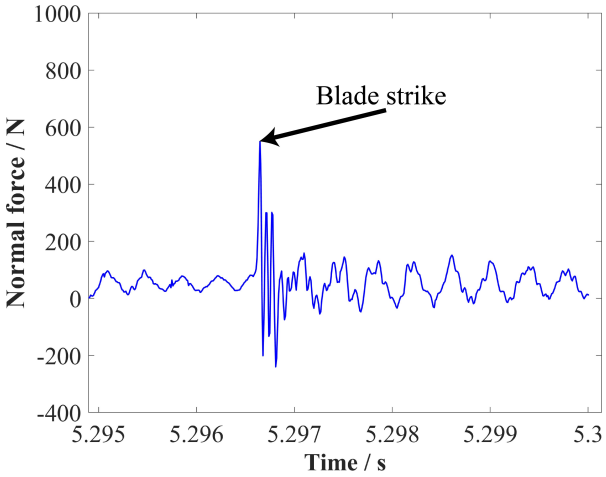

Fig. 4.2 A single segment of force data with the blade strike location highlighted.

It is important to note that in previous research it was found that the force peaks from dynamometer data were representative of contact forces and no dynamic compensation was required [48].

4.1.1 The normal force correction

It was found that normal force data were affected by thermal drift. This happened due to the heating up of the dynamometer throughout a test by air inside the containment heated by a fast-spinning disk. Tangential forces were not affected by the drift. To correct the drift in normal forces, the following procedure was used:

For each blade strike (force peak), the mean value of points from 200 to 75 before the location of a blade strike is calculated. An example area used to calculate the mean value is given in Fig. 4.3. The mean value corresponds to the dynamometer's current zero position. This is because there is no contact between an abradable and a blade during that time, so there is no external force exerted on the dynamometer, and it oscillates around its zero position. Several periods of the dynamometer vibrations were included in the selected area to obtain a representative value of the current zero position.

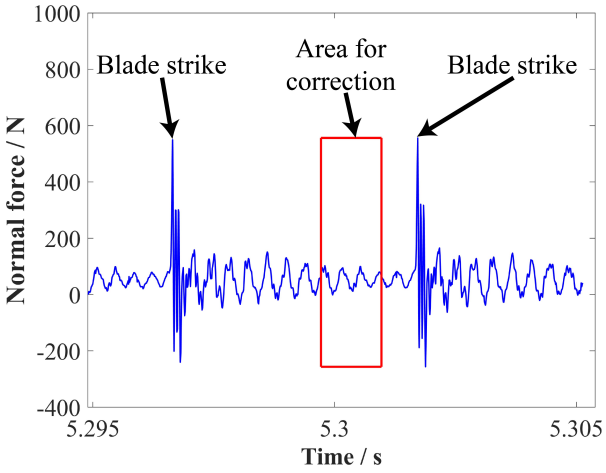

Fig. 4.3 Two segments of force data with blade strikes highlighted. The area used to calculate the current zero value for the second blade strike (points from 200 to 75 before the location of the blade strike) is within the red rectangle.

The obtained mean values are then smoothed using a 500 points Gaussian-weighted moving average filter. Smoothing was considered appropriate as the drift due to a temperature rise was expected to follow a smooth curve. The calculated mean and smoothed mean values throughout a test are shown in Fig. 4.4a. The smoothed mean values are then subtracted from normal forces to obtain corrected normal forces shown in Fig. 4.4b.

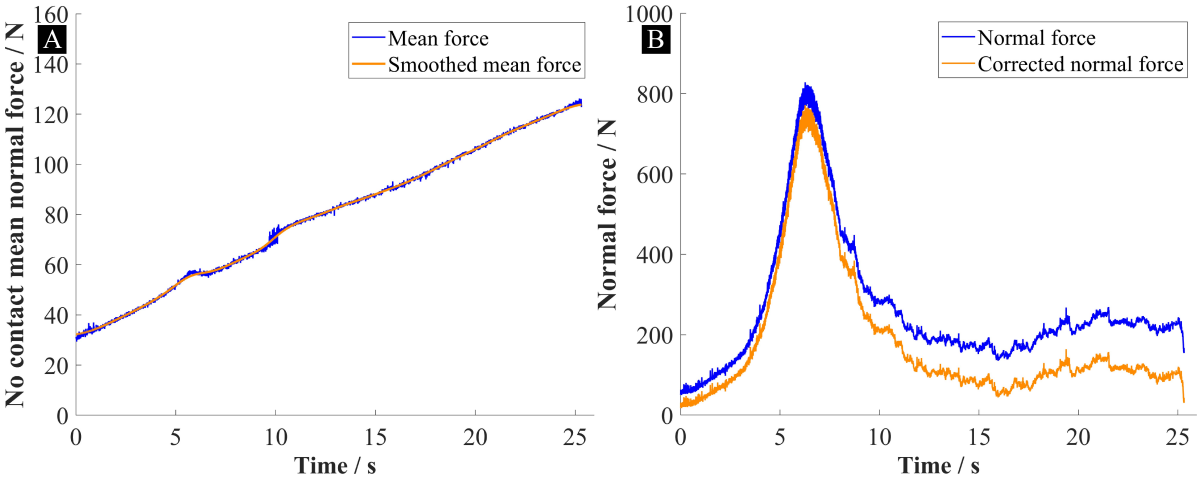

Fig. 4.4 a) No contact mean and smoothed mean normal force throughout a test, b) normal and corrected normal force throughout a test.

To highlight the importance of applying a correction, an example of a test when the worst-case conditions in terms of heating occur is shown. Such conditions are the highest used blade tip speed of 280m/s (due to the largest air temperature rise) and the lowest incursion rate of

0.02µm/pass (due to the long test duration). The mean and smoothed mean values for such a test are shown in Fig. 4.5a. The drift reached values of 1200N, while the corrected normal forces at the end of the test were in the order of 100-200N (Fig. 4.5b). Without a correction, normal forces would have been overestimated by about six times towards the end of the test.

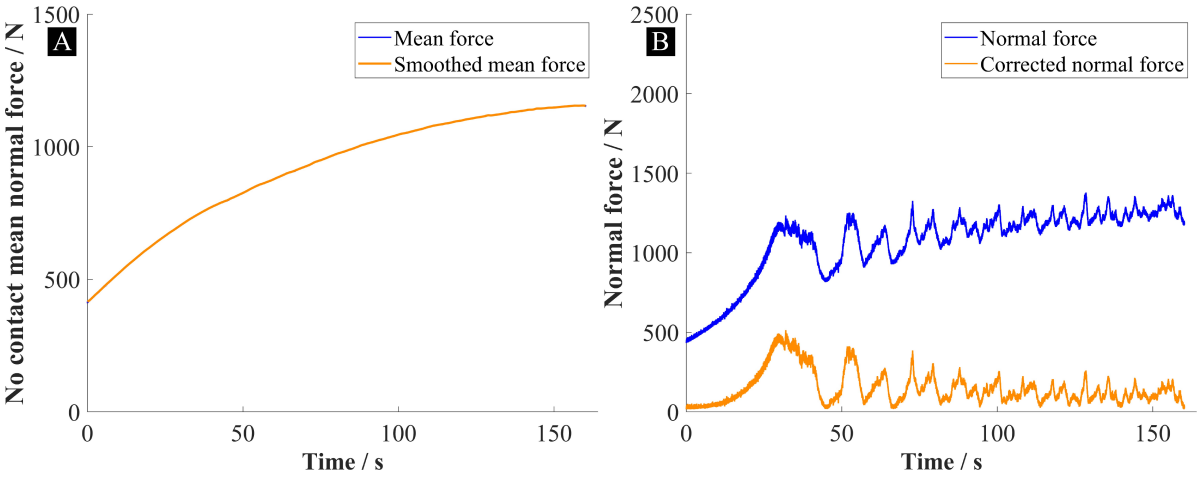

Fig. 4.5 No contact mean and smoothed mean normal force throughout a test, b) normal and corrected normal force throughout a test.

The force ratio is then calculated as a ratio of the tangential forces to corrected normal forces. The tangential force, corrected normal force and force ratio are then plotted against rub length. An example plot is shown in Fig. 4.6.

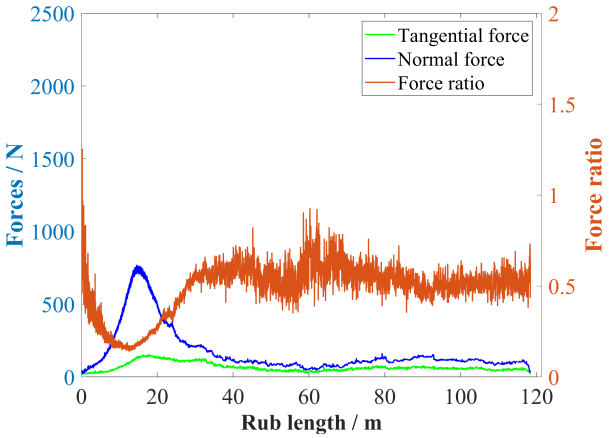

Fig. 4.6 A plot showing tangential and corrected normal forces and force ratio throughout a test.

The rub length is calculated as a sum of rub lengths per revolution of the disk for each revolution that was expected to be completed by the time of a given blade strike and is defined as:

$$l_{rtotal} = \sum_{n_r=1}^{n_{rcurrent}} 2r_{rtip} acos\left(\frac{2r_{rtip} - In_r}{2r_{rtip}}\right) \tag{4.2}$$

where l_{rtotal} is the rub length, I is the incursion rate in m/pass, n_r is the revolution number from the start of a test and $n_{rcurrent}$ is the number of revolutions completed by the time of a blade strike. The rub length is non-linearly related to time and blade revolution number. With an increase in time, rub length per revolution increases due to the arc of contact increasing with incursion depth; and so the total rub length grows faster than the time and revolution number.

4.2 Front-on imaging system

Blade length changes throughout a test performed on the high-speed rig are measured using images obtained with the front-on stroboscopic system. This is accomplished through the following steps:

First, a dataset is checked for images not suitable for processing. Such images can originate from false strobe triggers (a rare event, about 1% of the images were affected) or from sparks on an image (affecting only some of the tests with the AlSi-polyester abradable, primarily at the incursion rate of 2µm/pass). Examples of such images are shown in Fig. 4.7a and Fig. 4.7b respectively.

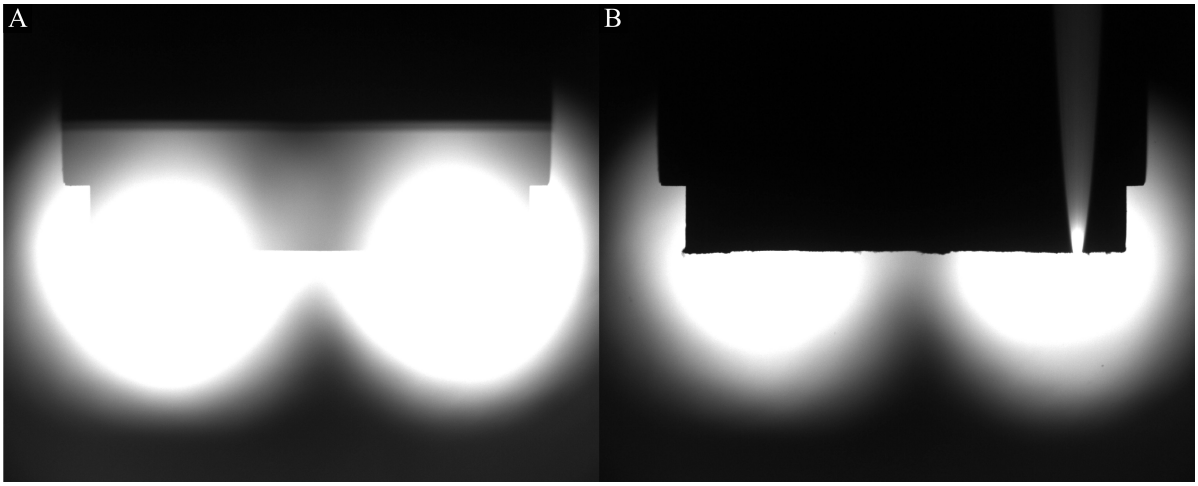

Fig. 4.7 a) an image affected by a false strobe trigger, b) an image affected by a spark.

Following a check for erroneous images, the remaining dataset is imported into MATLAB R2019b. An image is represented in MATLAB as a 1024x1280 array, with each value in the

array giving the colour of a pixel on the greyscale; with the value being between 0 - black and 255 – white.

Each image is then cropped into a smaller image showing only an area of interest. The cropping is done by manually selecting such a region on the first image in the dataset. All the subsequent images are cropped to the same pixel coordinates (for example, pixels from 100 to 1125 on the x-axis and 300 to 600 on the y-axis). The following criteria had to be fulfilled when selecting an area of interest:

- It is possible to observe the full length of a blade.
- It is possible to observe the part of the disk edge both to the left and right of a blade.
- There is enough space at the bottom of a blade to allow the analysis of adhesions to a blade throughout a test.

Examples of an original image with a sufficient area of interest selected shown in blue and a cropped image are shown in Fig. 4.8a and Fig. 4.8b respectively.

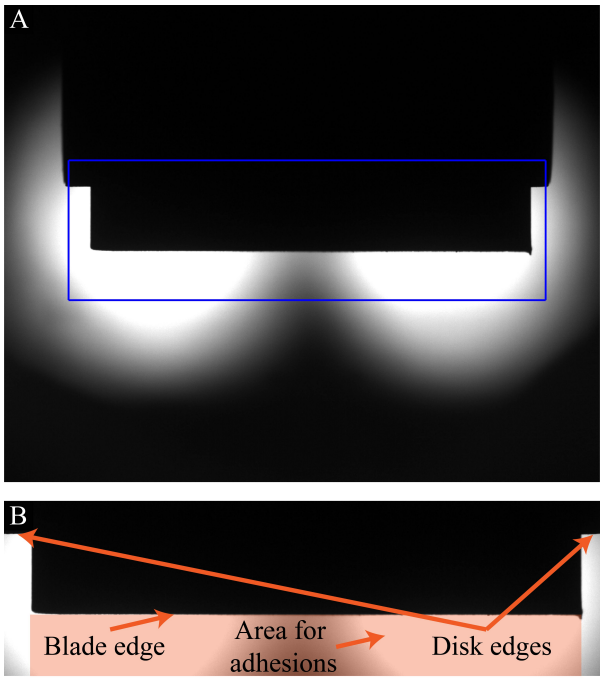

Fig. 4.8 a) The original image with an area of interest shown in blue, b) the cropped image with blade edge and disk edges indicated with arrows and area for the analysis of adhesions highlighted.

After cropping, an image is passed through three iterations of a 2-D median filter. This is done to remove small dots from an image which are not part of a blade or the disk. These dots

can be small broken particles of abradable flying inside the test area or dust that has settled on the camera lens. An example of a median filtered image is shown in Fig. 4.9.

Fig. 4.9 The median filtered image.

In the next step, a sharpening filter is applied to improve the contrast of an image. This improves blade edge detection, particularly for images where a blade edge is slightly blurry. Different combination of filter "Radius" and "Amount" parameters were tested for images that were identified as the most challenging for processing: with the largest amount of blurring, the lowest amount of LED light (for example, due to dust settling on LEDs), or the highest amount of blade glowing due to high blade tip temperatures. As a result of such testing, different settings were found optimal for the sharpening filter for tests with AlSi-polyester and NiCrAl-bentonite abradables. For tests with the AlSi-polyester abradable, a larger sharpening filter ('Radius',15, 'Amount',15) was applied to ensure that adhesions were sharp enough on an image to be detected using an edge detection function. For tests with the NiCrAl-bentonite abradable, a smaller filter ('Radius',5, 'Amount',5) was used to prevent images where a blade got too hot to be distorted by the filter. An example of a sharpened image is given in Fig. 4.10.

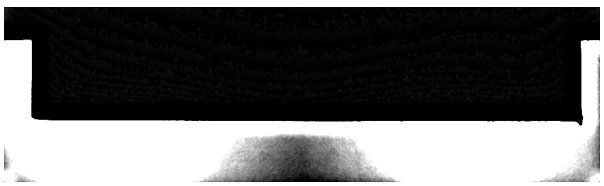

Fig. 4.10 The sharpened image.

After the application of the sharpening filter, edges on an image are detected using a "log" method. The blade and disk edge, along with several other small edges are detected (Fig. 4.11). Extra edges are selected due to the detection method being oversensitive. Such a method was selected to ensure that the blade and disk edge is effectively detected even in low-light conditions. Small extra edges are then removed using a command that removes all edges with a continuous pixel length of fewer than 1200 pixels (Fig. 4.12). The value of 1200 was determined by calculating the minimum expected blade and disk edge length for the scenario with the largest potential blade wear. This procedure for edge detection was checked across

a variety of image brightness conditions, and it was shown to produce accurate and reliable results.

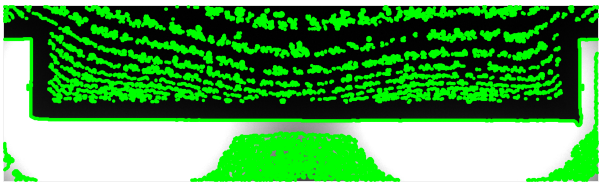

Fig. 4.11 The detected edges using the “log” method overlaid on the cropped image.

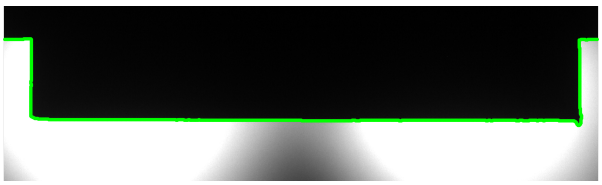

Fig. 4.12 The detected blade and disk edge using the “log” method overlaid on the cropped image after the small edges were removed.

After the blade and disk edges are detected, it is necessary to separate the blade edge from the combined blade and disk edge. This is done by finding the vertical lines of the edge (Fig. 4.13) and then defining the blade edge such that it is within the limit defined by the eight points to the right of the leftmost vertical line and eight points to the left of the rightmost vertical line. This limit and the extracted blade profile are shown in Fig. 4.14. Eight points were left on each side to allow for a variation in position of the vertical edges of blades.

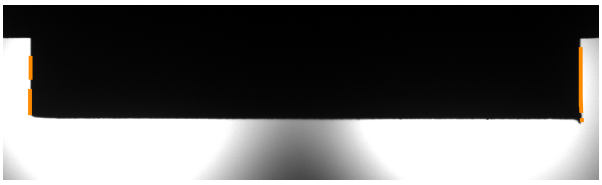

Fig. 4.13 The detected vertical edges of the blade shown in orange overlaid on the cropped image.

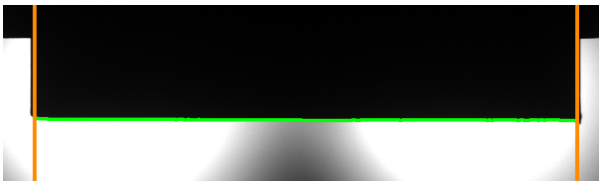

Fig. 4.14 The final blade profile in green overlaid on the cropped image with defined vertical limits shown in orange.

4.2.1 Blade length referencing

In previous iterations of stroboscopic imaging system design, blade position changed on images due to variation in the angle at which a blade image was captured [57], as shown in Fig. 4.15, due to uncertainty in the detection of reflection from the reflective tape (strobe triggering). A referencing method has been developed to compensate for variation in blade position on the images.

In experimental work, it is desirable to address the variation at the source rather than through post-processing. In line with that, further work has been performed to stabilise triggering and reduce variations observed on the images and ensure a blade is captured at the same angle on each occasion. The new reflective sensor equipped with a separate amplifier stabilised triggering even at the highest tested speed of 280m/s. Referencing, however, was kept in place as a data checking tool rather than a major post-processing step. The referencing effectiveness for old and new systems is discussed at the end of this section. All tests in this thesis were performed with the new reflective sensor.

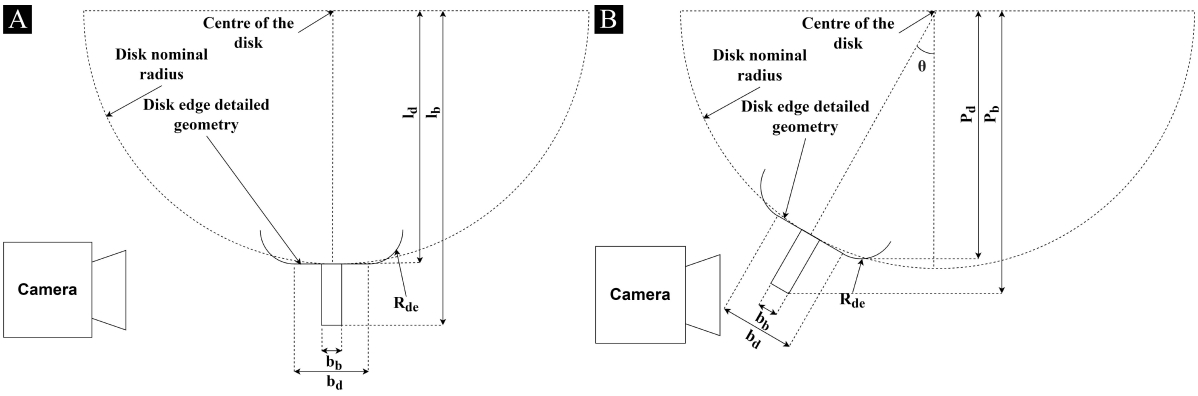

Fig. 4.15 The blade and the disk positions shown a) when a blade is perpendicular to the camera, b) when a blade is at an angle to the camera resulting in a blade moving up on an image. Key variables required for the calculation of the referenced blade edge position are labelled on the diagram.

The referencing works on the principle that the length from the centre of the disk to the edge of the disk is constant, so the disk edge should remain in the same position on the images. It is also assumed that any blade length change is uniform across the thickness of the blade. Although uniformity across the blade thickness is unlikely to be true for some cases, this assumption's importance on the referencing results is minimal.

Diagrams of the disk and blade with respect to the camera are shown in Fig. 4.15. The considered disk is not a perfect circle but rather has a flat section, b_d, symmetric to both sides of the blade. The following equations can be derived from geometry:

$$P_d = l_d cos(\theta) + \frac{b_d}{2} sin(\theta) + R_{de}(1 - cos(\theta)) \tag{4.3}$$

where P_d is the perpendicular projection length of the disk edge from the centre of the disk, l_d is the radial length of the disk (i.e. disk edge length from the centre of the disk), b_d is the length of the flat section at the edge of the disk, R_{de} is the radius of disk edge curvature, and θ is the angle of deviation of the blade position on an image from the vertical, and:

$$P_b = l_b cos(\theta) + \frac{b_b}{2} sin(\theta) \tag{4.4}$$

Where P_b is the perpendicular projection length of the blade's edge from the disk's centre, l_b is the combined radial length of the disk and blade edge (i.e. the blade edge length from the disk's centre, equivalent to r_{tip})), and b_b is the blade thickness.

In Equation 4.3, all the variables except for the angle of deviation from the vertical, θ, are known either from geometry or as is the case with the projected length of the disk edge from the centre of the disk, P_d, can be obtained from the processing of collected images. This allows solution for θ as follows:

$$\theta = acos\left(\frac{P_d - R_{de}}{\sqrt{(l_d - R_{de})^2 + \left(\frac{b_d}{2}\right)^2}}\right) + atan\left(\frac{\frac{b_d}{2}}{l_d - R_{de}}\right) \tag{4.5}$$

The projected length of the blade from the centre of the disk to the blade tip, P_b, is determined from an extracted blade profile shown in Figure 12 for each image in the dataset. Knowing θ, it is then possible to solve Equation 4.4 for the length from the disk's centre to the blade tip, l_b as follows:

$$l_b = \frac{P_b - \frac{b_d}{2} sin(\theta)}{cos(\theta)} \tag{4.6}$$

The next section explains how the value, P_d, was obtained for each processed image.

4.2.2 Disk edge extraction for use in referencing

At the start of data processing, 4 data points are selected, which create a limit for the disk edges on the left and the right of the blade, as shown in Fig. 4.16. Some space is left to the left and right of the actual disk edge to allow for some variation in the position of the disk and the blade on the images in a dataset. All the vertical position indexes for data points on the left of the blade are averaged to give a y-position index for the disk edge to the left of the blade. The same procedure is done for the disk edge to the right of the blade. These two values are averaged to obtain the average observed projection of the disk edge for this image, l_{do}.

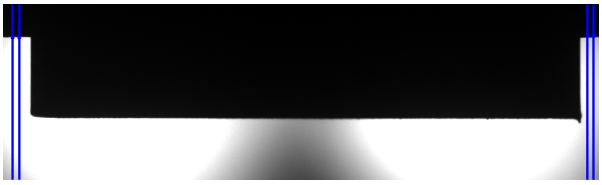

Fig. 4.16 The reference lines selected on the original image after it was cropped.

These values are y-positions of the disk edge projected onto the camera. P_d is equal to the vertical positions converted from the number of pixels to microns added to the unobserved part from the disk's centre to the camera field of view limit, l_du. l_du is found by assuming that when the disk edge and the blade edge are perpendicular to the camera, the projected edge length is the longest it could appear and $P_{d(max)} = l_d$. l_d is known from the disk geometry.

Then by finding the maximum observed projection of the disk edge, $l_{do(max)}$

$$P_{d(max)} = l_{du} + l_{do(max)} = l_d \tag{4.7}$$

Then

$$l_{du} = l_d - l_{do(max)} \tag{4.8}$$

Thus, it is possible to convert l_{do} values into P_d values for all the analysed images.

$$P_d = l_{du} + l_{do} \tag{4.9}$$

Similarly, it is possible to convert all the observed blade edge profiles, l_{bo}, into The projected lengths of the blade from the centre of the disk to the blade tip, P_b, and convert back from

combined radial lengths of the disk and blade edge, l_b, to the observed blade profiles after referencing, $l_{(bo(ref))}$, which is the last step of the referencing procedure.

4.2.3 Referencing effectiveness

To demonstrate the effectiveness of referencing, variation in the mean length of a blade at the start of a test (for the first 25 images) was considered to assess the repeatability of the measurements. No significant wear/adhesion is expected to occur by this point, so all the variations are primarily due to uncertainty in the measurements.

This calculation was performed for two tests: one with the old reflective sensor and one with the new. The test with the old reflective sensor was at 85m/s blade tip speed, 0.2µm/pass incursion rate, and 1000µm incursion depth with the Ti(6Al4V) blade rubbed against the AlSi-polyester H69 hardness abradable sample. The test with the new reflective sensor is the one used for the demonstration of data processing methods throughout this chapter. It was at a higher blade tip speed of 200m/s, with the other conditions being the same.

For a dataset obtained with the old reflective sensor, the standard deviation (standard uncertainty) of the blade mean length values for the unreferenced data was found to be 118µm and for the referenced data 14µm. The size of one pixel on an image is 21.2µm (half-uncertainty is then 10.6µm). Assuming rectangular distribution for uncertainty due to rounding to the nearest pixel, standard uncertainty due to this source is then $10.6/\sqrt{3} = 6.1$µm. The combined standard uncertainty for referenced blade length results was $\sqrt{14^2 + 6.1^2} = 15$µm.

For a dataset obtained with the new reflective sensor, the standard deviation (standard uncertainty) of blade mean length values for the unreferenced data was found to be 5µm and for the referenced data 12µm. The combined standard uncertainty for referenced blade length results was then 13µm.

The comparison between unreferenced and referenced data from the old sensor demonstrated the procedure's effectiveness in referencing blade length results. The standard deviation of the unreferenced blade mean length values with the new system was extremely small. This highlighted a significant improvement in triggering stability with the new reflective sensor.

With the new system, the referenced data had a higher standard deviation than the unreferenced data. This was due to some uncertainty in the detection of the disk edge, most likely due to the disk edge being in between two pixels leading to switching from one pixel to another on images even when an actual disk edge position variation on an image was small.

Despite the observed increase in uncertainty for this test, it was decided to still proceed with referencing images, as the increase in uncertainty was small (lower than the size of one data pixel) and procedure was shown to be highly effective for referencing blade length data when there is a variation in an angular position at which a blade is imaged on the example

of data with the old reflective sensor. Therefore, referencing was kept in place as a standard datuming and data checking tool as consistency of a dataset could be checked by comparing standard deviations of the blade mean length values before and after referencing.

4.2.4 Blade profile history maps

Each referenced blade profile is represented by two vectors: horizontal (blade width) and vertical (blade height) coordinates. As adhesions can have a complex shape, some horizontal coordinates can have more than one corresponding vertical coordinate as highlighted in Fig. 4.17.

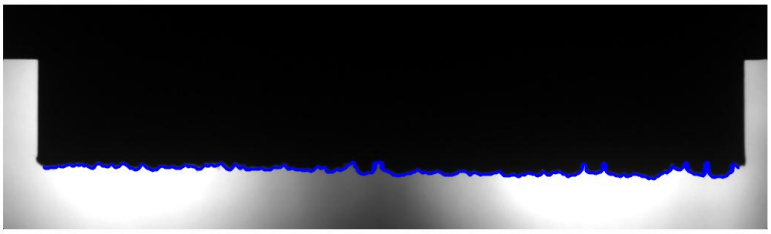

Fig. 4.17 An example of a processed image, with the detected blade edge shown in blue, where some horizontal coordinates can have more than one corresponding vertical coordinate due to the shape of adhesions.

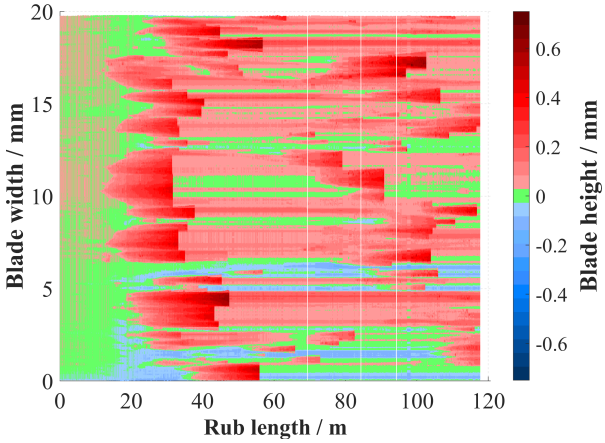

Fig. 4.18 An example of a blade profile history map.

To arrange all the blade profiles in a dataset into a matrix (rows corresponding to time, columns corresponding to blade width position and values corresponding to blade height), each

horizontal coordinate was assigned with a unique vertical coordinate value. The vertical coordinate value was defined by the mean value of all the vertical coordinates for a corresponding horizontal coordinate.

Blade profiles throughout a test are then plotted against rub length on the x-axis and blade width on the y-axis to create a blade profile history map, an example of which is shown in Fig. 4.18. Blade height is given by the blade profiles' vertical coordinates datumed to the mean height of the blade profile on the first image in a dataset and converted from pixels to mm. Negative blade height (blue) corresponds to blade wear and positive blade height corresponds to the formation of adhesions. Blade width is given by the blade profiles' horizontal coordinates converted from pixels to mm. With the help of such a map, it is possible to see at what positions on a blade adhesions or blade wear occurred, how each point on a blade changed throughout a test (by selecting a blade width position and looking at it along the rub length axis), and also understand how adhesions grew and fractured throughout a test.

4.2.5 Theoretical surface profiles

It was observed on the raw data that adhesions may fracture from a blade. An additional blade profile was constructed to understand how fractured adhesions contributed to a final tested abradable surface. This blade profile included the detached adhesions into its shape based on how deep they could have rubbed into the abradable material before they detached. This was done using the following procedure:

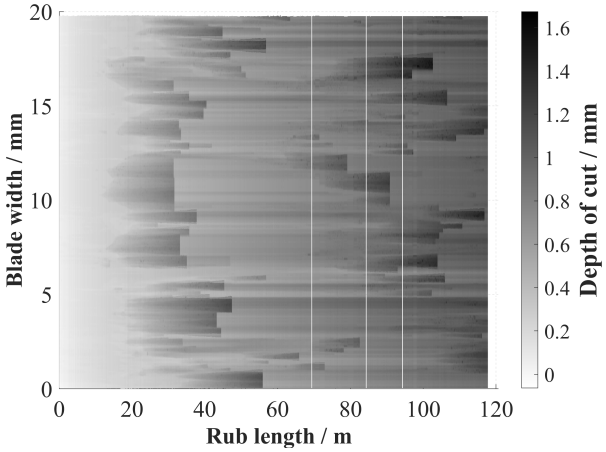

Fig. 4.19 The modified plot considering the current rub depth for the test at 0.2µm/pass and 85m/s.

Each extracted blade profile had the difference between the final and the current rub depths subtracted from it to calculate how deep the blade would have rubbed into the abradable at each

point along the blade width for this blade profile. Such a modified plot is shown in Fig. 4.19. A blade profile based on the highest depth of cut value for each blade width position was then extracted.

It was also noted that some of the very long sharp adhesions existed only on one image, after which they detached. An additional blade profile was created to check if they contributed to the final abradable shape, which consisted of the third-highest point for each blade width position. The third point was selected over the second one to ensure that for the case there are two short-lived sharp adhesions at the same location along the blade's width throughout a test, both are ignored. The expected abradable surface profile based on the highest depth of cut point is then referred to later in this work as the 1-point profile and the profile based on the third-highest point as the 3-points profile.

The final blade profile and the two constructed profiles are shown in Fig. 4.20. Such profiles can then be compared to post-test measurements of abradable surface profiles to understand how fractured adhesions could have contributed to the final abradable surface.

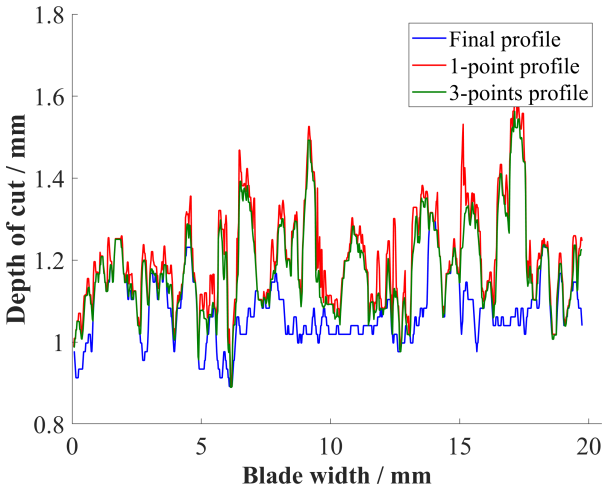

Fig. 4.20 The final and two constructed blade profiles for the test at 0.2µm/pass and 85m/s.

4.2.6 Adhesion rates analysis

Five lines corresponding to individual blade width locations were extracted for the test at 0.2µm/pass and 200m/s as shown in Fig. 4.21 to investigate the minimum number of lines required to obtain representative adhesion rate and peak height results.

Each line was then plotted on a separate 2D plot and for each adhesion event four points were selected: two points where adhesion growth was linear for adhesion rate calculation (blue) and two points for peak height and relative peak heights calculation (green) as shown in Fig. 4.22.

Adhesion rates were calculated by assuming a linear growth of adhesions. While for most cases this assumption held true, some of the adhesions were not fully linear as shown in Fig. 4.23. However, as the main interest of this analysis was the identification of general trends between testing conditions rather than the determination of exact adhesion rates throughout a single adhesion event, the assumption of adhesion growth linearity was considered appropriate.

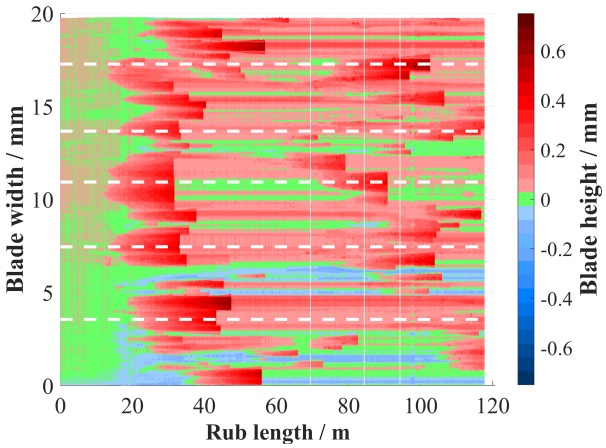

Fig. 4.21 The lines selected for further processing of adhesion rates.

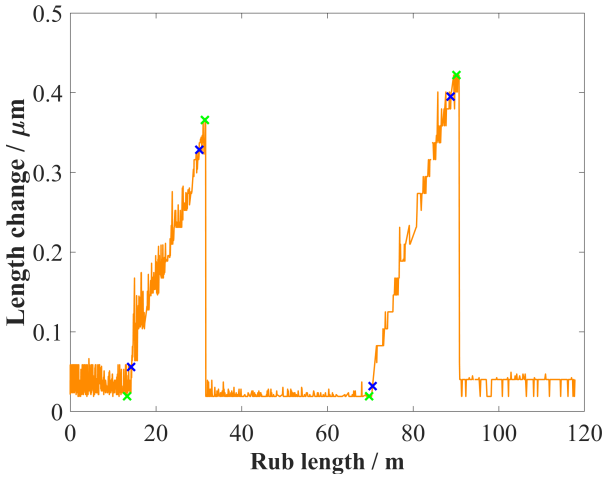

Fig. 4.22 The extracted line for blade width position of 10.9mm with the selected points.

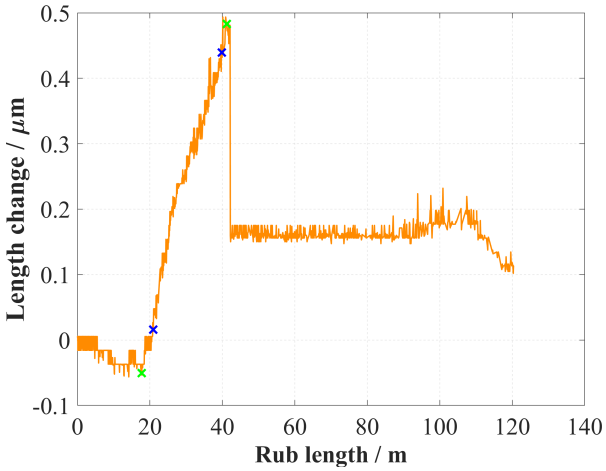

Fig. 4.23 An example of a not fully linear adhesion.

The mean value and standard deviation of adhesion rate and peak height were then plotted in Fig. 4.24 for the total number of considered lines between 1 and 5. The representative results could be achieved by using 3 lines with no significant increase in the accuracy of the mean value or decrease in the standard deviation with a further increase in the total number of considered lines. Therefore, where adhesion analysis was performed in this thesis, 3 lines were extracted for each test from the blade profile history maps in blade width locations where adhesions occurred.

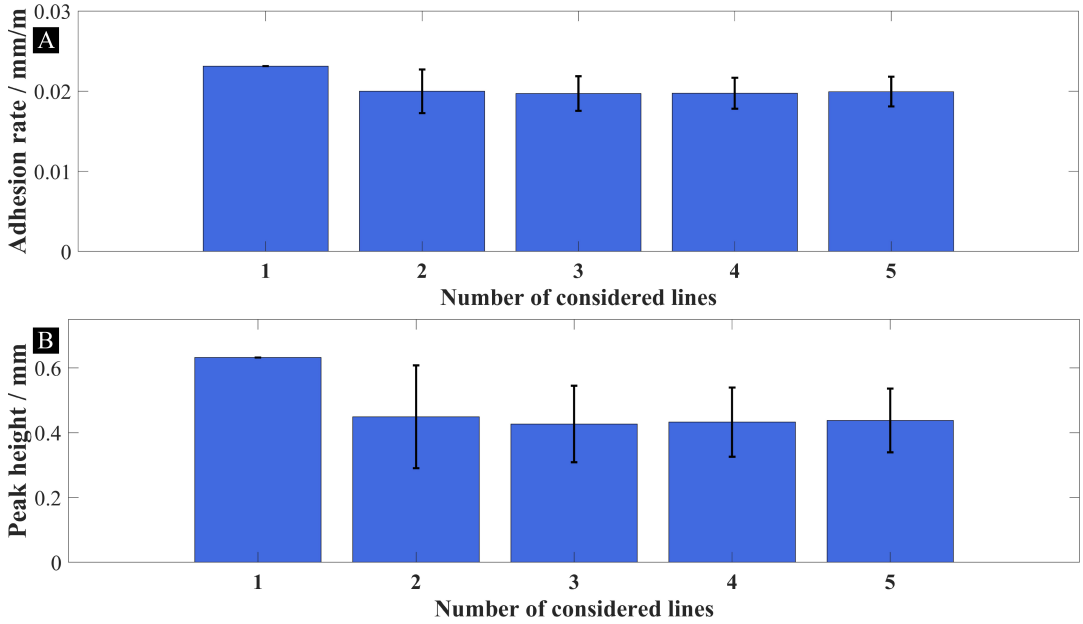

Fig. 4.24 The mean value and standard deviation of a) adhesion rate and b) peak height results for the total number of considered lines between 1 and 5.

4.3 Side-on imaging system

Changes in maximum blade length throughout a test performed on the low-speed rig are measured using images obtained with the side-on stroboscopic system. The procedure is similar to the one used for the high-speed rig front-on stroboscopic system, but the result of the processing is a vector of values of the maximum blade height rather than a matrix of blade profiles. The processing is accomplished through the following steps:

Each image in a dataset is imported into MATLAB R2019b. Following that, an area of interest is selected on the first image in a dataset (Fig. 4.25), and the remaining images are cropped to that area (Fig. 4.26a). After cropping, an image is passed through three iterations of a 2-D median filter (Fig. 4.26b). A filtered image is then converted to a binary image using a threshold of 0.3 (Fig. 4.26c). Edge is detected on the binarised image using the "Prewitt" method (Fig. 4.26d). The pixel corresponding to the maximum blade height is recorded and converted from the pixel number to the blade height. The recorded blade height vector is trimmed using the test start and end times recorded from the dynamometer processing. Blade height values are then datumed by the value of the blade height at the start of a test (first value in the trimmed vector) to obtain the maximum blade height change throughout a test. An example plot of the maximum blade height change throughout a test is shown in Fig. 4.27.

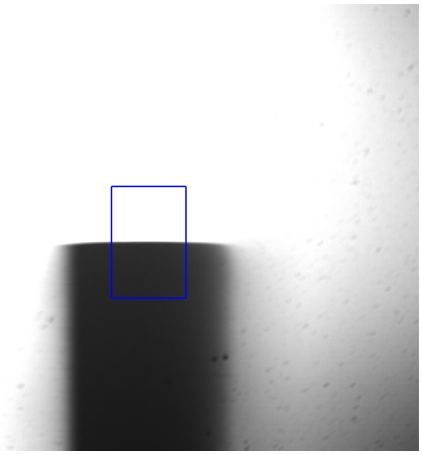

Fig. 4.25 An original image with an area of interest shown in blue.

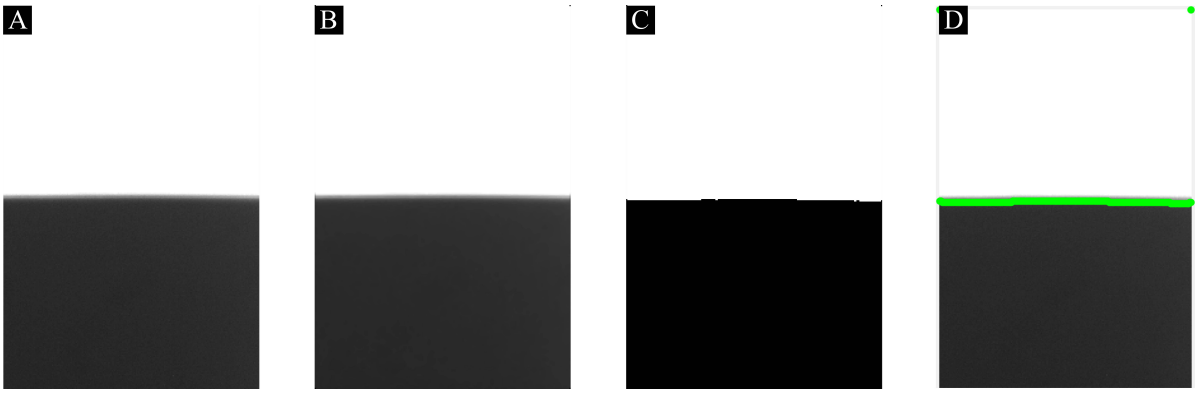

Fig. 4.26 a) The cropped image, b) the median filtered image, c) the binarised image, d) the edge detected using the “Prewitt” method overlaid on the cropped image.

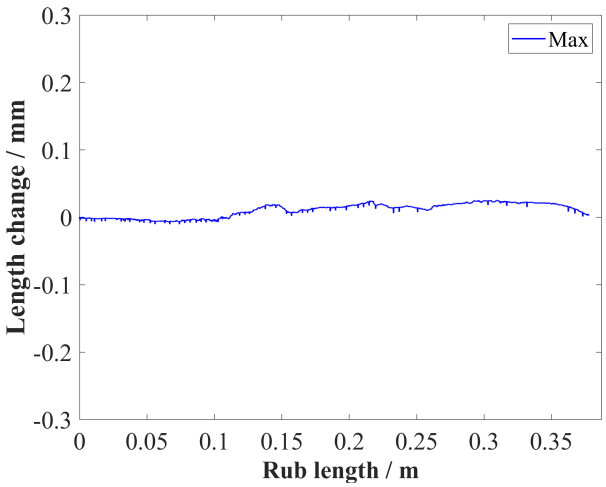

Fig. 4.27 An example plot of the maximum blade height change throughout the test at 200m/s blade tip speed, 0.06µm/pass incursion rate, 1000µm incursion depth with the Inconel 718 blade rubbed against the NiCrAl-bentonite H55 hardness abradable sample heat-treated for 100 hours.

4.4 Pyrometer

After importing temperature data into MATLAB R2019b, it was noticed that data from the pyrometers installed on both the high-speed and low-speed rigs was heavily affected by noise. An example dataset is shown in Fig. 4.28. Temperature values were between 150C and 6500C, as shown in Fig. 4.28a. The pyrometer can only record temperatures between 150C and 1000C, and so all the points above 1000C were considered to be noise.

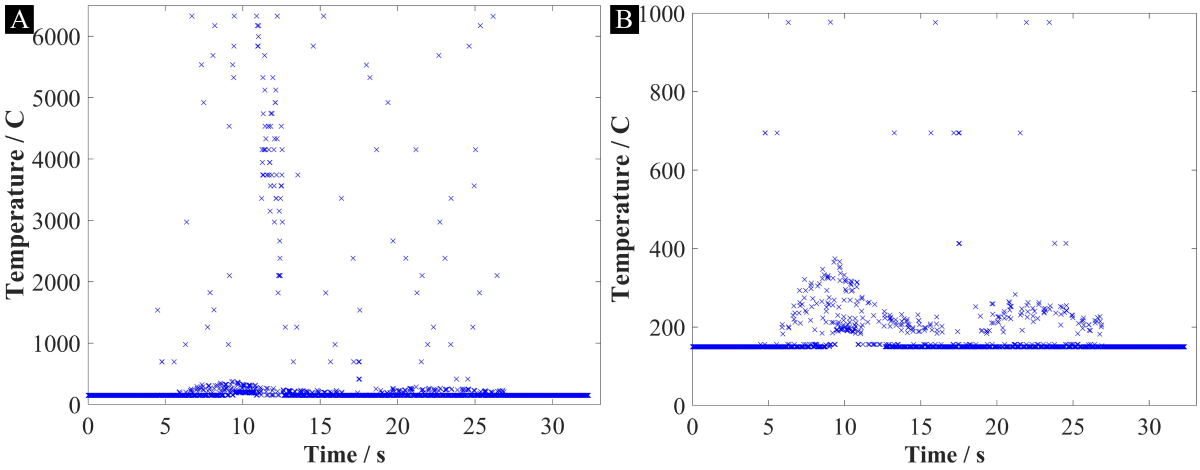

Fig. 4.28 The data obtained using the high-speed rig pyrometer a) all the recorded data points (between 150C and 6500C), b) the data points in the pyrometer nominal recording range (between 150C and 1000C).

However, even ignoring all the points above 1000C, it can be seen in Fig. 4.28b that data in the 150C and 1000C range was still heavily affected by noise. Currently, no procedure can effectively separate actual data from noise. The source of the noise is not fully understood either. Potentially, it could be due to heavy sparking occurring in a contact between a blade and an abradable sample.

Because of the unreliability of data due to noise, and already existing limitations with using a pyrometer for temperature measurements (looking only at a spot on the abradable rather than the entire abradable surface), it was decided to ignore data collected using the pyrometers installed on both the high-speed and low-speed rigs for the tests in this thesis.

4.5 Alicona surface measurements

Post-test abradable samples for some of the tests were measured using the Alicona SL equipment. As discussed in section 3.4.1, the area selected for the analysis of each sample was approximately 27mm x 20mm. The data are imported into MATLAB R2019b, and then the recorded space to the left and right of the rub width is removed. The cropped surface plotted in plan view is shown in Fig. 4.29.

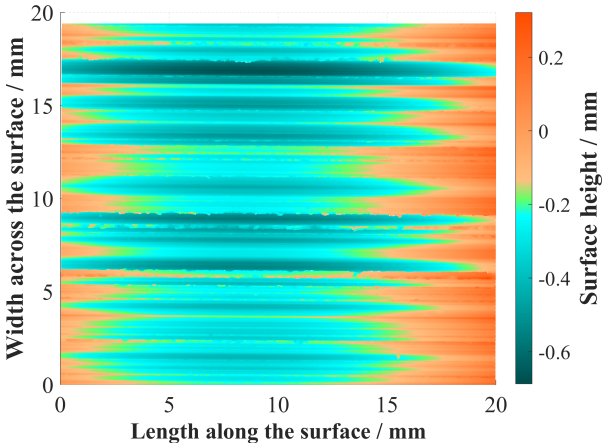

Fig. 4.29 The cropped Alicona surface measurements for the tested sample.

The curvature of the sample in the length direction (due to blade cutting the abradable sample in an arc) was compensated using a form removal procedure. The surface height was averaged across the width direction to obtain a line. A 2nd order polynomial was then fitted to the radius of the circle, as shown in Fig. 4.30. The 2nd order polynomial was sufficient as the surface arc was short. Each line across the surface was then subtracted by the value determined by the 2nd order polynomial, resulting in a surface datumed to its mean height. As a result, the surface profile with the form removed shown in Fig. 4.31 presents the surface shape created by the incursion test, but not how deep this surface was rubbed into.

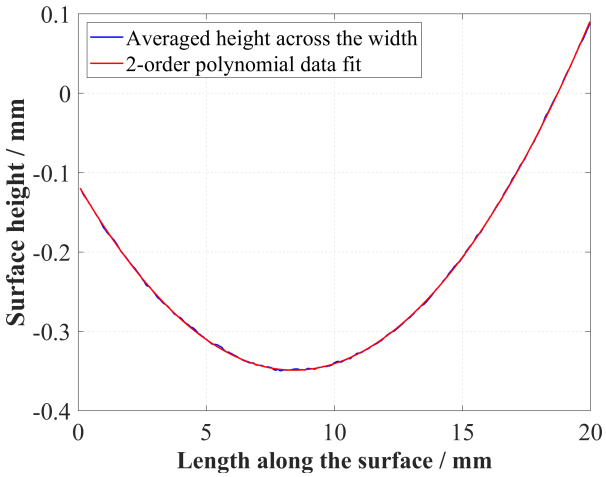

Fig. 4.30 The surface form along the length of the cut and the fitted 2-nd order polynomial.

Several areal surface roughness metrics were calculated using the compensated surface. They are the average height of the selected area, S_a, the root-mean-square height of the selected area, S_q, the maximum peak height of the selected area, S_p, the maximum valley depth of the

selected area, S_v, and the height of the selected area (sum of the absolute values of S_p and S_v), S_z.

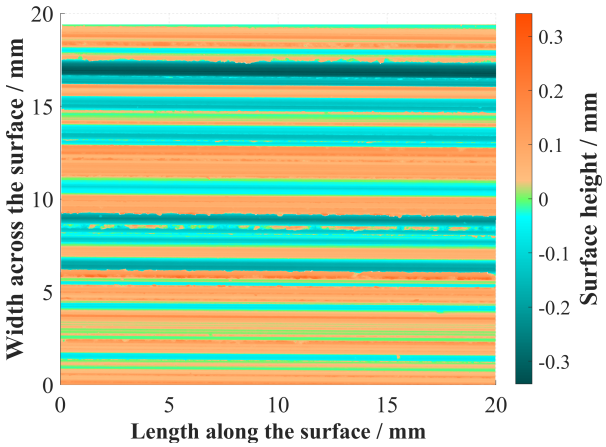

Fig. 4.31 The tested sample with the form removed.

An area dependence study was performed by considering the whole width of the sample and increasing the range of x-coordinates (length along the surface) considered. Based on the results shown in Fig. 4.32, roughness does not change significantly with an increase in the length of the sample considered. This result confirms that the area selected for Alicona analysis is representative of the rubbed surface. This is to be expected as from Fig. 4.31, it appears that the surface height for an AlSi-polyester abradable sample is consistent along the cutting direction and was produced by adhesive and abrasive wear or deformation of the abradable surface by the blade with no signs of macro rupture.

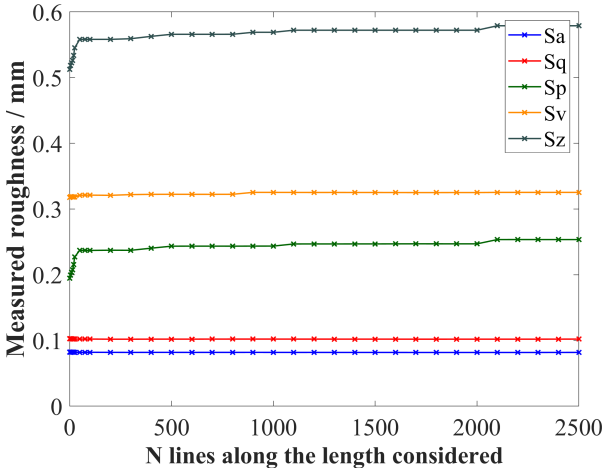

Fig. 4.32 The area dependence study for Alicona surface measurements.

4.6 Summary

In this chapter methods used to analyse data obtained during and post abradable incursion tests were discussed. In the next chapter, results obtained using these methods for contacts between Ti(6Al4V) blades and AlSi-polyester abradable samples will be presented.

Chapter 5

AlSi-polyester wear mechanisms

5.1 Introduction

In past research, wear mechanisms of AlSi-based abradables were assessed using a post-test investigation of blades and abradable samples [46] and using a side-on stroboscopic imaging system [41, 51]. The understanding of wear mechanisms was advanced using these methods, but there were some limitations.

For cases with simultaneous blade wear and adhesive mechanisms within a single test, Stringer et al. [40] showed that post-test average blade length and weight changes were insufficient to classify a wear mechanism. Measurement of a full blade profile post-test was shown to be a more appropriate way of classifying such contacts. However, this method still had limitations for the cases where adhesions have fractured during a test and so, a final profile was not representative of the overall adhesive transfer during a test. Indeed, previous results by Bounazef et al. [46], Fois et al. [41] and Watson et al. [51] have shown fracture of adhesions to occur under different testing conditions, leading to a range of tests with classification issues.

The side-on stroboscopic system was used for tracking the maximum length of a blade throughout a test allowing to capture fracture of adhesions. However, it still had several limitations. It wasn't possible to tell at what exact position along the blade width adhesions occurred, what was the width of an adhesion and if there were only one or multiple different adhesions on the blade at any given time. Additionally, coming back to tests with simultaneous blade wear and adhesions, the side-on stroboscopic system was not suitable for classifying a wear mechanism in such contacts as regions of wear were not observed on the images due to existing adhesions.

In this work, the front-on stroboscopic imaging system is used, where an entire blade front is imaged throughout a test to address the limitations of using the side-on imaging and post-test

blade length measurements, with the aim of improving the understanding of the adhesion and abrasion wear mechanisms.

5.2 Materials and methodology

The effects of incursion rate, blade tip speed and abradable hardness on wear mechanisms in AlSi-polyester abradable are investigated in this chapter. These variables were chosen based on previous findings, where they were shown to influence a test outcome for abradable samples of this type [51].

The investigation was performed using a full factorial matrix with three values for each variable, with a full test matrix consisting of 27 tests. Incursion rates were selected as 0.02µm/pass, 0.2µm/pass and 2µm/pass as it was previously shown that such rates produce representative wear mechanisms for an aero-engine compressor [40]. Speeds were selected as 100m/s, 200m/s and 280m/s with the upper limit defined by the current rig capabilities. Abradable hardness values were chosen as H70, H60.5 and H55, which were around the spraying range for the AlSi-polyester abradable [5]. All the tests were performed with Ti(6Al4V) blades with a 4mm stick-out from the blade holders.

5.3 Results

First, results from hardness testing of abradable samples are presented, followed by the results obtained from the experimental tests. Previous work on the AlSi-polyester abradable identified that the main factor influencing wear mechanisms is the incursion rate [51]. Therefore, to simplify the presentation of results, the following structure was employed for experimental data: results at each of the incursion rates are presented as a separate section, with influences of blade speed and hardness at each incursion rate being discussed within that section.

5.3.1 Hardness testing

The abradable hardness is the only independent variable in this study that cannot be directly controlled from the rig computer. Three samples from each batch were hardness tested in six locations each, according to the procedure described in section 3.4.3. The hardness results are presented below in Table 5.1.

The hardness measurements had some limitations. Since these were performed externally, there is no available estimate of the measurement uncertainty. Additionally, the number of

hardness measurements per sample was limited to six by the sample geometry, so accuracy of an average value might be affected by the number of available measurement locations.

Table 5.1 Hardness testing results

Test number	Hardness							
	Nominal	Measured						
		1	2	3	4	5	6	**Ave.**
1	**70**	67.8	72.1	67.7	68.4	68	68.6	**68.7**
2	**70**	68.9	69.4	64.9	66	71.3	71.1	**68.6**
3	**70**	68.7	69.7	70.9	68.5	70	71	**69.8**
4	**60.5**	63.1	63.2	63	65	66.2	65	**64.2**
5	**60.5**	63.1	64	62.6	64.6	62.7	61.2	**63**
6	**60.5**	58.9	58.6	58.2	56.7	62	59	**58.9**
7	**55**	54.7	54	54	50.5	54.1	55.5	**53.8**
8	**55**	52.2	55.5	55.9	52.5	52.1	52.4	**53.4**
9	**55**	52.6	51.4	50.3	50	55.4	53.2	**52.1**

Nonetheless, the measured hardness is the best available estimate of the true average hardness of a batch. For samples of H70 nominal hardness, the average measured hardness was H69, for H60.5 samples it was H62 and for H55 samples it was H53. The average measured hardness for a batch deviated from nominal hardness by no more than two points on the hardness scale. This is acceptable considering the inherent randomness of the abradable spraying process.

However, hardness could deviate in either direction. This led to smaller or larger differences between the batches than expected. For example, the nominal difference between H60.5 and H55 batches was 5.5 points on the hardness scale, while the measured difference was 9 points. To ensure that comparisons made between different batches of abradable used in this study are accurate with respect to hardness, batches in this chapter will be referred to by their measured rather than nominal hardness.

For the measured H69 and H53 (nominal H70 and H55) batches, the average hardness of samples within a batch was very close. For the measured H62 batch, however, the difference between the hardest and the softest measured sample was 5.3 points on the hardness scale. Such a difference in hardness for samples within a batch is undesirable. However, the existence of a deviation in the hardness values within a batch will be considered when discussing results from the tests in this chapter.

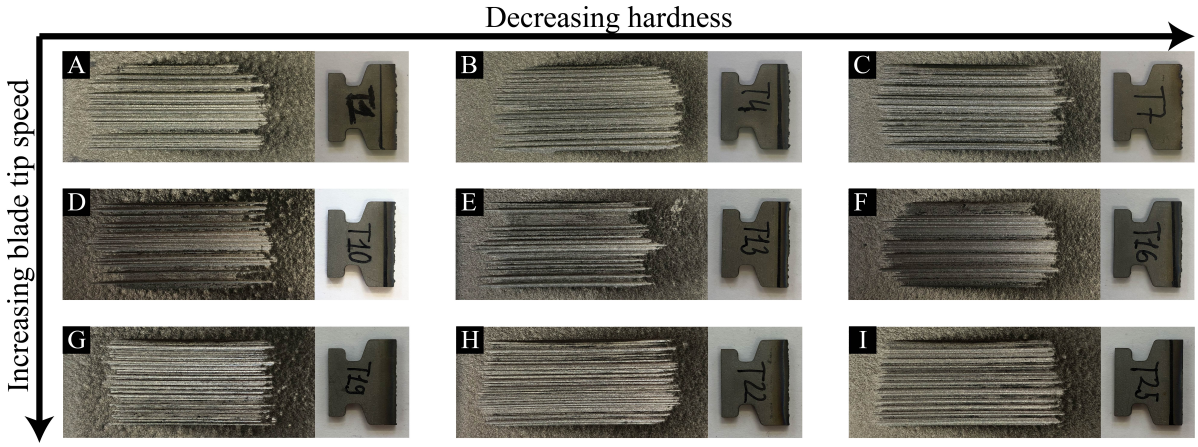

Fig. 5.1 The post-test images of the abradable samples and blades for the tests at the 0.02µm/pass incursion rate, 100m/s speed with a) H69 samples, b) H62 sample, c) H53 sample, 200m/s speed with d) H69 sample, e) H62 sample, f) H53 sample, 280m/s speed with g) H69 sample, h) H62 sample, i) H53 sample.

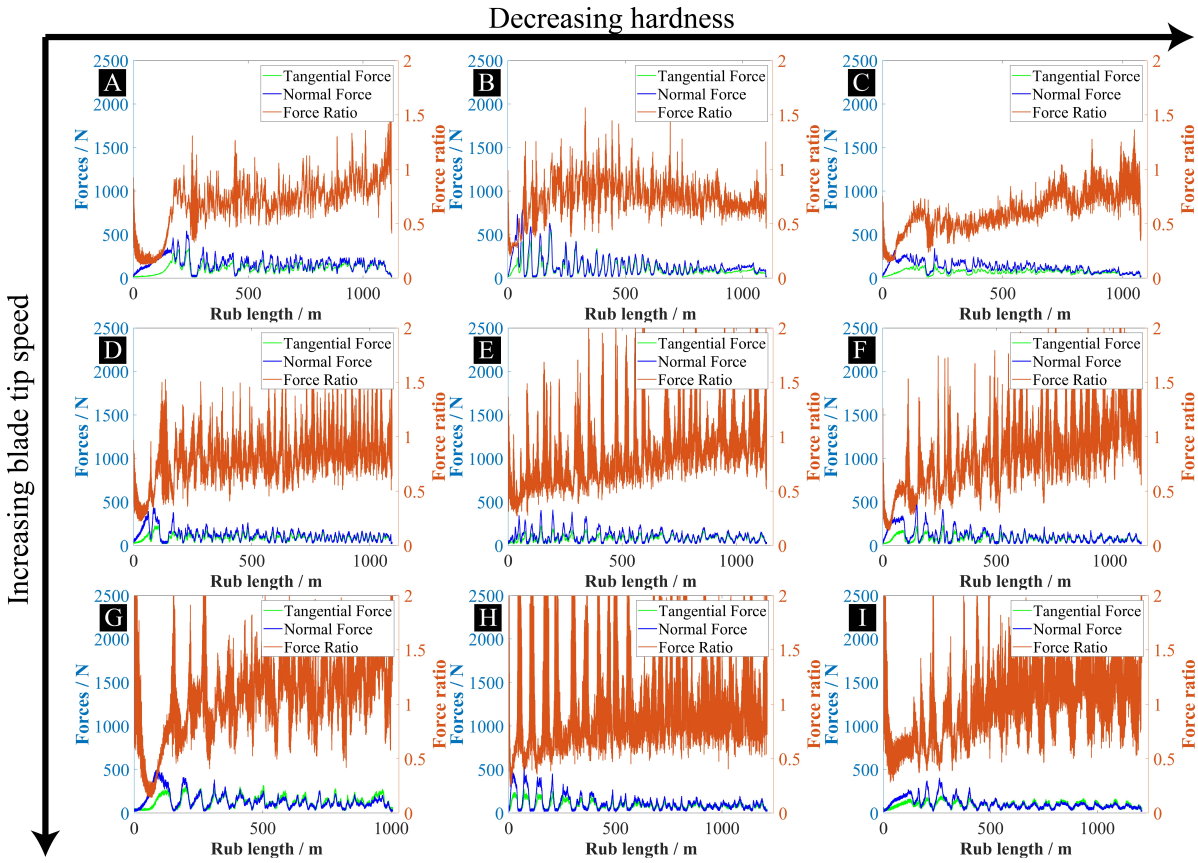

Fig. 5.2 The force data for the tests at the 0.02µm/pass incursion rate, 100m/s speed with a) H69 samples, b) H62 sample, c) H53 sample, 200m/s speed with d) H69 sample, e) H62 sample, f) H53 sample, 280m/s speed with g) H69 sample, h) H62 sample, i) H53 sample.

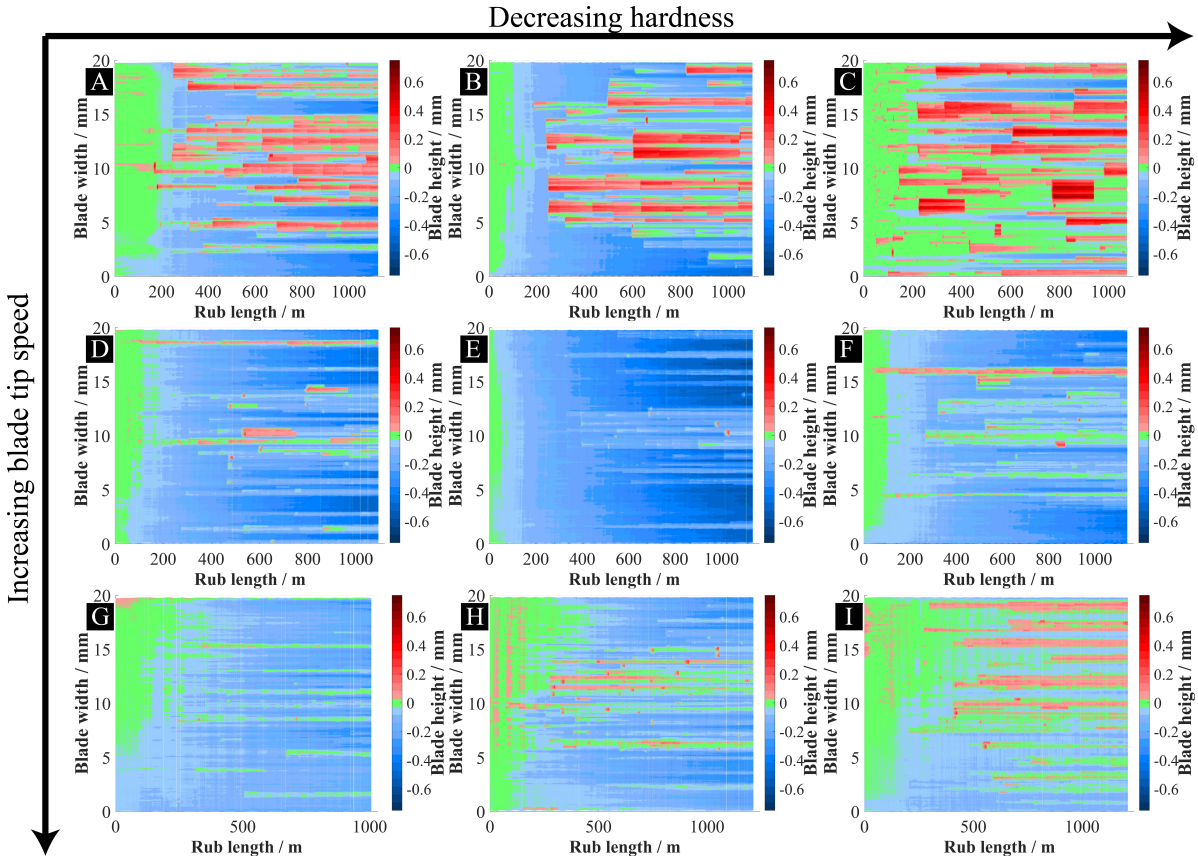

Fig. 5.3 The blade profile history maps for the tests at the 0.02µm/pass incursion rate, 100m/s speed with a) H69 samples, b) H62 sample, c) H53 sample, 200m/s speed with d) H69 sample, e) H62 sample, f) H53 sample, 280m/s speed with g) H69 sample, h) H62 sample, i) H53 sample.

5.3.2 Results at the 0.02µm/pass incursion rate

The post-test images of the abradable samples and blades, force data throughout a test and blade profile history maps are given for all the 9 tests at the 0.02µm/pass incursion rate in Fig. 5.1, 5.2 and 5.3 respectively.

The post-test blades appear to be severely worn and have very rough tips and visible thermal damage on them. As a result of high blade roughness, the abradable samples show a significant level of grooving. The force results show a similar trend, where some level of periodic behaviour is observed. This suggests compaction/elastic deformation and release abradable removal mechanism. The maximum normal force reached 500N in the beginning, while for the steady-state cyclic region, it was around 250N. The force ratio was low during the initial period of increasing forces. In the steady-state cyclic region, the force ratio was

significantly higher and stable around the 0.8-1.2 value, with force ratio being slightly higher for tests at higher speeds.

The blade length and force results are further summarised in Table 5.2 for all the 9 tests at the 0.02µm/pass incursion rate. For blade length, mean (including standard deviation of the full profile), minimum and maximum lengths at the end of a test are given. For forces, mean normal and tangential forces are given. The mean forces during a test were similar across all 9 conditions, with tests with H69 abradable samples having slightly higher forces. The minimum blade length at the end of a test was negative for all of the tests, indicating regions of wear. For most of the conditions, the blade maximum length at the end of the test was positive, showing the presence of adhesions as well. This suggests a mixed wear mechanism at this incursion rate with both localised wear and adhesions present, which can also be observed on the blade profile history maps in Fig. 5.3.

Table 5.2 Summary of the blade length and force results for the tests at the 0.02µm/pass incursion rate.

Blade tip speed / m/s	Hardness	Blade length at the end mean (std)	Blade min	Blade max	Mean normal force	Mean tangential force
100	H69	-0.09(0.19)	-0.43	0.27	165	102
100	H62	-0.07(0.16)	-0.53	0.26	160	106
100	H53	0.01(0.13)	-0.35	0.33	130	67
200	H69	-0.27(0.17)	-0.52	0.06	126	86
200	H62	-0.39(0.16)	-0.63	-0.05	104	73
200	H53	-0.21(0.14)	-0.47	0.10	122	76
280	H69	-0.17(0.07)	-0.34	0.00	149	126
280	H62	-0.14(0.10)	-0.33	0.10	130	91
280	H53	-0.02(0.07)	-0.14	0.22	111	91

5.3.2.1 Blade wear results

The blade length during a test at three blade width locations where wear occurred is plotted in Fig. 5.4 for three of the tests at the 0.02µm/pass incursion rate to show blade wear rate (rate of change in minimum blade length) variations within a single test. Only very small differences in wear rate can be seen at different locations of a blade for all three tests. Therefore, it was concluded that the blade wear rate is consistent for a given test.

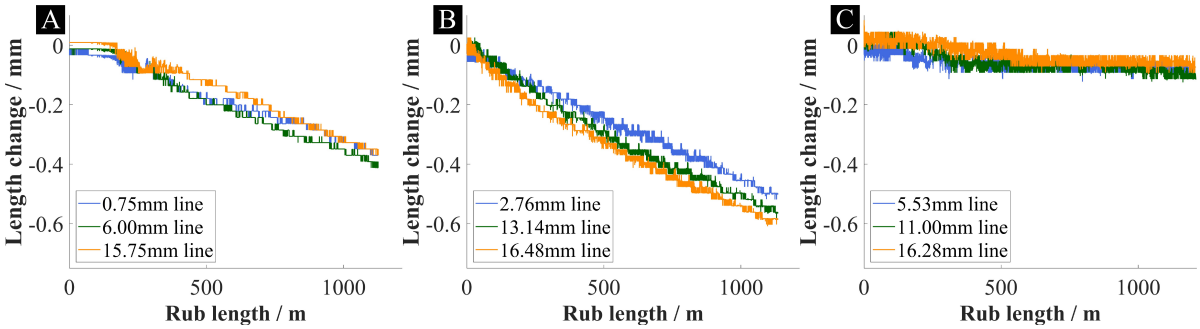

Fig. 5.4 The minimum blade length throughout a test at 3 blade width locations for the test at a) 100m/s with H70 abradable, b) 200m/s with H60.5 abradable and c) 280m/s with H55 abradable.

The minimum blade length during a test is then showed for all the 9 tests at this incursion rate in Fig. 5.5, with each plot corresponding to a single speed. Differences in wear rate between tests are more significant than differences between different blade width locations within a single test shown in Fig. 5.4. For all three speeds, blade wear increased from hardness H70 to H60.5 and then decreased between hardnesses H60.5 and H55. Similarly, there was an increase in blade wear between speeds of 100m/s and 200m/s and then a subsequent large decrease at the speed of 280m/s.

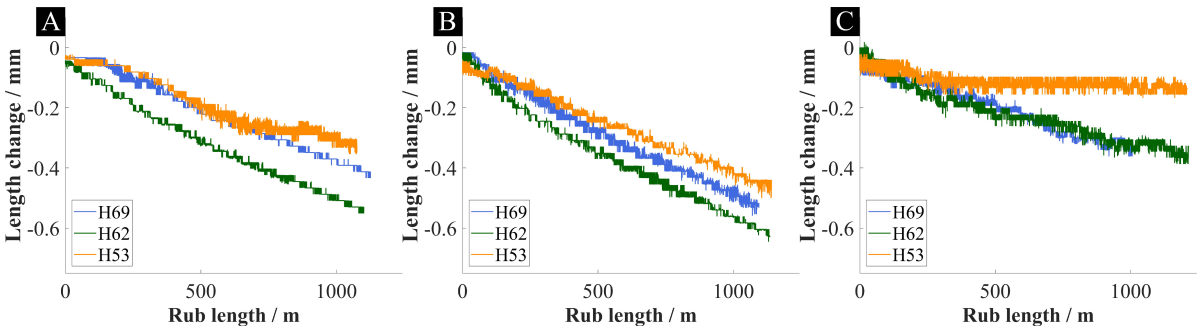

Fig. 5.5 The minimum blade length throughout a test for tests at a) 100m/s, b) 200m/s c), 280m/s.

These results demonstrated a highly non-linear correlation between the testing parameters considered in this study and blade wear rate. This may be explained by testing parameters non only directly influencing the blade wear rate, but also influencing parameters having a secondary influence on the wear rate such as heat generation in a system.

5.3.2.2 Adhesion results

Adhesions were observed for all the nine tests at the 0.02µm/pass incursion rate. To show a typical adhesive behaviour at this incursion rate, the blade profile history map, accompanied by post-test images of the abradable and blade and force data throughout a test are given in Fig. 5.6 for the test at 100m/s with the H69 abradable sample. This test was selected, as clear differences between adhesions and wear can be seen on the blade history map. However, trends in the formation of adhesions were similar for all the 9 tests at this incursion rate.

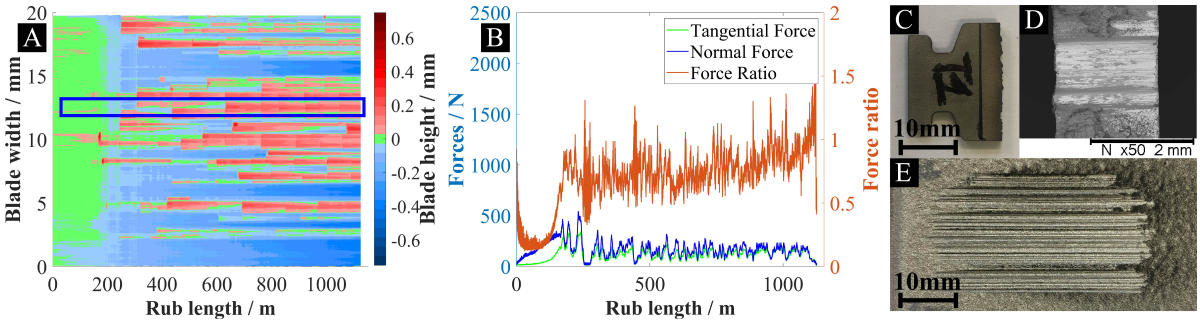

Fig. 5.6 Results for the test at 0.02µm/pass, 100m/s with H69 abradable a) the blade profile history map, b) forces during the test, c) post-test image of the blade, d) post-test SEM of the blade, e) post-test image of the abradable sample.

The adhesions that formed during the test were stable. These adhesions wore off with rub length, and re-adhesions occurred, as seen in the area inside the blue rectangle in Fig. 5.6a. However, in a few places during the test (for example, around the 6mm blade width line), the adhesions have fractured (where red has rapidly changed into green/light blue) and re-adhesions have not immediately reappeared in these places.

Additionally, it can be seen, that in a few areas, where wear has initiated (for example around the 3mm and 7.5mm lines), adhesions occurred later during the test. This suggests that wear in a certain location on a blade does not exclude a possibility of an adhesion formation in that location later during a test. This possibility likely depends on the local abradable composition at a given incursion depth [42].

It can be seen on the blade SEM image in Fig. 5.6d, that adhesions formed at the trailing edge of the blade. The lighter phase shows titanium from the blade and the darker phase AlSi adhesions transferred from the abradable sample.

5.3.2.3 Effect of blade tip speed and abradable hardness on adhesion results

The blade tip speed played a significant role in the likelihood of adhesion formation as shown in Fig. 5.3. At the lowest speed of 100m/s, adhesions were the most common, highest and widest

among the three considered speeds. At 200m/s, adhesions were rarer and shorter in height. At the highest speed of 280m/s, the adhesions were the least common with the test performed with the H69 abradable sample having almost no adhesions. Also, adhesions appeared stable at the 100m/s blade tip speed, while fracture increased with speed, which was a contributor to the lower overall number of stable adhesions at the higher speeds.

At the incursion rate of 0.02µm/pass, only small differences in adhesion formation can be observed between samples of different hardness. At the speed of 100m/s, it can be seen that adhesions in the test with the H53 abradable sample shown in Fig. 5.3c are the highest (the darker shade of red) and widest. Fracture of adhesions was also more common for the test with the H53 sample because of the increased maximum height of adhesions leading to higher contact moments acting on adhesions when contact with an abradable occurred.

5.3.2.4 Comparison of blade profiles with Alicona measured abradable surface

To better understand the influence of adhesions fracture on the final abradable surface, Alicona measurements were performed on the H69 abradable sample tested at 100m/s and 0.02µm/pass.

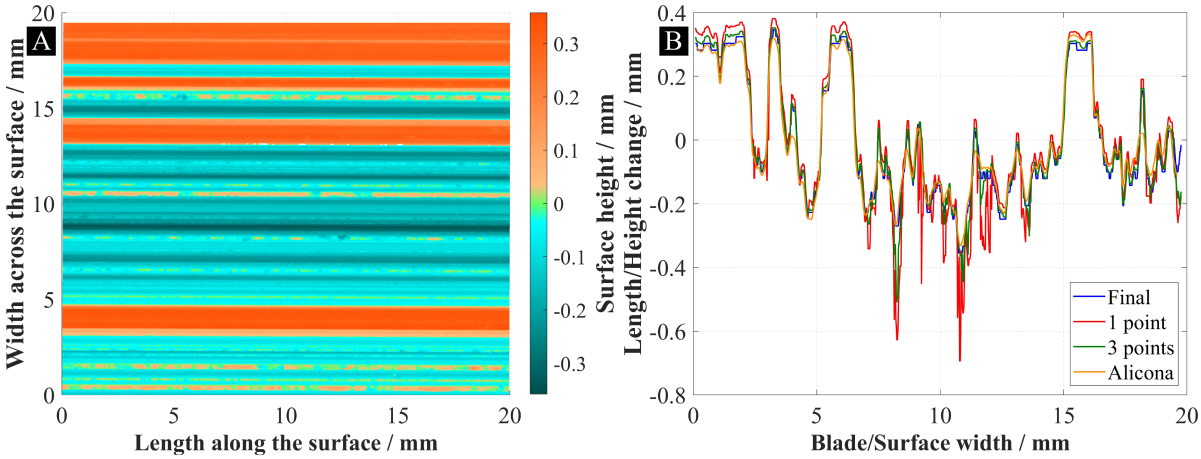

Fig. 5.7 a) The Alicona measured surface with the form removed, b) the comparison of the Alicona averaged surface profile and the blade-based profiles the test at 0.02µm/pass and 100m/s.

The post-test abradable surface profile measured using Alicona is given in Fig. 5.7a and a plot showing the comparison of blade profiles constructed following the methodology described in section 4.5 (final blade profile and profiles considering how deep would have fractures adhesions rubbed into a corresponding abradable surface) with the averaged Alicona abradable surface profile is shown in Fig. 5.7b illustrating a typical result for this incursion rate. The alicona results in Fig. 5.7b were inverted and the negative of the blade profiles was plotted to ensure that all the plots are shown in the same orientation.

It can be seen in Fig. 5.7b that both the final blade profile and the expected surface profiles based on previous adhesions on the blade match well with each other and with the Alicona result. This is because for this test, there was only a very small number of adhesions that fractured, and adhesions tended to gradually wear off instead. This resulted in almost no gaps between the final blade and the abradable surface. Some spikes can be seen in the results for the 1-point blade profile (shown in red), which are not seen on the other three plots, which is consistent with previous results obtained for tests with AlSi-polyester abradable samples [57]. These spikes are due to very long adhesions that existed briefly and have fractured thereafter.

5.3.3 Results at the 0.2µm/pass incursion rate

The post-test images of the abradable samples and blades, force data throughout a test and blade profile history maps are given for all the 9 tests at the 0.2µm/pass incursion rate in Fig. 5.8, 5.9 and 5.10 respectively.

The post-test blades show less blade wear and thermal damage on them than for the tests at the 0.02µm/pass incursion rate. However, it can be seen that the blades had adhesions attached to them, which resulted in the abradable samples having a significant level of grooving. The level of grooving was larger for the tests with H69 and H62 samples than with H53 samples. This is likely because adhesions had a lower maximum height for the tests with H53 samples as seen in Fig. 5.10.

Forces for the tests at this incursion rate showed a similar trend, where first a peak in the normal force was reached and then the the normal force reduced to a lower stable value. This happened because at the start of a test an entire blade rubbed an abradable. Once some of adhesions fractured, only parts of a blade were contacting an abradable reducing the total force in a contact.

The force ratio was the lowest in the region of normal force growth at the start of a test when adhesions were growing. This was likely caused by the adhesion rate being high leading to a local temporary increase in the incursion rate (attached adhesions would incur into an abradable at that blade width location resulting in the true incursion rate being higher than the nominal) leading to an increase in the normal force.

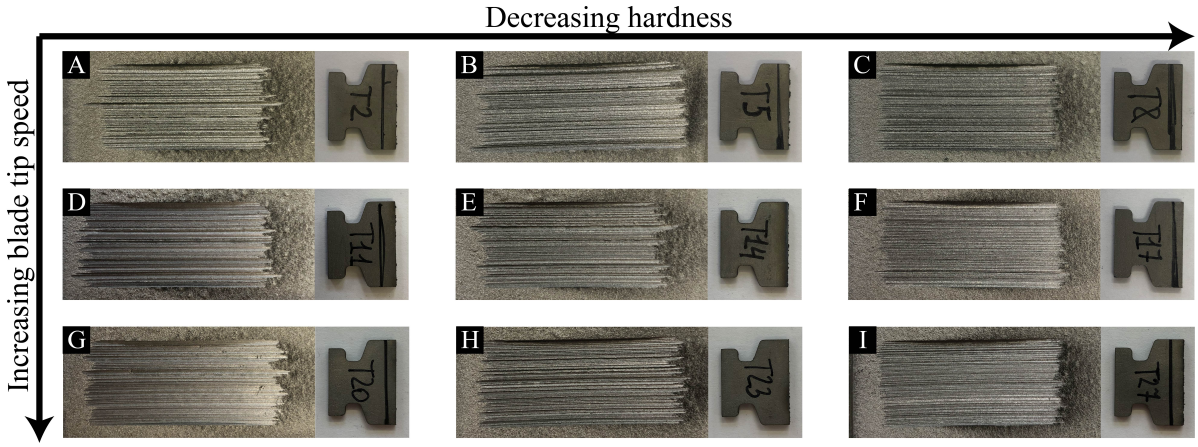

Fig. 5.8 The post-test images of the abradable samples and blades for the tests at the 0.2µm/pass incursion rate, 100m/s speed with a) H69 samples, b) H62 sample, c) H53 sample, 200m/s speed with d) H69 sample, e) H62 sample, f) H53 sample, 280m/s speed with g) H69 sample, h) H62 sample, i) H53 sample.

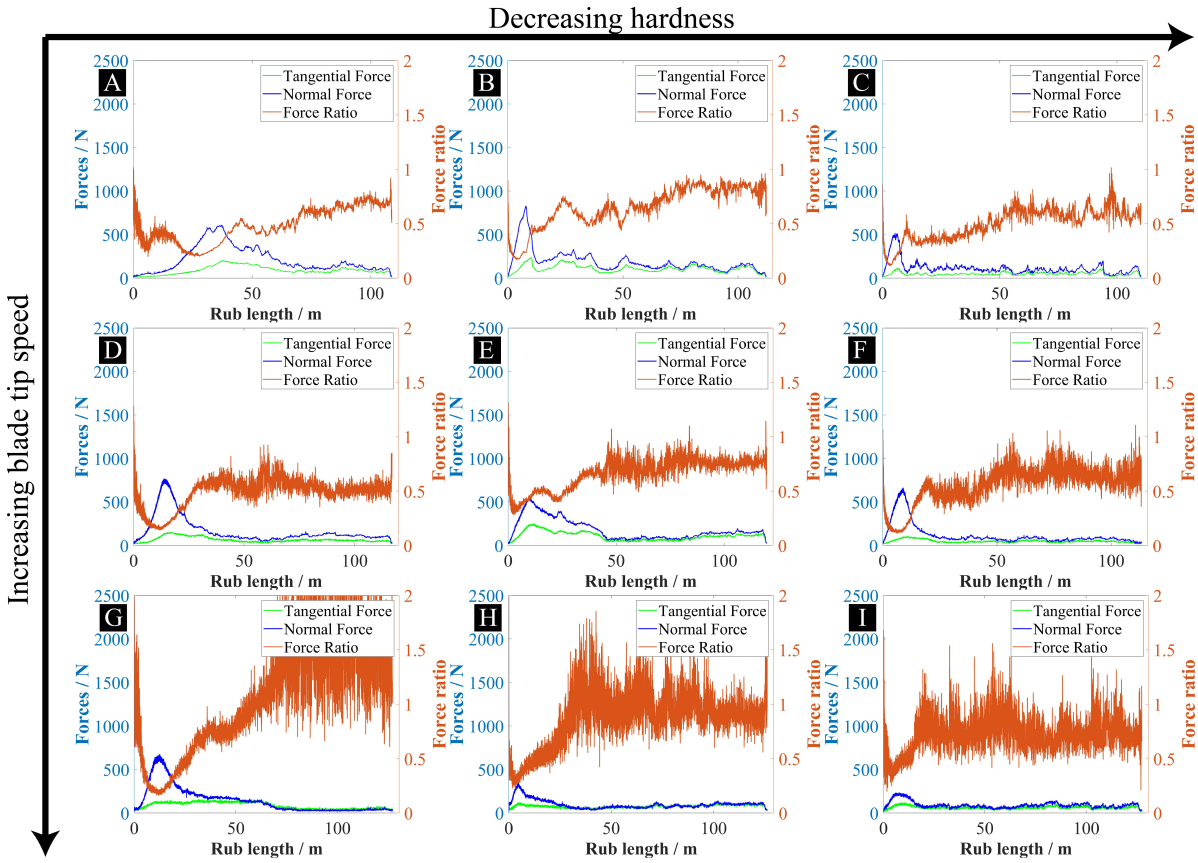

Fig. 5.9 The force data for the tests at the 0.2µm/pass incursion rate, 100m/s speed with a) H69 samples, b) H62 sample, c) H53 sample, 200m/s speed with d) H69 sample, e) H62 sample, f) H53 sample, 280m/s speed with g) H69 sample, h) H62 sample, i) H53 sample.

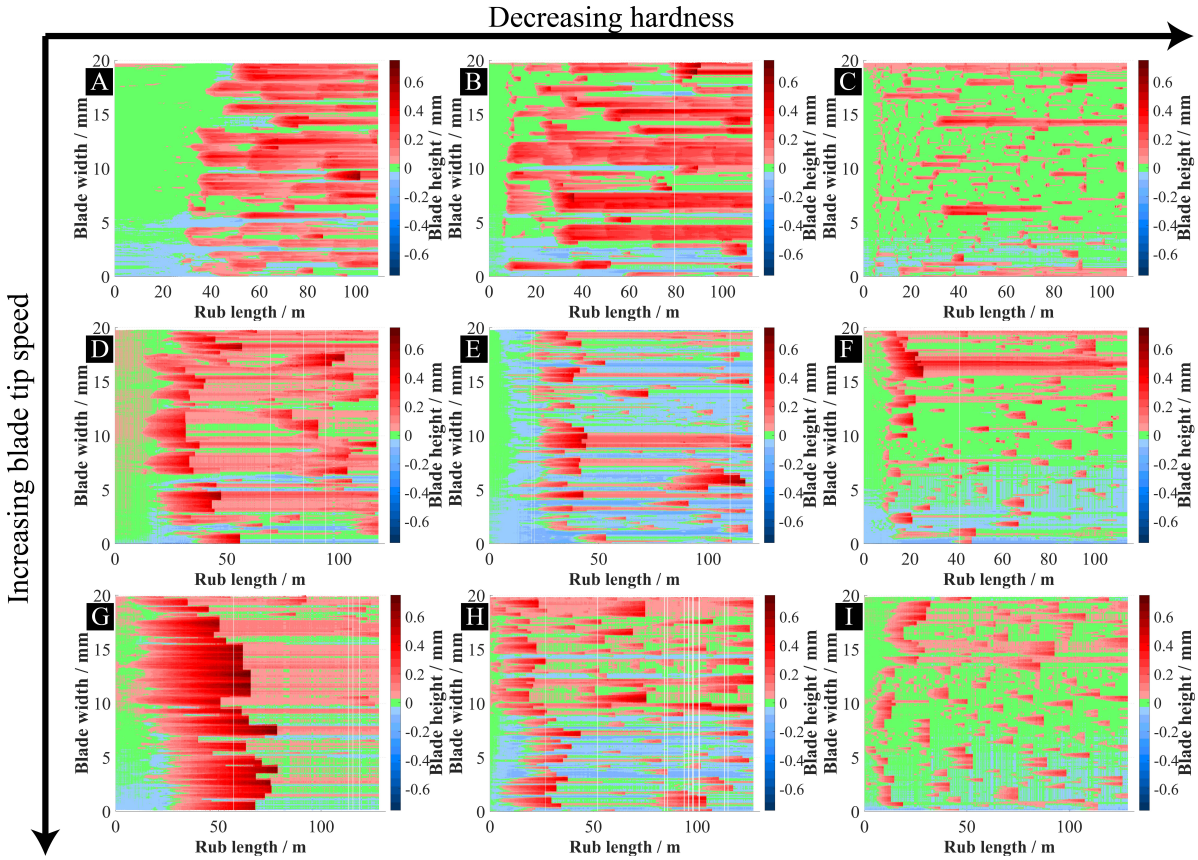

Fig. 5.10 The blade profile history maps for the tests at the 0.2µm/pass incursion rate, 100m/s speed with a) H69 samples, b) H62 sample, c) H53 sample, 200m/s speed with d) H69 sample, e) H62 sample, f) H53 sample, 280m/s speed with g) H69 sample, h) H62 sample, i) H53 sample.

The blade length and force results are further summarised in Table 5.3 for all the 9 tests at the 0.2µm/pass incursion rate. The mean normal forces increased at the higher incursion rate of 0.2µm/pass compared to the tests at 0.02µm/pass. However, this increase was much smaller than the tenfold increase in the incursion rate. This is likely due to tests at the 0.02µm/pass incursion rate experiencing the compaction/elastic deformation and release mechanism resulting in increased forces for that incursion rate.

The largest force occurred for the test at 100m/s speed with the H62 abradable sample and the lowest force occurred for the test at 280m/s with the H53 abradable sample. The mean forces decreased with speed. They were similar for the tests with H69 and H62 abradable samples and decreased for H53 samples.

The minimum blade length at the end of the tests was much higher (less negative) than for the tests at 0.02µm/pass indicating low blade wear across all the testing conditions at 0.2µm/pass. For all the conditions, the blade maximum length at the end of a test was positive,

showing the presence of adhesions. The adhesion was the predominant wear mechanism at this incursion rate, which can also be observed in Fig. 5.10.

Table 5.3 Summary of the blade length and force results for the tests at the 0.2µm/pass incursion rate.

Blade tip speed / m/s	Hardness	Blade length at the end mean (std)	Blade min	Blade max	Mean normal force	Mean tangential force
100	H69	0.08(0.09)	-0.08	0.32	199	80
100	H62	0.10(0.12)	-0.14	0.45	218	108
100	H53	0.02(0.04)	-0.03	0.25	130	48
200	H69	0.08(0.08)	-0.11	0.32	187	67
200	H62	-0.03(0.07)	-0.18	0.20	202	111
200	H53	-0.01(0.05)	-0.13	0.29	146	51
280	H69	0.05(0.05)	-0.05	0.22	172	89
280	H62	0.04(0.10)	-0.12	0.36	111	74
280	H53	-0.02(0.07)	-0.14	0.22	111	91

5.3.3.1 Adhesion results

To show a typical adhesive behaviour at this incursion rate, the blade profile history map, accompanied by post-test images of the abradable and blade and force data throughout a test are given in Fig. 5.11 for the test at 100m/s with the H69 abradable sample.

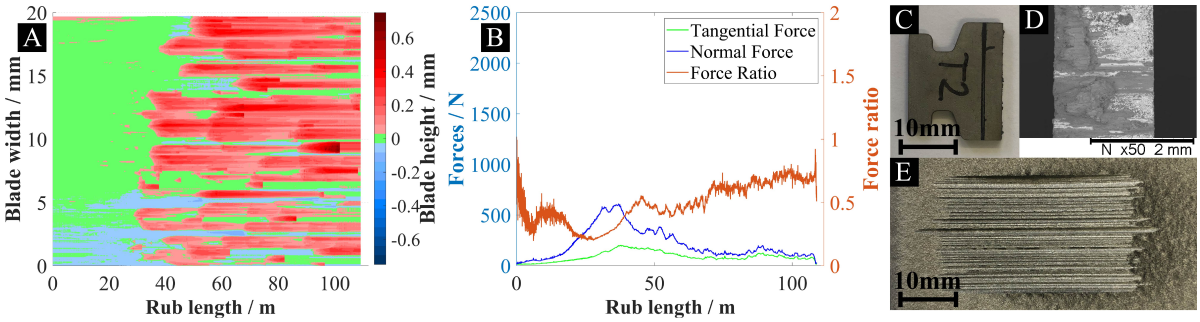

Fig. 5.11 Results for the test at 0.2µm/pass, 100m/s with H69 abradable a) the blade profile history map, b) forces during the test, c) post-test image of the blade, d) post-test SEM of the blade, e) post-test image of the abradable sample.

Adhesions formed across the entire blade width. Some of the adhesions were stable for the duration of the test and some fractured. The maximum height of adhesions was similar to the tests at 0.02µm/pass and reached about 0.5mm. On the blade SEM image in Fig. 5.11d, it

can be seen that adhesions formed at the trailing edge of the blade, similarly to the test at the 0.02µm/pass incursion rate.

5.3.3.2 Effect of blade tip speed and abradable hardness on adhesion results

To further understand the effect of blade tip speed and abradable hardness on adhesion formation, three lines corresponding to individual blade width locations where adhesions formed were plotted for all 9 tests at the 0.2µm/pass incursion rate in Fig. 5.12.

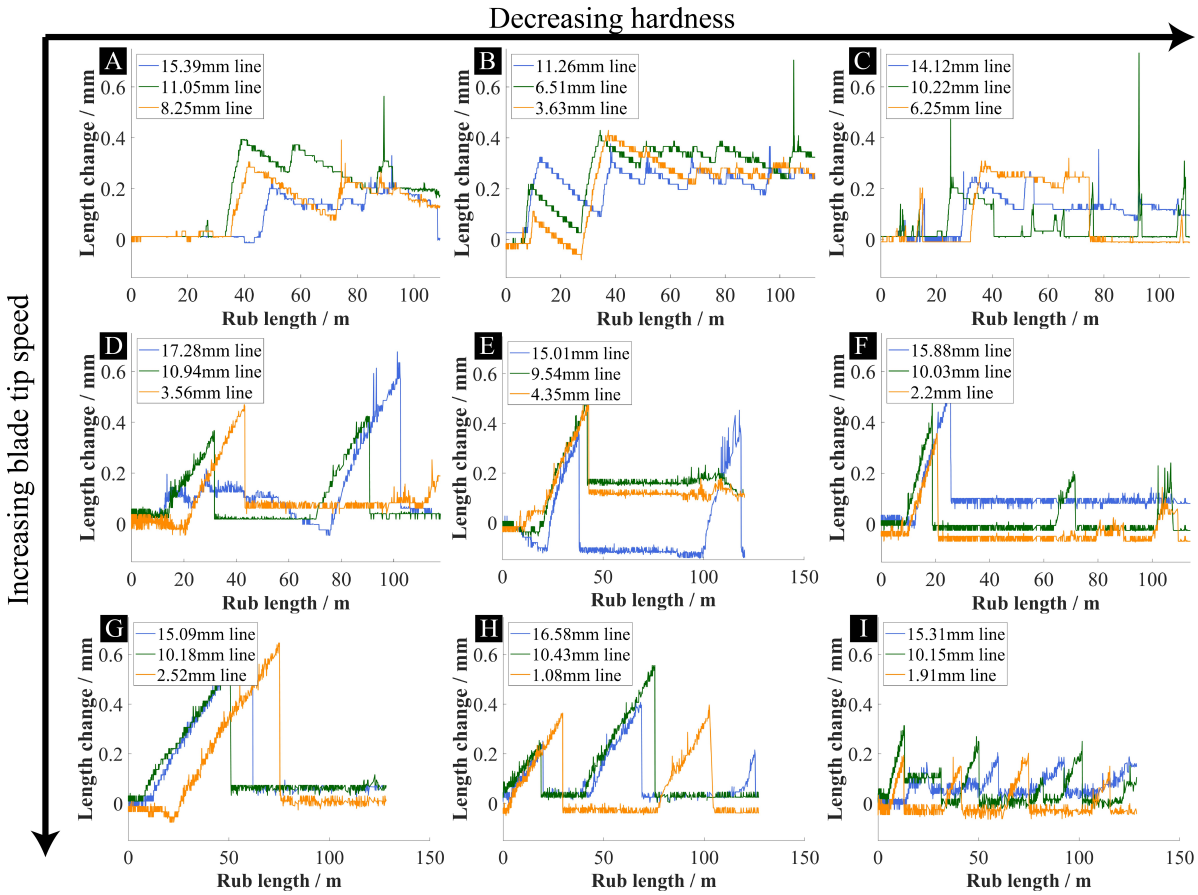

Fig. 5.12 The individual lines where adhesions occurred for the tests at the 0.2µm/pass the incursion rate, 100m/s speed with a) H69 samples, b) H62 sample, c) H53 sample, 200m/s speed with d) H69 sample, e) H62 sample, f) H53 sample, 280m/s speed with g) H69 sample, h) H62 sample, i) H53 sample.

For the tests at 0.2µm/pass, significant differences in adhesion formation were seen both with speed and some difference was seen with abradable hardness.

At the speed of 100m/s adhesions were relatively stable and a low amount of fracture was observed. Adhesions were wearing off with rub length and re-adhesions occurring. With an

increase in speed, adhesions fracture significantly increased for samples of all three hardnesses. The difference in the fracture frequency can be explained by the presence of critical height for an adhesion, where the moment acting on an adhesion on contact with an abradable becomes too large leading to an adhesion fracture. For the tests at 100m/s, most adhesions stopped growing before a critical length was reached, while for the tests at 200m/s and 280m/s adhesions kept growing until they fractured. Some cyclic behaviour can be seen for the tests where fractures occurred (for example, for the test at 200m/s speed with H69 samples shown in Fig. 5.12d), where re-adhesions occurred once a gap created by a previous adhesion fracture was closed with the increase in incursion depth.

The trend observed with hardness was different to the one seen for the tests at 0.02µm/pass. For the tests at 0.2µm/pass, the formation of stable adhesions at the 100m/s speed was lower for the tests with H53 abradable samples. Furthermore, for the H53 samples at all 3 speeds, adhesions generally fractured at lower adhesion heights indicating lower strength of adhesions.

5.3.3.3 Comparison of blade profiles with Alicona measured abradable surface

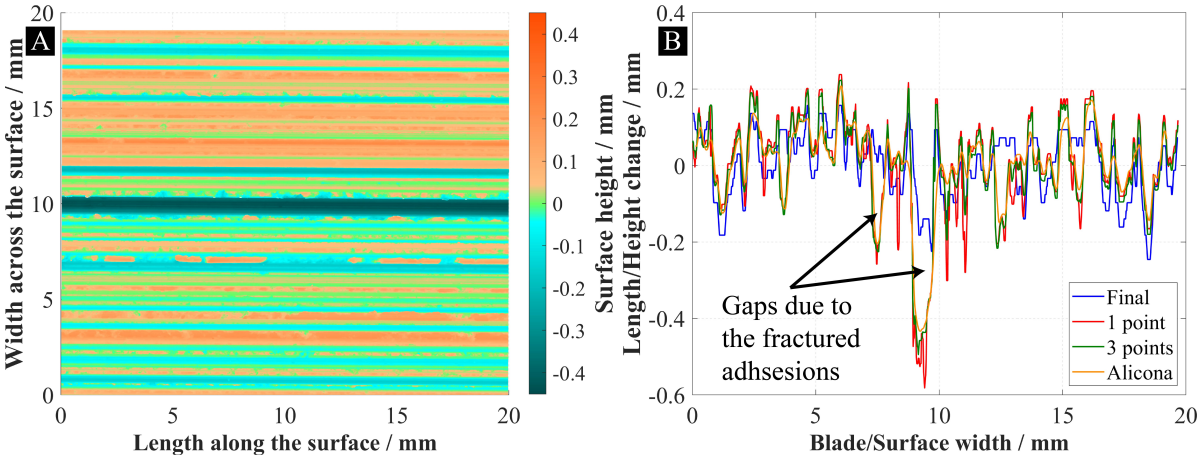

Fig. 5.13 a) The Alicona measured surface with the form removed, b) the comparison of the Alicona averaged surface profile and the blade-based profiles the test at 0.2µm/pass and 100m/s.

The Alicona profile and the comparison of the Alicona and the blade-based profiles for the test at 0.2µm/pass, 100m/s with H69 abradable sample are shown in Fig. 5.13 illustrating a typical result for this incursion rate. The final blade profile does not match the abradable surface profile at some points along the blade width, while, the 3-points based profile, which considers adhesions that have broken off, shows a very close match with the Alicona result. The 1-point profile has spikes similar to the ones observed for the 1-point based profile in the test at 0.02µm/pass and likewise, these spikes are not seen on the surface profile measured with the Alicona.

5.3.4 Results at the 2µm/pass incursion rate

The post-test images of the abradable samples and blades, force data throughout a test and blade profile history maps are given for all the 9 tests at the 2µm/pass incursion rate in Fig. 5.14, 5.15 and 5.16 respectively.

The post-test blades show no blade wear but some thermal damage (at higher speeds). Despite the small number of adhesions on the post-test blades, abradable samples have a significant level of grooving. This is because of the large amount of adhesions observed during the tests as seen in Fig. 5.16. The adhesions at different blade width locations initiated and fractured at different times during a test which created an uneven blade surface, which then led to the grooving of an abradable surface. Based on results in Fig. 5.16, most of the blades had a significant level of adhesions at the end of a test, but only a small amount when they were imaged post-test (Fig. 5.14). This means that adhesions have delaminated from the blade post-test. During the test, adhesions were strong enough to withstand high contact forces until a critical length was reached, so adhesion bonding strength during a test was high. It is then likely than bonding was weakened post-test, during the cool-down of a blade. This suggests there was a large temperature difference between the blade bulk temperature and adhesions leading to adhesions cracking on the cool-down.

Forces for the tests at this incursion rate showed a similar trend and were relatively stable throughout a test. The regions with a decrease in normal force occurred after the fracture of some adhesions due to the reduced contact area between a blade and an abradable.

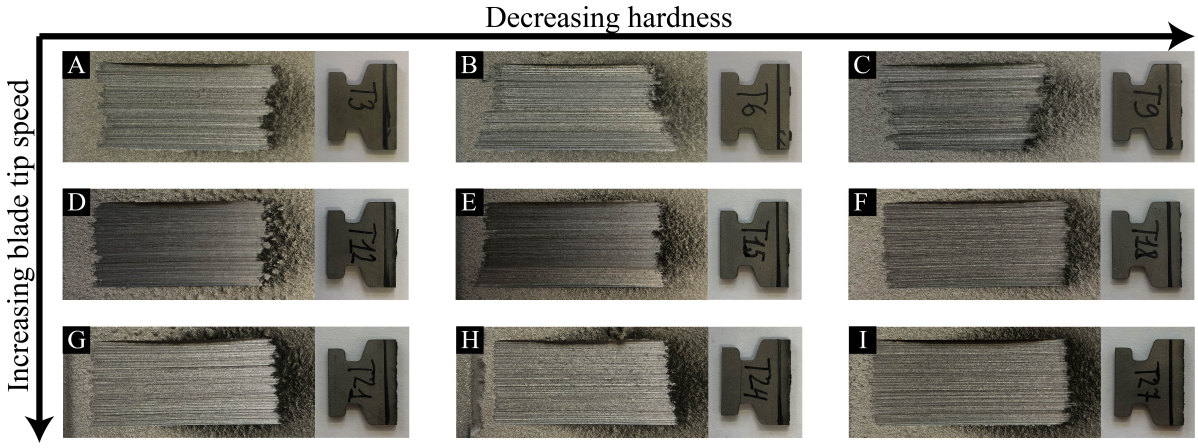

Fig. 5.14 The post-test images of the abradable samples and blades for the tests at the 2µm/pass incursion rate, 100m/s speed with a) H69 samples, b) H62 sample, c) H53 sample, 200m/s speed with d) H69 sample, e) H62 sample, f) H53 sample, 280m/s speed with g) H69 sample, h) H62 sample, i) H53 sample.

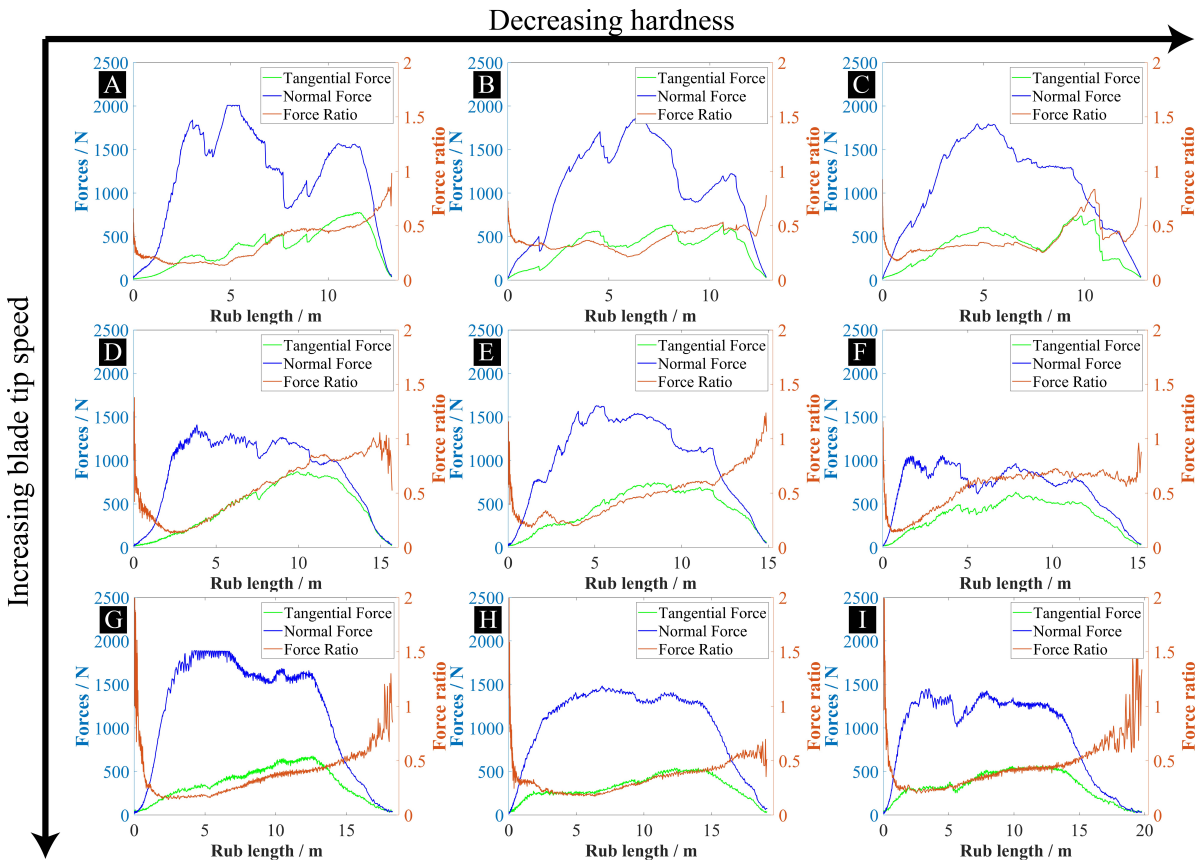

Fig. 5.15 The force data for the tests at the 2µm/pass incursion rate, 100m/s speed with a*) H69 samples, b) H62 sample, c) H53 sample, 200m/s speed with d) H69 sample, e) H62 sample, f) H53 sample, 280m/s speed with g*) H69 sample, h) H62 sample, i) H53 sample. For tests marked with * the normal force was capped at around 2000N due to the maximum force setting on the dynamometer amplifier. In that region the normal force was above 2000N, but the exact value of force was not known due to that setting.

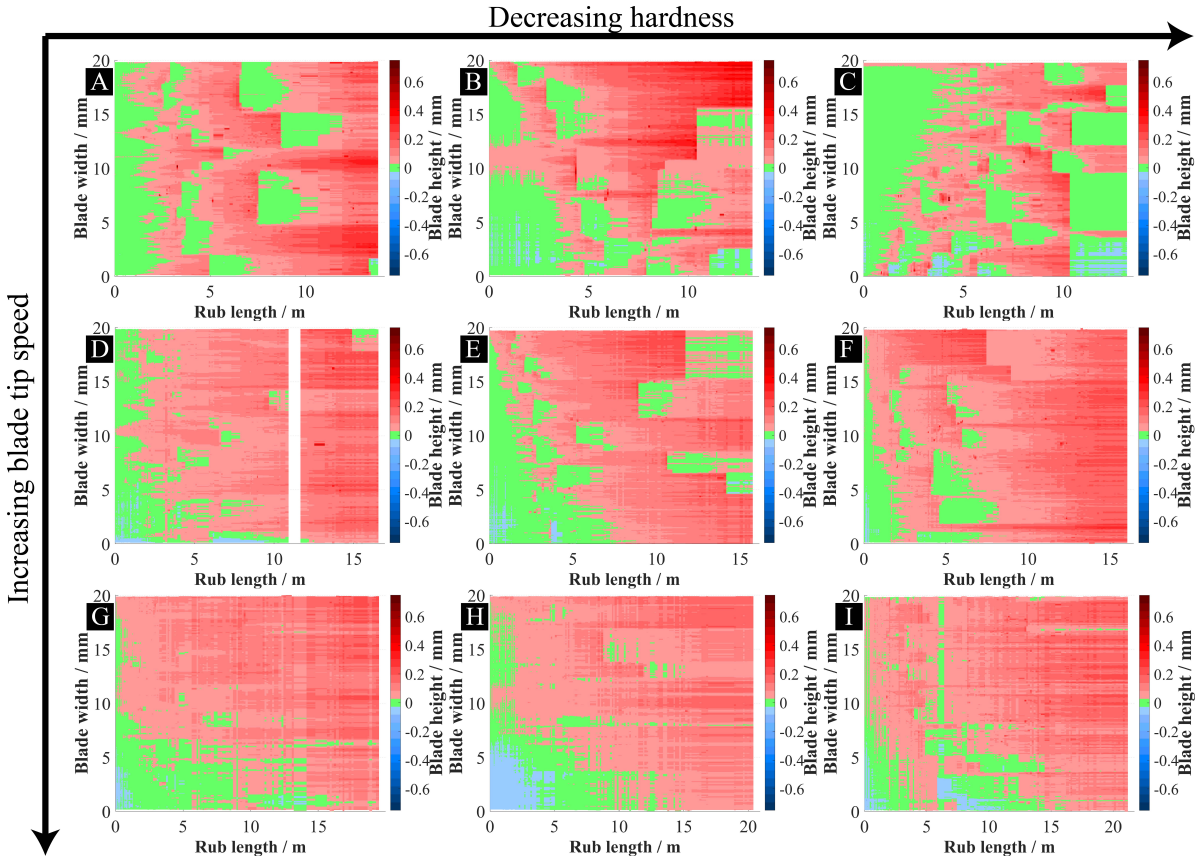

Fig. 5.16 The blade profile history maps for the tests at the 2µm/pass incursion rate, 100m/s speed with a) H69 samples, b) H62 sample, c) H53 sample, 200m/s speed with d) H69 sample, e) H62 sample, f) H53 sample, 280m/s speed with g) H69 sample, h) H62 sample, i) H53 sample.

The blade length and force results are further summarised in Table 5.4 for all the 9 tests at the 2µm/pass incursion rate.

The mean normal forces increased significantly at the higher incursion rate of 2µm/pass compared to the tests at 0.2µm/pass. This increase is roughly proportional to the tenfold increase in incursion rate, suggesting no significant improvement in the contact mechanism occurred. Forces were similar across all the testing conditions; although for the tests with H53 abradable samples they were slightly lower.

The minimum blade length at the end of the tests was close to zero indicating no blade wear across all the testing conditions at 2µm/pass. For all the conditions, the blade maximum length at the end of the test was positive, showing the presence of adhesions. The adhesion was the predominant wear mechanism at this incursion rate.

Table 5.4 Summary of the blade length and force results for the tests at the 2m/pass incursion rate.

Blade tip speed / m/s	Hardness	Blade length at the end mean (std)	Blade min	Blade max	Mean normal force	Mean tangential force
100	H69	0.17(0.08)	-0.03	0.35	1078	313
100	H62	0.12(0.12)	-0.02	0.45	969	338
100	H53	0.03(0.06)	-0.04	0.18	991	343
200	H69	0.15(0.05)	0.01	0.27	818	384
200	H62	0.09(0.06)	-0.04	0.24	943	383
200	H53	0.19(0.03)	0.12	0.31	679	331
280	H69	0.13(0.04)	0.01	0.22	1132	318
280	H62	0.11(0.04)	0.01	0.18	986	288
280	H53	0.13(0.05)	0.02	0.23	916	315

5.3.4.1 Adhesion results

To show a typical adhesive behaviour at this incursion rate, the blade profile history map, accompanied by post-test images of the abradable and blade and force data throughout a test are given in Fig. 5.17 for the test at 100m/s with the H69 abradable sample.

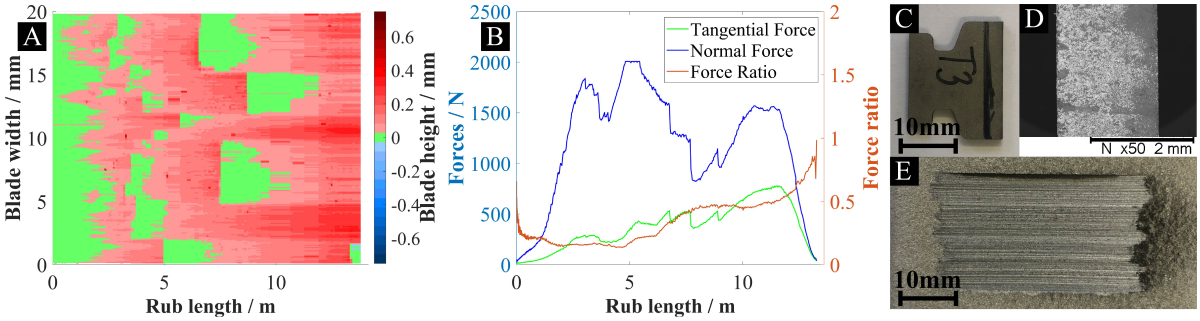

Fig. 5.17 Results for the test at 2µm/pass, 100m/s with H69 abradable a) the blade profile history map, b) forces during the test, c) post-test image of the blade, d) post-test SEM of the blade, e) post-test image of the abradable sample.

Adhesions formed across the entire blade width. Most of adhesions fractured once they reached the critical length for this test condition. The maximum height of adhesions was lower than for the test at 0.2µm/pass and reached about 0.3mm. This was due to higher contact forces leading to higher moments acting on adhesions causing fractures at lower adhesion heights.

The blade in Fig. 5.17c and on the SEM image in Fig. 5.17d had no adhesions attached to it as they delaminated post-test.

5.3.4.2 Effect of blade tip speed and abradable hardness on adhesion results

To further understand the effect of blade tip speed and abradable hardness on adhesion formation, three lines corresponding to individual blade width locations where adhesions formed were plotted for all 9 tests at the 2µm/pass incursion rate in Fig. 5.18.

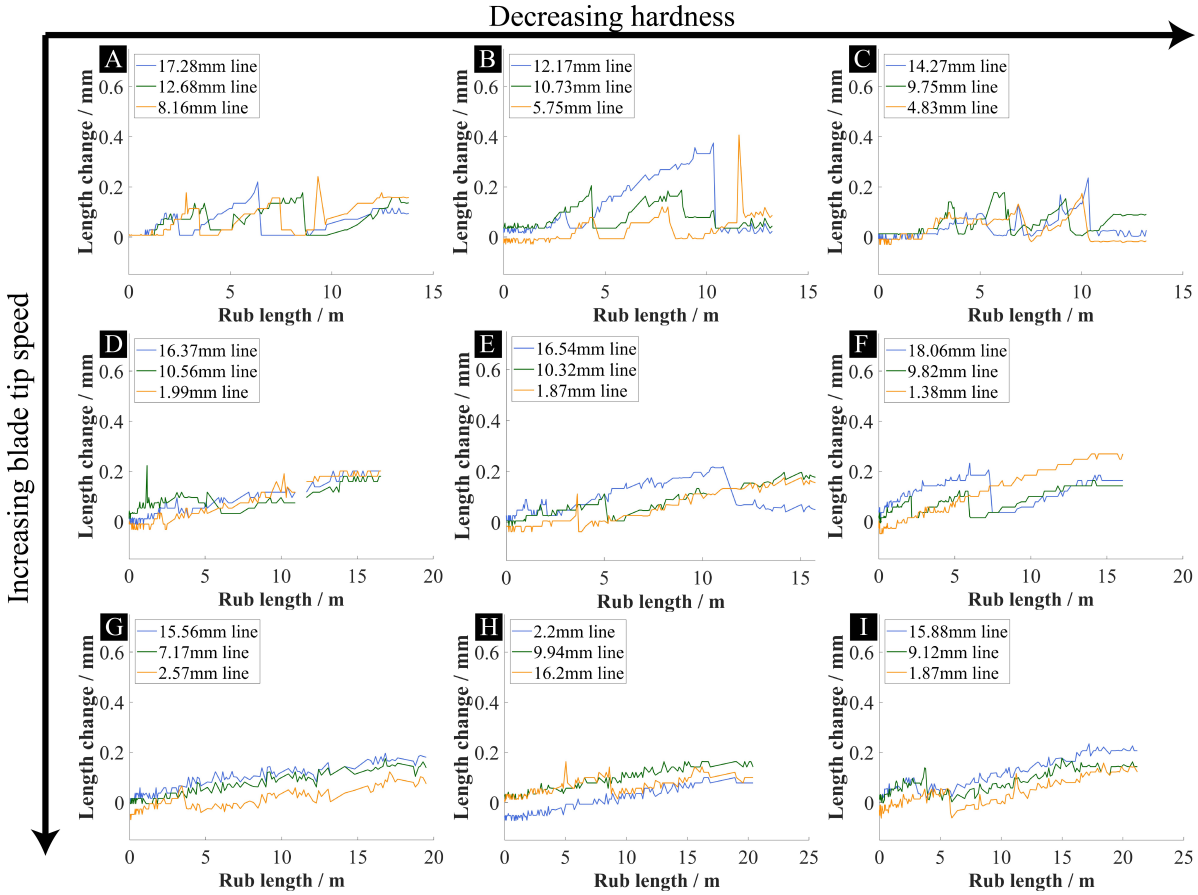

Fig. 5.18 The individual lines where adhesions occurred for the tests at the 2µm/pass the incursion rate, 100m/s speed with a) H69 samples, b) H62 sample, c) H53 sample, 200m/s speed with d) H69 sample, e) H62 sample, f) H53 sample, 280m/s speed with g) H69 sample, h) H62 sample, i) H53 sample.

For the tests at 2µm/pass shown in Fig. 5.16 and 5.18, no significant differences in the likelihood of adhesion formation can be seen with either speed or abradable hardness. For all of the 9 conditions, uniform adhesions formation was seen across an entire blade width. Fractures, however, were more common at the speed of 100m/s than at the higher speeds of 200m/s

and 280m/s. This was due to higher rate of adhesion growth at 100m/s leading to adhesions reaching critical height earlier in a test. In places where adhesions fractured, re-adhesions occurred once a gap created by a fracture was closed with the increase in incursion depth. It also appears that at the higher speeds of 200m/s and 280m/s the rub depth used in these tests was not sufficient to observe a full life cycle of adhesions as some adhesions were still growing when the target incursion depth was reached.

5.3.4.3 Comparison of blade profiles with Alicona measured abradable surface

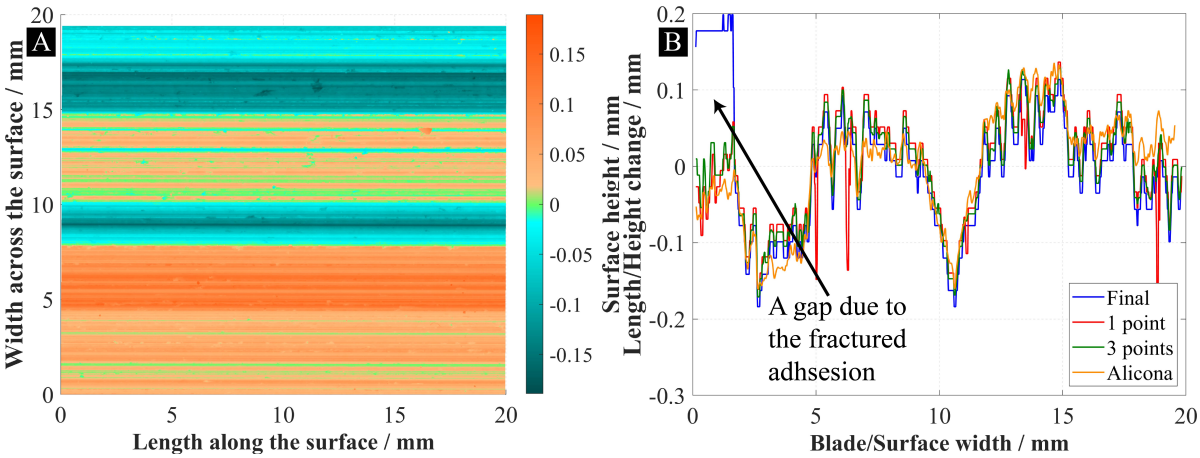

Fig. 5.19 a) The Alicona measured surface with the form removed, b) the comparison of the Alicona averaged surface profile and the blade-based profiles the test at 2µm/pass and 100m/s.

The Alicona profile and the comparison of the Alicona and the blade-based profiles for the test at 100m/s, 2µm/pass with H69 abradable sample are shown in Fig. 5.19 illustrating a typical result for this incursion rate. The final blade profile does not match the abradable surface profile at a location where an adhesion fractured, while the 3-points based profile shows a very close match with the Alicona result. The 1-point profile has spikes similar to the ones observed for the 1-point based profiles in the tests at 0.02µm/pass and 0.2µm/pass and, likewise, these spikes are not seen on the surface profile measured with the Alicona.

5.4 Discussion

The results in this study give real-time insights into the blade tip wear mechanisms along an entire blade front, something that has been inferred in previous studies either from post-mortem analysis, or more limited in-situ measurements. Adhesive transfer of material from the liner onto the blade tip and blade wear were identified as the dominant wear mechanisms for the

incursion conditions used in this study. Incursion rate was the dominant factor in determining what wear mechanism occurred, which is consistent with the results from previous studies, where similar conditions were investigated [5, 25].

5.4.1 Blade wear mechanism

For the tests in this study, the blade wear mechanism occurred where adhesions have not formed and the bare blade rubbed against an abradable. Once an adhesion formed, it was in contact with the abradable, preventing any further blade wear from occurring in that location on the blade. As a result of this, blade wear was predominantly seen for the tests at the 0.02µm/pass as adhesions were the least common at that condition, while the rub lengths were the longest.

Previously it was assumed that the wear mechanism was continuous and progressive [42]. Taking the results shown in Fig. 5.3 as an example, this is not the case. As shown in Fig. 5.3a, whilst between 0 and 2mm along the blade width the area of progressive wear occurred, at approximately 4mm and 7.5mm, blade wear occurred for a period before an adhesion initiated. Some blade wear was also seen for the tests at the 0.2µm/pass incursion rate, but it stopped once adhesions initiated.

The observed variation for the test at the 0.02µm/pass incursion rate is likely due to changes in the local thermal diffusivity of the material, caused as localities in microstructure are either removed, or indeed come into increased proximity of the blade tip, given the established connection between material microstructure and wear mechanism [42], and that the incursion event represents a process through which material is progressively removed from the liner. This gives further insight into the transient nature of wear in abradable lining sealing systems identified by multiple authors [25, 46, 38].

For the tests at the 0.2µm/pass incursion rate, it is likely adhesions initiated once the abradable temperature was hot enough for adhesions to start forming as it was previously shown that during the initial part of an incursion, abradable surface temperature rises with rub length until a stable temperature is reached (unless the cyclic behaviour occurs where forces and temperatures oscillate throughout a test) [48, 52].

5.4.1.1 Blade wear rate

When blade wear occurred, the wear rate throughout a given test was constant or close to constant with respect to rub length for all of the testing conditions at the 0.02µm/pass incursion rate. This is consistent with the Archard's law, where the wear volume depends on a constant of proportionality and is proportional to the normal force, the sliding distance, and inversely proportional to the hardness of the softer contact partners. However, Archard's law gives only a

limited ability to compare tests at different testing conditions. This is due to contact hardness values being a function of the instantaneous temperature of each contacting material and the difficulty in estimating the constant of proportionality with it dependent on a large number of contact parameters.

Wear results at 0.02µm/pass showed a highly non-linear correlation with blade tip speed and hardness. Blade wear increased between speeds of 100m/s and 200m/s and then significantly decreased at the speed of 280m/s. This is likely due to combination of several factors. First, with an increase in speed, the time between consecutive blade strikes decreased, reducing the amount of conduction and radiation cooling of the blade and abradable samples, but significantly increasing convection cooling. It was therefore suggested, that between speeds of 200m/s and 280m/s, convection cooling became the dominant heat removal mechanism, which led to lower blade temperatures and blade wear at that speed (the correlation between temperature, blade hardness and subsequent wear was previously suggested by multiple authors [24, 6]).

Additionally, the higher speed might have increased the amount of material removed through cutting in front of the blade and decreased the amount of rubbing. While this was not previously experimentally shown for the AlSi-polyester abradable, for AlSi-hBN abradable, which differs only by the dislocator phase, wear maps by multiple authors indicated that the amount of cutting increased with speed [25, 48]. Extension of the work on abradable ejection direction [52] to multiple speeds can help to understand if the amount of cutting increases with speed for the AlSi-polyester abradable as well.

Blade wear slightly increased from H69 samples to H62 samples and then significantly decreased for H53 samples. The difference between H69 and H62 samples can be explained by the fact that H62 samples have lower thermal conductivity [14] leading to higher heat partition into the blade according to the heat partition criterion defined by Barber [58]. This resulted in higher blade temperature and considering the forces between tests with H69 and H62 samples were similar, led to higher blade wear with H62 samples. With H53 samples, the proportion of heat partitioned into the blade was even higher due to even lower thermal conductivity [14], but this was counteracted by lower forces in the contact, leading to lower blade wear.

5.4.2 Adhesion mechanism

Adhesions occurred at all the considered test conditions. The incursion rate had the dominant impact on the frequency and shape of the formed adhesions and is going to be discussed first, followed by the discussion of the influences of the blade tip speed and abradable hardness.

5.4.2.1 Influence of the incursion rate on the adhesion mechanism

An increase in incursion rate significantly increased the likelihood of adhesion formation. For the tests at 0.02µm/pass, adhesion formation frequency ranged from very rare for the tests at 280m/s to occurring at 50% to 75% of the blade width at 100m/s. For the tests at 0.2µm/pass, adhesions occurred at close to 100% of the blade width for all the tests except for the test with the H53 abradable sample at 100m/s. For the tests at 2µm/pass, adhesions occurred at the entirety of blade width for all the testing conditions. To further illustrate the increase in adhesion formation with incursion rate, the blade profile history maps for all 3 incursion rates for tests at 200m/s with H69 samples are given in Fig. 5.20.

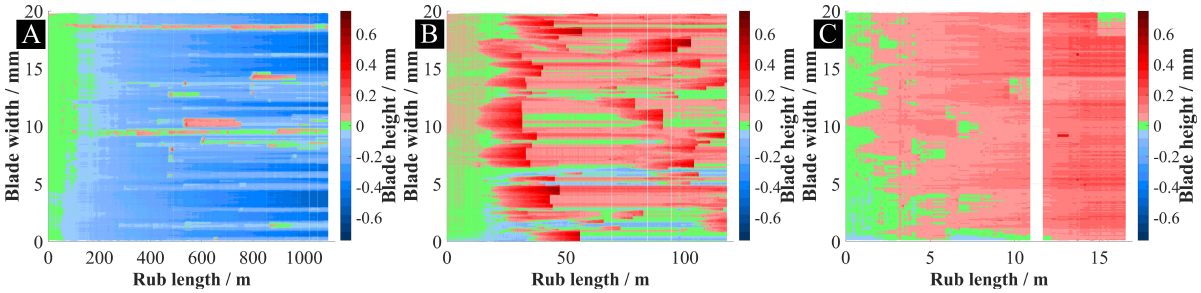

Fig. 5.20 The blade profile history maps for tests with H69 samples at 200m/s and a) 0.02µm/pass, b) 0.2µm/pass, and c) 2µm/pass.

The increase in adhesion formation between the incursion rates of 0.2µm/pass and 2µm/pass was due to the significant increase in contact forces leading to much higher contact flash temperatures [59]. If the contact temperature was high enough, that led to localised abradable melting, resulting in the transfer of an abradable material to a blade [52].

The trend between the tests at 0.02µm/pass and 0.2µm/pass was more complicated. For tests at the same speed with samples of the same abradable hardness, contact forces were very close or sometimes even larger for the tests at 0.02µm/pass due to the presence of the compaction/elastic deformation and release mechanism.

Therefore, based on the initial application of the flash temperature concept, it was expected that the adhesion formation at both incursion rates would have been similar. This was not the case for the performed tests, with tests at the 0.2µm/pass having much higher formation of adhesions.

It was then hypothesised that compaction rather than just elastic deformation happened at the 0.02µm/pass incursion rate increasing localised hardness value leading to a decreased formation of adhesions. It was previously shown that, for example, for AlSi-polyester abradable of H82 nominal hardness, adhesions formed at neither 0.02µm/pass nor 0.2µm/pass incursion rates despite high contact forces [52]. To verify this, the H69 samples from tests at all three

incursion rates and 100m/s speed were sectioned and analysed on the Desktop SEM TM3030 equipment. The post-test microstructure across the cut direction for all three samples is shown in Fig. 5.21.

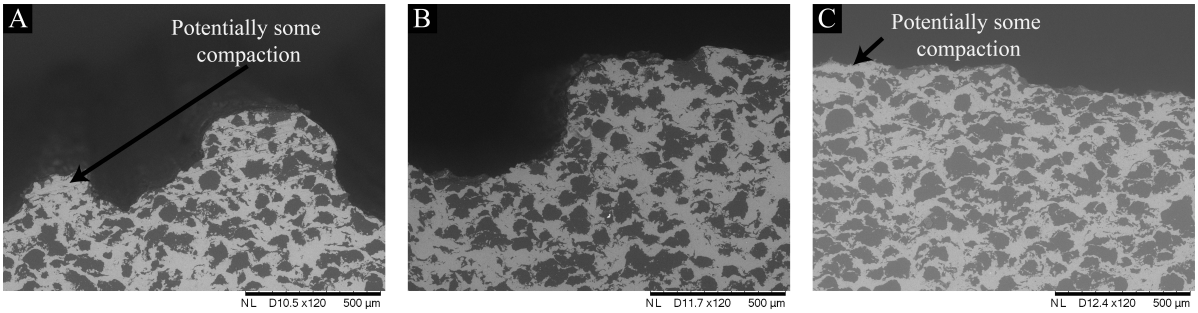

Fig. 5.21 The post-test SEM measurements for tests with H69 samples at 100m/s and a) 0.02µm/pass, b) 0.2µm/pass, and c) 2µm/pass.

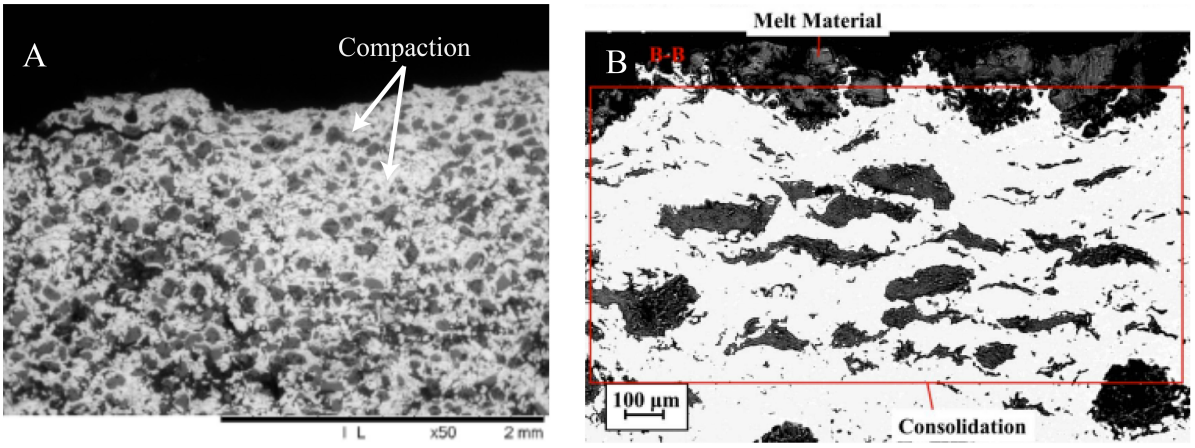

Fig. 5.22 The SEM iamges from past research, which show areas of significant compaction for a) NiCrAl-bentonite abradable [6] and b) AlSi-hBN abradable [48].

In Fig. 5.21 can be seen that no macroscopic compaction occurred at any of the incursion rates. For comparison, SEM images from past research, where significant macroscopic compaction was observed for AlSi-hBN and NiCrAl-bentonite are shown in Fig. 5.22a and Fig. 5.22b respectively. Some areas with AlSi phase densification were observed at 0.02µm/pass (Fig. 5.21a) and potentially at 2µm/pass (Fig. 5.21c) (due to some polyester particles appearing squashed rather than spherical), however, these areas were very localised. No such areas were noticed for the test at 0.2µm/pass. While there is a possibility that the presence of such densified regions is what decreased the likelihood of adhesion formation at 0.02µm/pass for a given amount of force in comparison to tests at 0.2µm/pass, the results from the SEM imaging do not appear conclusive enough to confirm or disprove this suggestion as such areas were

small and present only on the surface level with no global compaction of the sample. Further research is required to better understand the differences in adhesion formation at 0.02µm/pass and 0.2µm/pass.

5.4.2.2 Influence of the blade tip speed and abradable hardness on the adhesion mechanism

The impact of blade tip speed on the frequency of adhesions depended on the considered incursion rate. At the incursion rate of 0.02µm/pass, the frequency of adhesion formation decreased with speed, while at the incursion rate of 0.2µm/pass the trend was opposite and adhesions were more frequent at the higher speeds. To further illustrate this, blade profile history maps for tests at all 3 considered speeds with H69 samples at 0.02µm/pass are given in Fig. 5.23, and at 0.2µm/pass in Fig. 5.24.

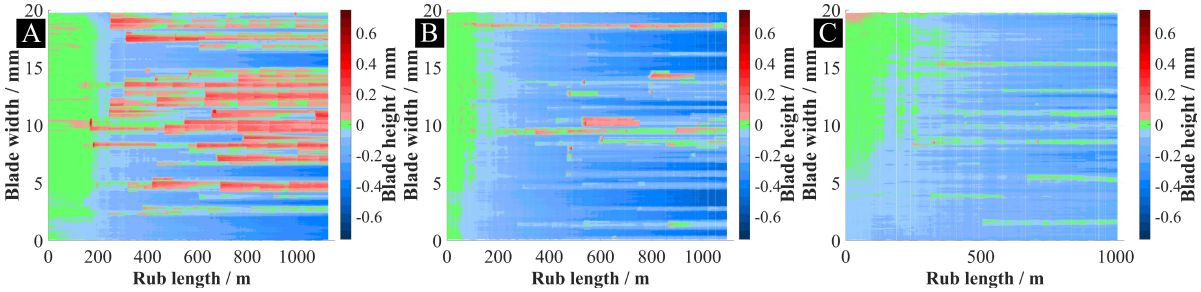

Fig. 5.23 The blade profile history maps for tests with H69 samples at 0.02µm/pass and a) 100m/s, b) 200m/s, and c) 280m/s.

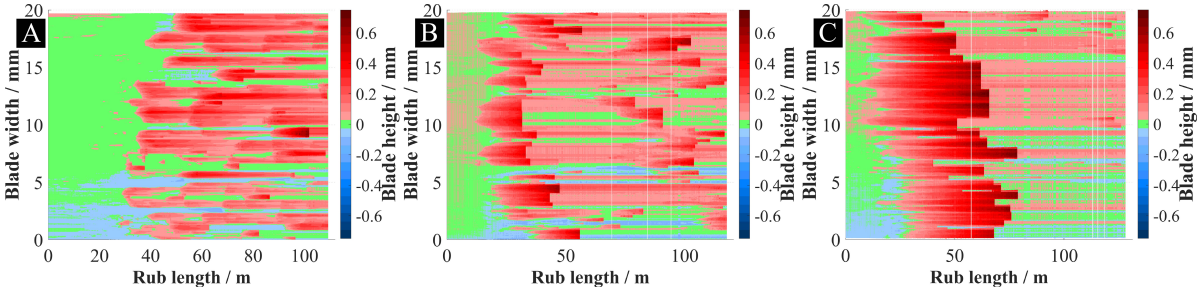

Fig. 5.24 The blade profile history maps for tests with H69 samples at 0.2µm/pass and a) 100m/s, b) 200m/s, and c) 280m/s.

It is likely that bulk temperatures of the contacting materials were more important in determining the probability of adhesion formation at the lowest incursion rate of 0.02µm/pass due to lower flash temperatures. This would explain the decrease in adhesion formation at 280m/s speed, as bulk temperatures appeared to be lower for tests at this speed based on blade

wear results. At the incursion rate of 0.2µm/pass, higher formation of adhesions with increased speed was promoted by increased flash temperatures at higher speeds [59].

The changes in the frequency of adhesion formation were small with abradable hardness, with tests at a lower hardness having a small increase in the frequency of adhesion formation at the lowest incurion rate of 0.02µm/pass as can be seen on the example of the test with the H53 abradable sample at the 0.02µm/pass incursion rate and 280m/s speed shown in Fig. 5.3i.

5.4.2.3 Adhesion rate and peak height analysis

Three lines were extracted from the blade profile history maps for each test (Fig. 5.3, 5.10 and 5.16) according to the procedure described in section 4.2.6 for adhesion rate and peak heights calculations to further aid the comparison of tests at different conditions for tests at 0.2µm/pass and 2µm/pass incursion rates. Tests at the 0.02µm/pass incursion rate were not included due to difficulty in selecting individual adhesions and lack of significant adhesions at the highest speed of 280m/s.

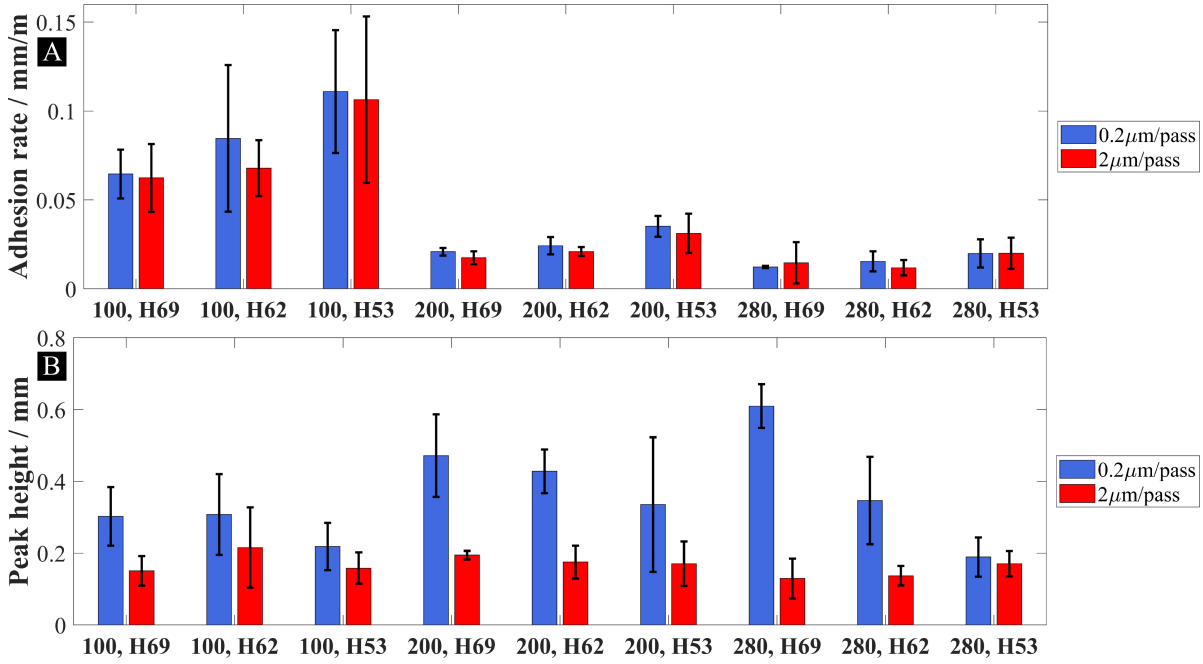

Fig. 5.25 a) the adhesion rate results, b) the adhesion peak height results for tests at the 0.2µm/pass and 2µm/pass incursion rates.

The blade tip speed was the major factor influencing adhesion rates with an increase in speed significantly decreasing the adhesion rate as can be seen in Fig. 5.25a. The abradable hardness had a smaller impact on adhesion rate, with a lower hardness leading to a higher adhesion rate. Interestingly, the adhesion rate was almost independent of the incursion rate.

The decrease in adhesion rate with blade tip speed can be explained by heat propagation through an abradable on contact and a decrease in contact residency time. At a higher speed, there is less time for heat to propagate resulting in a decrease in the abradable surface volume that reaches a temperature high enough to transfer to the blade as an adhesion. The results here are consistent with the results of Fois et al. [41] obtained for tests with AlSi-hBN abradables, where adhesion rate at a given incursion condition was also seen to drop with blade speed.

The adhesion rate increased with a decrease in hardness. However, a lower abradable hardness also increased the fracture of adhesions, particularly for the tests at 0.2µm/pass, where adhesions during the tests with the H53 samples were the least stable and fractured at lower peak height as shown in Fig. 5.25b. The decrease in adhesion stability and an increase in adhesion rate could potentially be explained by adhesions being less densely packed due to lower normal forces. However, a more detailed analysis of adhesions morphology and measurements of their density for different testing conditions is needed to offer more insights into how abradable hardness affects adhesions.

The incursion rate had the biggest influence on peak heights, with peaks at 2µm/pass being significantly lower. This is likely due to higher contact forces leading to fracture at lower adhesion heights. Additionally, peak height results for some tests at 2µm/pass, particularly at the highest speed of 280m/s could be affected by the rub depth used in this study being too low to observe a full life cycle of an adhesion as some of the adhesions were still growing at the end of a test.

5.4.2.4 Analysis of the Adhesion Cyclic Mechanism

The adhesion results here offer new insights into the cyclic formation and removal of adhesions. Two types of cyclic formation of adhesions were observed: driven by the existence of an already adhered material in a given spot for the tests at 0.02µm/pass, and driven by adhesion fracture and re-initiation in the same location for the tests at 0.2µm/pass and 2µm/pass.

For the tests at 0.02µm/pass, once an adhesion initiated, peaks grew and were removed at a broadly consistent rate as shown by the lines extracted from the test at 0.02µm/pass and 100m/s with H70 abradable shown in Fig. 5.26. It is also interesting to note, that where previous studies [41] have assumed fracture of the adhered material once a critical length is reached, more gradual wear is also evident for this test. Five individual adhesion events from the 12.2mm line were overlaid onto each other to further illustrate the similar adhesion rates and maxima shown in Fig. 5.27a and subsequent gradual wear shown in Fig. 5.27b, further supporting this view.

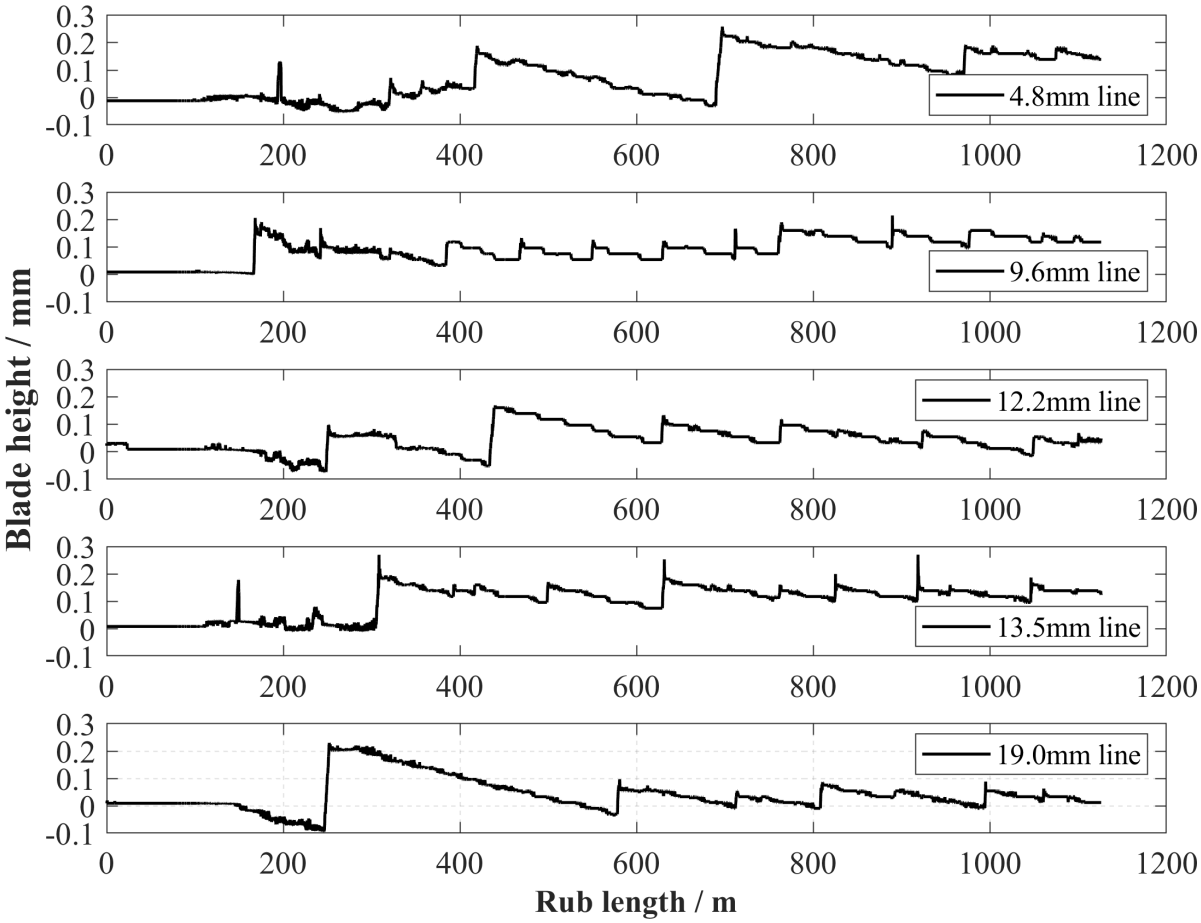

Fig. 5.26 Lines extracted for the test at 0.02µm/pass and 100m/s with H70 abradable at 4.8mm, 9.6mm, 12.2mm, 13.5mm and 19.0mm blade width.

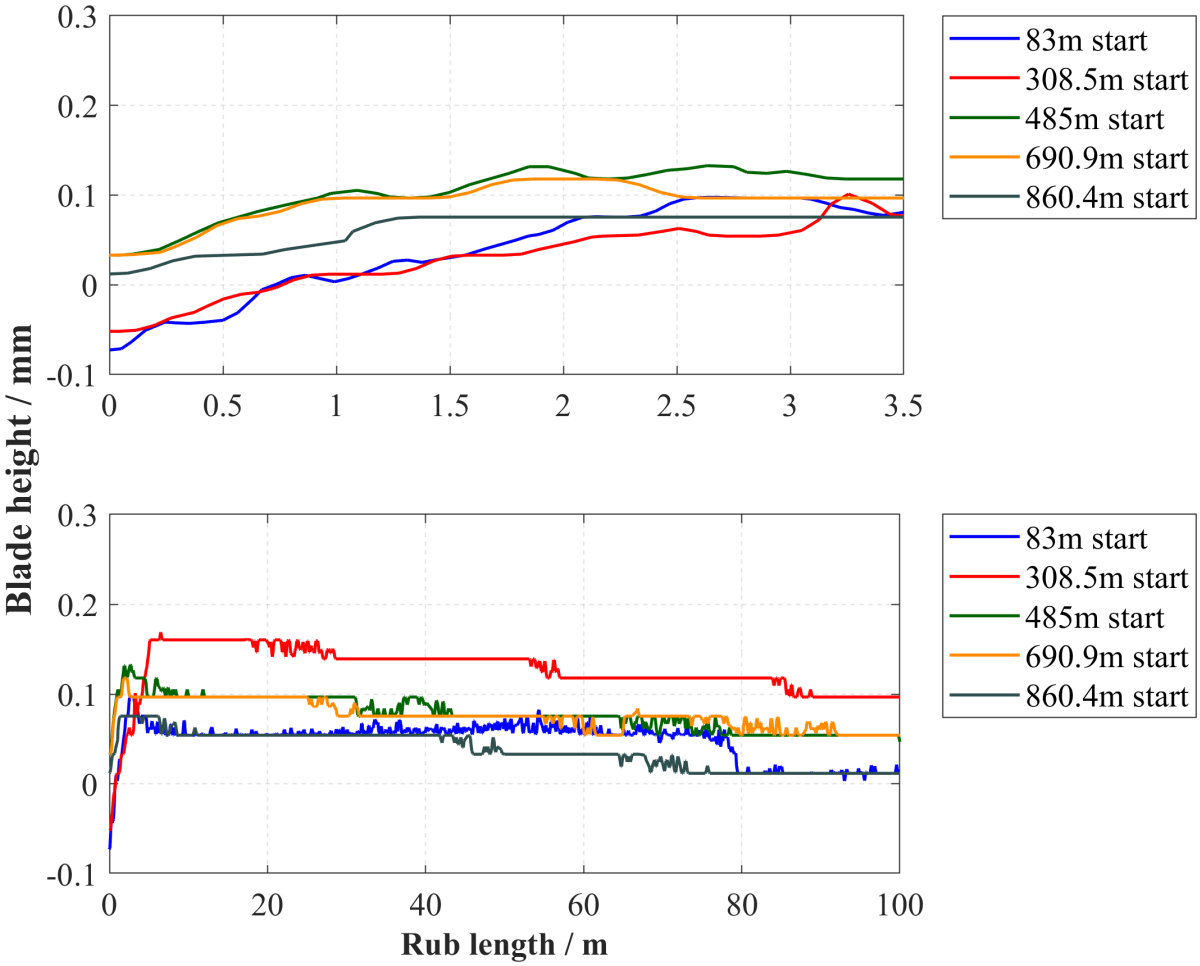

Fig. 5.27 Individual adhesion events overlaid onto each other for the 12.2mm line showing a) adhesive growth phase, b) adhesive growth and subsequent wear phase (steps in blade wear are due to discrete pixel size of 0.0212mm; wear is believed to be continuous).

5.4.2.5 Fracture of adhesions

The fracture of adhesions was first inferred by Bounazef et al. [46] from post-test blade length measurements, and, later observed by Fois et al. [41] using a side-on stroboscopic imaging technique. In the latter study, only the maximum length of a blade was captured, and it was not possible to determine how many adhesions existed on a blade and how many of them fractured.

Results in this study show that the probability of adhesions fracture is greatly dependent on the testing conditions. The fracture occurred frequently for the tests with high heat generation (at 0.2µm/pass and 2µm/pass) where adhesions grew continuously until they reached the critical length for a given condition and fractured. The critical length before a fracture was dependent on contact forces – for tests at 2µm/pass shown in Figure 8, adhesions fractured at lower heights (Fig. 5.25b) due to high contact forces.

The fracture of adhesions led to gap formation between a blade and a corresponding abradable (gap formation is undesirable as it leads to aerodynamic losses) as can be seen from the comparison of blade profiles and Alicona abradable surface measurements for the tests at the 0.2µm/pass and 2µm/pass incursion rates (Fig. 5.13 and 5.19).

Such comparison highlights that an abradable surface at the end of a given test is a product of the adhesions and wear history, as opposed to being solely dependent on the instantaneous blade form. These findings further support the idea that post-test blade length and weight measurements commonly used in literature [25, 46, 40, 41, 38, 44] are not always representative of the overall adhesive transfer during a test and hence, are insufficient to fully quantify the severity of wear mechanisms present under certain testing conditions.

5.5 Conclusions

Twenty-seven tests have been performed to investigate wear mechanisms observed during contacts between Ti(6Al4V) blades against AlSi-polyester abradables. The incursion rates of 0.02µm/pass, 0.2µm/pass and 2 µm/pass, blade tip speeds of 100m/s, 200m/s and 280m/s and abradable hardnesses of H69, H62 and H53 were considered.

This work offered new insights into wear mechanisms in such contacts, the distribution of adhesions on blade surfaces, frequency of adhesion formation at different testing conditions, two types of cyclic mechanisms of adhesions formation and removal, and the effect of testing conditions on the fracture of adhesions and the resultant formation of gaps between blades and abradable surfaces.

The incursion rate was found to be the main driving factor for the wear mechanisms during a test. Simultaneous wear and adhesions were observed at the lowest incursion rate of 0.02µm/pass, small amounts of blade wear and predominantly adhesions at the higher incursion rate of 0.2µm/pass, and only adhesions at the highest incursion rate of 2µm/pass.

Thermal properties of a system were shown to have a large influence on the wear mechanisms. For blade wear, bulk temperatures and heat partition were related to wear rate due to effect of temperature on Ti(6Al 4V) hardness. For adhesions, the flash temperature concept offered a good explanation of the trends observed in data. However, further testing and adhesion measurements are required to verify the hypotheses suggested in this work.

Chapter 6

NiCrAl-bentonite wear mechanisms

6.1 Introduction

Only limited research is currently available on the contacts between Inconel 718 blades and NiCrAl-bentonite samples, with the majority of results produced by Taylor et al. [53] and Watson et al. [8, 51, 6]. In that work, several trends have been established. The incursion rate and abradable hardness were shown to be the dominant factors in determining the severity of wear observed in such contacts, with speed being a lesser but still an important factor.

However, in the published work, the maximum tested blade tip speed was 200m/s [51]. As the speed was identified to be an important parameter in determining the severity of blade wear, the necessity to extend the research to higher speeds was identified to understand if the trends seen in previous research hold up till the engine representative speed of 400m/s. It was decided to partially address this limitation by performing tests at up to 280m/s blade tip speed on the high-speed rig.

However, the preliminary tests for this chapter have shown that there was a significant difference in forces and blade wear between the tests on the high-speed (HSR) and low-speed (LSR) rigs for tests, where conditions were identical, apart from using blades of different lengths (4mm stick-out from a blade holder on the high-speed rig and 16mm stick-out on the low-speed rig). The preliminary tests have also shown a different type of contact behaviour. It was shown that for tests on the high-speed rig at identical conditions, significantly different results may be obtained with the maximum force during a test being different by an order of magnitude (Fig. 6.1). Such significant changes in contact forces could not be explained by direct influences of small variations in abradable hardness (due to normal sample-to-sample variation) or other test conditions on the contact force.

The suggested explanation for such a difference in forces for tests at identical conditions was that there are two distinct contact modes: one leading to high forces and one with low forces,

with the transition from one contact mode to another occurring not at a single incursion rate, but over a certain range of incursion rates. The test in Fig. 6.1b transitioned to the high-force contact mode.

The presence of two contact modes explained why there was an order of magnitude difference in results between the tests on the low-speed and high-speed rigs. However, the explanation was still needed why the preliminary tests on the high-speed rig were below the transition with low forces occurring and the tests on the low-speed rig were above the transition with high forces and blade wear occurring.

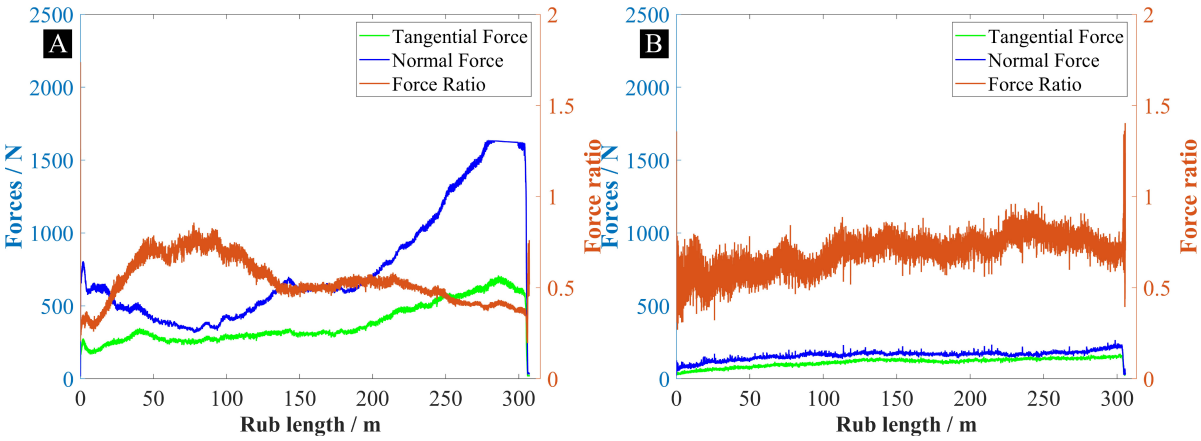

Fig. 6.1 The force data for two tests performed on the high-speed rig at identical conditions of 0.08µm/pass incursion rate and 200m/s speed tested with Inconel 718 blades against abradable samples of H55 nominal hardness heat treated for 100 hours. On plot a, at the end of the test, the normal force was capped at around 1500N due to the maximum force setting on the dynamometer amplifier. In that region the normal force was above 1500N, but the exact value of force was not known due to that setting.

The discussed preliminary results have then shaped the direction of the experimental work for this chapter. The difference in results obtained between the rigs was investigated by performing tests on both rigs with blades of identical length and performing a separate investigation focusing on the effect of blade length on test outcomes on the low-speed rig. The transition behaviour was then investigated in detail on the high-speed rig at both 200m/s and 280m/s speeds.

6.2 Materials and methodology

Based on the preliminary results, it was decided to perform two parts of experimental work for this chapter. In the first part, tests on the low-speed rig investigating the influence of blade

length on a test outcome were performed and results were compared with tests done on the high-speed rig, which used an identical blade length.

The six different blade lengths were tested with two repeats for each blade length, resulting in a total of twelve tests. The tested blade lengths were selected in a range that covered blades with a very little stick-out from a blade holder (very stiff blades), similar to the ones used on the high-speed rig to the ones with a large stick-out (more flexible blades due to the increased distance between contact force application at the blade tip and blade fixture at the blade holder), similar to the ones used on the low-speed rig. The stick-out of the tested blades was 3.1mm, 4.1mm, 5.1mm, 7.1mm, 10.1mm and 16.1mm. All the tests were done with samples from a batch with the nominal hardness of H55 heat treated for 100 hours and at the 0.06µm/pass incursion rate as in the preliminary work it was shown that the transition to the high-force mode consistently occurred with long blades at this incursion rate. The tests done with 4.1mm stick-out blades were then compared to the tests with standard 4mm stick-out blades (the 0.1mm difference in the stick-out length was due to machining tolerances between different batches of blades) performed on the high-speed rig. Three repeats have been done on the high-speed rig with the 4mm blades and an additional repeat with the 4mm blade was done on the low-speed rig so that there were 3 repeats with 4mm (4.1mm) blades on both rigs. The tests performed for this part are summarised in Table 6.1.

Table 6.1 The test matrix for the first experimental part.

Test	Rig	Blade / mm	Speed / m/s	Incursion rate / µm/pass	Rub depth / µm	Repeats
1	LSR	3.1	200	0.06	1000	2
2	LSR	4.1	200	0.06	1000	2
3	LSR	5.1	200	0.06	1000	2
4	LSR	7.1	200	0.06	1000	2
5	LSR	10.1	200	0.06	1000	2
6	LSR	16.1	200	0.06	1000	2
7	LSR	4	200	0.06	1000	1
8	HSR	4	200	0.06	1000	3

In the second part, tests exploring the transition behaviour were performed on the high-speed rig. The testing was performed at two different blade tip speeds (200m/s and 280m/s), and three incursion rates that were selected based on the blade tip speed. The incursion rates used for the tests at 200m/s were 0.06µm/pass, 0.10µm/pass and 0.14µm/pass. The incursion rates used for the tests at 280m/s were higher due to expected improved wear behaviour at the

higher speed that was previously demonstrated by both Taylor et al. [53] and Watson et al. [51], and were 0.14µm/pass, 0.22µm/pass and 0.30µm/pass. To establish the probability of transition occurring for a given test condition, five repeats were done for each condition, resulting in a total of thirty tests for this part. All the tests were done with samples from a batch with the nominal hardness of H50 heat treated for 100 hours. The tests performed for the second part are summarised in Table 6.2.

Table 6.2 The test matrix for the first experimental part.

Test	Rig	Blade / mm	Speed / m/s	Incursion rate / µm/pass	Rub depth / µm	Repeats
1	HSR	4	200	0.06	1000	5
2	HSR	4	200	0.10	1000	5
3	HSR	4	200	0.14	1000	5
4	HSR	4	280	0.14	1000	5
5	HSR	4	280	0.22	1000	5
6	HSR	4	280	0.30	1000	5

The H50 and H55 batches were used for the tests in this chapter as they were the hardest batches available for use. The behaviour at the higher end of the spraying hardness spectrum was of primary interest due to the potential of unfavourable wear mechanisms occurring at such hardnesses based on the previous research [51].

6.2.1 Hardness testing

Twenty-one samples from a single batch were hardness tested in 9 locations each, according to the procedure described in section 3.4.3 to establish the statistics of hardness variations within a batch. All the samples were from a batch with the H55 nominal hardness and were hardness tested after heat treatment for 100 hours. The average measured value of hardness for the batch after heat treatment was H60.6. The difference between the measured average hardness values for all 21 samples and the average value for a batch is given in Fig. 6.2. The dashed lines show the 2.5 points deviation from the mean value, which was considered acceptable for samples within a batch. This threshold was chosen based on the past experience of working with sprayed NiCrAl-bentonite coatings.

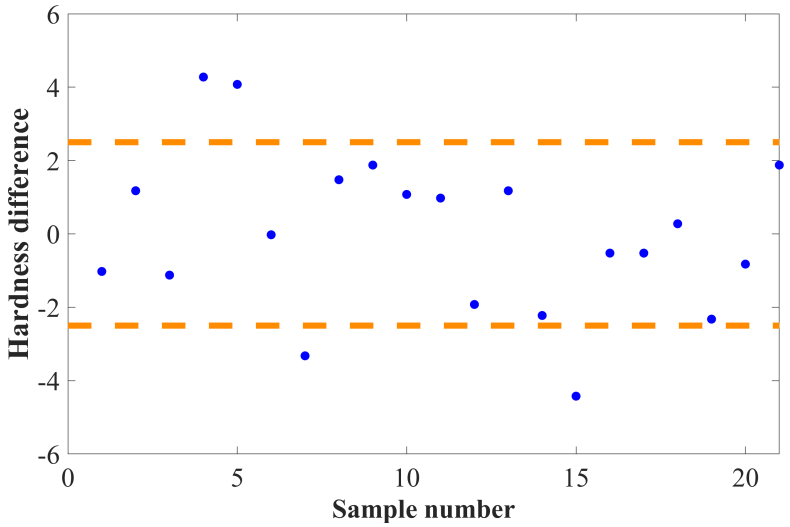

Fig. 6.2 The measured hardness deviation for the 21 NiCrAl-bentonite samples of the same nominal hardness from the average measured hardness for the batch.

The results have shown that the average hardness for most samples was very close to the average value for a batch. For 17 out of 21 samples (81%), the average hardness value was within the defined threshold. Some of the samples were outside of the threshold, 2 were too hard and 2 were too soft. This showed that there is a possibility of outliers occurring in performed tests due to variations in hardness of samples within a batch. This highlighted the importance of performing repeats to confirm that observed trends are repeatable and are not due to the presence of outliers.

It is also important to note that within the defined threshold, there was a range of hardnesses for the samples. While the differences were small, they are likely a contributor to variations in forces and contact modes observed for tests at identical conditions with samples of the same nominal hardness.

6.3 Results

First, results obtained on the low-speed rig with blades of different length are presented, followed by the comparison of results obtained with 4mm stick-out blades on the the low-speed and high-speed rigs. After, results from the tests completed on the high-speed rig focused on improvements in the understanding of transition between two contact modes are given. In this chapter, the primary focus is given to the force data as it was previously shown that forces are a good indicator of contact conditions in tests with the NiCrAl-bentonite abradable [51]. Post-test images of blades and abradable samples and blade wear results are also presented to further support the observations.

6.3.1 Tests with the blades of different lengths on the low-speed rig

The force data throughout a test for all the 12 tests performed at the 200m/s speed and 0.06μm/pass incursion rate with blades of 6 different lengths are given for repeats 1 in Fig. 6.3 and repeats 2 in Fig. 6.4.

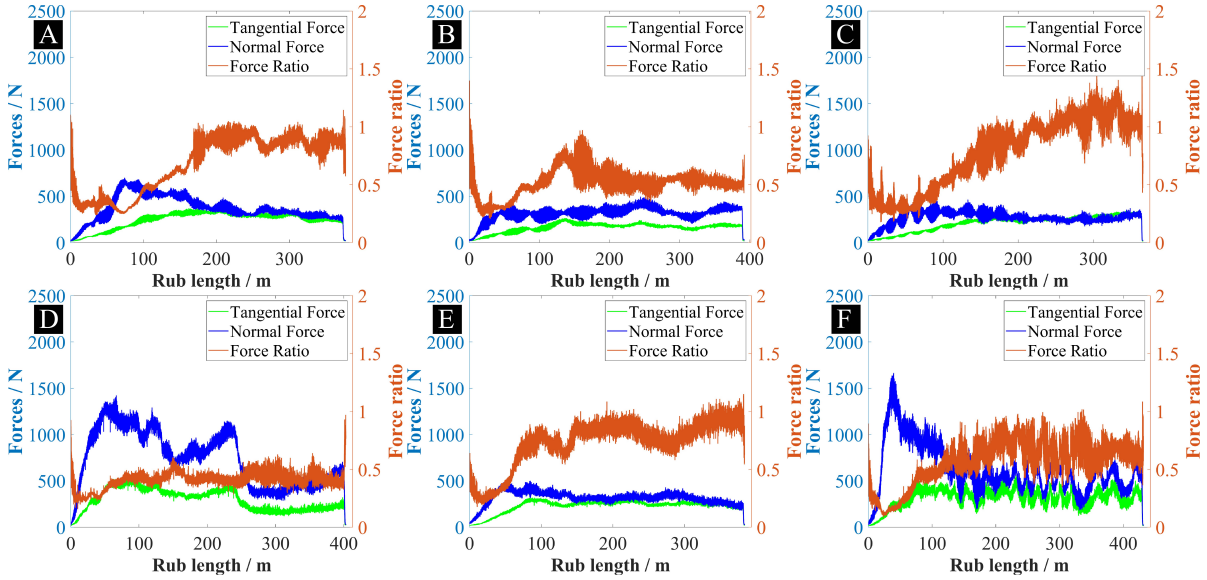

Fig. 6.3 The force data for the repeats 1 at 0.06μm/pass, 200m/s with a) 3.1mm blade, b) 4.1mm blade, c) 5.1mm blade, d) 7.1mm blade, e) 10.1mm blade, f) 16.1mm blade.

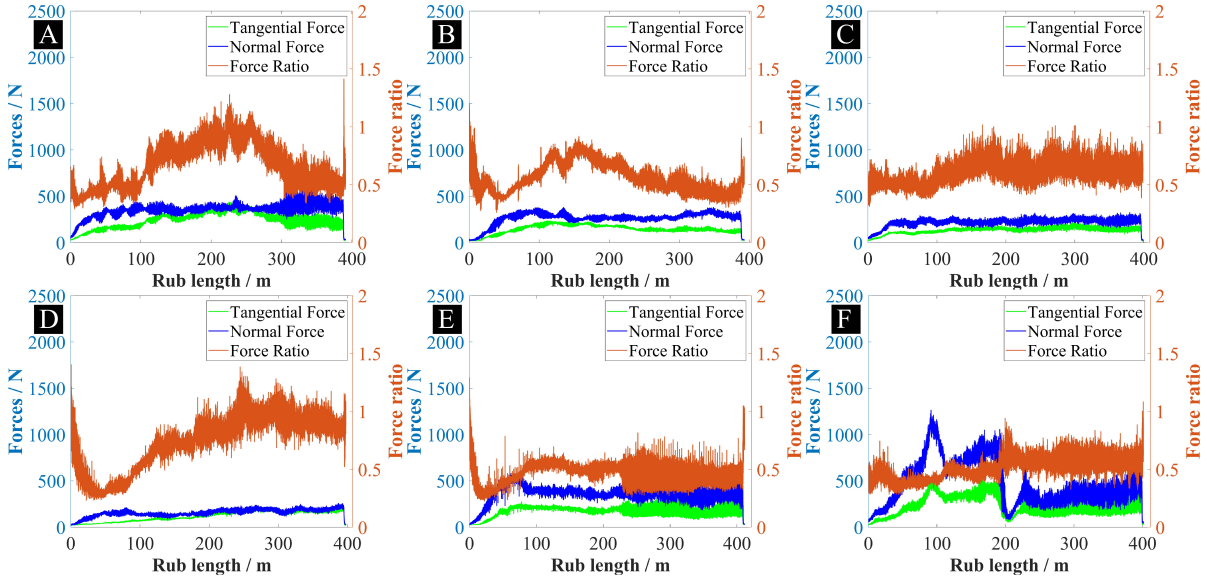

Fig. 6.4 The force data for the repeats 2 at 0.06μm/pass, 200m/s with a) 3.1mm blade, b) 4.1mm blade, c) 5.1mm blade, d) 7.1mm blade, e) 10.1mm blade, f) 16.1mm blade.

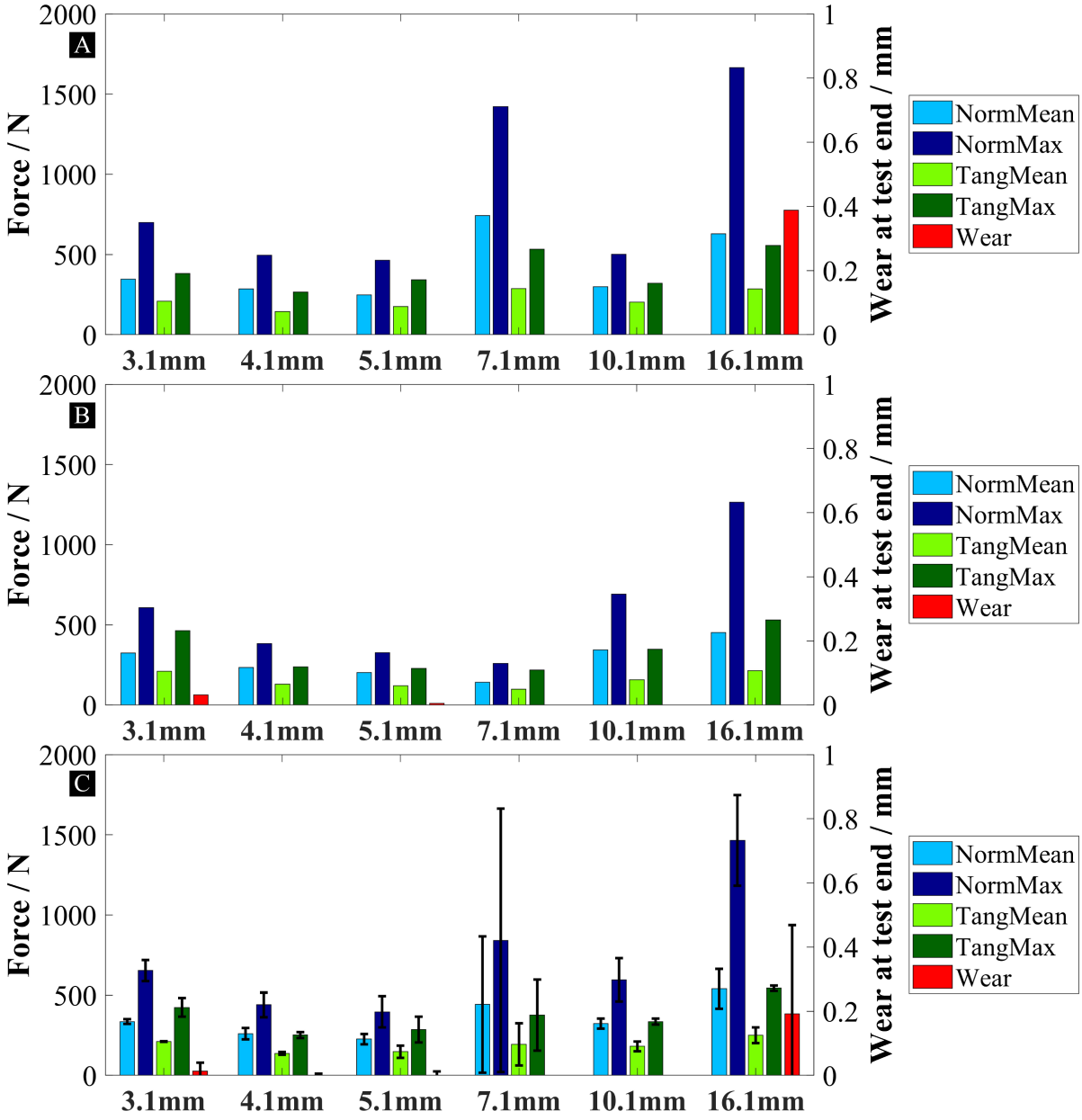

Fig. 6.5 The histograms showing the mean and maximum normal and tangential forces throughout a test and blade wear at the end of a test for each of the 6 blade lengths for tests at 200m/s speed and 0.06µm/pass incursion rate, a) repeats 1, b) repeats 2, c) average of two repeats with error bars given by one standard deviation.

It can be seen that the highest contact forces occurred with the blade stick-out length of 16.1mm for both repeats. High forces also occurred in the first repeat with the 7.1mm blade, but low forces were seen with such blade in the second repeat. The force results for all the 12 tests were summarised using histograms with blade length at the end of a test added as a separate column. The histograms in Fig. 6.5a and Fig. 6.5b present results for repeats 1 and 2

for each of the blade lengths. The histogram in Fig. 6.5c presents the results averaged over the two repeats with error bars given by one standard deviation.

In Fig. 6.5 it can be seen that only with the 16.1mm blades, the transition to the high-force mode was observed for both tests. The first repeat with the 16.1mm blade was also the only test with a significant amount of blade wear during a test. Such result is consistent with previous findings by Watson et al. [51], where high contact forces were correlated with increased blade wear in contacts with the NiCrAl-bentonite abradable.

Additionally, by assessing the general trend in the results and taking the results from the hardness measurements into consideration, where the possibility of outliers was identified, it appears that the first repeat with the 7.1mm blade could have been an outlier (due to a harder than expected sample).

6.3.2 Comparison of tests with 4mm blades on the low-speed and high-speed rigs.

In this section, 2 of the tests performed on the low-speed rig with 4.1mm blades shown in the previous section together with an additional test with a 4mm blade were compared to 3 tests done on the high-speed rig with 4mm blades. The force data throughout a test for all the 6 tests performed at the 200m/s speed and 0.06µm/pass incursion rate are given in Fig. 6.6.

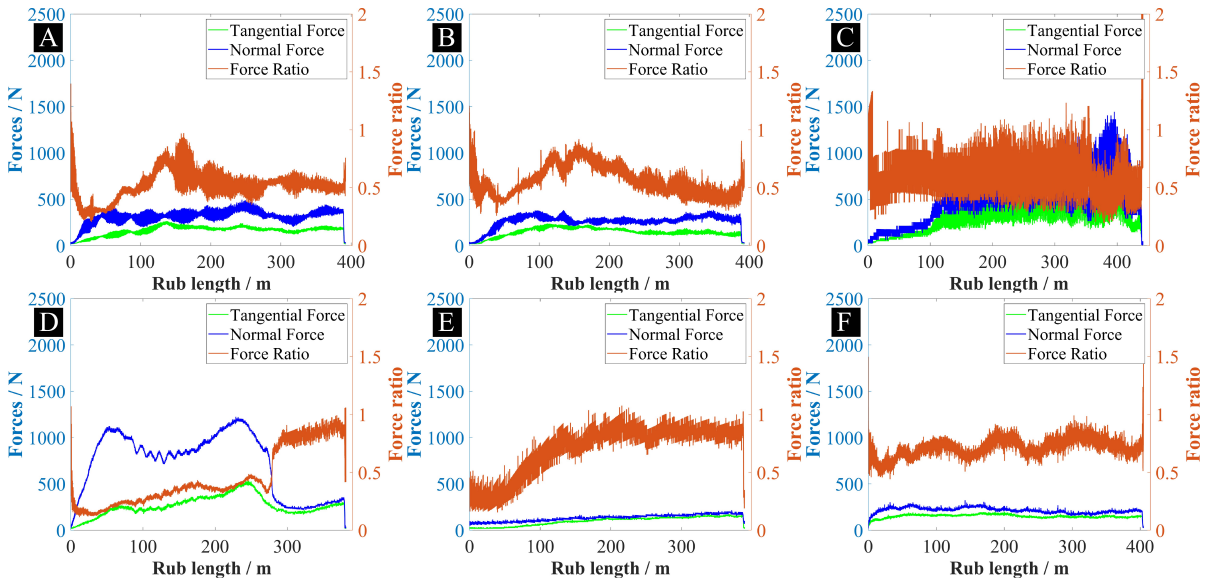

Fig. 6.6 The force data for the tests at the 0.06µm/pass incursion rate, 200m/s speed with a) 4.1mm blade on the LSR, b) 4.1mm blade on the LSR, c) 4mm blade on the LSR, d) 4mm blade on the HSR, e) 4mm blade on the HSR, f) 4mm blade on the HSR.

It can be seen in Fig. 6.6 that similar results were obtained on both the low-speed and high-speed rigs. Out of the 3 tests performed on each rig, 2 had low contact forces and 1 of them had high contact forces (transitioned to the high-force contact mode). The differences in results between two rigs were smaller than the differences between the short and long blades tested in the previous section. It was then suggested that the main difference observed between preliminary results on the low-speed and high-speed rigs was due to the use of blades of different length rather than due to rig differences.

In this set of results, it could once again be seen that different test outcomes could occur for identical test conditions with 1 out of 3 tests transitioning to the high-force contact mode for tests on both the low-speed and high-speed rigs. In the next two sections, the transition between the two contact modes will be investigated in more detail.

6.3.3 Transition incursion rate at 200m/s

First, the comparison of tests where transition was and was not observed is going to be shown. This will be followed by a histogram summarising the test results for all the 15 tests at 200m/s.

To illustrate the differences in wear behaviour between tests that transitioned and that did not the blade profile history map, accompanied by post-test images of the abradable and blade and force data throughout a test are given for repeats 1 and 2 at the 0.10 µm/pass incursion rate in Fig. 6.7 and 6.8 respectively.

Forces for the test, that did not undergo transition were increasing throughout the test, but this increase was small, and the normal force stabilised at around 250N as shown in Fig. 6.7b. For the transitioned test, the increase in forces was very quick as shown in Fig. 6.8b. The normal force stabilised around 1200N and some cyclic behaviour in force was seen once blade wear initiated.

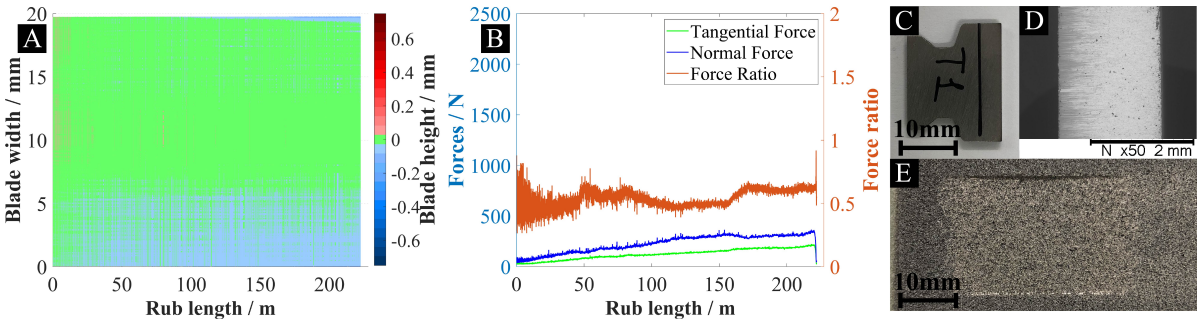

Fig. 6.7 Results for the repeat 1 at 0.10µm/pass, 200m/s with H50 abradable a) the blade profile history map, b) forces during the test, c) post-test image of the blade, d) post-test SEM of the blade, e) post-test image of the abradable sample. This test did not transition to the high-force contact mode.

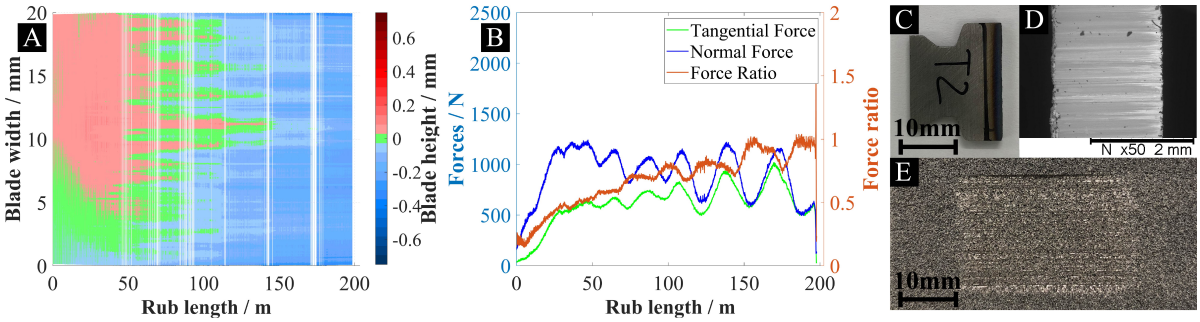

Fig. 6.8 Results for the repeat 2 at 0.10µm/pass, 200m/s with H50 abradable a) the blade profile history map, b) forces during the test, c) post-test image of the blade, d) post-test SEM of the blade, e) post-test image of the abradable sample. This test transitioned to the high-force contact mode.

The clear differences in wear behaviour can be seen on the wear history maps and from post-test images of the blades. For the test that did not transition, the blade appears undamaged in Fig. 6.7c and only some discolouration at the blade trailing edge can be seen in Fig. 6.7d. Virtually no wear can be seen on the blade profile history map (Fig. 6.7a). On the other hand, for the test, that transitioned, it can be seen on the blade profile history map that blade wear initiated and propagated at all the blade width locations (Fig. 6.8a). Thermal damage can be seen on the blade in Fig. 6.8c, and thermal discolouration is seen across the entire blade thickness in Fig. 6.8d. This suggests that blade wear is thermally driven and blade temperatures were high enough to cause the softening of Inconel 718.

The abradable surfaces for both tests look similar, however, the surface for the transitioned test has spots that appear shinier than the rest of the surface, which could be due to transfer of Inconel 718 from a blade to the surface due to blade wear. Previous research has shown that such transfer occurs for test conditions, where blade wear was observed [51]. Both surfaces are rough with the microstructure resembling the as-sprayed condition. This is very different to the tests with AlSi-polyester abradables, where surfaces were shaped by the blade tip and very little roughness was seen along the rub track (surfaces had a lot of areal roughness due to grooving across the blade width direction, but appeared smooth along the rub track).

The force and blade length results for all the 15 tests at 200m/s are summarised in Fig. 6.9 indicating the number of transitioned tests for each of the considered incursion rates. The mean normal forces are shown in light blue, maximum normal forces in dark blue, mean tangential forces in light green, maximum tangential forces in dark green and mean blade wear at the end of a test in red. The mean blade wear was obtained by averaging the blade length change at all blade width locations at the end of a test.

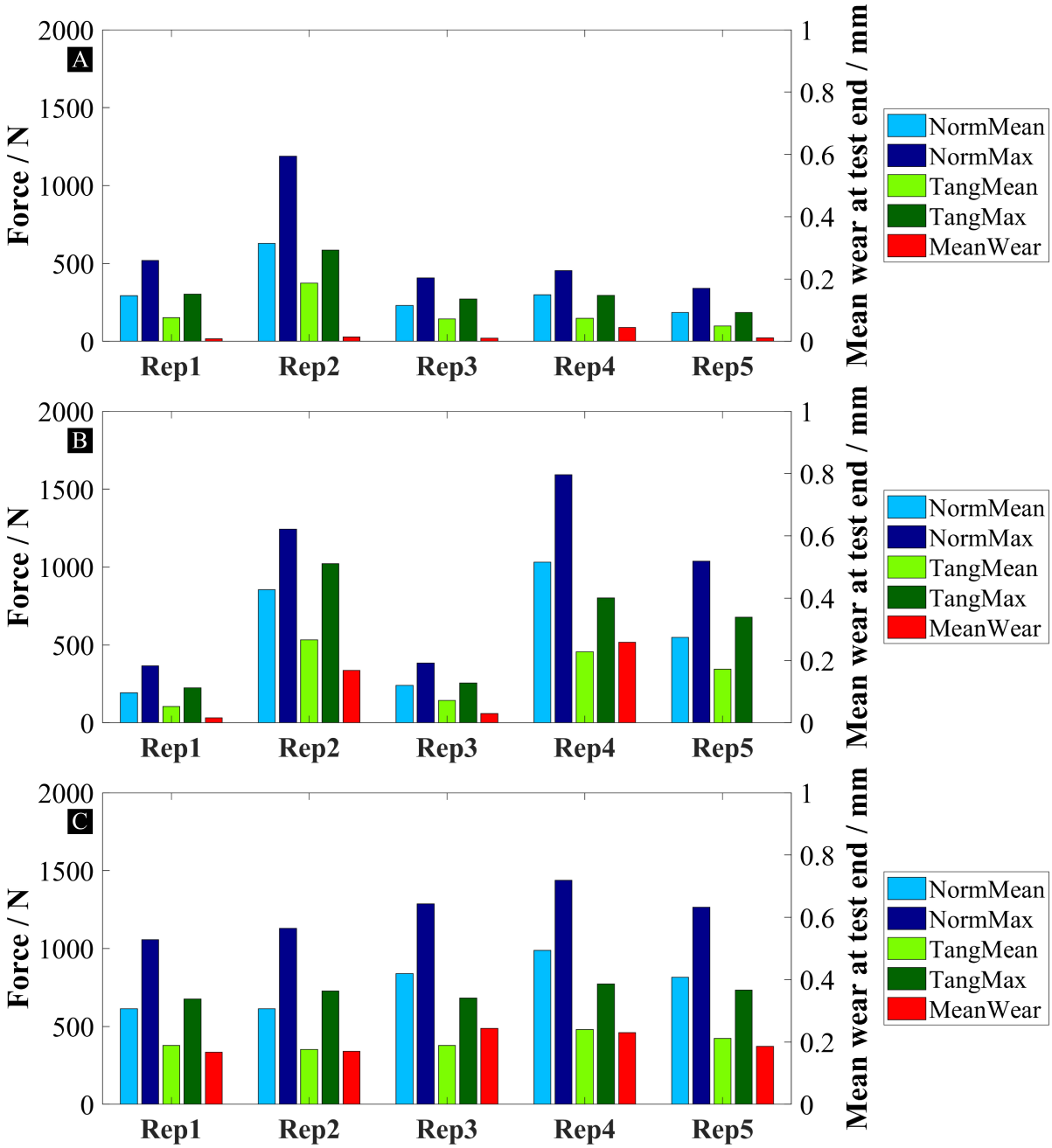

Fig. 6.9 The histograms showing the mean and maximum normal and tangential forces throughout a test and mean blade wear at the end of a test for each of the 5 repeats for tests at 200m/s speed and a) 0.06µm/pass incursion rate, b) 0.10µm/pass incursion rate, c) 0.14µm/pass incursion rate.

It can be seen that at the 0.06µm/pass incursion rate, 1 test had high forces, while at 0.10µm/pass and 0.14µm/pass, 3 and 5 tests had high forces respectively. These results showed that at the speed of 200m/s, the transition between the two contact modes occurs over a range of

incursion rates for the samples in a given batch. The two contact modes were very distinct. For example, for the tests at 0.10µm/pass, the maximum normal force for the tests that transitioned was 3 to 5 times higher than for the tests that did not.

The trend in blade wear results followed the trend in contact forces. For all of the tests that transitioned, apart from the repeat 2 at 0.06µm/pass and repeat 5 at 0.10µm/pass, significant blade wear was observed. No significant blade wear was seen for these two tests because despite a temporary region of high forces, they decreased later in the tests indicating that abradable fracture improved as can be seen in Fig. 6.10a and Fig. 6.10b. This is in contrast to the repeat 5 at 0.14µm/pass shown in Fig. 6.10c, where the maximum reached force was similar, but no decrease in forces was seen and they stayed around the maximum value, leading to larger blade wear.

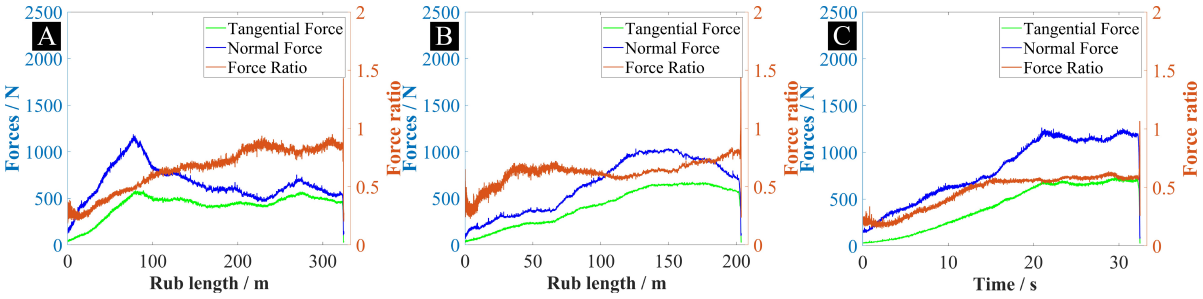

Fig. 6.10 Force results for the tests at 200m/s and a) repeat 2 at 0.06µm/pass, b) repeat 5 at 0.10µm/pass and c) repeat 5 at 0.14µm/pass

6.3.4 Transition incursion rate at 280m/s

Once again, first, the comparison of tests where transition was and was not observed is going to be shown. This will be followed by a histogram summarising the test results for all the 15 tests at 280m/s.

To illustrate the differences in wear behaviour between the tests that transitioned and that did not, a blade profile history map, accompanied by post-test images of the abradable and blade and force data throughout a test are given for repeats 3 and 2 at the 0.22µm/pass incursion rate in Fig. 6.11 and Fig. 6.12 respectively.

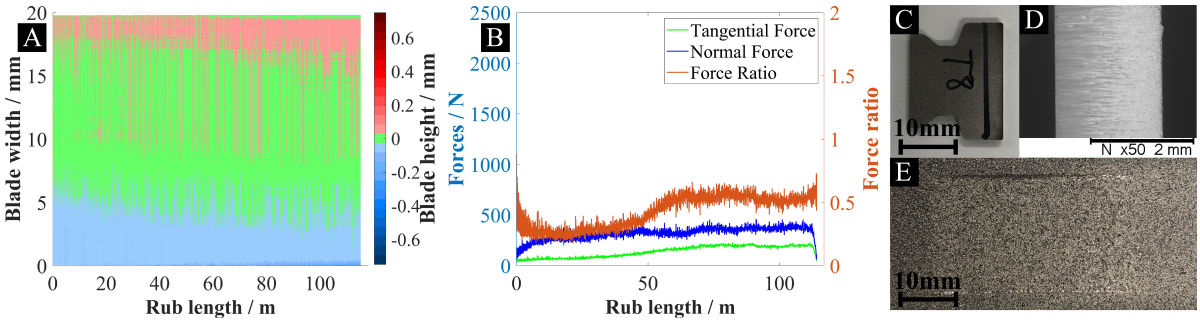

Fig. 6.11 Results for the repeat 3 at 0.22µm/pass, 200m/s with H50 abradable a) the blade profile history map, b) forces during the test, c) post-test image of the blade, d) post-test SEM of the blade, e) post-test image of the abradable sample. This test transitioned to the high-force contact mode.

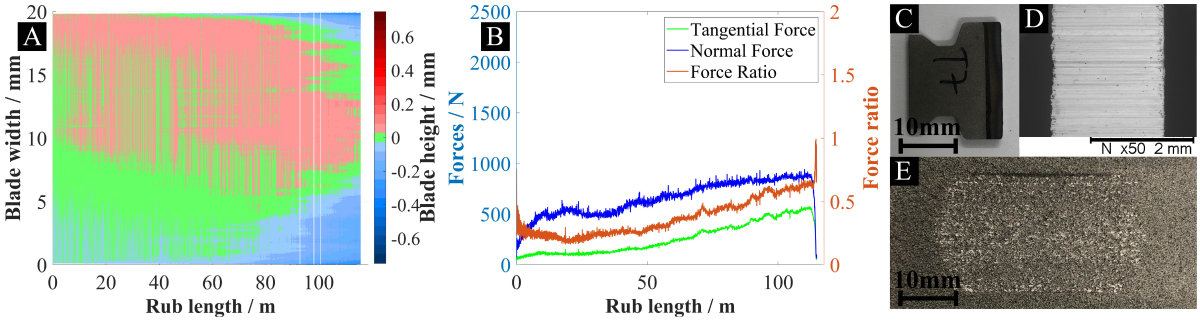

Fig. 6.12 Results for the repeat 2 at 0.22µm/pass, 200m/s with H50 abradable a) the blade profile history map, b) forces during the test, c) post-test image of the blade, d) post-test SEM of the blade, e) post-test image of the abradable sample. This test did not transition to the high-force contact mode.

Forces for the test, that did not undergo the transition were stable with the normal force reaching about 450N as shown in Fig. 6.11b. For the transitioned test shown in Fig. 6.12b, the normal force reached about 1000N towards the end of the test, however, the increase in force was not as rapid as for the transitioned test at 200m/s shown in Fig. 6.8.

The differences in wear between tests that transitioned and that did not transition are similar to the ones observed at 200m/s. For the transitioned test, thermal damage can be seen on the blade in Fig. 6.8c, and some shiny spots on the abradable surface in Fig. 6.8e. Interestingly, on the blade history map in Fig. 6.8a, it can be seen that blade wear first started at the blade edges. This is likely related to blade temperature distribution with blade edge getting to hot temperatures first due to rubbing both the abradable under the blade and to the sides of the blade as shown in Fig. 6.13.

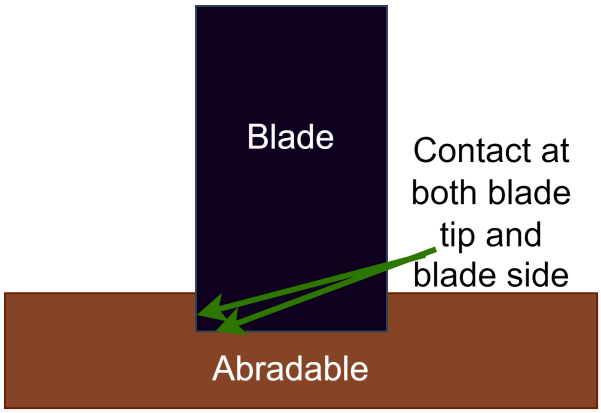

Fig. 6.13 A diagram showing how blade edge contacts abradable at both the edge and the side leading to higher temperatures. Blade rotation direction is out of the page.

The force and blade length results for all the 15 tests at 200m/s are summarised in Fig. 6.14 indicating the number of transitioned tests for each of the considered incursion rates. The mean normal forces are shown in light blue, maximum normal forces in dark blue, mean tangential forces in light green, maximum tangential forces in dark green and mean blade wear at the end of a test in red. The mean blade wear was obtained by averaging the blade length change at all blade width locations at the end of a test.

The trend was similar to the tests at 200m/s. No tests had high forces at 0.14µm/pass, 2 tests at 0.22µm/pass and 5 tests at 0.30µm/pass. Similarly to the tests at 200m/s, higher blade wear was seen for the tests that transitioned to high forces. This result further supported that the transition between the two contact modes occurs over a range of incursion rates for the samples in a given batch.

Once again, the two contact modes were very distinct. However, the ratio between the maximum force for the tests that transitioned and that did not was lower than for the tests at 200m/s. For example, for the tests at 0.22µm/pass, such ratio was around 2.

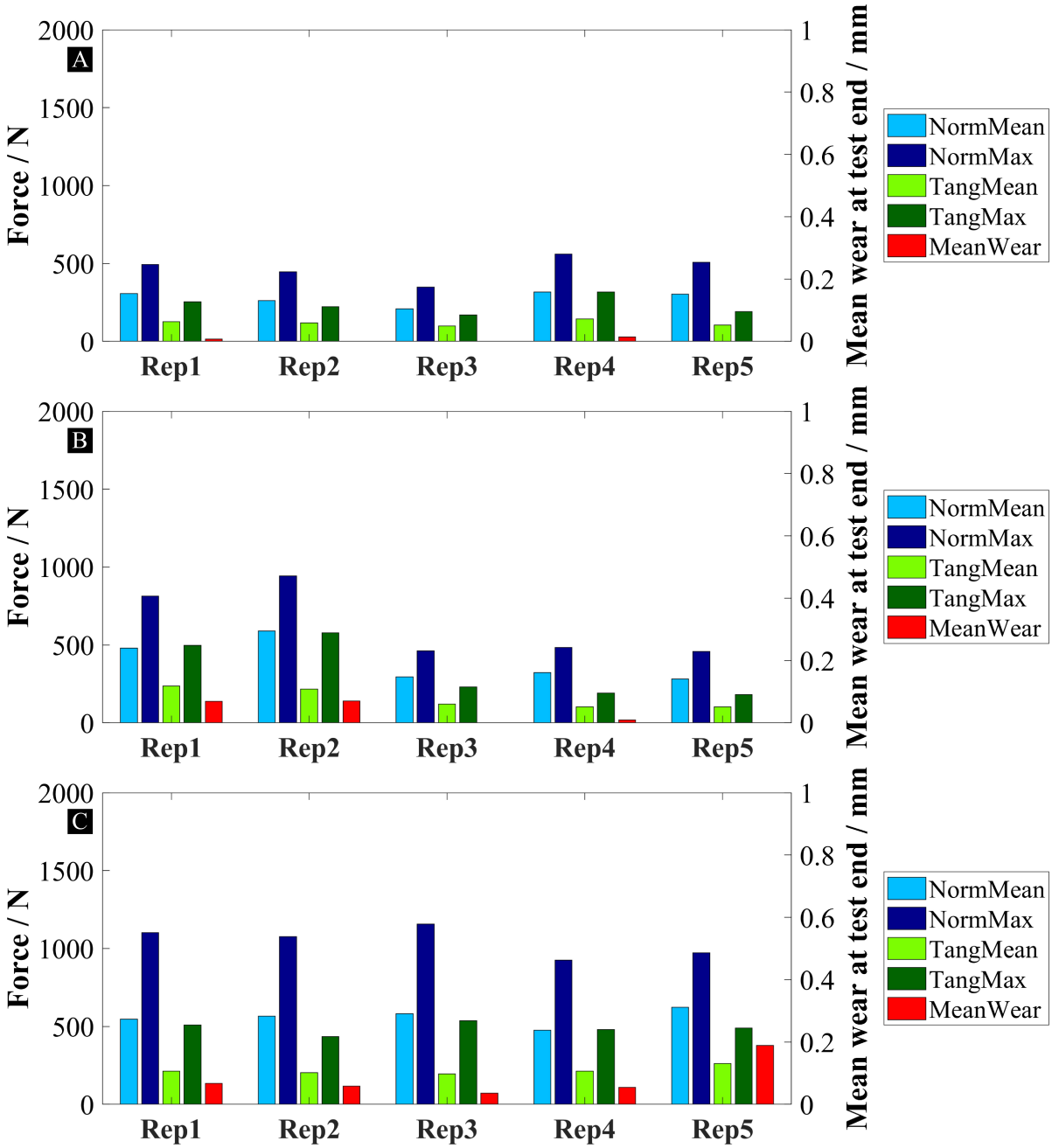

Fig. 6.14 The histograms showing the mean and maximum normal and tangential forces throughout a test and mean blade wear at the end of a test for each of the 5 repeats for tests at 280m/s speed and a) 0.14µm/pass incursion rate, b) 0.22µm/pass incursion rate, c) 0.30µm/pass incursion rate.

6.4 Discussion

The results in this work allowed to further improve the understanding of contacts with the NiCrAl-bentonite abradable, building on the findings by Taylor et al. [53] and Watson et al. [8, 51, 6]. The abradable removal mechanism for all of the tests performed in this chapter was identified to be fracture and release due to the rough as-sprayed like appearance of abradable wear track for both the tests that transitioned and that did not, showing an agreement with results by Watson et al. [51], where such mechanism was hypothesised for contacts with the NiCrAl-bentonite abradable.

In addition to the abradable hardness, incursion rate and blade tip speed that were previously identified to be important in determining test outcomes in the work by Watson et al. [51], in this work the blade stick-out length (blade stiffness) was shown to have an influence on outcomes too. It was shown that a significant increase in blade length increased the likelihood of transition to the high-force contact mode with this mode occurring in both tests with the 16.1mm blades.

In addition to the blade stiffness, the rig stiffness was also investigated by comparing results obtained on the low-speed and high-speed rigs at identical testing conditions. It should be noted that the disk assembly on the low-speed rig is significantly less stiff than on the high-speed rig due to the low-speed rig having a cantilever arrangement and high speed rig disk being supported by two sets of bearings (behind and in front of the disk). It was shown that tests on both rigs produced similar results with 1 out of 3 tests transitioning to the high-force contact mode for each of the rigs. It was then suggested that the blade stiffness had a more significant influence on test outcomes than the rig stiffness, likely, due to very high contact speed (200m/s for the tests comparing the two rigs in this work) and short arc of contact resulting in localised differences such as blade stiffness being more important than the large scale differences such as rig stiffness and arrangement.

However, it is important to note that the data available in this work was only limited to 6 blade lengths and was affected by a potential outlier. More repeats are desirable to establish clearer trends with the blade length and to verify the independence of test outcomes from the rig design for high-speed contacts.

6.4.1 The transition between the two contact modes

In the preliminary work for this chapter, the existence of two contact modes and a transition between them was identified, which was then explored in more detail. The transition between the two contact modes occurred over a range of incursion rates, rather than at a single incursion rate as could be seen from the results at both speeds of 200m/s and 280m/s. The existence of a transition region could be explained by how an increase in abradable hardness leads to

a decrease in abradable fracture effectiveness shown in the work by Watson et al. [51] and variations in local abradable sample hardness for samples within the same batch as was shown in section 6.2.1, which are due to the inherent randomness of the abradable spraying process [5]. This means that no two samples are identical and whilst a nominal transition incursion rate exists, it varies from sample to sample due to sample surface hardness variations. For the transition the following was then observed:

- If the incursion rate was low, only the low-force contact mode occurred.
- In the transition region either mode could occur with a higher incursion rate increasing the likelihood of the high-force contact mode.
- If the incursion rate was high, only the high-force contact mode occurred.

The presence of the two contact modes with a sharp transition from low forces to high forces, and a transition occurring over a range of incursion rates for samples within a batch rather than at a single incursion rate explained the very large difference in maximum contact forces observed for tests at identical conditions as seen in the preliminary results for this study (Fig. 6.1).

6.4.2 Contact modes mechanisms

In this section the mechanisms through which the identified contact modes occur are going to be discussed. The following mechanism based on the balance between the incursion rate and the rate at which an abradable surface fractures was proposed:

The low-force contact mode occurs when the rate of NiCrAl-bentonite fracture is the same as the incursion rate, so the forces stay stable. The forces stay low enough for Inconel 718 blades to not overheat and no significant blade wear occurs.

The high-force contact mode occurs when NiCrAl-bentonite fractures slower than the incursion rate, leading to the build up of forces with time due to an effective increase in incursion rate per pass (as material from previous incursion passes is not removed yet) and the amount of NiCrAl phase that comes into contact with a blade at a given time. The increase in forces continues until either forces are sufficient to continuously fracture the abradable for a given incursion rate or until temperatures get high enough to initiate blade wear. Once blade wear initiates, it decreases the incursion rate experienced by an abradable sample as part of the incursion rate is accommodated by the blade wear. The presence of blade wear during the high-force contact mode is consistent with the results by Watson et al. [51], where it was shown that high-forces were correlated with high temperatures and blade wear.

It is important to note that there could be alternative explanations to the occurrence of the high-force contact mode: accumulation of dynamometer vibrations leading to an increase in forces and blunting of a blade tip after the initial contact period leading to the less efficient wear of abradable and increase in forces.

At the moment, there is no reliable technique to decouple the effect of dynamometer vibrations. However, in the past research with abradable materials performed using similar experimental set-ups, contact forces could always be related to the mechanics of blade-abradable interactions [6, 48, 52]. Therefore, while it is likely that dynamometer vibrations are a contributor to the increase in forces, it is unlikely that they are the primary and only cause of the occurrence of the high-force contact mode.

For the blade blunting, there is evidence suggesting that it is not an important factor. Previous research [51] and findings in this work pointed to the fact that the NiCrAl-bentonite removal mechanism is fracture and release. Therefore, the work in fracturing abradable is done by the whole blade thickness rather than just the tip. This is further supported by the SEM images of blades from both the tests that transitioned and that did not (Fig. 6.7c, 6.8c, 6.11c and 6.12c) as discolouration occurred on the trailing edge of the blades rather than on the tip of the leading edge.

Additionally, in the preliminary work, there was a test when forces first went up and then down as shown in Fig. 6.15. Such behaviour is difficult to explain by blunting of the blade tip as it is unlikely that a tip re-sharpened further into the test. However, it is probable that once a local slightly denser region of M314 is removed through fracture, overall fracture gets back to being more efficient and forces become low once again.

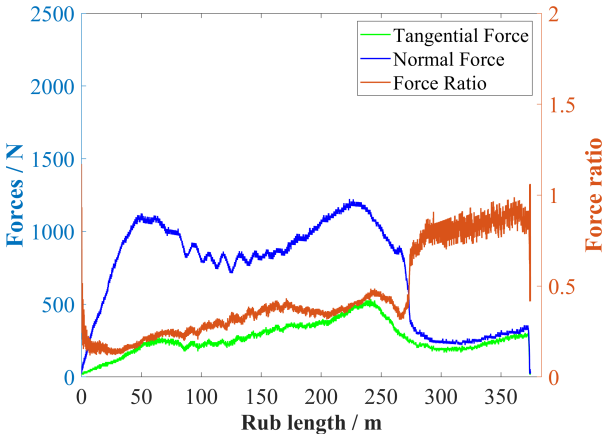

Fig. 6.15 An example of a test where the transition to the high-force contact mode occurred during a test, and then the transition back to the low-force contact mode occurred later in the test

In addition to the two contact modes described above, a third contact mode was potentially observed in the previous study by Watson [6] for tests at very high incursion rates (2µm/pass), where compaction of an abradable sample followed by macro-rupture of abradable was observed.

Such behaviour can be explained through the same framework applied to the two contact modes discussed above. At a very high incursion rate, NiCrAl-bentonite fractures much slower than the incursion rate and forces build up. There is not enough time for blade to get hot enough and so, for blade wear rate to be sufficient to accommodate the incursion rate. Then, the only way the incursion can be accommodated is through abradable compaction. This is consistent with the mechanism suggested for abradable compaction in the study by Watson [6]. The compaction leads to a very large increase in abradable surface hardness, contact forces and then, the subsequent rupture of an abradable. It is, therefore, suggested that blade wear due to high blade temperatures might be in some way beneficial for preventing abradable compaction and rupture.

6.4.3 Factors affecting contact modes

Previous research has identified that the incursion rate and abradable hardness are the dominant factors in contacts between NiCrAl-bentonite abradables and Inconel 718 blades, with the blade tip speed also playing an important role [53, 51]. It was shown that increase in abradable hardness leads to an increase in contact forces. While hardness was not explicitly considered in this work, it was suggested that the variations in the contact modes for a given set of testing conditions were due to small variations in hardness of abradable samples within a batch shown in section 6.2.1. The effect of hardness can be explained by higher hardness decreasing the amount of abradable fracture due to the higher density of NiCrAl phase leading to an increase in the likelihood of the high-force contact mode occurring.

Similarly, the increase in incursion rate increased the likelihood of a high force contact mode occurring. This was because if the incursion rate was high enough, fracture of abradable was not occurring at a fast enough rate and a build-up of contact forces occurred. This suggests that not only the contact force is important in fracturing NiCrAl-bentonite surface, but also the total number of blade strikes (lower incursion rate leads to the higher number of blade strikes for a given incursion depth) with fatigue of the surface layer being important for effective surface removal.

The increase in blade tip speed improved abradable fracture for the tests in this study and led to transition to the high-force mode to occur at a higher incursion rate, which is consistent with past research where blade tip speed was shown to lead to better test outcomes [53, 51]. However, it was difficult to quantify the exact influence of speed on the incursion rate at which

transition occurs due to some difference between the abradable samples used for the tests 200m/s and 280m/s that were identified only after completion of the tests. Tests with samples from a completely identical batch would be needed to decouple the effects of these two factors.

It was also shown in this work that an increase in the likelihood of the high-force contact mode occurring was observed with very long blade (16.1mm stick-out length) in comparison to shorter blades.

6.5 Conclusions

The experimental work for this chapter consisted of two pats: tests investigating the influence of blade stiffness and rig stiffness on contacts between Inconel 718 blades NiCrAl-bentonite abradable samples, and tests investigating the transition behaviour between the two contact modes initially observed in the preliminary work in such contacts.

Two distinct contact modes were identified. These contact modes were then explained through the balance between the incursion rate and the rate of abradable fracture. It was identified that for abradable samples from the same batch, the transition between the two contact modes occurs over a range of incursion rate rather that at a single incursion rate. This was explained by the small variations in abradable hardness between samples within the same batch and the effect surface hardness has on abradable fracture effectiveness.

Factors influencing the likelihood of the high force mode occurring have been identified as follows:

- Higher incursion rate increases the likelihood of the high-force contact mode.
- Higher abradable hardness increases the likelihood of the high-force contact mode.
- Higher blade tip speed decreases the likelihood of the high-force contact mode.
- Very high blade length (low blade stiffness) increases the likelihood of the high-force contact mode.
- Rig stiffness was shown to not have a strong effect on the likelihood of the high-force contact mode.

Chapter 7

Angled blades in contacts with NiCrAl-bentonite abradable

7.1 Introduction

Previous research has identified that angled blades can improve test outcomes at low incursion rates in comparison to standard blades with a flat tip [8, 6]. The comparison of flat tip and angled blade geometries is shown in Fig. 7.1. It was shown that an increase in the blade tip angle significantly reduced contact forces and blade wear when tested against angles up to 20 degrees (Fig. 7.2). It was suggested that angled blades improved abradable fracture through concentrating forces on a local part of an abradable material and allowed easier release of abradable material post fracture due to decreased tip thickness.

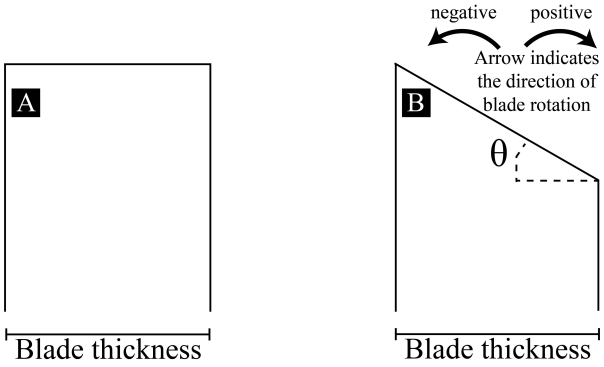

Fig. 7.1 The geometry of a a) flat blade, b) angled blade

However, whilst the previous work on the low-speed rig with long blades has clearly showed that the inclusion of an angle had a benefit in making abradable fracture more efficient, work in the previous chapter highlighted how using shorter (stiffer) blades can also result

in an improvement in abradable fracture in comparison to long blades. It is then of interest to consider whether adding an angle to the stiffer short blades results in the same abradable fracture improvement as it did for the longer blades.

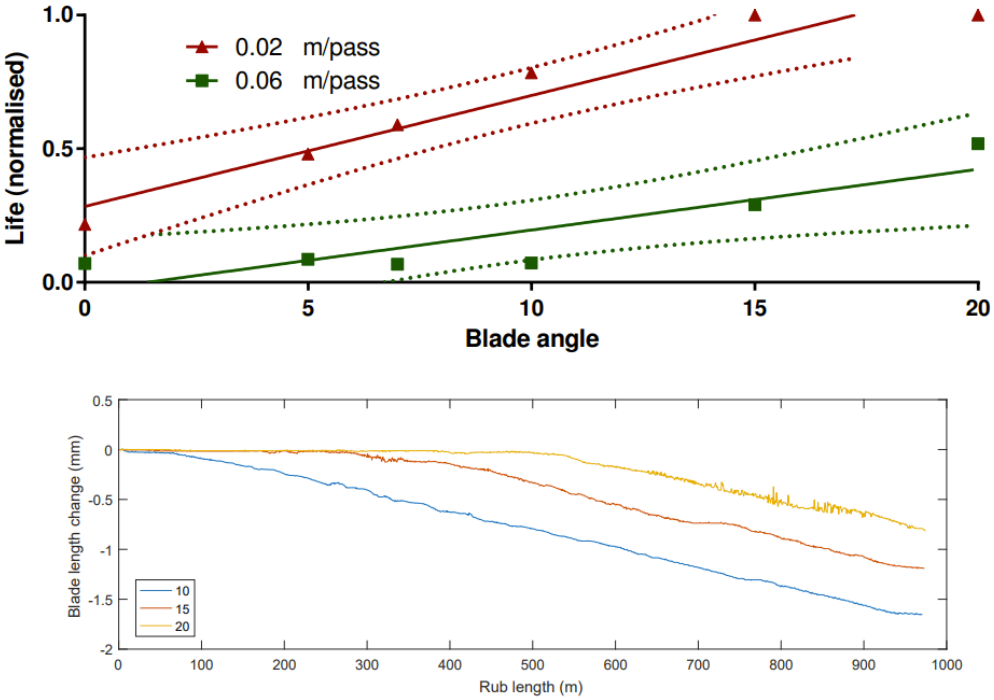

Fig. 7.2 The life of the blades from tests at 0.02µm/pass and 0.06µm/pass with tip angles from 0 - 20 degrees with lines of best fit and 95% confidence bounds normalised by the total expected test rub length (top plot) and full blade length results from tests at 0.06µm/pass (bottom plot) [6].

Additionally, In the study by Watson [6] angled blades were positioned in a way that the longest edge of a blade was the leading edge. Proprietary data from Rolls-Royce plc. has shown that using angled blades with longest edge being the trailing edge is favourable from aerodynamic perspective.

In this work, the potential of angled blades for reducing blade wear in aero-engines will be further assessed building on the original results [8, 6], and including new knowledge on the favourable cutting direction, contact modes and the effect of blade length on test outcomes.

7.2 Materials and methodology

The tests in this chapter focused on characterising the performance of angled blades in comparison to the standard flat blades. The considered angles were neg10 (negative (neg) means the

longest edge is the leading edge, positive (pos) means the longest edge is the trailing edge as indicated in Fig. 7.1), neg30 and pos30. It was decided to test neg10 and neg30 blades to have a direct comparison to results in the previous research, where neg direction was used for angled blades. The 30 degree angle was selected as the upper limit as it is the largest permissible angle to be used in an engine due to design constraints. The angle of 30 degrees was selected for the pos direction to perform comparison with the neg blades at the predicted optimal angle value, as it was previously shown that the a larger angle offers the best improvement in performance [6].

The testing consisted of two parts. In the first part, general comparisons in performance between the angled and flat blades were done at two speeds of 200m/s and 280m/s. Then, further characterisation tests were performed at 200m/s. For the first part, two incursion rates were considered for each speed. The first incursion rate was 0.02µm/pass for both speeds. This incursion rate was used as a control, where no transition to the high-force contact mode was expected for both the angled and flat blades. The second incursion rate was selected depending on the speed, such that the incursion rate is above the upper bound of the transition region and transition to the high-force mode would occur with the flat blades, so that the performance of the angled blades could be compared to the flat blades. The second incursion rate was selected as 0.30m/pass for the speed of 200m/s and 0.60µm/pass for the speed 280m/s due to better outcomes at the higher speeds identified in previous research [51].

The selected transition incursion rates of 0.30µm/pass and 0.60µm/pass were higher than the transition incursion rates of 0.14µm/pass and 0.30µm/pass identified for respective speeds in the previous chapter. This is because during the preliminary work, the abradable samples used in this chapter showed better surface fracture than the samples in the previous chapter. It is believed to be due to samples used in this chapter being softer, as decrease in abradable hardness was previously linked with better NiCrAl-bentonite abradable fracture [6]. The summary of the tests for the first experimental part is given in Table 7.1. The tests in the second experimental part were focused on further comparison of the blade wear amount and mechanisms between flat and angled blades and will be described after the presentation of results for the first part, as testing conditions were selected based on the results of the first part.

Table 7.1 The test matrix for the first experimental part

Test	Blade type	Speed / m/s	Incursion rate / μm/pass	Rub depth / μm
1	flat	200	0.02	1000
2	neg10	200	0.02	1000
3	neg30	200	0.02	1000
4	pos30	200	0.02	1000
5	flat	200	0.30	1000
6	neg10	200	0.30	1000
7	neg30	200	0.30	1000
8	pos30	200	0.30	1000
9	flat	280	0.02	1000
10	neg10	280	0.02	1000
11	neg30	280	0.02	1000
12	pos30	280	0.02	1000
13	flat	280	0.60	1000
14	neg10	280	0.60	1000
15	neg30	280	0.60	1000
16	pos30	280	0.60	1000

7.3 Results

The results comparing the performance of flat and angled blades at two incursion rates for two different speed of 200m/s and 280m/s are presented below.

7.3.1 Comparison of flat and angled blades at 200m/s

The post-test images of the abradable samples and blades and force data throughout a test are given for all the 8 tests at the 200m/s speed in Fig. 7.3 and 7.4 respectively. The blade profile history maps are not used in this section as blade wear was generally uniform across the blade width, and so mean blade length change results are presented instead throughout this chapter for easier comparison of test results at different conditions.

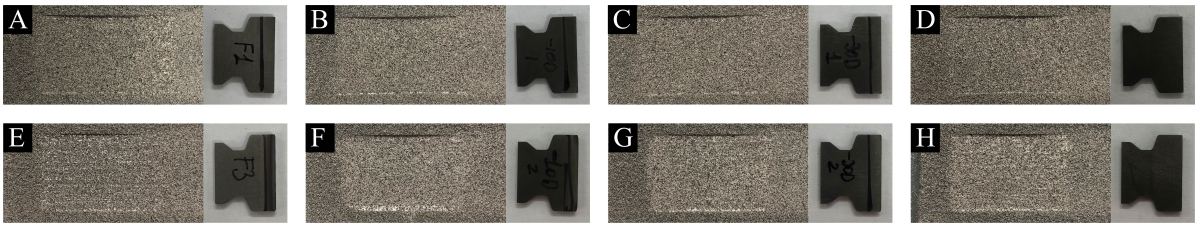

Fig. 7.3 The post-test images of the abradable samples and blades for the tests at the 200m/s speed and 0.02µm/pass incursion rate with a) flat blade, b) neg10 blade, c) neg30 blade, d) pos30 blade, 0.3µm/pass incursion rate with e) flat blade, f) neg10 blade, g) neg30 blade, h) pos30 blade.

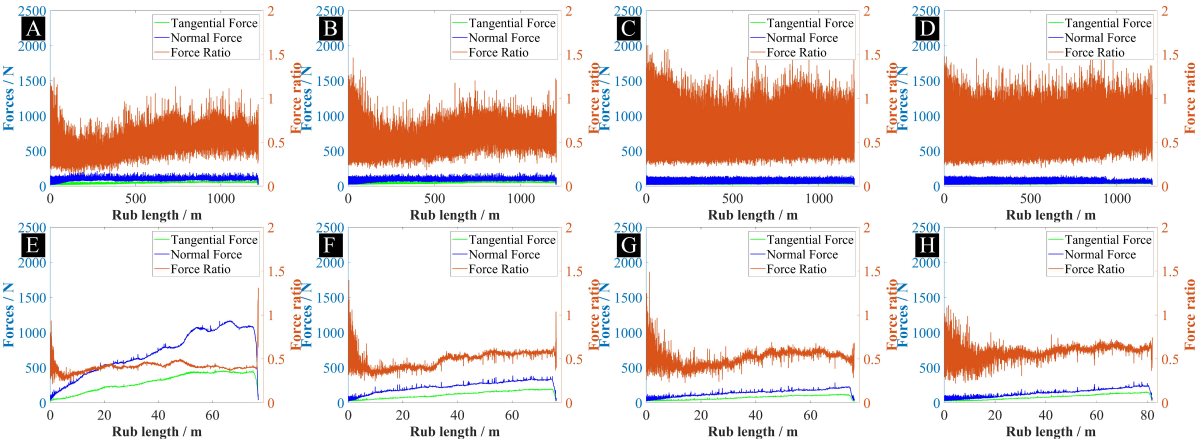

Fig. 7.4 The force data for the tests at the 200m/s speed and 0.02µm/pass incursion rate with a) flat blade, b) neg10 blade, c) neg30 blade, d) pos30 blade, 0.3µm/pass incursion rate with e) flat blade, f) neg10 blade, g) neg30 blade, h) pos30 blade.

It can be seen in Fig. 7.3 that post-test abradable samples appear similar for all of the testing conditions with rough surface similar to what was observed in the previous chapter indicating that abradable was removed through the fracture and release mechanism [51]. It can also be seen that contact forces were lower with angled blades at the higher tested incursion rate of 0.30m/pass.

The force and blade length results for all the 8 tests at 200m/s are further summarised in Fig. 7.5. The mean normal forces are shown in light blue, maximum normal forces in dark blue, mean tangential forces in light green, maximum tangential forces in dark green and mean blade wear at the end of a test in red. The mean blade wear was obtained by averaging the blade length change at all blade width locations at the end of a test.

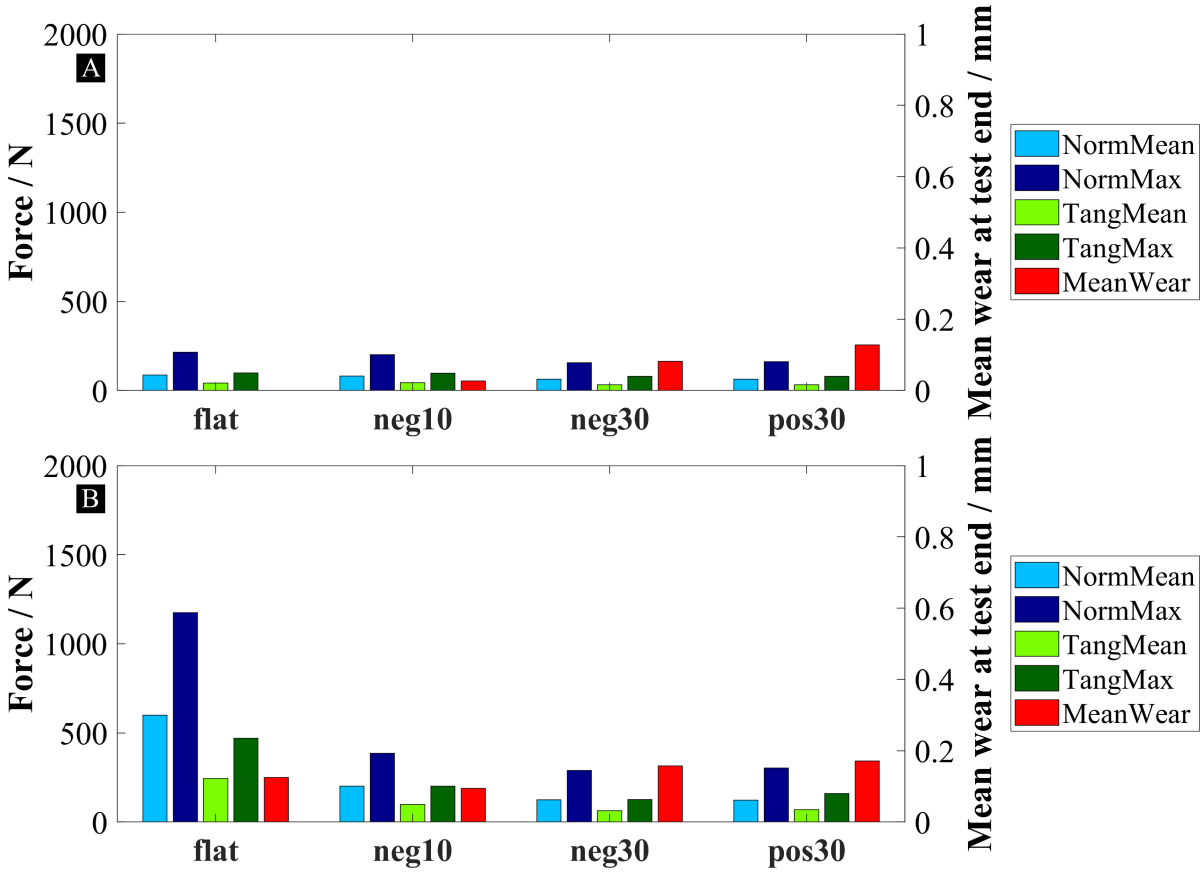

Fig. 7.5 The histograms showing the mean and maximum normal and tangential forces throughout a test and mean blade wear at the end of a test for each of the 4 blade types for tests at 200m/s speed and a) 0.02µm/pass incursion rate, b) 0.30µm/pass incursion rate.

For the tests at the 0.02µm/pass incursion rate, forces were comparable for all of the 4 blade types. None of the tests transitioned to the high-force contact mode and the maximum normal force was around 200N.

Despite similar forces, blade wear differed between different blade types. The flat blade experienced no blade wear as expected. The angled blades, however, experienced blade wear with an increase in angle increasing the amount of wear. This is due to even low forces being sufficient to wear out the very thin contacting face of the angled blades. This was especially noticeable for the pos30 and neg30 blades, where thickness grew slower with blade wear than for the neg10 blade as illustrated in Fig. 7.6, where the blade thickness as a function of the depth below an original tip is given.

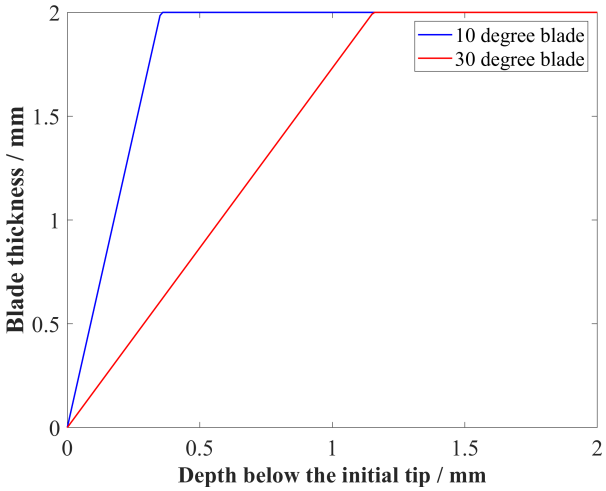

Fig. 7.6 the blade thickness as a function of the depth below an original tip for 10 degree and 30 degree angled blades.

At the higher incursion rate of 0.30µm/pass, the transition to the high-force contact mode occurred with the flat blade. The maximum normal force was about 1200N, which is consistent with the value for the tests where transition occurred in the previous chapter. The angled blades showed a significant improvement in performance in terms of contact forces in comparison to the flat blades. The contact forces for the angled blades at 0.30µm/pass were higher than at 0.02µm/pass, but significantly lower than for the flat blade at 0.30µm/pass. This indicates that transition to the high-force contact mode did not occur for the angled blades even at 0.30µm/pass. The neg30 blade had the lowest forces, followed by the pos30 and then the neg10 blades.

The blade wear results, however, had a different trend. The neg10 blade had the lowest wear, followed by the flat blade, which despite very high contact forces still experienced lower blade wear than the pos30 and neg30 blades. This was once again due to lower forces being sufficient to wear the very thin contacting face of the angled blades even before the transition to the high-force contact mode. The neg30 and pos30 blade were particularly affected by this.

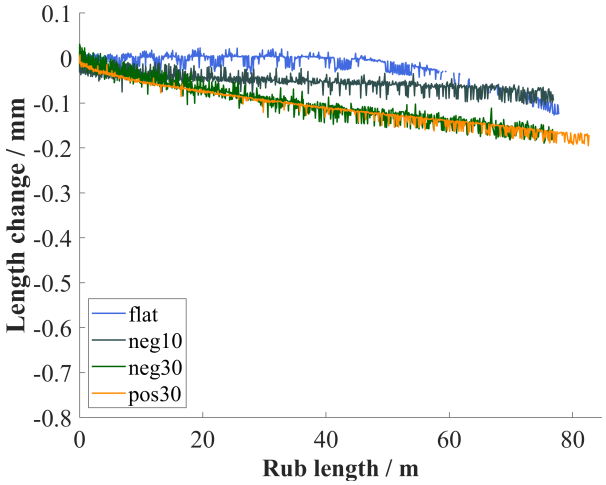

Fig. 7.7 The mean blade length change throughout a test for the tests at the 0.30µm/pass incursion rate for all 4 blade types

To evaluate the differences in how blade wear initiated and propagated throughout a test between the flat and angled blades, the mean blade length change throughout a test was plotted for tests at 0.30µm/pass in Fig. 7.7. It can be seen that despite similar absolute wear at the end of the test for all of the blade types, the way the wear occurred was different.

The flat blade experienced no wear until transition occurred and thermally driven wear initiated. For the pos30 and neg30 blades, however, the wear rate was highest at the beginning of the test, when the very thin tip was abraded. The neg10 blade performance was in between the flat and 30 degree angled blades.

From the results in Fig. 7.7 it was predicted that if the rub depth was increased to a larger value of 2000µm, which can occur in aero-engines, the 30 degree angled blades would outperform the flat blade in terms of blade wear. This hypothesis then guided the further testing presented in section 7.3.3.

7.3.2 Comparison of flat and angled blades at 280m/s

The post-test images of the abradable samples and blades and force data throughout a test are given for all the 8 tests at the 280m/s speed in Fig. 7.8 and 7.9 respectively.

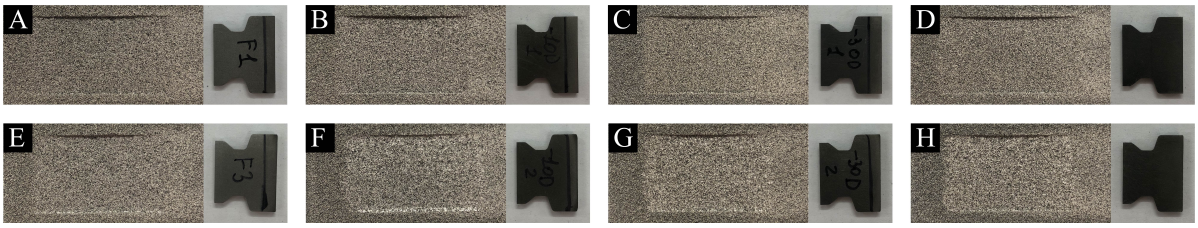

Fig. 7.8 The post-test images of the abradable samples and blades for the tests at the 280m/s speed and 0.02µm/pass incursion rate with a) flat blade, b) neg10 blade, c) neg30 blade, d) pos30 blade, 0.3µm/pass incursion rate with e) flat blade, f) neg10 blade, g) neg30 blade, h) pos30 blade.

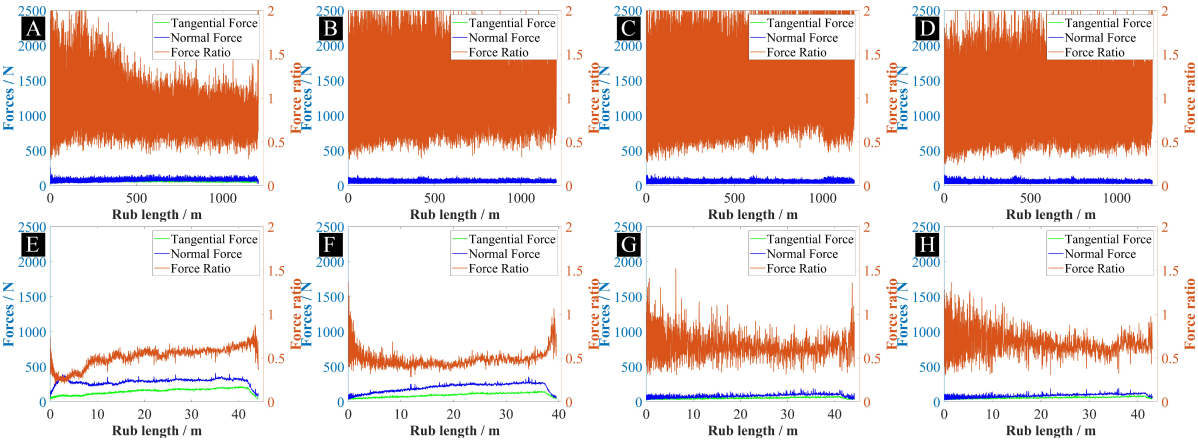

Fig. 7.9 The force data for the tests at the 280m/s speed and 0.02µm/pass incursion rate with a) flat blade, b) neg10 blade, c) neg30 blade, d) pos30 blade, 0.3µm/pass incursion rate with e) flat blade, f) neg10 blade, g) neg30 blade, h) pos30 blade.

It can be seen in Fig. 7.8 that post-test abradable samples once again appear similar for all of the testing conditions with a rough as-sprayed like surface. The force and blade length results for all the 8 tests at 280m/s are further summarised in Fig. 7.10. The results for the tests at 0.02µm/pass are given in Fig. 7.10a and for the tests at 0.6µm/pass in Fig. 7.10b.

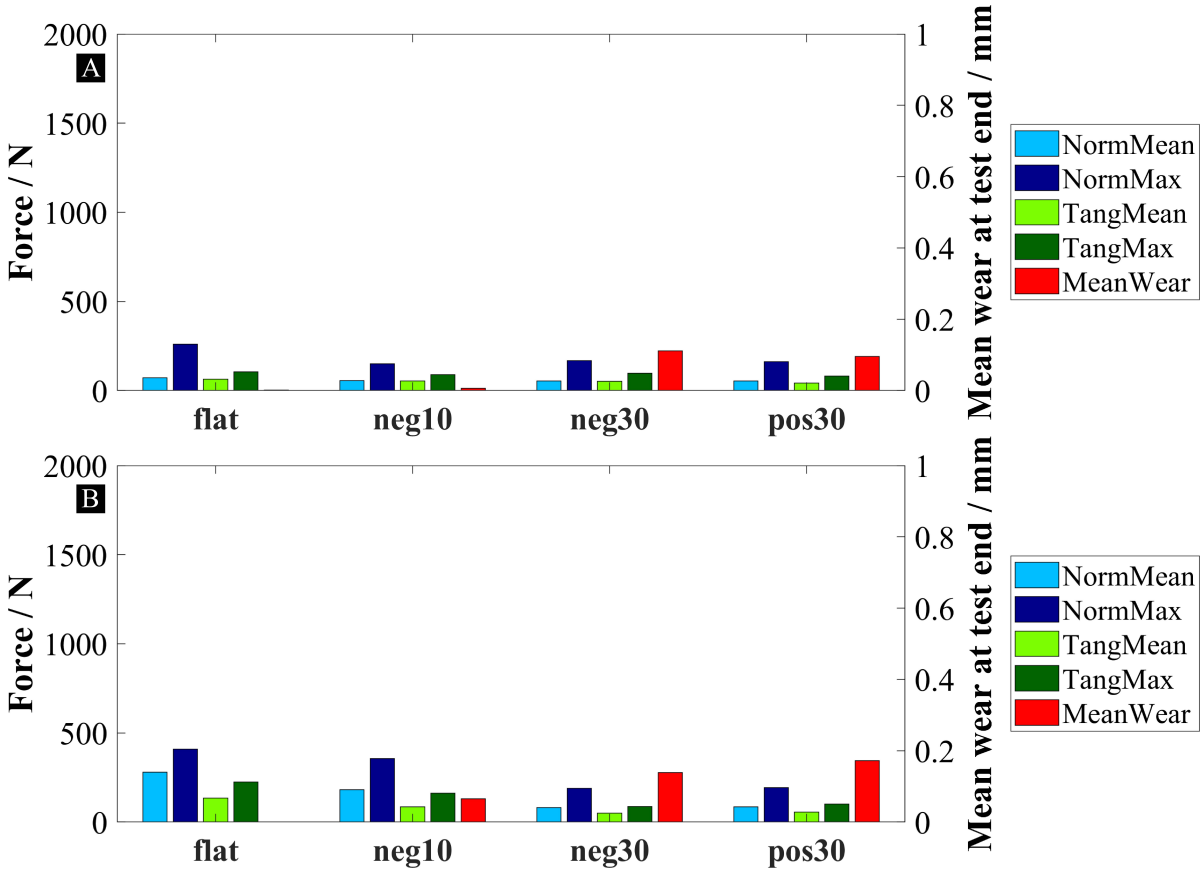

Fig. 7.10 The histograms showing the mean and maximum normal and tangential forces throughout a test and mean blade wear at the end of a test for each of the 4 blade types for tests at 280m/s speed and a) 0.02µm/pass incursion rate, b) 0.60µm/pass incursion rate.

For the test at the 0.02µm/pass incursion rate forces were once again comparable between the tested blades, with angled blades having slightly lower forces than the flat blade. None of the blades transitioned to the high-force contact mode and the maximum normal force was around 200N, similar to the tests at 200m/s speed and 0.02µm/pass incursion rate.

The blade wear also showed a similar trend to the tests at 200m/s. The flat blade experienced no blade wear, the neg10 blade experienced little wear and the neg30 and pos30 blades experienced the highest amount of blade wear.

The forces for the tests at the 0.60µm/pass incursion rate were higher than for the respective tests at the 0.02µm/pass incursion rate. However, unlike for the test at the higher incursion rate at 200m/s, the test with the flat blade did not transition to the high-force contact mode. This indicated that the chosen incursion rate of 0.60µm/pass was not sufficiently high to cause transition at 280m/s with this batch of samples.

However, a number of observations could still be made for the tests at 280m/s and the higher incursion rate of 0.60µm/pass. Despite transition did not occur, the maximum normal

force still occurred with the flat blade. It was closely followed by the neg10 blade, with both the neg30 and pos30 blades showing a significant improvement in contact forces.

The blade wear had a similar trend to the other incursion conditions, where a flat blade did not experience transition to the high-force contact mode. The flat blade experienced no blade wear, the neg10 blade had the second lowest blade wear. The blade wear increased with angle and both the neg30 and pos30 blades experienced higher blade wear than the neg10 blade.

7.3.3 Further comparison of flat and angled blades at 200m/s

The results at the 200m/s and the 0.30µm/pass incursion showed that despite a similar amount of blade wear at the end of a test between the flat and angled blades, the wear rate at the end of a test was higher for the test with the flat blade. It was then suggested that for tests with the larger rub depth of 2000µm, angled blades can show an improvement in performance in terms of blade wear in comparison to flat blades.

To investigate this hypothesis, a further set of tests was performed at 200m/s and 0.3µm/pass. All the 4 blade types were considered and two repeats were done for each blade type. These tests were performed with samples that had a worse abradable fracture behaviour than the ones used in 7.3.1 and were the same as the ones used in section 6.3.3. The summary of tests for the second experimental part is given in Table 7.2.

Table 7.2 The test matrix for the second experimental part

Test	Blade type	Speed / m/s	Incursion rate / µm/pass	Rub depth / µm	Repeats
1	flat	200	0.30	2000	2
2	neg10	200	0.30	2000	2
3	neg30	200	0.30	2000	2
4	pos30	200	0.30	2000	2

First, the post-test images of the abradable samples and blades, force data and blade mean wear throughout a test are given for all the 8 tests to highlight the differences in the way forces grew throughout a test and blade wear occurred for the flat and the angled blades. Then, these results will once again be summarised using histograms. The post-test images of the abradable samples and blades and force results are given in Fig. 7.11 and 7.12 respectively.

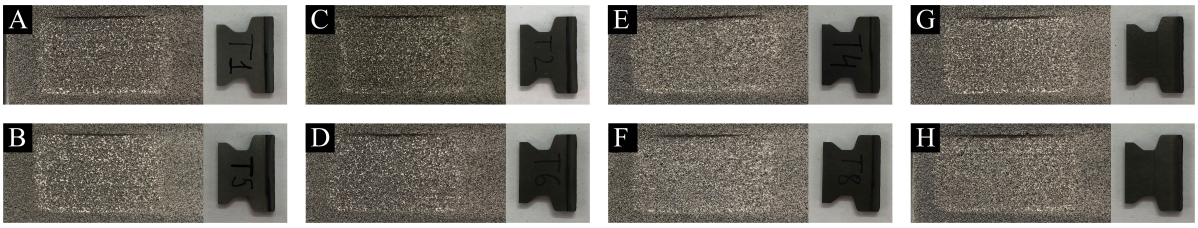

Fig. 7.11 The post-test images of the abradable samples and blades for all 8 tests, a, e) repeats 1 and 2 with flat blades, b, f) repeats 1 and 2 with neg10 blades, c, g) repeats 1 and 2 with neg30 blades, d, h) repeats 1 and 2 with pos30 blades.

Fig. 7.12 The force data for the tests for all 8 tests, a, e) repeats 1 and 2 with flat blades, b, f) repeats 1 and 2 with neg10 blades, c, g) repeats 1 and 2 with neg30 blades, d, h) repeats 1 and 2 with pos30 blades.

It can be seen in Fig. 7.11 that post-test abradable samples once again appear similar for all of the testing conditions with a rough as-sprayed like surface. In addition, it can be seen that the tips of all the 8 tested blades appear thermally damaged. In terms of forces, clear differences in the rub length at which the maximum normal force was reached can be seen in Fig. 7.12 between the different blade types. With the flat blades, transition to the high-force contact mode occurred very early in a test and the force remained stable around this value. For the angled blades, the slope at which the normal force increased throughout a test was much lower. With the neg10 blades, the maximum normal force was reached at the rub length of around 100m, while for the neg30 and pos30 forces were still in the growth phase at the end of the tests, when the rub length was around 200m.

From the results in Fig. 7.12, it can be concluded that the transition to the high-force contact mode occurred for both the flat and neg10 blades. For the tests with the pos30 and neg30 blades, the transition was more difficult to define as forces grew not only due to transition but, also due to thickening of the blade contacting face due to removal of the angled section of the blade with an increase in blade wear. The proportionality between the blade thickness and the contact forces for NiCrAl-bentonite abradables was established by Watson for blades with thickness between 1mm and 2mm [6].

However, the maximum normal force at the end of a test was around 1000N for all the blades with the 30 degrees angle, which is significantly higher than the maximum normal force for the test conditions, where transition did not occur in this and previous chapter, for which it did not exceed 500N. It then appears that the abradable fracture was not efficient and the transition to the high-force mode occurred.

$$l_{AngSection} = b_b tan(\theta) \tag{7.1}$$

where b_b is the blade tip thickness.

This is further reinforced by considering the blade wear results given in Fig. 7.13. The plots in Fig. 7.13a and Fig. 7.13b present results for repeats 1 and 2 respectively for each of the blade types. From Equation 7.1, the blade wear at which all of the angled section is abraded is 0.35mm for neg10 blades and 1.15mm for neg30 and pos30 blades. For both tests with the neg10 blades, more than 0.35mm was worn during a test, and the contact forces at the end of the tests were similar to the forces for the flat blades. On the other hand, the mean blade wear at the end of a test for the neg30 and pos30 blades was below 1.15mm.

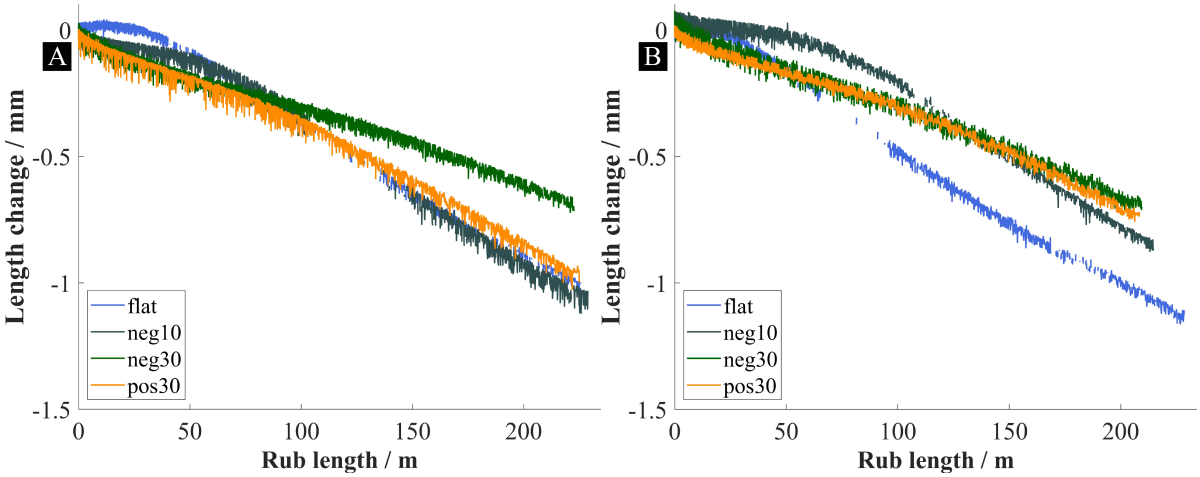

Fig. 7.13 The mean blade length change throughout a test for all 4 blade types, a) repeats 1, b) repeats 2.

The mean blade thickness at the end of the test was estimated from the amount of blade wear for a given blade. The maximum normal force was then divided by the blade thickness to obtain a value of the maximum normal force per blade thickness. Such analysis was considered appropriate as the blade thickness at the end of a test for all the 8 tests was within the 1mm and 2mm range considered by Watson for which proportionality was shown [6]. The results of this calculation are given in Table 7.3.

After such correction, all the maximum normal forces appeared similar. This suggests that lower forces at the end of a test with the neg30 and pos30 blades were primarily due to lower thickness of the contacting face for the tests in this section rather than due to improved abradable fracture, further reinforcing the idea that the transition to the high-force contact mode

occurred for the neg30 and pos30 blades as well at some point in the rub due to wear in essence returning them to being a flat blade.

Table 7.3 The calculation of the ratio between the maximum normal force and the blade tip thickness at the end of a test for all 8 completed tests

Blade type	Blade length change / mm	Tip thickness at test end / mm	Max normal force / N	Ratio of the max normal force and thickness at test end
flat	-1.00	2.00	2050	1025
neg10	-1.03	2.00	1822	911
neg30	-0.72	1.24	964	778
pos30	-1.00	1.73	1691	977
flat	-1.12	2.00	1791	896
neg10	-0.87	2.00	1642	821
neg30	-0.70	1.21	1154	953
pos30	-0.74	1.28	1104	864

Focusing on the comparison of the blade length results, it can be seen that the neg30 blade had the lowest blade wear amongst the tested blade types. The results here further support the observations made in section 7.3.1, where it was suggested that for the larger rub depths, angled blades can offer improved performance compared to flat blades when a larger rub depth is used.

It can be seen in Fig. 7.13 that the flat made had the lowest amount of wear until a transition to the high-force contact mode occurs. After the transition, the flat blade wore more quickly than the angled pos30 and neg30 blades. Once the angled section of a blade was worn out, angled blades wore similarly to flat blades as can be seen by comparing the wear rate of the flat and neg10 blades, which was similar towards the end of the tests. The wear rate of the neg30 blades was the lowest at the end of the tests, suggesting that the presence of an angled tip section decreased the blade wear rate during the high-force contact mode.

To present the trends in the test outcomes more clearly, the force and blade wear results at the end of tests were summarised in histograms in Fig. 7.14. The results were averaged over the two repeats with error bars given by one standard deviation.

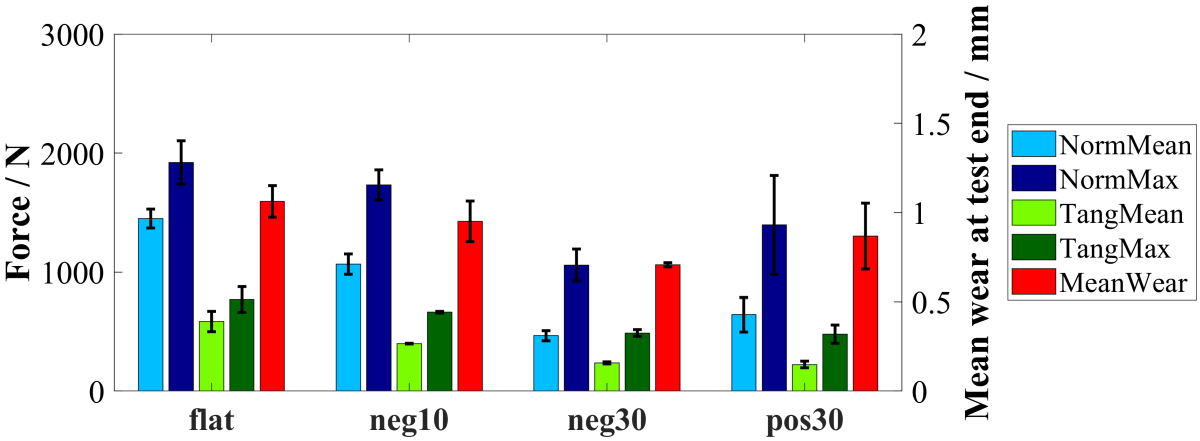

Fig. 7.14 The histograms showing the mean and maximum normal and tangential forces throughout a test and blade wear at the end of a test for each of the 4 blade types for tests at 200m/s speed and 0.30µm/pass incursion rate, the results are averaged over 2 repeats and the error bars are given by one standard deviation.

The relative performance of the blade types for the tests in this section can be clearly seen in Fig. 7.14. The use of the flat blades led to the highest force and blade wear, closely followed by the neg10 blades as the angled surface was removed during a test. The use of 30 degree angled blades gave the best improvement in performance in terms of both the contact forces and blade wear, with the neg30 blades outperforming the pos30 ones. However, this improvement was very limited.

Finally, it is interesting to note that the contact forces for this series of tests were higher than for the tests at the 200m/s speed and 0.30µm/pass incursion rate in section 7.3.1. This is due to the use of the harder batch of samples (samples having a worse fracture effectiveness) leading to the higher force at which a stable behaviour is reached. This is because with a harder sample more force is required to cause the same amount of fracture.

7.4 Discussion

The results in this work allowed to further explore the effects of using angled blades on wear mechanisms and test outcomes in contacts between NiCrAl-bentonite abradables and Inconel 718 blades building on the earlier results obtained by Watson [6].

The main difference between that study and the current work was the use of shorter (stiffer) blades, which were identified to improve test outcomes in the previous chapter. Additionally, the differences between having the longest edge as the leading edge and trailing edge were explored.

Before making comparisons with the earlier study by Watson [6], it is important to note that in that work harder samples (they had a similar nominal, but larger measured hardness) were used with longer blades meaning the transition to the high-force contact mode occurred even at incursion rates as low as 0.02µm/pass for the two hardest batches. It is therefore more practical to compare the tests in that study and in the current work not by the absolute values of the incursion rates but by how close they were to the transition incursion rate. Then, a comparison between the tests in this chapter performed at incursion rates above transition can be made to the tests at low incursion rates in the study by Watson [6] as both were performed close to the respective transition incursion rates for the given conditions.

7.4.1 Effect of angled blades on test outcomes

In the current study, there were some similarities and some clear differences with the work by Watson [6]. In that earlier study utilising longer blades it was shown that angled blades always improve tests outcomes in terms of contact forces and blade wear at low incursion rates (0.02µm/pass - 0.06µm/pass) and offer improvement in terms of contact forces but experience similar blade wear to flat blades at higher incursion rates. That suggested angled blades had a window of incursion rates where they offered clear benefits without having any drawbacks at any of the considered incursion conditions.

This is not what was found in this work using stiffer blades. The angled blades were still effective in reducing blade wear, but only within a very specific set of testing conditions: when incursion rate was above the transition incursion rate, and the rub depth was large enough. At incursion rates below the transition rate, angled blades had an improved performance in terms of contact forces, but had a significantly worse performance in terms of blade wear in comparison to flat blades.

The blades with a larger angle offered a bigger improvement in performance at incursion rates above the transition with a large rub depth, but also had the highest blade wear at incursion rate below the transition. The neg10 blades were in between flat blades and 30 degree angled blades. They had lower improvement in performance at incursion rates above the transition with a large rub depth, but did not experience as much blade wear at incursion rates below the transition as 30 degree angled blades.

Such significant differences in outcomes of angled blades in terms of effectiveness in reducing blade wear between the current work and the previous study by Watson [6] can be explained through the interaction between the blade stiffness and blade angle.

The results in the previous chapter showed that the use of longer (less stiff) blades worsens abradable fracture and leads to the transition to the high-force contact mode to occur at a lower incursion rate than for stiffer blades. The use of angled blades on the other hand reduces

contact forces, which was the consistent finding across both the current work and the study by Watson [6]. Such decrease in contact forces then neglected the effect of using less stiff blades in the study by Watson [6], which resulted in improved blade wear outcomes at low incursion rates, where the transition behaviour was improved. In this work, however, such improvement in transition behaviour did not occur with angled blades due to the use of stiff blades.

However, some improvement in wear rate was still observed with angled blades for incursion rates above transition at high incursion depths when comparing blades with the 30 degree angle to flat blades. The improvement in wear rate with angled blades in the thermally driven wear region with blade angle can for example be seen be seen in Fig. 7.13b (thermally driven wear occurred for all 4 blade types between rub lengths of 100m and 200m). The pos30 and neg30 blades experienced lower amount of wear in that region that the flat blade and the neg10 blade (for which the angled section was already removed in that region).

This result is consistent with what was seen with angled blades in the results by Watson [6]. Interestingly, a different set of results by Watson demonstrated that blades of a decreased thickness (the minimum considered thickness was 1mm) had decreased contact forces but had the same amount of blade wear as 2mm thick blades [6]. This highlights that the improvement in the wear rate with the angled blades is not just due to the reduction in blade tip thickness, but mainly due to the shape of the blade tip, where the thickness grows below the tip.

This suggests that the angled tip shape leads to an improved balance between contact forces and heat dissipation from the blade tip compared to blades with a constant thickness below the tip. It was shown in Table 7.3 that the normal force at the end of a test was close to proportional to blade thickness, which is consistent with the model proposed by Watson [6], where force was suggested to be proportional to contact area for the fracture and release mechanism hypothesised for contacts with the NiCrAl-bentonite abradable. The improvement in heat dissipation form the blade tip for a given tip thickness due to the angled geometry then led to the lower tip temperature and reduction in thermally driven wear, which is the main wear mechanism seen with flat blades. The improvement in the balance between contact forces and heat dissipation was also suggested by Watson [6] in the earlier study on angled blades and this suggestion is consistent with what was observed in this work.

7.4.2 Blade wear mechanisms

The previous section focused on why angled blades can offer benefits in performance and how these benefits compared between the current work and the previous study by Watson [6] using the long blades. In this section the focus will be given to the differences in blade wear mechanisms observed between the flat and angled blade types and why the trade-off in performance exists between them for the stiff blades used in this work.

Two types of blade wear mechanisms were observed in the performed tests. The first mechanism is the two-body abrasive wear occurring at low temperatures. Wear rate observed for this mechanism was quite small and so, such wear was insignificant for flat blades. This mechanism was significant for angled blades due to a sharp tip with a very thin edge, which led to some blade wear even at the lowest considered incursion rate of 0.02µm/pass.

The second mechanism is the two-body abrasive wear facilitated by the softening of a blade through an increase in blade temperature (this mechanism is later referred to in this work as the thermally driven abrasive wear). This is the mechanism observed for flat blades in the previous chapter, when transition to the high-force contact mode occurred. This mechanism also occurred with angled blades in the tests at 200m/s rubbed to 2000µm. However, the wear rate for this mechanism was lower for angled blades than for flat blades.

7.4.2.1 Comparison of flat and angled blades performance

Above the transition incursion rate, the flat blades only experienced the thermally driven abrasive wear, while the angled blades experienced both the low temperature abrasive wear and thermally driven abrasive wear with a wear rate lower than for flat blades (until the angled part of a blade was fully removed through blade wear). Additionally, angled blades delayed the onset of the thermally driven wear mechanism as heat was not building up at the blade tip as quickly as for the flat blades.

Such difference in the experienced wear mechanism between flat and angled blades led to an existence of the trade-off between them in terms of blade wear performance. For the incursion rates below the transition, where thermally driven wear did not occur for flat blades, they had no wear and outperformed all angled blade types. Once the incursion rate was high enough, thermally driven wear occurred and the wear rate of flat blades was higher than for the angled blade types. If an incursion depth was high enough, that higher rate led to the amount of blade wear first matching that of angled blades and then exceeding it with the further growth in rub length. The wear mechanisms and their significance for each of the considered blade types are summarised in Table 7.4. It should be noted that an improvement in the thermally driven wear occurs with angled blades only while the angled geometry remains. Once the angled section is worn out, such blades wear at the same rate as the flat blades.

Table 7.4 The summary of blade wear mechanisms and their significance for all 4 blade types

Blade type	Low temperature abrasive wear	Thermally driven abrasive wear
flat	No wear	High
neg10	Small (can be 10% of incursion depth for low-force contact mode)	High (small improvement over flat blades)
neg30	Medium (can be 20% of incursion depth for low-force contact mode)	Medium (good improvement over flat blades and neg10, some improvement over pos30 blades)
pos30	Medium (can be 20% of incursion depth for low-force contact mode)	Medium (good improvement over flat and neg10 blades)

7.4.3 Design considerations

In the previous two sections it was shown how changes in blade stiffness and blade angles interact and how this affects the amount of blade wear seen during a test. With this knowledge it is possible to address the questions of which parameter is more important from the blade design perspective for reducing the amount of blade wear seen during a contact.

From the results in this chapter, it appears that using a stiffer blade and adding a blade angle both offer improvement in terms of preventing inefficient abradable fracture due to blades of low stiffness. However, while increasing stiffness does not appear to lead to any trade-off in blade wear performance, angles lead to such trade-off due to the sharp tip getting worn out even at low temperatures through abrasive wear.

It then appears that the first factor to be addressed is the blade stiffness. However, if the blade stiffness has to be in the region where abradable fracture efficiency decreases, adding a blade angle can be an effective way to counteract low blade stiffness.

A different blade design can be considered for stiff blades. Such design is shown in Fig. 7.15, where the maximum permissible blade angle of 30 degrees is added to the blade, but instead of a sharp tip, it has a flat tip of reduced thickness. In this way the section of the low-temperature abrasive wear experienced by angled blades, where the initial sharp tip is quickly abraded is avoided. The angled blade tip geometry then allows for a lower rate of thermally driven wear in comparison to flat blades when the thermally driven wear initiates resulting in a overall reduction in the amount of blade wear.

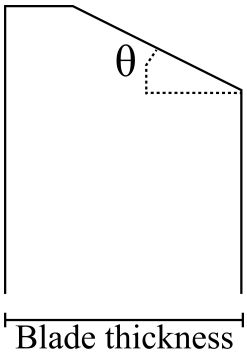

Fig. 7.15 A proposed tip design modification for stiff blades, angled geometry is used for improved heat removal for a given tip thickness, while the initial tip has a flat section to prevent low temperature abrasive wear seen with angled blades with a sharp tip.

With respect to whether the longest edge should be the leading or trailing edge, it was shown that both the neg30 (longest edge is the leading edge) and pos30 (longest edge is the trailing edge) offer a similar improvement in contact force and blade wear performance, with neg30 blades offering slightly larger improvement than the pos30 blades.

However, based on the proprietary data from Rolls-Royce plc., pos30 was the preferred orientation from the aerodynamic perspective. Then, when making a decision on blade orientation, the slightly improved wear performance of neg30 blades needs to be weighed against aerodynamic benefits of pos30 blades.

7.5 Conclusions

A total of 24 tests were performed investigating the benefits and drawbacks of using angled blades in contacts between Inconel 718 blades against NiCrAl-bentonite abradables.

A difference in the effectiveness of angled blade in improving test outcomes was identified between this work and the previous study by Watson [6]. In this work, angles were found effective in reducing blade wear only under a specific set of testing conditions rather than across all the conditions close to the transition incursion rate. This difference was explained by the use of shorter stiffer blade in this work, which provided part of the benefit of adding angles to the blade resulting in angled blades not being as effective.

The difference in wear performance between flat and angled blades was also further explored. The observed difference was explained by flat blade experiencing only the thermally driven abrasive wear and angled blades experiencing both the low temperature and thermally driven abrasive wear. The rate of the thermally driven wear was lower and the onset of thermally driven wear was delayed with the angled blades in comparison to the flat blades.

Adding angles with a sharp tip to the blades was suggested to be an effective tip modification when the blade stiffness is low and cannot be increased. An angled blade with a flat tip of reduced thickness was proposed as a potential blade tip design modification for stiff blades.

Chapter 8

Representativeness of tests on scaled rigs

8.1 Introduction

Previous research has shown that tests on scaled test rigs can produce wear mechanisms representative for aero-engines. However, some discrepancies in test outcomes between scaled test rigs and full-scale engine tests have also been observed. An example of such would be the severity of abradable compaction seen for tests at high incursion rates in the work by Watson [6]. While some compaction was observed in aero-engines as well, it was reported to not be as severe with no catastrophic failure of abradable [60].

To understand why such differences in results occur, it is important to understand how differences between test rigs and aero-engines can influence test outcomes. Such differences include testing blade tip speed, disk radius, small arc of contact, use of a single incursion rate while in engines varying incursion rates can occur, testing temperature (whether tests are performed at room temperatures or engines temperatures), and blade geometries (for example for standard flat blades, features such as a twist, lean, camber and a variable chord thickness are ignored).

For some of the variables, such as blade tip speed or disk radius good estimates of their effects can be made by extrapolating trends observed with these parameters. For example, it was shown that for NiCrAl-bentonite samples the disk radius is likely to not play a significant role in test outcomes as results on the low-speed and high-speed rigs were similar despite different disk radii.

Despite not reaching the engine representative speeds of 400m/s on both the low-speed and high-speed rigs, the effects of speed on test outcomes can be inferred from previous results with NiCAl-bentonite abradables. Results in previous and current studies have consistently shown that higher speeds improve abradable fracture and test outcomes, but the numerical improvement is yet to be quantified. Similarly, the effects of engine temperatures can be

inferred from past research where such temperatures were considered [25, 53, 38] and from numerical studies [24]. Based on previous findings, it was seen that while testing at more representative speed and temperature conditions might influence the incursion rates at which particular wear mechanisms occur or the severity of these mechanisms, but not the wear mechanisms themselves, which were consistent across the testing on both full-scale and scaled experimental rigs. Extending the experimental work to engine speeds of 400m/s and engine representative temperatures might be of interest for future research to better understand the effect of these variables on test outcomes, but this is currently limited by the low-speed and high-speed rig capabilities.

The effect of variables such as having a variable incursion rate or a more representative blade geometry can be predicted by applying the existing knowledge of contacts with abradable materials, but such predictions were not previously verified through experimental testing.

As such, the exploration of these factors presents a scope for two things: a) better understanding of the effects of these factors on test outcomes allowing better understanding of how results on scaled test rigs translate to aero-engines and b) verification of the current understanding of contacts with abradable materials by comparing the effects of these factors to the predictions of these effects based on current hypothesis.

In this chapter, the preliminary testing exploring the effects of two such factors is performed for two types of abradable: NiCrAl-bentonite and AlSi-polyester. The first chosen factor was the use of blades with a variable chord thickness rather than a fixed 2mm thickness. Understanding of the effects of having a variable chord thickness was considered important for both abradable types based on the observations made in the previous chapters. For NiCrAl-bentonite abradables, the comparison of results obtained with flat and angled blades indicated that the tip shape can have an influence on the amount of blade wear observed during a test. For AlSi-polyester abradables, it was suggested that flash temperatures have a large influence on the probability of adhesion formation, and the flash temperature can be dependant on blade thickness.

The second factor chosen for consideration was the variable incursion rate. In aero-engines, incursion rates during running and handling procedure can be significantly larger than during normal flight conditions. Previous work on the NiCrAl-bentonite abradables by Watson [51] has shown that very high incursion rates (in the order of 2µm/pass) can lead to abradable compaction. The results of that work indicated the need to decrease the incursion rates for the running and handling procedure. In that work it was also found that despite the transition to the high-force contact mode and presence of blade wear, only a small amount of surface compaction was observed at lower incursion rates (around 0.2µm/pass) indicating almost no damage to the abradable. This suggested that efficient fracture of abradable could once again occur once

incursion rates decreased to values below transition. It was then decided to experimentally investigate whether transition to the high-force contact mode (which leads to blade wear) during running and handling at a high incursion rate could influence contact forces and blade wear at a lower incursion rate, which can occur during flight conditions.

8.2 Materials and methodology

The tests in this chapter consisted of two parts. In the first part, blades with a more representative geometry were used. The blades had a variable chord thickness, but still ignored features such as lean, twist and camber. It was decided to incorporate the variable chord thickness into the blade design first, as it was expected to be of the biggest influence on blade wear mechanisms. The modified blades were 1.3mm in the thickest part at the blade centre and 0.2mm in the thinnest part at the blade edges. The dimensions were selected based on the proprietary data from Rolls-Royce plc. The dimensions of the modified blades are shown in Fig. 8.1.

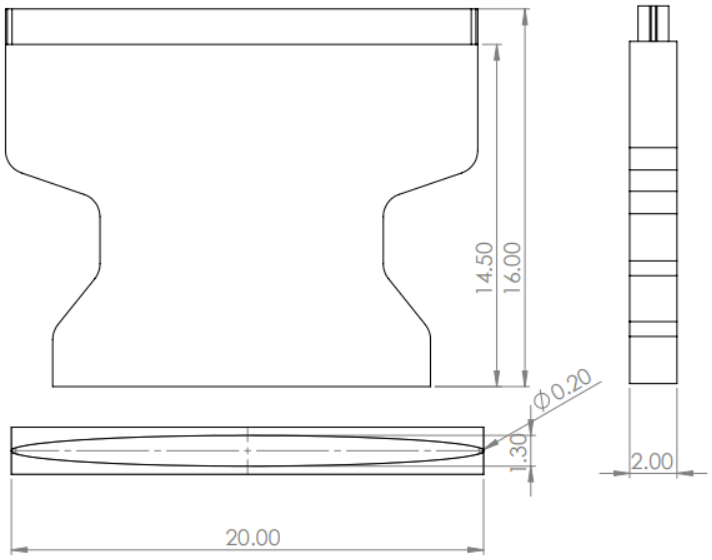

Fig. 8.1 The dimensions of the modified blades.

Tests with blades with a variable chord thickness (blades with modified geometry) were performed at two speeds and three incursion rates for each speed for each of the abradables. The selected speeds were 200m/s and 280m/s in line with the testing conditions used in the previous chapters. For the tests with NiCrAl-bentonite abradable samples, the incursion rates were 0.02µm/pass, 0.4µm/pass and 0.6µm/pass. The incursion rate of 0.02µm/pass was used as a control where no transition to the high-force contact mode was expected. At the incursion rates of 0.4µm/pass and 0.6µm/pass, transition to the high forces was expected to occur, and

so they were selected to investigate wear properties of blades with variable chord thickness in comparison to flat blades. For the tests with AlSi-polyester abradable samples, the incursion rates were 0.02µm/pass, 0.2µm/pass and 2µm/pass in line with previous work. The summary of conditions for the tests with blades with modified geometry is given in Table 8.1 and 8.3 for the NiCrAl-bentonite and AlSi-polyester abradables respectively.

In the second part, tests with two incursion rates were performed. All the testing was performed at 200m/s. Different incursion rate conditions were selected for NiCrAl-bentonite and AlSi-polyester abradables based on the findings in the previous chapters. For the NiCrAl-bentonite abradable the highest considered incursion rate was 0.4µm/pass as the main interest was in understanding if the transition to the high-force contact mode introduces any permanent damage to the contact conditions. For the AlSi-abradable the highest considered incursion rate was 2µm/pass to understand the differences in adhesive behaviour between tests with two incursion rates in this chapter and single incursion rate in chapter 5.

For the NiCrAl-bentonite abradable samples, 6 tests were performed. Two tests were at a low incursion rate for 500µm followed by 500µm at a high incursion rate. Two tests were at the same conditions but with an opposite sequence of incursion rates. Two additional tests were performed with 1000µm at a high incursion rate followed by 500µm at a low incursion rate. It was decided to perform tests with a higher initial incursion depth at a high incursion rate, as for the two tests starting with 500µm at a high incursion rate, it was found that such rub depth was insufficient to reach a steady wear behaviour at a high incursion rate before the start of a lower incursion rate section.

For the AlSi-polyester abradable samples, 4 tests were performed. Two tests started with 500µm at 0.02µm/pass followed by 500µm at either 0.2µm/pass or 2µm/pass to investigate how potential blade damage introduced at 0.02µm/pass can affect the adhesion formation if high-incursion rate occurs after. Two tests started with 500µm at 2µm/pass followed by 500µm at either 0.02µm/pass or 0.2µm/pass to investigate how incursion conditions during running and handling can influence wear mechanisms at incursion rates observed during normal flight operation. The summary of conditions for the tests with two incursion rates is given in Table 8.2 and 8.4 for the NiCrAl-bentonite and AlSi-polyester abradables respectively.

Table 8.1 The summary of conditions for the tests with the NiCrAl-bentonite abradable with blades with modified geometry.

Abradable	Blade material	Speed m/s	Incursion rate / µm/pass	Rub depth / µm
H55 NiCrAl-bentonite	Inconel 718	200m/s	0.02	1000
H55 NiCrAl-bentonite	Inconel 718	200m/s	0.4	1000
H55 NiCrAl-bentonite	Inconel 718	200m/s	0.6	1000
H55 NiCrAl-bentonite	Inconel 718	280m/s	0.02	1000
H55 NiCrAl-bentonite	Inconel 718	280m/s	0.4	1000
H55 NiCrAl-bentonite	Inconel 718	280m/s	0.6	1000

Table 8.2 The summary of conditions for the tests with the NiCrAl-bentonite abradable with two incursion rates.

Abradable	Blade material	Speed m/s	Incursion rate / µm/pass	Rub depth / µm	incursion rate 2 / µm/pass	Rub depth 2 / µm
H55 NiCrAl-bentonite	Inconel 718	200m/s	0.02	500	0.2	500
H55 NiCrAl-bentonite	Inconel 718	200m/s	0.02	500	0.4	500
H55 NiCrAl-bentonite	Inconel 718	200m/s	0.2	500	0.02	500
H55 NiCrAl-bentonite	Inconel 718	200m/s	0.4	500	0.02	500
H55 NiCrAl-bentonite	Inconel 718	200m/s	0.2	1000	0.2	500
H55 NiCrAl-bentonite	Inconel 718	200m/s	0.4	1000	0.2	500

Table 8.3 The summary of conditions for the tests with the AlSi-polyester abradable with blades with modified geometry.

Abradable	Blade material	Speed m/s	Incursion rate / µm/pass	Rub depth / µm
H70 AlSi-polyester	Ti(6Al 4V)	200m/s	0.02	1000
H70 AlSi-polyester	Ti(6Al 4V)	200m/s	0.2	1000
H70 AlSi-polyester	Ti(6Al 4V)	200m/s	2	1000
H70 AlSi-polyester	Ti(6Al 4V)	280m/s	0.02	1000
H70 AlSi-polyester	Ti(6Al 4V)	280m/s	0.2	1000
H70 AlSi-polyester	Ti(6Al 4V)	280m/s	2	1000

Table 8.4 The summary of conditions for the tests with the AlSi-polyester abradable with two incursion rates.

Abradable	Blade material	Speed m/s	Incursion rate / µm/pass	Rub depth / µm	incursion rate 2 / µm/pass	Rub depth 2 / µm
H70 AlSi-polyester	Ti(6Al 4V)	200m/s	0.02	500	0.2	500
H70 AlSi-polyester	Ti(6Al 4V)	200m/s	0.02	500	2	500
H70 AlSi-polyester	Ti(6Al 4V)	200m/s	2	500	0.02	500
H70 AlSi-polyester	Ti(6Al 4V)	200m/s	2	500	0.2	500

8.3 Results NiCrAl-bentonite

In this section results obtained for tests between Inconel 718 blades and NiCrAl-bentonite abradables will be presented. First, results obtained with modified blades will be given, followed by results for the double incursion rate tests.

8.3.1 Modified blade geometry tests

First, the post-test images of the abradable samples and blades, force and blade length results throughout a test are given for all the 6 tests to highlight the differences in the way forces grew throughout a test and blade wear occurred for the blades of modified tip geometry at different incursion rates. Then, these results will be further analysed by calculating the ratio of the maximum normal force to the average blade thickness and by comparing blade profiles at the end of a test to such profiles from the tests with flat blades where a similar amount of mean blade wear occurred. The post-test images of the abradable samples and blades for all the tests are given in Fig. 8.2, force results in Fig. 8.3 and blade profile history maps in Fig. 8.4.

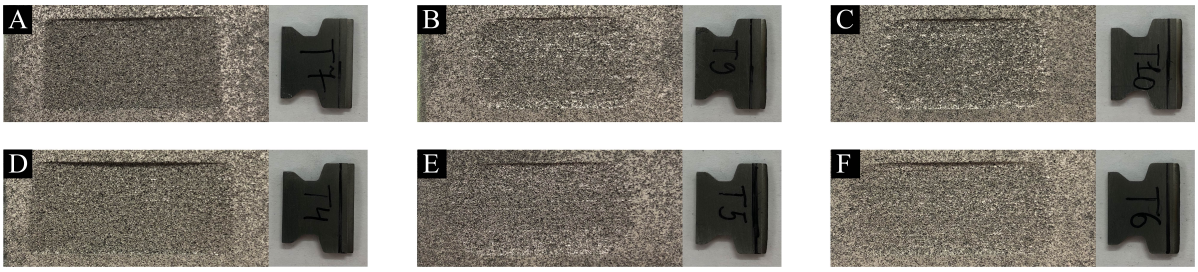

Fig. 8.2 The post-test images of the abradable samples and blades for the tests at 200m/s and a) 0.02µm/pass, b) 0.4µm/pass, c) 0.6µm/pass, for the tests at 280m/s and d) 0.02µm/pass, e) 0.4µm/pass, f) 0.6µm/pass.

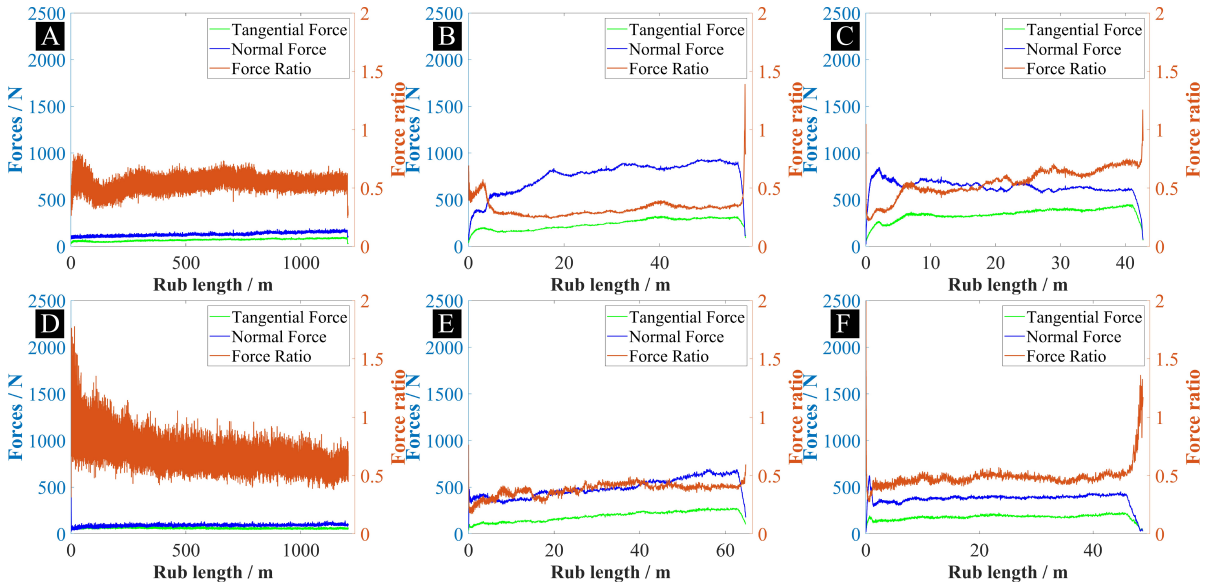

Fig. 8.3 The normal and tangential forces and force ratio throughout a test for the tests at 200m/s and a) 0.02µm/pass, b) 0.4µm/pass, c) 0.6µm/pass, for the tests at 280m/s and d) 0.02µm/pass, e) 0.4µm/pass, f) 0.6µm/pass.

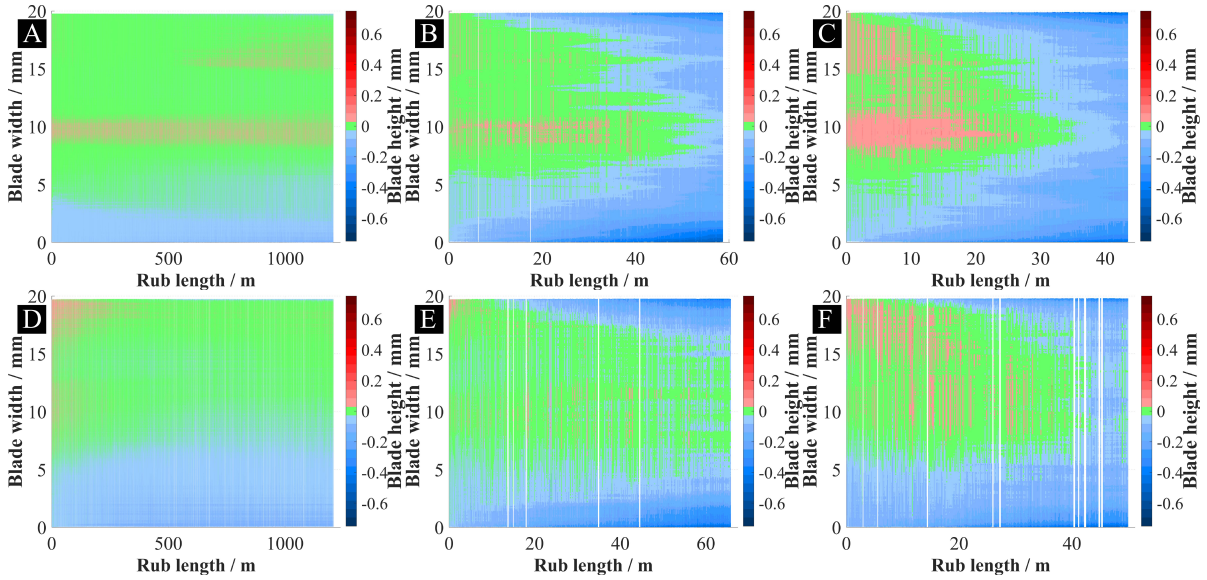

Fig. 8.4 The blade profile history maps for the tests at 200m/s and a) 0.02µm/pass, b) 0.4µm/pass, c) 0.6µm/pass, for the tests at 280m/s and d) 0.02µm/pass, e) 0.4µm/pass, f) 0.6µm/pass.

The overall trend in results was similar to the standard flat blades used against NiCrAl-bentonite abradables. The post-test abradable surfaces shown in Fig. 8.2 appeared as-sprayed for all of the testing conditions with them being the most uniform across the width and least shiny for the tests at 0.02µm/pass. As can be seen in Fig. 8.3, forces for the tests at the

0.02µm/pass incursion rate and both the 200m/s and 280m/s speeds were low and transition to the high-force contact mode did not occur. This is confirmed by the blade profile history maps in Fig. 8.4, where it can be seen that no significant blade wear occurred at these conditions.

At both higher incursion rates of 0.4µm/pass and 0.6µm/pass transition to the high-force contact mode occurred for tests at both the 200m/s and 280m/s speeds. The maximum normal force for these tests was around 600-950N, which is lower than for tests with flat blades where transition occurred in previous chapters. However, the tip surface area of the modified blades was lower than that of 2mm thick flat blades.

The maximum normal force was then divided by the average blade thickness to obtain a value of the maximum normal force per blade thickness. This was done because the proportionality between the blade thickness and the contact forces for NiCrAl-bentonite abradables was established by Watson for blades with thickness between 1mm and 2mm [6]. A part of the blade was outside the 1mm end of the range considered in that study. However, a large section of the blade was within that range or only slightly below the 1mm thickness and so, such analysis was considered appropriate (79% of the blade width was above the 0.8mm thickness, which was considered close enough to the 1mm to 2mm thickness range for conclusions of the study by Watson [6] to be extended to it).

For modified blades, the average thickness was calculated by dividing the blade area obtained from SolidWorks blade geometry by blade width (20mm) and was found to be 1.02mm. The results of the calculation of the ratio of the maximum normal force to average blade thickness are then given in Table 8.5.

Table 8.5 The calculation of the ratio between the maximum normal force and the average blade tip thickness

Speed / m/s	Incursion rate / µm/pass	Average tip thickness / mm	Max normal force / N	Ratio of the max normal force and average tip thickness
200	0.4	1.02	941	922
200	0.6	1.02	848	831
280	0.4	1.02	698	684
280	0.6	1.02	622	610

Table 8.6 The calculation of the ratio between the maximum normal force and the blade tip thickness at the end of a test for all 8 completed tests

Blade type	Blade length change / mm	Tip thickness at test end / mm	Max normal force / N	Ratio of the max normal force and thickness at test end
flat	-1.00	2.00	2050	1025
neg10	-1.03	2.00	1822	911
neg30	-0.72	1.24	964	778
pos30	-1.00	1.73	1691	977
flat	-1.12	2.00	1791	896
neg10	-0.87	2.00	1642	821
neg30	-0.70	1.21	1154	953
pos30	-0.74	1.28	1104	864

When considering the calculated ratio for the tests at 200m/s, it can be seen that it is comparable to the tests in the previous chapter with both the flat and angled blades performed at 200m/s with samples of comparable hardness shown once again in Table 8.5 to aid the comparison, where such ratio was between 778N and 1025N.

The ratio for the tests at 280m/s was lower – 610N and 684N. This suggests that the lower amount of force is required at the higher speed to cause the same amount of abradable fracture, which further reinforces the previous findings by Watson [6] and in the previous chapters in this work, where higher speed was shown to improve tests outcomes for tests with NiCrAl-bentonite samples. This is also seen from blade wear results in Fig. 8.4, where it can be seen that lower blade wear was observed at the higher speed when comparing tests at both the 0.4µm/pass and 0.6µm/pass incursion rates.

Focusing on the blade wear results, it can be seen that blade wear initiated at the edges for all of the tests where blade wear occurred. This is likely related to blade temperature distribution with the blade edge getting to hot temperatures first due to rubbing both the abradable under the blade and to the sides of the blade. Such a pattern of wear is consistent with results with flat blades where transition occurred and they experienced the thermally driven wear mechanism.

However, the difference between blade wear at the edges and the middle of the blade appeared to be more severe for the blades with modified geometry than for the flat blades. To verify this, the blade profile distribution at the end of a test was plotted for 2 blades with modified geometry and flat blades in Fig. 8.5 for the tests where there was a similar amount of mean blade wear at the end of a test. It is important to note that tests with modified blades and flat blades were performed with different batches of samples and so, the effect of using

modified blades on the transition incursion rates cannot be inferred from the results in this section.

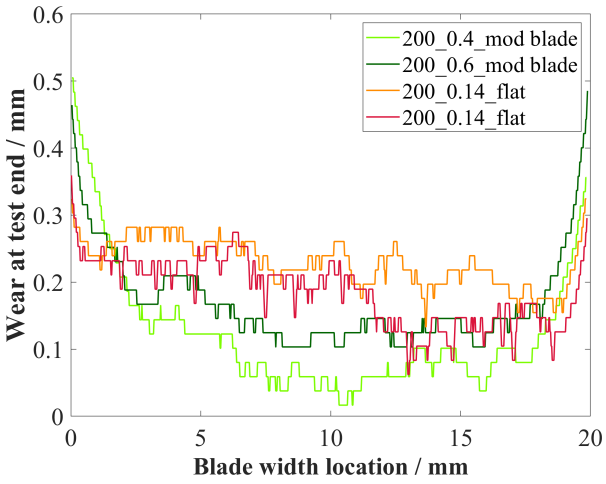

Fig. 8.5 The amount of blade wear along blade width at the end of a test for two tests with modified blades and two tests with flat blades (repeats 1 and 2 at 0.14µm/pass and 200m/s from section 5.3.2).

Results in Fig. 8.5 confirm the initial observations. While the differences are not very large, it can be seen that with modified blades more wear occurred at blade edges (around 0mm and 20mm blade width locations) in comparison to flat blades and distribution of wear along the edge is less even. This suggests that edge effects (stress concentrator and potentially the increased heat generation per surface area due to rubbing both the abradable under the blade and to the sides of the blade) are more pronounced with blades with modified geometry. This is due to edges being much thinner that the rest of the blade in contrast to flat blades where, blade thickness is constant along the whole blade width.

8.3.2 Double incursion rate tests

First, the post-test images of the abradable samples and blades, force and blade length results throughout a test are given for all the 6 tests to highlight the differences in the way forces grew throughout a test and blade wear occurred for the tests with two incursion rates. The left half of each plot corresponds to the first incursion rate part and the right half of each plot corresponds to the second incursion rate part. The post-test images of the abradable samples and blades for all the tests are given in Fig. 8.6, force results in Fig. 8.7 and blade profile history maps in Fig. 8.8.

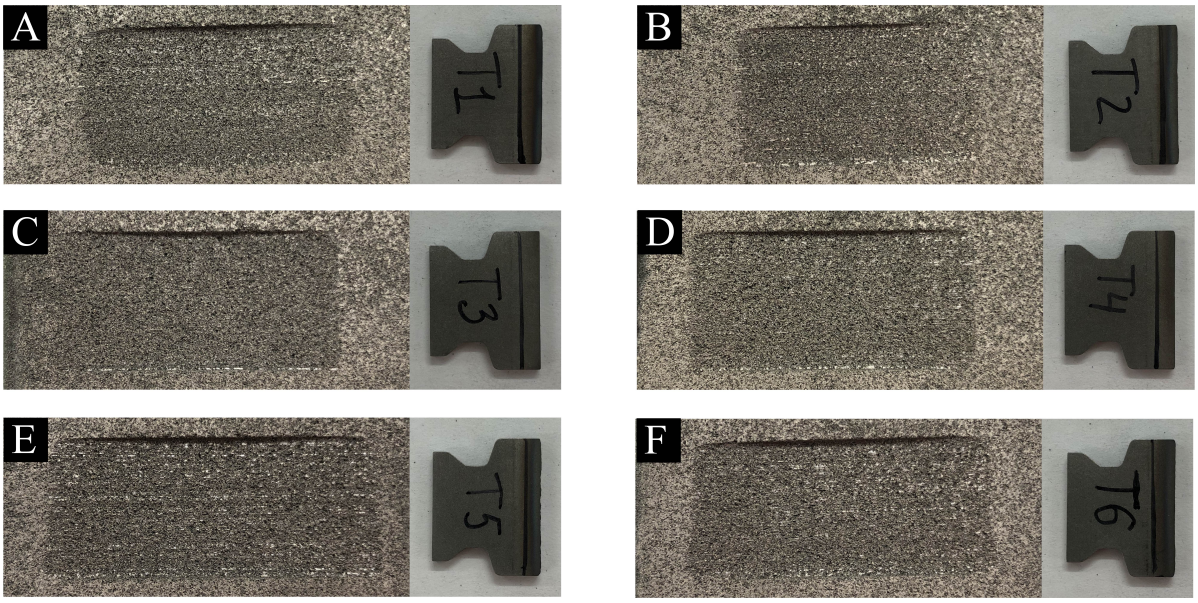

Fig. 8.6 The post-test images of the abradable samples and blades for the tests at a) 0.02µm/pass for 500µm and 0.2µm/pass for 500µm, b) 0.02µm/pass for 500µm and 0.4µm/pass for 500µm, c) 0.2µm/pass for 500µm and 0.02µm/pass for 500µm, d) 0.4µm/pass for 500µm and 0.02µm/pass for 500µm, e) 0.2µm/pass for 1000µm and 0.02µm/pass for 500µm, f) 0.4µm/pass for 1000µm and 0.02µm/pass for 500µm.

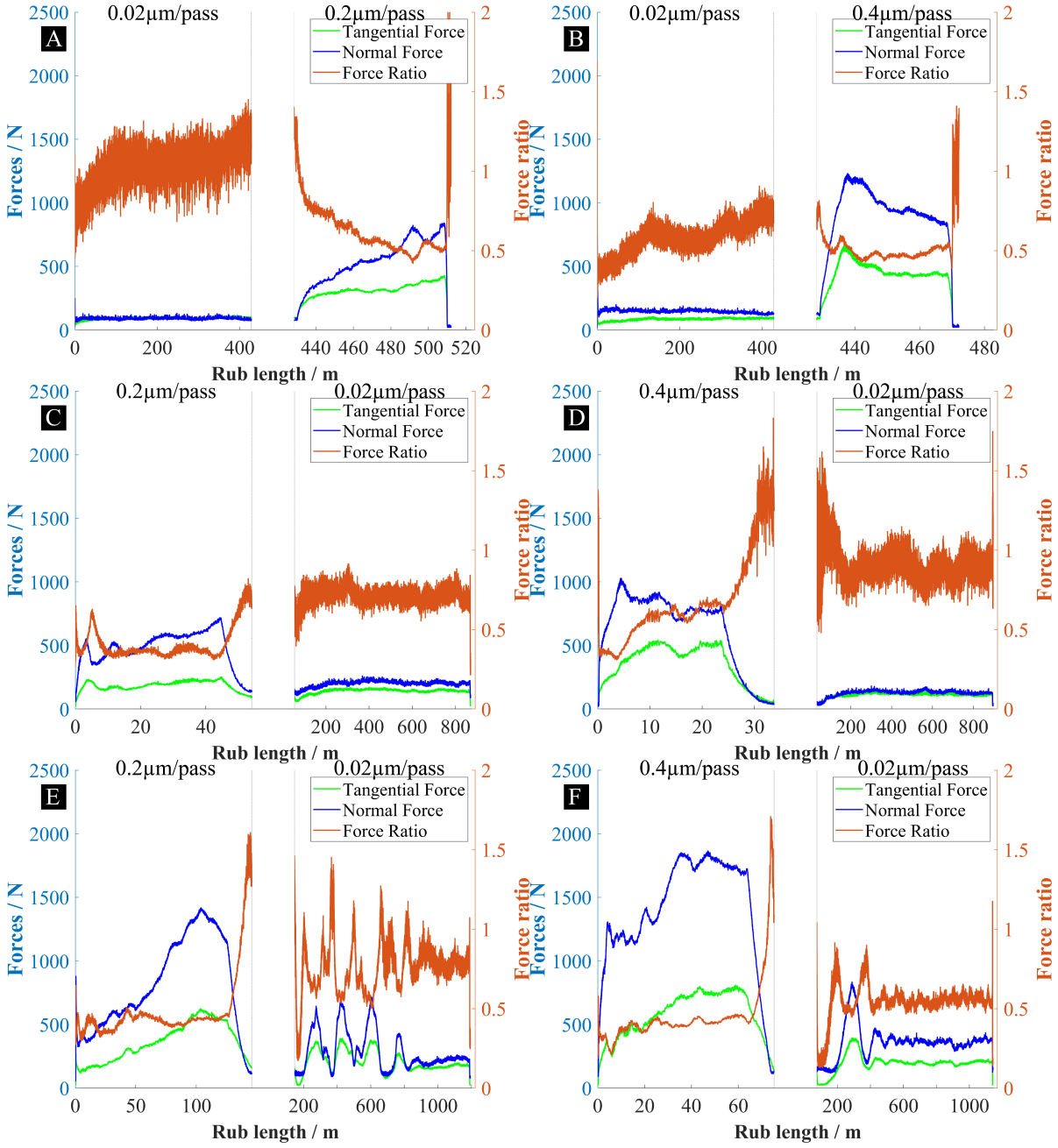

Fig. 8.7 The normal and tangential forces and force ratio throughout a test for the tests at a) 0.02µm/pass for 500µm and 0.2µm/pass for 500µm, b) 0.02µm/pass for 500µm and 0.4µm/pass for 500µm, c) 0.2µm/pass for 500µm and 0.02µm/pass for 500µm, d) 0.4µm/pass for 500µm and 0.02µm/pass for 500µm, e) 0.2µm/pass for 1000µm and 0.02µm/pass for 500µm, f) 0.4µm/pass for 1000µm and 0.02µm/pass for 500µm.

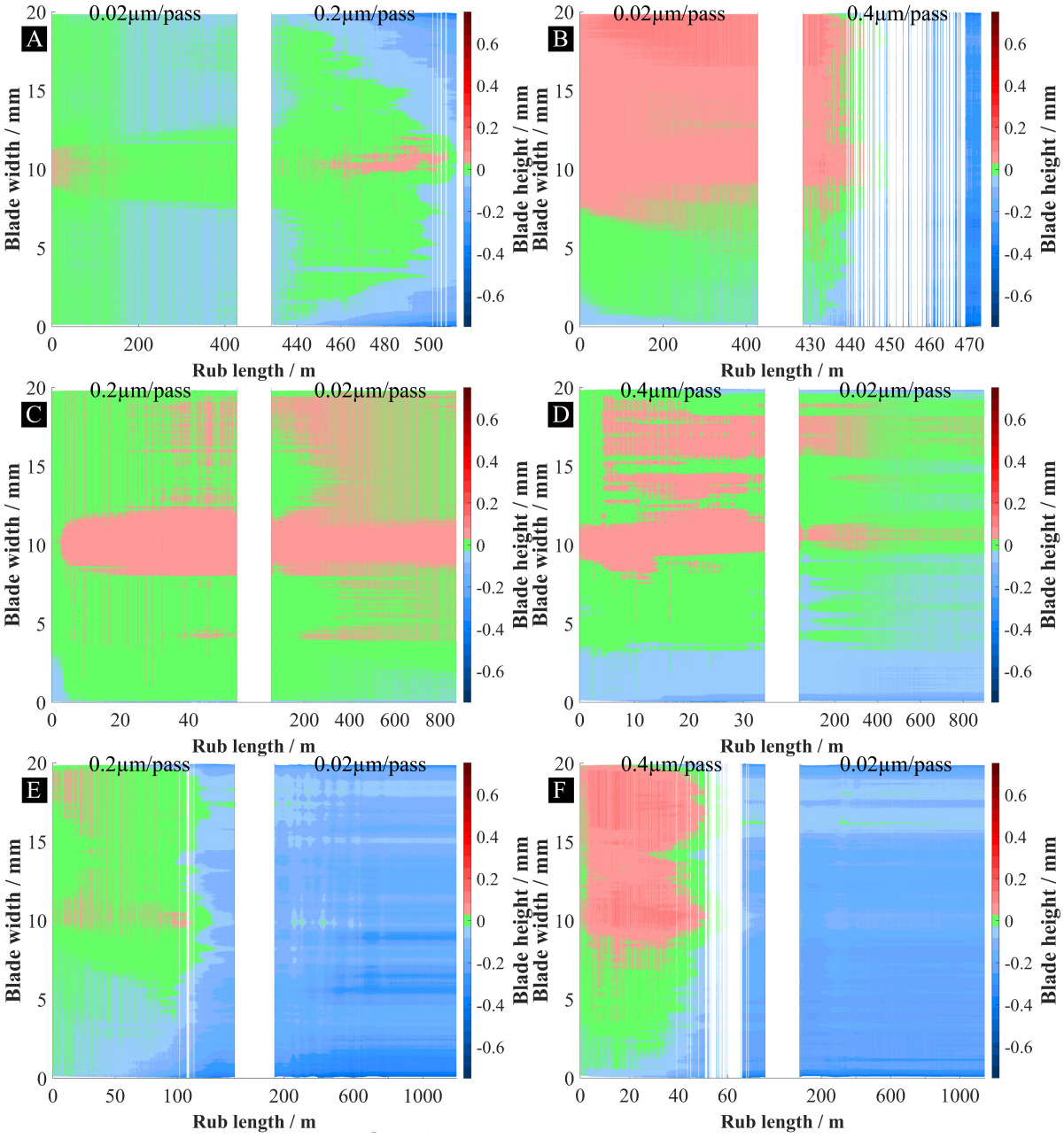

Fig. 8.8 The blade profile history maps for the tests at a) 0.02µm/pass for 500µm and 0.2µm/pass for 500µm, b) 0.02µm/pass for 500µm and 0.4µm/pass for 500µm, c) 0.2µm/pass for 500µm and 0.02µm/pass for 500µm, d) 0.4µm/pass for 500µm and 0.02µm/pass for 500µm, e) 0.2µm/pass for 1000µm and 0.02µm/pass for 500µm, f) 0.4µm/pass for 1000µm and 0.02µm/pass for 500µm.

By analysing results in Fig. 8.7, it can be seen that the section at the low incursion rate does not influence the forces that occur during the high incursion rate section. Forces during the second section in Fig. 8.7a were comparable to forces during the first section in Fig. 8.7c.

Similarly, forces during the second section in Fig 4b were comparable to forces during the first section in Fig. 8.7d.

The outcome in terms of blade wear, however, depended on the order of incursion rates. In Fig. 8.8a and Fig. 8.8b some blade wear was observed when a section at 0.2µm/pass or 0.4µm/pass followed a section at 0.02µm/pass, while in Fig. 8.8c and Fig. 8.8d there was a very limited amount of blade wear when a section at 0.02µm/pass followed a section at 0.2µm/pass or 0.4µm/pass. This is likely due to differences in blade temperature before the start of the high incursion rate section. In tests, where the higher incursion rate section was first, a blade was at room temperature at the start of a test and there was some time until a blade got hot enough for thermally driven wear to initiate. For the tests where the high incursion rate was second, despite no blade wear, some heat likely built-up in the blade during the low incursion rate section. That led to the decreased time till the point when a blade got hot enough for thermally driven wear to initiate. Additionally, for the tests where the higher incursion rate was tested second, the rub length at the higher incursion rate was higher. This is due to the arc of contact with an abradable increasing with an increase in rub depth. That could have also led to the faster rate of heat build-up at the blade tip.

From the results in Fig. 8.7, it can be seen that the force history during a high incursion rate section influences forces seen during a low incursion rate section. Mean forces for the low incursion rate sections are shown in Table 8.7 to further illustrate this point. Forces were the lowest when the low incursion rate section was the first one. A slight increase in forces was seen for a low incursion rate section when it came after 500µm at a high incursion rate and a large increase in force was seen for a low incursion rate section when it came after 1000µm at a high incursion rate. However, it can also be seen in Fig. 8.8e and Fig. 8.8f that despite an increase in forces for a low incursion rate section, they were still low enough to prevent further blade wear past the end of a high incursion rate section.

Table 8.7 The mean contact forces for a low incursion rate section for all the 6 tests

Test	Mean normal force for the low incursion rate section / N	Mean tangential force for the low incursion rate section / N
0.02µm/pass for 500µm then 0.2µm/pass for 500µm	89	88
0.02µm/pass for 500µm then 0.4µm/pass for 500µm	153	81
0.2µm/pass for 500µm then 0.02µm/pass for 500µm	196	140
0.4µm/pass for 500µm then 0.02µm/pass for 500µm	124	111
0.2µm/pass for 1000µm then 0.02µm/pass for 500µm	288	204
0.4µm/pass for 1000µm then 0.02µm/pass for 500µm	358	195

8.4 Results AlSi-polyester

In this section results obtained for tests between Ti(6Al4V) blades and AlSi-polyester abradables will be presented. First, results obtained with modified blades will be given, followed by results for the double incursion rate tests.

8.4.1 Modified blade geometry tests

First, the post-test images of the abradable samples and blades, force and blade length results throughout a test are given for all the 6 tests to highlight the differences in the way forces grew throughout a test and blade wear occurred for the blades of modified tip geometry at different incursion rates. The post-test images of the abradable samples and blades are given in Fig. 8.9, force results in Fig. 8.10 and blade profile history maps in Fig. 8.11.

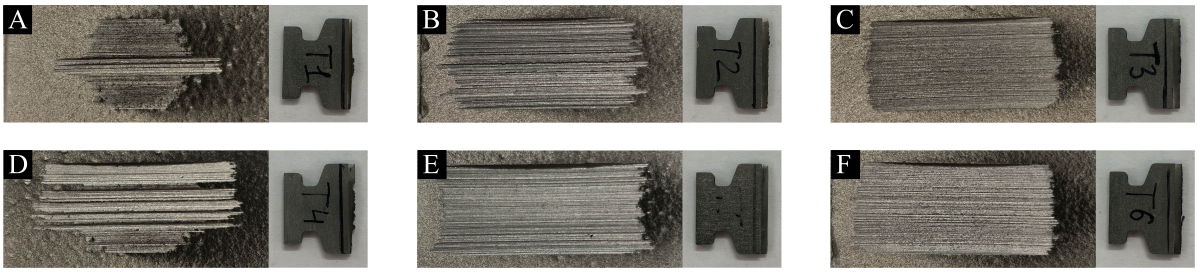

Fig. 8.9 The post-test images of the abradable samples and blades for the tests at 200m/s and a) 0.02µm/pass, b) 0.2µm/pass, c) 2µm/pass, for the tests at 280m/s and d) 0.02µm/pass, e) 0.2µm/pass, f) 2µm/pass.

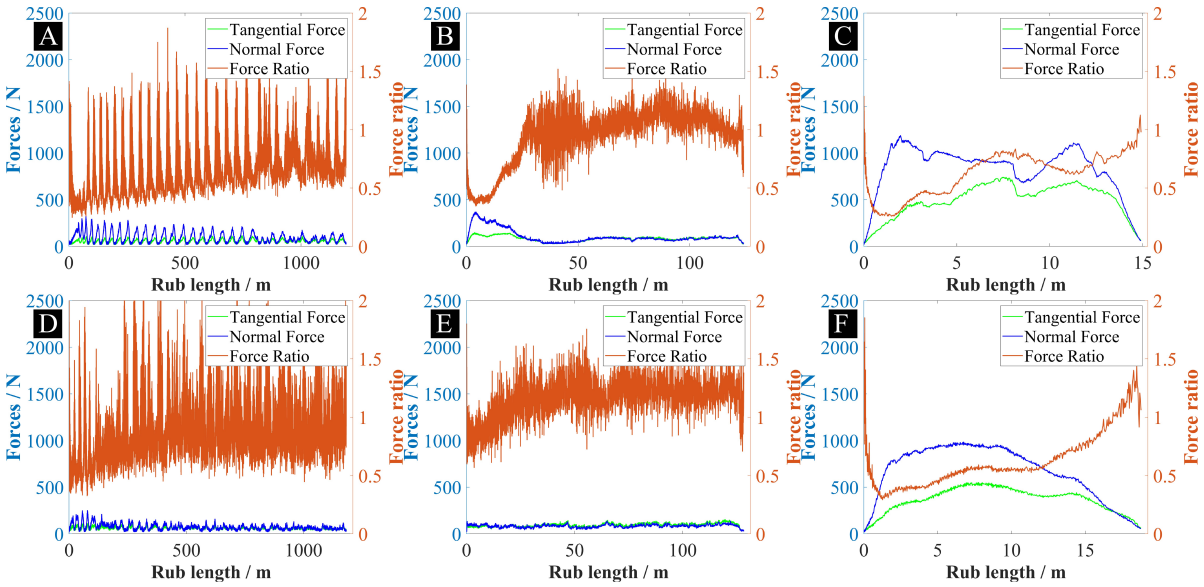

Fig. 8.10 The normal and tangential forces and force ratio throughout a test for the tests at 200m/s and a) 0.02µm/pass, b) 0.2µm/pass, c) 2µm/pass, for the tests at 280m/s and d) 0.02µm/pass, e) 0.2µm/pass, f) 2µm/pass.

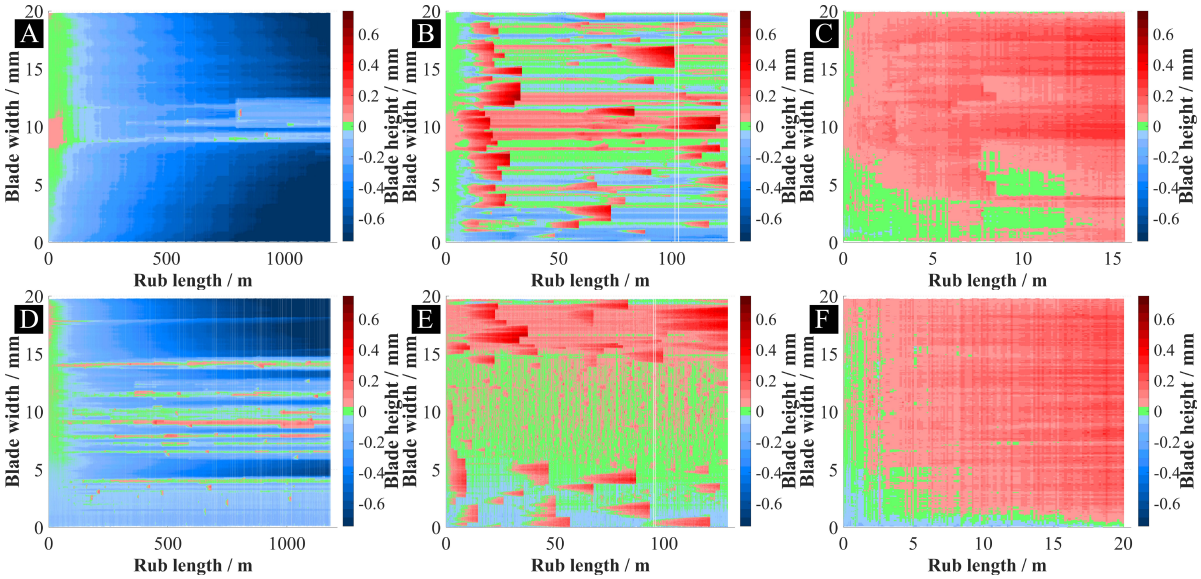

Fig. 8.11 The blade profile history maps for the tests at a) 0.02µm/pass for 500µm and 0.2µm/pass for 500µm, b) 0.02µm/pass for 500µm and 0.4µm/pass for 500µm, c) 0.2µm/pass for 500µm and 0.02µm/pass for 500µm, d) 0.4µm/pass for 500µm and 0.02µm/pass for 500µm, e) 0.2µm/pass for 1000µm and 0.02µm/pass for 500µm, f) 0.4µm/pass for 1000µm and 0.02µm/pass for 500µm.

The overall trend in results was similar to the standard flat blades used against AlSi-polyester abradables. At the lowest incursion rate of 0.02µm/pass some periodic behaviour in forces was observed, while at higher incursion rates of 0.2µm/pass and 2µm/pass forces were more consistent throughout a test. As can be seen in Fig. 8.10, at the lowest incursion rate of 0.02µm/pass there was a combination of blade wear and adhesions, at the incursion rate of 0.2µm/pass there was a small amount of blade wear, and adhesions occurred at most blade width locations, and at the highest incursion rate of 2µm/pass adhesions occurred along an entire blade width.

A significant amount of grooving can be seen for all of the abradable samples in Fig. 8.9, particularly for the tests at the 0.02µm/pass incursion rate shown in Fig. 8.9a and Fig. 8.9d. Such grooving occurred due to the presence of both adhesions and blade wear at this incursion rate. As can be seen in Fig. 8.11a, the amount of blade wear was the highest at the edges (where the blade was the thinnest), with it decreasing towards the middle of the blade. At the centre of the blade, adhesions formed, which stopped the blade wear and led to a deeper cut into the abradable sample. Such change in wear mechanism with an increase in blade thickness resulted in a heavily grooved abradable surface seen in Fig. 8.9a.

The increase in the likelihood of adhesion formation with an increase in blade width is consistent with the flash temperature concept used to explain the likelihood of adhesion

formation in chapter 5 as flash temperature increases with an increase in blade thickness. It is also interesting to note that for blade wear, at 0.02µm/pass much higher blade wear rate was observed in the tests with blades with a modified geometry than in the tests with flat blades at similar conditions. This was particularly evident at blade edges where the blades with a modified geometry had the lowest thickness. This is consistent with findings by Watson, where it was shown that blade wear increased with a decrease in blade thickness [6].

Some atypical behaviour was seen for two of the tests at 280m/s - at 0.02µm/pass and 0.2µm/pass. At blade width locations between 0mm and 4.5mm for the test at 0.02µm/pass and 5 and 15mm for the test at 0.2µm/pass, virtually no wear or adhesions can be seen. The result at 0.02µm/pass contradicts the previous findings on blade wear rates, where it was shown that rate increases with a decrease in blade tip thickness. Additionally, at the other blade edge (blade width locations between 15mm and 20mm) during the same test, a significant amount of blade wear occurred agreeing with the previous findings. Similarly, the result at 0.2µm/pass contradicts the previous findings where it was suggested that blade width should increase flash temperature and likelihood of adhesion formation.

It appears that results at these highlihgted blade width locations are outliers to the general trends seen in chapter 5 with flat blades and in this chapter. It was then suggested that the combination of a higher blade tip speed and deburring the blades after CNC machining of a modified geometry might have been enough to create locations where blade tips were sharp enough to trigger a cutting rather than rubbing mechanism.

8.4.2 Double incursion rate tests

First, the post-test images of the abradable samples and blades, force and blade length results throughout a test are given for all the 6 tests to highlight the differences in the way forces grew throughout a test and blade wear occurred for the tests with two incursion rates. The left half of each plot corresponds to the first incursion rate part and the right half of each plot corresponds to the second incursion rate part. The post-test images of the abradable samples and blades for all the tests are given in Fig. 8.12, force results in Fig. 8.10 and blade profile history maps in Fig. 8.11.

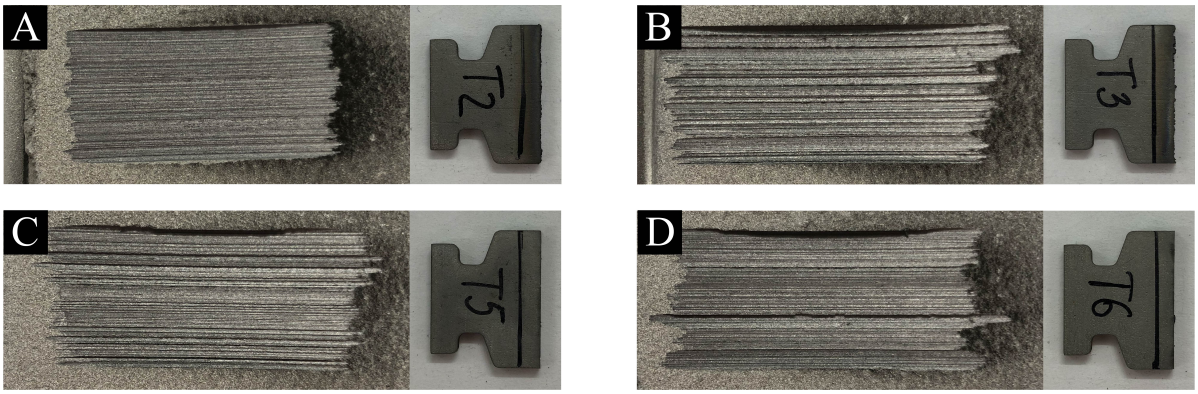

Fig. 8.12 The post-test images of the abradable samples and blades for the tests at a) 0.02µm/pass for 500µm and 2µm/pass for 500µm, b) 0.02µm/pass for 500µm and 0.2µm/pass for 500µm, c) 2µm/pass for 500µm and 0.02µm/pass for 500µm, d) 2µm/pass for 500µm and 0.2µm/pass for 500µm.

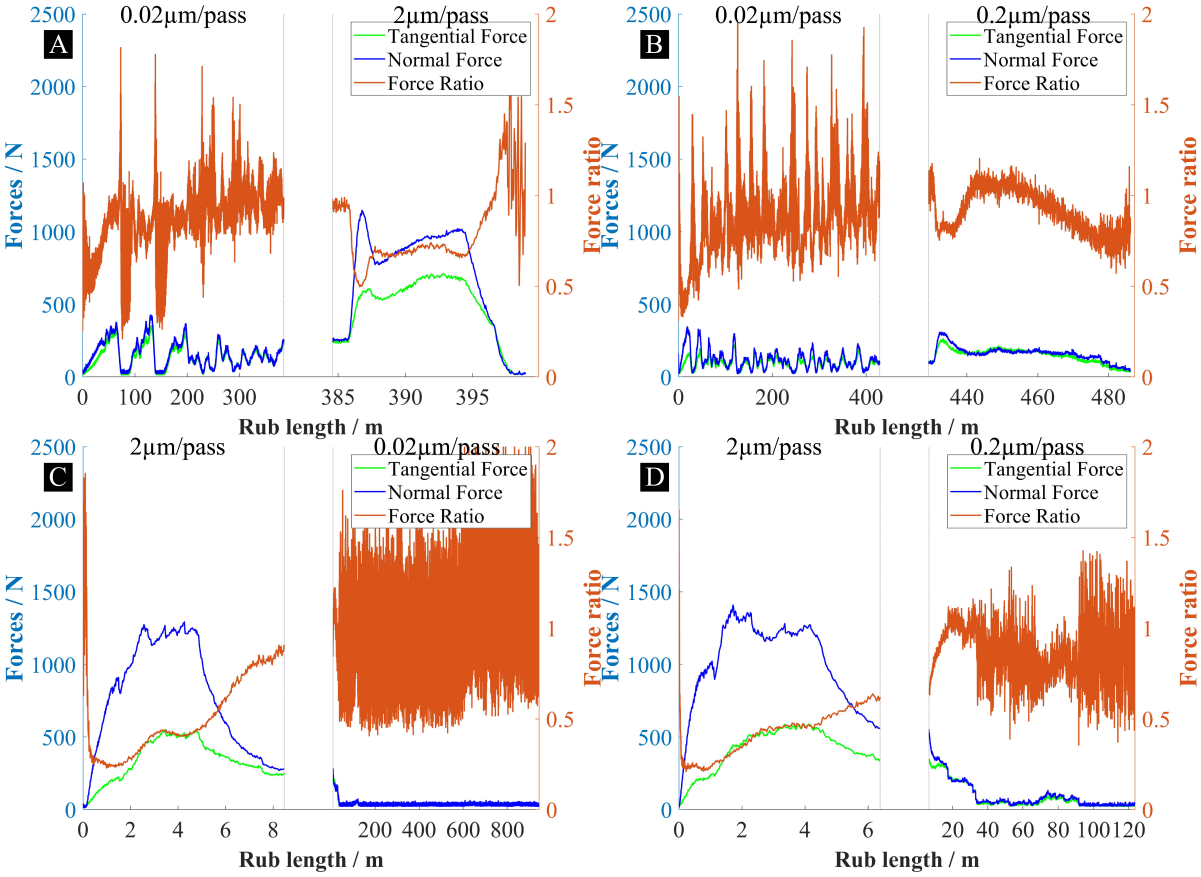

Fig. 8.13 The normal and tangential forces and force ratio throughout a test for the tests at a) 0.02µm/pass for 500µm and 2µm/pass for 500µm, b) 0.02µm/pass for 500µm and 0.2µm/pass for 500µm, c) 2µm/pass for 500µm and 0.02µm/pass for 500µm, d) 2µm/pass for 500µm and 0.2µm/pass for 500µm.

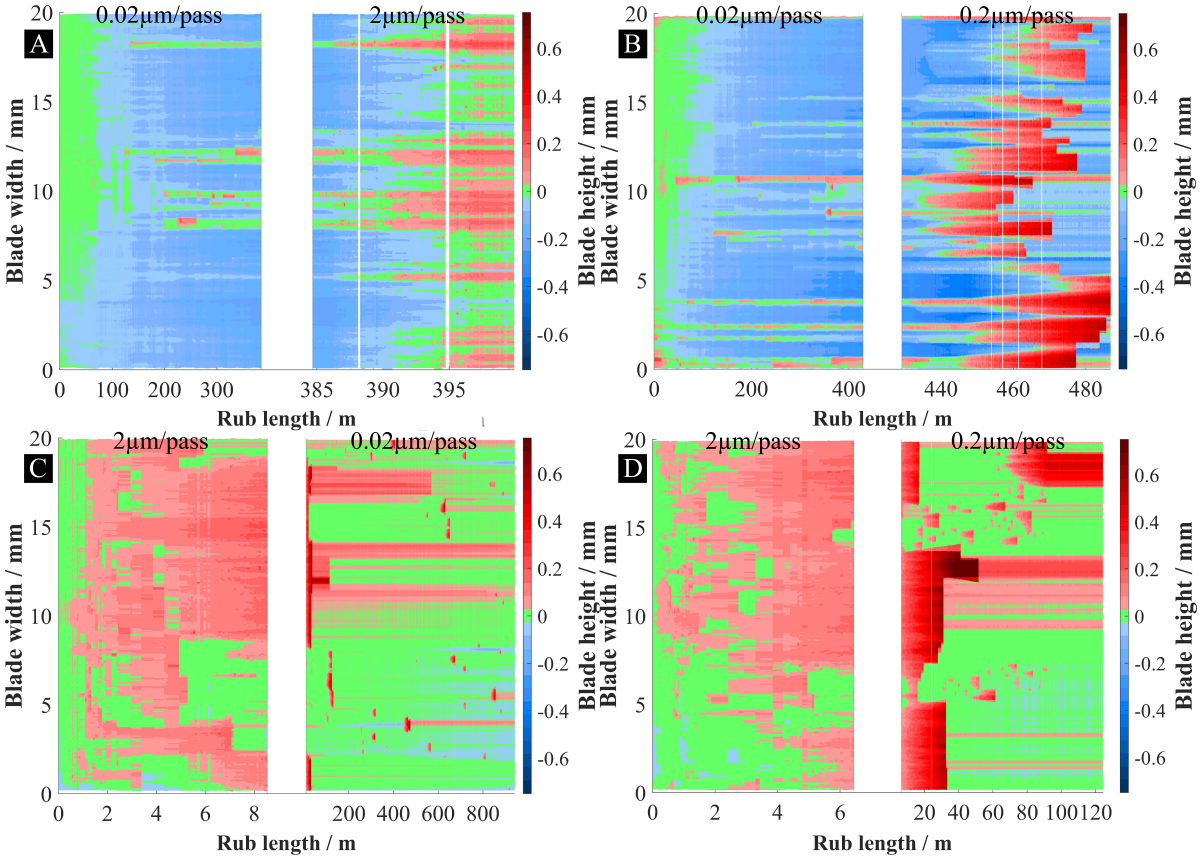

Fig. 8.14 The blade profile history maps for the tests at a) 0.02µm/pass for 500µm and 2µm/pass for 500µm, b) 0.02µm/pass for 500µm and 0.2µm/pass for 500µm, c) 2µm/pass for 500µm and 0.02µm/pass for 500µm, d) 2µm/pass for 500µm and 0.2µm/pass for 500µm.

As can be seen from Fig. 8.12, the post test abradable samples once again demonstrate a significant level of grooving as was the case for all the test with AlSi-polyester abradables performed for this thesis.

From Fig. 8.14 it can be seen that starting with the 2µm/pass incursion had more influence on test outcomes at subsequent incursion rates than starting with the 0.02µm/pass incursion rate. For the tests that started with the 0.02µm/pass incursion rate (Fig. 8.14a and Fig. 8.14b), it can be seen that parts at 2µm/pass and 0.2µm/pass experienced similar wear mechanisms to the ones that occur at these incursion rates if an entire test is performed at such incursion rate. At 2µm/pass (the right part of Fig. 8.14a) adhesions started forming at the entire blade width, while at 0.2µm/pass (the right part of Fig. 8.14b) adhesions formed at most blade width locations.

Interestingly, in Fig. 8.14b it can be seen that at blade width locations where adhesions existed during the 0.02µm/pass part, adhesions continued or initiated earlier during the 0.2µm/pass

part than at blade width locations where there was blade wear the end of the 0.02µm/pass part (for example around the 5mm blade width location).

When the starting incursion rate was 2µm/pass, several things were observed. In locations where adhesions existed at the the end of a 2µm/pass part, they continued growing during both the 0.02µm/pass (Fig. 8.14c) and 0.2µm/pass (Fig. 8.14d) parts until they fractured. At blade width locations where there were no adhesions at the end of a 2µm/pass part, the amount of blade was significantly reduced for the 0.02µm/pass part and the size of the forming adhesions reduced for the 0.2µm/pass part (for example around the 15mm blade width location in Fig. 8.14d). It can also be seen in Fig. 8.13c that forces were lower and no periodic behaviour was observed for the 0.02µm/pass part when it was after the 2µm/pass part.

8.5 Discussion

The results in this chapter allowed to further explore the effects simplifications used on the scaled test rigs have on test outcomes. The effects of using blades with a variable chord thickness rather than a fixed thickness and using a variable incursion rate rather than a single incursion rate were explored on the example of two abradable materials: NiCrAl-bentonite and AlSi-polyester.

The influences of using blades with a variable chord thickness are going to be discussed first, followed by the discussion of results from the double incursion tests.

8.5.1 Effect of using modified blades

In the tests with modified blades against NiCrAl-bentonite abradable there were clear similarities with the results obtained with flat and angled blades but also some differences. Firstly, the general trend in results was similar to the tests with flat blades. The low-force contact mode was observed for the tests at the low incursion rate of 0.02µm/pass and the high-force contact mode was observed for the test at the higher incursion rates of 0.4µm/pass and 0.6µm/pass.

Additionally, the ratio of maximum normal force to the average blade thickness was consistent with the results obtained with the flat and angled blades. While it was not possible to establish the effect of using a modified blade geometry on the transition incursion rate due to the use of a different batch of samples preventing back to back comparison to the results obtained with flat blades in chapter 6, it was clear that the contact modes themselves were similar with the flat blades.

The key difference found in this study was the increased amount of blade wear at the blade edges for the blades with modified geometry in comparison to 2mm thick flat blades.

This highlighted the importance of considering the edge effects and that such effects can be exacerbated by the low blade edge thickness as was the case for the blades with modified geometry.

Interestingly the increased amount of blade wear at the edges for this type of blades can offer a potential explanation to the anecdotal evidences obtained by Rolls-Royce plc. that in aero-engines there is an increased amount of NiCrAl-bentonite abradable compaction at the locations corresponding to the centre of a blade than to the blade edges [60].

Such decrease in compaction at the blade edges can be explained by combining the observations made about the edge effects with the contact modes hypothesis presented in chapter 6. If the incursion rate during a test is higher than the rate at which an abradable can fracture, forces go up leading to transition to the high-force contact mode and triggering some blade wear. If the blade wear cannot accommodate enough of the incursion rate to stabilise the forces, a further increase in forces can occur leading to compaction. The higher temperature at the edges allows faster rate of blade wear, particularly for the blades with a small thickness at the edges as shown in this chapter. That faster wear rate then allows to accommodate more of the incursion rate through wear decreasing the amount of incursion rate that needs to be accommodated through abradable compaction.

Similarly, for the tests against AlSi-polyester abradables, clear similarities were observed with the results obtained with flat blades. The incursion rate was the dominant factor in determining what wear mechanism occurred, which agrees with previous results in this work and in the study by Watson [51] obtained using flat blades.

However, there were still some important observations. There was an increase in the likelihood of adhesion formation with an increase in blade tip thickness providing further evidences to the importance of flash temperatures for formation of adhesion as flash temperature increase with an increase in the width of a moving surface [59].

On the other hand, results for some sections of a blade at 280m/s and 0.02µm/pass (at blade width locations between 0mm and 4.5mm) and 0.2µm/pass (at blade width locations between 5mm and 15mm) were in disagreement with previous results. It appears that at those location a different type of a contact mode occurred, which was not previously observed in contact with AlSi-polyester abradables at the incursion rates considered in this chapter. The low amount of blade wear or adhesions at both incursion conditions in respective blade width locations suggest that the contact mode could have been cutting. However, the evidences in this chapter are insufficient for a definite conclusion on the contact mode and further research in this area is required.

8.5.2 Double incursion rate tests

The tests with two incursion rates allowed to explore how the presence of a variation in incursion rates experienced by an abradable throughout engine life-cycle can affect outcomes of individual incursion events.

For the NiCrAl-bentonite abradables it was that seen that starting with a low incursion rate (0.02µm/pass) did not have a detrimental effect on subsequent incursion conditions, while starting at a higher incursion rate (0.2µm/pass or 0.4µm/pass for tests in this chapter) led to increased contact forces for a subsequent incursion at 0.02µm/pass.

It was also shown that the rub depth at a higher incursion rate had an influence as forces for the incursion section at 0.02µm/pass were progressively higher from starting a test at 0.02µm/pass to having the 0.02µm/pass section after 500µm at a higher incursion rate to having the 0.02µm/pass section after 1000µm at a higher incursion rate.

Interestingly, in the previous study by Watson [51] it was shown that at incursion rates close to the values used in this chapter (0.2µm/pass) no measurable large scale compaction of abradable was observed despite blade wear and high contact forces (levels of compaction in that study were measured from post-test SEM images of sectioned tested abradable samples). However, there were some evidences that some local compaction occurred at abradable surfaces at incursion rates as low as 0.02µm/pass for the harder batches.

The results in this work indicate that there was a detriment in the overall abradable fracture efficiency after rubbing at incursions rates above transition (0.2µm/pass and 0.4µm/pass in this work) inferred from increased forces for the 0.02µm/pass incursion parts. This detriment could have been due to such local abradable surface compaction introduced by rubbing at a higher incursion rate identified in the work by Watson [51]. Such detriment could have also been caused by the damage to the blade contacting surface due to blade wear leading to a decrease in a blade's ability to fracture an abradable surface. It will be possible to decouple the these effects by rubbing a worn blade against a previously untested abradable surface at 0.02µm/pass and comparing contact forces to the results from the double incursion tests.

Overall, these results are important for further understanding of effects of incursion rates used during running and handling on incursion event outcomes. While the study by Watson [51] highlighted the dangers of using very high incursion rates(2µm/pass) during running and handling due to them causing significant levels of abradable compaction, results in this work demonstrated that rubbing even at lower incursion rates (0.2µm/pass and 0.4µm/pass) can also have a detrimental effect on wear mechanisms at subsequent lower incursion rates that can be expected during normal in-flight conditions (0.02µm/pass).

While for the tests in this chapter, despite an increase, the forces were still low enough at 0.02µm/pass not to cause further blade wear, for harder abradable batches, such decrease

in abradable fracture efficiency after a section at a higher incursion rate can be sufficient to cause transition to the high-force contact mode to occur even at the 0.02µm/pass incursion rate potentially leading to further blade wear.

For the AlSi-polyester abradable, a section at 0.02µm/pass had only a small influence on subsequent sections at 0.2µm/pass and 2µm/pass. A section at 2µm/pass, however, led to a difference in wear mechanisms observed at subsequent sections at 0.02µm/pass and 0.2µm/pass.

While the exact mechanism through which such a difference occurred is not fully understood, this results is important in understanding the effects of high incursion rates used during running and handling on subsequent incursion events. While the decrease in blade wear at 0.02µm/pass was desirable, the continuation of adhesion growth in locations where adhesions existed at the end of a 2µm/pass part could be undesirable due to these adhesion leading to grooving of abradable surfaces. The fracture of these adhesions also leads to the formation of gaps between a blade and an abradable as was demonstrated in chapter 5 by comparing blade profiles with post-test abradable surface measurement done using Alicona.

8.5.3 Implications on testing of abradable materials

Finally, it is important to discuss the importance of findings in this chapter on understanding the results obtained from simplified tests on experimental rigs in the context of their applicability to aero-engines.

For the NiCrAl-bentonite abradables, it was shown that despite the edge effect being more significant for blades with a variable chord thickness, the overall trend in results was similar between such and flat blades, highlighting that representative results can be obtained with flat blades. Similarly, despite some differences between the blades with a variable chord thickness and flat blades for tests with AlSi-polyester abradables, overall trends were similar, and representative results can be obtained with flat blades.

For both types of abradable, running at a higher incursion rate was seen to influence the wear mechanisms seen at subsequent lower incursion rates. This highlighted the importance of understanding the running and handling conditions and the effects they can have on subsequent incursion events. The potential effects of running and handling incursion conditions then need to be accounted for when comparing results obtained from single incursion rate tests on experimental test rigs to wear mechanisms observations made in actual aero-engines.

8.6 Conclusions

The influences of two simplifications used in scaled rig tests on test outcomes were explored on the example of two abradable materials: NiCrAl-bentonite and AlSi-polyester. This was achieved by performing a total of 22 tests; 12 of them were with NiCrAl-bentonite abradable samples, with 6 each with blades with a variable chord thickness and with double incursion rates; 10 of them were with AlSi-polyester abradable samples with 6 tests with blades with a variable chord thickness and 4 tests with double incursion rates.

It was found that both of the explored test conditions modifications had an influence on test outcomes in comparison to tests with simplified conditions. The effect of blades with a variable chord thickness on test outcomes was less important than that of using double incursion rates. By using blades with a variable chord thickness it was found that with such blades, edge effects were more significant in tests with NiCrAl-bentonite abradable samples. In tests with AlSi-polyester abradable samples, blade thickness variation had an influence on the likelihood of adhesion formation, which was expected based on the influence of flash temperatures on adhesion formation suggested in chapter 5, and blade wear rates were higher at 0.02µm/pass than those observed with flat blades tested at similar conditions, which was likewise expected based on the results obtained by Watson for blades with a lower constant blade thickness [6].

For double incursion rate tests, it was found that for both considered abradable materials, a section at a lower incursion rate had only a small influence, while a section at a higher incursion rate influenced the wear mechanisms at subsequent incursion rates. For NiCrAl-bentonite abradable samples, a decrease in abradable fracture efficiency was observed after a section at a higher incursion rate, with an increase in rub depth at a higher incursion rate increasing the detrimental effect on abradable fracture. For AlSi-polyester abradable samples, it was seen that contact forces and the amount of blade wear decreased at 0.02µm/pass after a section at a high incursion rate of 2µm/pass. For both incursion rates of 0.02µm/pass and 0.2µm/pass adhesions continued growing until they fractured after a section at 2µm/pass at blade width locations where adhesions existed at the end of a 2µm/pass section.

Chapter 9

Discussion

One of the first studies on abradable materials was undertaken by Borel et al. [25], where representative aero-engine wear mechanisms were achieved on a full-scale testing rig for a range of different abradable materials and blade combinations. The analysis in that work was based on post-test observations of blade and abradable wear scars and the observed wear mechanisms were related to testing conditions and how the material properties drove these mechanisms. Following this work, various authors [46, 53, 40, 41, 38, 44, 51] have investigated different abradable and blade material combinations focusing on improvements in classification of wear mechanisms as well as developing techniques to gain further insights into how these mechanisms occur. This work makes a contribution in both areas.

The advancements in experimental methods and how they contributed to the improved knowledge of abradable materials are going to be discussed first. Then, the abradable wear mechanisms and how abradable material properties impact these mechanisms will be discussed. Finally, an overview of how the understanding of wear mechanisms can be used to improve contacts between aero-engine blades and abradable materials will be given.

9.1 Advancements in experimental methods

Following the initial work by Borel et al. [25], authors have sought to improve data capture to gain more insights into wear mechanisms. This was achieved through a number of different approaches. Multiple authors have used contact force and temperature measurements to guide the discussion of wear mechanisms [47, 43, 51]. For example, in the work by Watson et al. [51] the correlations between testing parameters and contact forces and temperature measurements were used to verify the wear mechanisms suggested for the AlSi-polyester and NiCrAl-bentonite abradables. In the work by Fois [41] the side-on stroboscopic measurement system was developed to measure the maximum blade length throughout a test, which was

an improvement on the post-test blade length and weight measurements used by multiple authors [25, 46, 40, 38, 44] and allowed to improve the understanding of the adhesion wear mechanism. However, as noted in the literature review, there were still a number of limitations to the blade length measurements techniques. By measuring from the side, it wasn't possible to tell at what exact position along the blade width adhesions occurred, if there were only one or multiple different adhesions on a blade along its width at any given time or if blade wear occurred at other blade width locations.

In this work, this limitation for classifying the adhesion and blade wear mechanisms was addressed through the development of the front-on stroboscopic imaging system, where the entire blade width was seen. For tests with NiCrAl-bentonite abradable samples, only little improvements in wear classification were achieved – better understanding of edge effects on blade wear – as blade wear was usually progressive and uniform across most of blade width locations. However, for tests with AlSi-polyester abradable samples, this system was shown to be fundamental for better understanding of the blade wear and adhesion mechanisms.

Through the use of the front-on imaging system it became possible to compare blade wear rates at different blade width locations within a single test, perform comparisons of blade profiles that included fractured adhesions to post-test abradable surface measurements obtained using Alicona to identify the importance of such fractures on formation of gaps between blades and abradable samples, understand what proportion of a blade is covered in adhesions at different testing conditions and how these testing conditions influenced the average values of adhesion rates and heights.

In addition to the development of the front-on stroboscopic system for blade length measurements, improvements in the post-processing of force results were introduced that allowed better understanding of wear mechanisms of both types of abradable materials considered in this study. Accurate representation of how force values progressed throughout a test were important for tests with NiCrAl-bentonite abradable samples as normal force values were correlated to how effectively an abradable surface was fracturing and allowed a clearer understanding of the transition between the two contact modes. Likewise, for tests with AlSi-polyester abradable samples, the comparisons of force results at different conditions were used for the explanation of the likelihood of adhesion formation at different conditions through the effect of contact forces on flash temperatures.

These improvements in data acquisition and analysis methods has allowed further insights into the wear mechanisms observed in contacts with abradable materials and allowed to consider them as a class of materials going through the engine. In the next section, the findings in this work will be combined with results from the past research to give an overview of the wear mechanisms observed with abradable materials used in aero-engine compressor stages.

9.2 Abradable wear mechanisms

Going back to the work by Borel et al. [25], that work attempted to bring a more fundamental level of understanding of the types of wear mechanisms that occur in contacts with abradable materials by analysing the abradable materials that were run in-service. In the same work, first abradable wear maps were created from the tests on a full-scale rig correlating testing parameters and wear mechanisms (what wear mechanism occurs based on the testing parameters) for two AlSi-based abradables. In the later work by multiple researchers the understanding of relationships between testing parameters and wear mechanisms was further improved. As such, in the work by Bounazef et al. [46] the wear mechanisms occurring in contacts with the AlSi-hBN abradable were further investigated. Additionally, in the work by Fois et al. [42], abradable hardness was shown to influence wear mechanisms in contacts with the AlSi-hBN abradable, leading to the creation of a more detailed wear map for such abradable. Similarly, the understanding of the influences of different testing parameters on wear mechanisms in contacts with the AlSi-polyester abradable [38, 51, 52] and NiCrAl-bentonite abradable [53, 51] were investigated by multiple researchers.

In this work, the understanding of contacts with the AlSi-polyester and NiCrAl-bentonite abradables was further improved, but in addition the new insights into these types of contacts have allowed to look at wear mechanisms occurring in contacts with abradables as a class of materials, something that was attempted in the work by Borel et al. [25]. In this section, first, the wear mechanisms occurring with individual types of abradable materials will be discussed, followed by a more general overview of wear mechanisms occurring in contacts with abradables.

In agreement with past research, in this work it was seen that the wear properties observed in contacts depend heavily on blades and abradables material properties. For example, adhesion and blade wear mechanisms were observed with AlSi-polyester abradable, and only blade wear mechanism with NiCrAl-bentonite abradable. Such a difference in adhesion formation was likely due to much higher density and melting temperature of Ni-based alloys than that of Al-based alloys. The material properties also heavily affected how different testing parameters influenced wear mechanisms. A clear example of that is the difference in the way the incursion rate influenced test outcomes in contact with AlSi-based and NiCAl-bentonite abradables.

In AlSi-polyester and AlSi-hBN abradables, the removal of abradable at low incursion rates (0.02µm/pass) was inefficient. The starting contact forces were not very high and adhesions occurred at some but not all blade width locations. Where adhesions did not occur, blade wear or abradable compaction (compaction was seen for the AlSi-hBN abradable [42]) occurred.

With an increase in incursion rate, the starting contact forces increased, leading to the increased amount of adhesion formation for the AlSi-polyester abradable as seen in this work for

tests at 0.2µm/pass and 2µm/pass. The transfer of an abradable to a blade prevented compaction of an abradable surface. The formation of adhesions was still however an undesirable wear mechanism as it led to grooving of an abradable surface and formation of gaps between a blade and an abradable after the fracture of these adhesions. For the AlSi-hBN abradable, previous research has shown that cutting mechanisms can occur with an increase in incursion rate (cutting was observed at the incursion rate of 2µm/pass in the work by Fois [42]) preventing blade wear and the formation of adhesions.

In tests with the NiCrAl-bentonite abradable a different trend was observed. The abradable material in this type of contact was removed through accumulation of damage on an abradable surface and subsequent surface fracture as suggested by Watson [51]. At low incursion rates, repeated blade strikes promoted accumulation of surface damage leading to efficient abradable removal. At the higher incursion rates, fracture could not keep up with the incursion rate and blade wear initiated accommodating part of the incursion rate. In the work by Watson [51], where very high incursion rates (2µm/pass) were also considered, at such high incursion rates blade wear was not fast enough to accommodate the difference in incursion rate and abradable surface fracture, and the remainder of the incursion rate was accommodated through abradable surface compaction due to very high contact forces.

It can be seen that for both materials inefficient abradable surface removal resulting in surface compaction could occur. However, for AlSi-based abradables it occurred as a result of low incursion rates, where abradable surface was not removed through either transfer of an abradable to a blade or through cutting, and for NiCrAl-bentonite abradable it occurred at very high incursion rates as a result of inefficient fracture of an abradable surface.

9.2.1 The wear mechanisms as a function of incursion accommodation mechanisms

Bringing these results together, it is possible to start building a framework for understanding the wear mechanisms as a function of abradable and blade materials properties and testing parameters and look at abradables as a class of materials as was attempted in the work by Borel et al. [25]. As seen above, the way the incursion rate is accommodated plays a significant influence on wear mechanisms. In the tests with abradable materials the following incursion accommodation mechanisms were observed in this and previous works: cutting of abradable [46, 41], adhesion and abrasion due to rubbing [46, 51, 52], abradable surface fracture due to rubbing [51], and abradable surface compaction due to rubbing [51].

The cutting mechanisms was seen to lead to the best test outcomes for abradable materials that can be cut such as AlSi-hBN abradables tested at high incursion rates as was shown by

Fois [42]. For strong brittle materials such as NiCrAl-bentonite, cutting mechanism was not observed at the incursion rates experienced by abradable materials in aero-engines and rubbing was always observed.

When rubbing occurred, the incursion accommodation mechanism depended primarily on the incursion rate, and abradable and blade properties. For softer materials such as AlSi-based abradables, the incursion was accommodated through either adhesion of an abradable to a blade (abradable surface removed efficiently) due to abradable temperatures getting high enough or through a combination of abrasion of both an abradable surface and a blade.

The blade wear occurred as a result of the abrasion mechanism due to high heat generation in the system during rubbing in locations where adhesions did not form as could be seen from the results shown in chapter 5 for AlSi-polyester abradable samples tested at 0.02µm/pass. The amount of blade wear depended on the relative abrasion rates for a blade and an abradable, which were dependent on secondary parameters such as relative hardness, thermal properties of a system (the heat partition between a blade and an abradable, and the heat removal rates from an abradable and a blade), and blade thickness (chapter 8). For the AlSi-hBN abradable similar trends were observed, however, with a more significant amount of compaction occurring as a result of rubbing as was shown in the work by [42] than what was observed for the AlSi-polyester abradable in this work in chapter 5.

When rubbing occurred for hard brittle abradables, the amount of abradable material removed through abrasion was minimal. The adhesion mechanism also did not occur in tests with NiCrAl-bentonite abradable samples. The incursion rate was then accommodated either through abradable surface fracture due to repeated blade strikes, through abrasion of a blade or through compaction of an abradable surface.

The abradable surface fracture was identified as the desirable mechanism as it led to the lowest contact forces and as a result the lowest blade wear. Such fracture mechanism was possible because of the microstructure of the NiCrAl-bentonite abradable with high levels of porosity and high surface roughness. When the rate of abradable fracture was lower than the incursion rate, transition to the high-force contact mode occurred leading to the initiation of the thermally driven blade wear (chapter 6). At very high incursion rates compaction could occur with it being progressive as compaction led to harder surface layer leading to even higher contact forces [51].

This framework of considering the incursion accommodation mechanisms and the resultant wear mechanisms is summarised in Fig. 9.1.

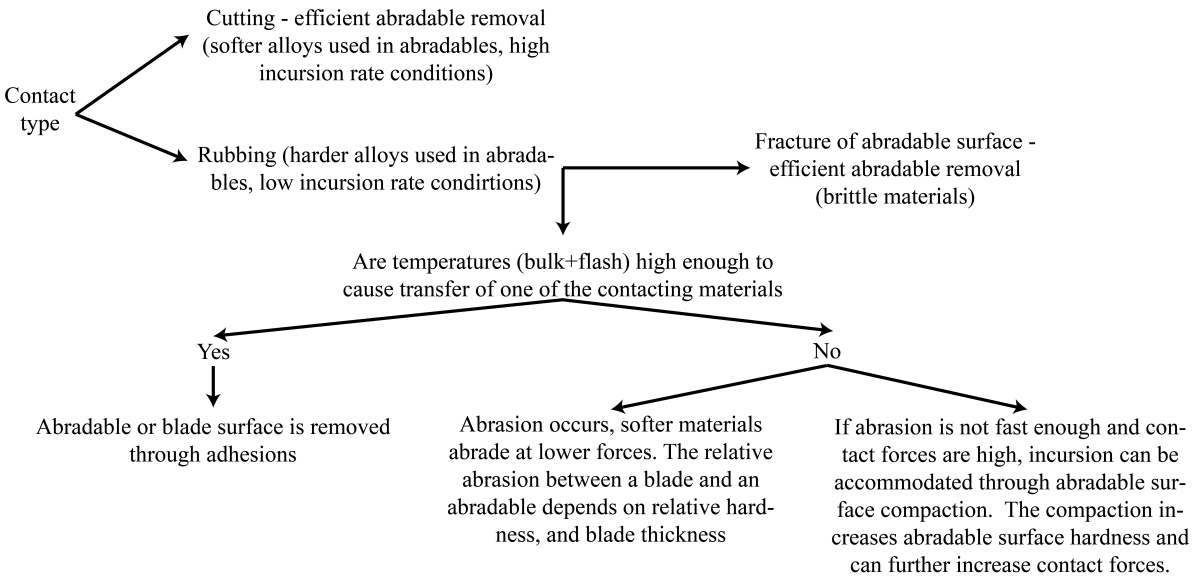

Fig. 9.1 The summary of the incursion accommodation and resulting wear mechanisms.

9.3 Improvements to abradable materials

In this section, potential areas for improvements will be suggested in relation to desirable incursion event outcomes: low amount of blade wear or abradable grooving.

It can be seen in Fig. 9.1 that despite large differences in microstructure, abradable materials can be considered through the same framework by combining the understanding of incursion accommodation mechanisms and wear mechanisms that occur as a result. It was shown that cutting and abradable surface fracture were the desirable incursion accommodation mechanisms leading to the lowest amount of wear in contacts. The question then becomes if it is possible to activate these incursion accommodation mechanisms at all of the incursion conditions experienced by abradable materials in aero-engines.

The research in this work has shown that there is a potential to achieve this for materials such as NiCrAl-bentonite where abradable surface fracture occurs. It was shown that the limiting factor for this incursion accommodation mechanism is the maximum incursion rate at which the rate of surface fracture can keep up with the incursion. It is then possible to optimise the performance in two ways: increasing the effectiveness of abradable fracture and by limiting the maximum incursion rate experienced by an abradable material. As discussed in chapters 6 and 7, the rate of abradable fracture can be improved by decreasing abradable hardness, using stiffer blades or introducing the angled tip shape to less stiff blades. The minimum hardness is limited by erosion resistance requirements and so needs to be considered in conjunction with that design requirement.

However, even if by optimising all of the factors, it is not possible to achieve effective abradable fracture at all incursion rates experienced during engine operation, the improvements in fracture still result in improved outcomes at two incursion accommodation mechanisms that occur when fracture is not fast enough to keep up with incursion rate: abrasive blade wear and abradable surface compaction. This is important as it shows that improvements in fracture improve performance at all of the considered conditions without a trade-off. Additionally, the maximum incursion rate experienced by an abradable can be somewhat controlled by controlling the maximum incursion rate during the running and handling procedure minimising the amount of damage introduced to a blade and an abradable. There is less control over incursion rates occurring during in-flight conditions, but they are generally lower than incursion rates used during the running and handling procedure.

This decreased control over in-flight incursion rates is what created a challenge for abradable materials, where cutting is the desired incursion accommodation mechanism, as this mechanism was limited primarily by the low, not high incursion rates, when it was observed, for example, for AlSi-hBN abradable [42]. Unless, a solution to promote cutting at all the incursion rates is found by modifications to abradable microstructure or blade tip design, the consequences of the rubbing mechanism need to be considered. As discussed in the previous section, three incursion accommodation mechanisms occurring as a result of rubbing were observed in contacts with AlSi-based abradable materials: adhesion of abradable to a blade, abrasion of blade and abradable surfaces and abradable surface compaction.

From the results in this thesis it was seen that when the adhesion of an abradable to a blade occurred, an abradable surface was removed effectively preventing blade wear or abradable surface compaction. However, the probabilistic nature of adhesion formation led to very non-uniform blade tip surfaces, particularly for test conditions where simultaneous blade wear and formation of adhesion occurred (chapter 5) resulting in heavily grooved abradable surface.

It was suggested based on the results in this work that adhesion mechanism occurs as a result of high abradable temperatures due to the combination of abradable bulk temperature and contact flash temperatures. The adhesions could then be decreased by decreasing the contact temperature of an abradable, which can be achieved by increasing melting point, thermal conductivity, density, and specific heat capacity of an abradable based on the flash temperature equation. Additionally, there might be some potential in decreasing the size of adhesions or preventing them by reducing the strength of adhesion bonding to a blade surface through blade material or surface modifications. If the maximum size of adhesions is significantly reduced, this mechanism could be used for improving test outcomes as during it the abradable surface is removed effectively and no blade wear occurs.

If the adhesions did not form, the two mechanisms activated during rubbing against AlSi-based abradables were the abrasion and abradable surface compaction. To minimise the severity of compaction and blade wear, the abrasion of abradable surface needs to be improved. This could be achieved by using softer abradable materials, but once again as it was the case with NiCrAl-bentonite abradable at the expense of erosion resistance. It should also be noted that if the adhesion mechanism is stopped, the severity of the abrasion and abradable compaction mechanisms could be significantly increased at higher incursion rates (such as 0.2µm/pass and 2µm/pass for the AlSi-polyester abradable) where previously adhesions formed.

It appears that the best case scenario for an AlSi-based abradable would occur if the adhesion mechanism occurs at all incursion rate conditions with the maximum size of adhesions significantly reduced or through a combination of cutting mechanism at medium and high incursion rates (0.2-2µm/pass) and removal of abradable surface through abrasion at low incursion rates. Based on the current results and knowledge of wear mechanisms, the second approach appears to be more achievable, however, further research in promoting the cutting mechanism and minimising the likelihood of adhesion formation is required.

Lastly, the potential of using the controlled compaction for improving test outcomes is going to be explored. For the abradable materials considered up to now such as AlSi-based and NiCrAl-bentonite abradables the compaction is undesirable as it occurs on the surface leading to an increase in forces and significant blade wear or at extreme conditions abradable surface rupture. The use of a foam material with a highly porous structure designed to accommodate large amounts of compaction with an abradable coating sprayed on top of a foam to provide the required sealing could offer potential for using compaction as an effective incursion accommodation mechanism.

However, there are a number of challenges associated with such abradable system design (foam + abradable coating on top). It was shown in this work that compaction occurs as a result of inefficient abradable removal mechanism. To activate the compaction in a foam, rubbing with significant normal forces may be required. For abradables such as AlSi-polyester this might result in the same problem - adhesion formation due to large rubbing forces.

However, there is a potential use case for abradables, where abrasion with abradable compaction mechanisms occur. During these incursion accommodation mechanisms high normal forces occur as abradable surface is not removed effectively. Then, part of the incursion rate could then be accommodated by a foam resulting in a compaction of the foam structure rather than the abradable itself, which has a potential for reducing the severity of abrasive blade wear and abradable compaction mechanisms.

While such use case appears plausible, there is still a large number of unknowns regarding the use of foam structures: finding the balance between the strength of a foam to prevent

its fracture and failure and its compactability, or the possibility of spraying brittle abradable coatings such as NiCrAl-bentonite on the foams with them forming a stable layer.

9.3.1 Summary

The current knowledge on wear mechanisms and how they are related to the ways incursion rate is accommodated in contacts between blades and abradable samples were discussed in this chapter. A framework summarising these relations was made based on the findings in this work and previous research on abradable materials.

The areas for potential improvements to the ways abradable materials are used were then suggested based on potential modifications that could promote the occurrence of the desirable incursion accommodation mechanisms and improve test outcomes when undesirable ones occur.

It was shown that the incursion accommodation mechanisms undesirable in contacts with current abradable materials like the adhesive transfer from an abradable to a blade or abradable surface compaction could be used to promote better test outcomes. For adhesions, the ability to effectively remove abradable surface could be of benefit if the maximum size of adhesions is significantly decreased. For compaction, it could be effectively used for reducing the amount of abradable surface compaction by using a foamed structure underneath that could compact under lower normal forces that the abradable with the ability to accommodate large amounts of compaction.

Chapter 10

Conclusions

The key aim of this work was to improve the understanding of contact mechanics between blades and abradable materials used in compressor stages of aero-engines. To achieve this aim, a new high-speed rig was commissioned and instrumented, front-on stroboscopic imaging system installed and a number of data processing methods developed to increase the fidelity of data collected during tests. Then, a series of tests were performed to improve the understanding of contacts with AlSi-polyester and NiCrAl-bentonite abradables. The key outcomes of this thesis are highlighted below:

- A representative test rig was commissioned and instrumented, which currently has a capability to achieve speeds of up to 280m/s with the aim of achieving engine representative speed of 400m/s in the future. This enabled the capability of testing at higher speeds than was previously possible on the low-speed rig, which is limited to 200m/s.

- The design of the front-on imaging system was finalised and the system was installed on the high-speed rig. A referencing method was developed to correct for blade variations in plane due to variation in the angle at which a blade image was captured due to uncertainty in the detection of reflection from the reflective tape (strobe triggering). Later in this work, the uncertainty in the reflective tape detection was solved through the installation of a different reflective sensor with a separate amplifier, and referencing was kept in place as a data checking tool rather than a major post-processing step.

- The post-processing of normal force data was improved through correcting the thermal drift that was affecting the data. This allowed better understanding of how normal forces evolved during a test, particularly for long tests at low incursion rates such as 0.02µm/pass as they were the most affected by the thermal drift. This also enabled an easier comparison of forces between tests at different incursion rate conditions.

- The post-processing methods for the analysis of images obtained using the front-on stroboscopic system were developed including the extraction of individual blade profile from each image, plotting these profiles as blade profile history maps, creation of blade profiles that considered how deep fractured adhesions would have rubbed into an abradable sample for comparisons with post-test abradable surface measurements using Alicona, and calculation of adhesions rates and height for tests where adhesions occurred.

10.1 AlSi-polyester abradable

- The understanding of the AlSi-polyester wear mechanisms was improved through the advancements in data capturing and analysis methods and conducting tests at more representative engine conditions.

- It was established that rubbing occurs at all the testing conditions considered in this work (speeds of 100-280m/s and incursions rates of 0.02-2µm/pass and abradable hardnesses of H55-H70). This finding agrees with previous research at the lower incursion rates (0.02µm/pass and 0.2µm/pass), and adds to the understanding of the wear mechanism at 2µm/pass, where previous results by Watson [6] indicated that cutting might be an incomplete description of the wear mechanism at this incursion rate and Hadjisoteriou [52] showed that while a higher percentage of an abradable material releases from the front of a blade at this incursion rate, a significant amount is still ejected from behind. In the current work, it was shown, that less grooving of abradable samples at 2µm/pass occurred not due to cutting behaviour but because of a more uniform formation of adhesions. Additionally, the comparison of normal forces between incursion rates of 0.2µm/pass and 2µm/pass suggested that while some improvement has occurred (forces were not 10, but about 5 times larger at 2µm/pass), this improvement in contact mechanism was small and the rubbing was still the dominant mechanism at 2µm/pass leading to the significant formation of adhesions at this incursion rate.

- With the help of the front-on imaging system, the understanding of how blade wear and adhesions occur in contacts with AlSi-polyester samples was advanced. For blade wear, it was shown that it is consistent at different blade location for a given test. It was also shown that it increases linearly with rub length, which is consistent with Archard's law of wear. It was shown that the correlation between the testing conditions and wear rate is complex and non-linear with both speed and abradable hardness. It was suggested that such non-linearity was due to the way these factors influenced the secondary parameters such as heat generation and dissipation in a system. It was also shown that having blades

with a reduced thickness increased blade wear on the example of blades with a variable chord thickness, which is consistent with the study by Watson, where it was shown that blade wear increased with a decrease in a blade thickness (that study used a constant blade tip thickness) [6].

- For adhesions, it was shown that the combination of bulk temperature and flash temperature concepts was able to explain all of the observations in this work. It was shown that the likelihood of adhesions formation increased with contact forces (chapter 5) and decreased with blade tip thickness (chapter 8).

- The flash temperature concept was also able to explain findings in previous research, where it was shown that for the very hard AlSi-polyester samples (H80-H82), no adhesions occurred at 0.02µm/pass and 0.2µm/pass but some occurred at 2µm/pass. This was likely due to the increase in thermal conductivity with hardness being more significant than increase in contact forces thus decreasing flash temperatures at very high hardnesses. This was somewhat further supported by the comparison of results at 0.02µm/pass and 0.2µm/pass, where the formation of adhesions was much more prevalent at 0.2µm/pass despite similar contact forces, as it is likely that the surface layer at 0.02µm/pass was harder due to the compacted surface layer.

- While the suggestions made about temperatures offered good explanations of experimental observations, it was highlighted that the results in this work are lacking temperature data to verify these suggestions. It was therefore suggested that advancements in test temperature measurements are essential for improved understanding of adhesion mechanism in contacts with AlSi-based abradables.

10.2 NiCrAl-bentonite abradable

- The understanding of contact modes and wear mechanisms in contacts with NiCrAl-bentonite abradables was advanced building on the earlier study by Watson [51].

- The observations in this work supported the fracture and release mechanism suggested by Watson [51] for NiCrAl-bentonite abradable samples. It was suggested that the improved fracture behaviour observed at low incursion rates was due to fatigue mechanism being important for fracture of abradables.

- In this work two distinct contact modes were identified. These contact modes were then explained through the balance between the incursion rate and the rate of abradable

fracture. It was identified that for abradable samples from the same batch, the transition between the two contact modes occurs over a range of incursion rate rather that at a single incursion rate due to small variations in abradable hardness between samples within the same batch.

- The factors influencing the transition to the high-force mode were summarised based on findings in this work and previous research. It was suggested that increase in incursion rate and abradable hardness decrease the effectiveness of the abradable surface fracture, while the increase in blade tip speed increases it.

- It was also shown in this work, that blade length plays a significant role in the effectiveness of abradable surface fracture, with very long (low stiffness) blades leading to inefficient fracture.

- The importance of transition to the high-force contact mode was also highlighted through the tests with double incursion rates, where it was shown that even at lower incursion rates that are above the transition incursion rate to the high-force contact mode, where no significant compaction was observed (only small surface compaction) by Watson [51], some detriment in abradable fracture efficiency was seen at 0.02µm/pass indicating that contact forces observed during the high-force contact mode are enough to introduce some damage to the abradable and blade surfaces leading to detriment in overall fracture efficiency even at incursion rates below the transition. It was then suggested that this decrease in fracture effectiveness could decrease the transition incursion rate, leading to the high-force contact mode and blade wear occurring at incursion rates, at which they would otherwise would have not occurred.

- The presence of the third contact mode – progressive abradable compaction was inferred from the results by Watson [51] and explained through the same framework used to explain the two contact modes observed in this work. It was suggested that compaction occurs when incursion rate is too high to be accommodated by either abradable fracture or blade wear (particularly, at very high incursion rates, where there is not enough time for a blade to reach temperatures high enough for wear rate to significantly increase). Then, the incursion rate can only be accommodated by the compaction of abradable surface leading to the further decrease of abradable fracture efficiency (harder surface layer), increased forces and further compaction.

- It was therefore suggested that blade wear is in some way protective against the occurrence of significant abradable surface compaction for NiCrAl-bentonite samples. It was also suggested that compaction in aero-engines would be less severe than in scaled rig

tests due to blades initial temperatures being higher during engine operation, meaning less time needed for blades to reach a sufficient temperature for the initiation of the thermally driven wear.

- Results from the blades with a variable chord thickness potentially offer further support to blade wear being protective against compaction. It was seen in these tests, that edge effects were significant for blades with a variable chord thickness with significantly more blade wear at blade edges than in the blade centre. This might be explaining anecdotal observations by Rolls-Royce plc., where in aero-engines more compaction was reported at locations corresponding to a blade centre than to a blade edge for NiCrAl-bentonite abradables [60]. It should be noted that the blade wear in aero-engines is still undesirable due to effects on engine efficiency and should be avoided where possible, but it could be beneficial in preventing the catastrophic failure of abradable due to severe compaction.It is preferable to tackle blade wear in contacts with NiCrAl-bentonite samples not by making blade harder or more resistant to wear but by making improvements in abradable fracture.

- The effect of angled blades was investigated with short (stiff) blades and compared to their effectiveness when they were introduced to long blades. It was shown that with short blades, angles did not offer the same increase in abradable fracture effectiveness. It was then suggested that both an increase in stiffness and introduction of an angle to long (less stiff) blades improve abradable fracture in a similar manner, and with stiff blades angles do not offer further performance improvements.

- The difference in blade wear performance between flat and angled blades was explained through the presence of low temperature abrasive wear and thermally driven abrasive wear. The low temperature abrasive wear rate was low and no wear was observed with flat blades. With angled blades, however, some wear occurred due to the very low thickness at the sharp blade tip. The thermally driven wear occurred for tests that transitioned to the high-force contact mode. This type of wear occurred earlier during a test and the wear rate was higher for flat blades than for angled blades. However, due to angled blades also experiencing some wear at low temperatures, flat blades outperformed angled blades for all of the testing conditions, except when transition to the high-force contact mode occurred and rub depth was large enough for flat blade wear to first match that of angled blades and then exceed it with the further growth in rub length due to a higher rate of thermally driven wear.

- Further work opportunities were highlighted, where better control of abradable hardness and performance of targeted tests at different condition can allow to establish quantitative trends between the effects of different parameters on the transition incursion rate, as currently such trends are primarily qualitative. Additionally, statistical analysis of the results will then allow to establish interactions between different testing parameters and their effect on the transition. For example, it will be of interest if statistical analysis would confirm the interaction between the blade stiffness and introduction of an angled sharp tip on the transition incursion rate.

Chapter 11

Further work

The results in this thesis gave new insights into the wear mechanisms of AlSi-polyester and NiCrAl-bentonite abradables and the applicability of scaled rig test results to observations made in actual aero-engines. However, there were also a number of limitations to this work, which will be highlighted in this section. First, the potential modifications to methodology will be discussed, followed by an overview of areas of research that have a potential to further improve the understanding of wear mechanisms in abradable-blade contacts.

11.1 Methodology

A number of potential improvements to the methodology have been identified with a potential to either improve the consistency of results or provide new insight into the properties of contacts between blades and abradable materials.

- Both the low-speed and high-speed rigs are currently unable to reach the engine representative speed of 400m/s. While the commissioning of the high-speed rig allowed to better understand the effects of blade tip speed on contacts with abradable materials by bringing the testing speed capability from 200m/s to 280m/s, further improvement in the maximum speed capability would allow to verify that the trends observed with speed hold up to the engine speed of 400m/s. This is of interest as speed was shown to have an influence on either the wear mechanisms or the severity of wear mechanisms for both the NiCrAl-bentonite and AlSi-polyester abradable considered in this thesis.

- The better control of abradable hardness, particularly for NiCrAl-bentonite samples, where hardness was found to be one of the most dominant factors determining test outcomes is required for better repeatability of results and clearer comparison of trends observed with other testing parameters. As it is not possible to completely eliminate

hardness variations between batches of the same nominal hardness and even between samples within a single batch due to the inherent randomness of abradable spraying process, mitigation measures need to be used.

- All the sprayed samples need to be hardness tested using the same testing equipment to establish the average hardness for the sprayed batch and to discard too soft or too hard samples to reduce the occurrence of outliers in testing data. Additionally, the repeatability of hardness measurements needs to be established for abradable materials and the minimum number of locations to obtain the average hardness measurement for a sample with an unacceptable uncertainty (the acceptable uncertainty can be determined using engineering judgement, but should not exceed 1 or 2 points on the on the HR15Y Superficial Rockwell hardness scale) needs to be determined – the limit of locations is 6 for tested samples and 9 for untested samples due to the limitations in the size of an area available for hardness measurements.

- Alternatively, a different method capable of classifying abradable samples/batches may be developed if it is determined that the hardness measurements on the HR15Y Superficial Rockwell hardness scale cannot be performed to the required measurement uncertainty. It is unknown to the author if a more appropriate method for classifying abradable samples exists and this could be an area of further research.

- The tests in this thesis lacked thermal data due to challenges with using a pyrometer on the high-speed rig. The quality of temperature data in previous research was also limited due to pyrometers only measuring temperature in a single spot rather than temperature distribution across an entire abradable or blade surface. The first attempts to use thermal camera imaging on the low-speed rig were done in the study by Hadjisoteriou [52]. Thermal imaging data was shown to have a high potential for improved temperature measurements, but further improvements in thermal data acquisition and analysis are required.

- The representation of thermal conditions of aero-engines can be another improvement to the methodology as most of the wear mechanisms discussed in this thesis appear to be thermally driven. This can be achieved by heating a blade and an abradable samples to temperatures of a compressor stage of interest. Additionally, with more information on the cooling rates of blades and abradables in aero-engines, it will be possible to understand if they could be matched on scaled test rigs.

- Some improvements in force measurements can also be achieved. It was seen that for some of the tests the dynamometer vibrations did not fully damp down after a blade

strike before the next blade strike comes in even after the introduction of a rubber sheet in between an abradable sample and sample holder. Improved damping solutions for the dynamometer can improve signal quality for some of the testing conditions.

- Alternatively, different force measurement solutions may be explored. For example, an accelerometer might be installed on the stage plate instead of a dynamometer in between the stage and an abradable sample. Then, the signal processing techniques could be used to convert accelerometer measurements into contact forces once relevant FRFs are known. If such measurement technique is to be attempted, it can first be installed in parallel to a dynamometer (a dynamometer in between the stage and an abradable sample and an accelerometer on the stage plate) to validate measurements from an accelerometer.

- Finally, the pre-test measurements and if needed, the control of such parameters as blade tip radius, blade and abradable surface roughness can be done to improve understanding if any of these parameters have an influence on test outcomes.

11.2 Wear mechanisms in abradable-blade contacts

- Based on the findings in this work and previous research, there are two main areas for further research of contacts with AlSi-based abradable materials: understanding how to minimise the blade wear and preventing the formation of adhesions when rubbing occurs, and understanding if there is a possibility to transition the contacts to cutting at all the considered incursion conditions.

- For improvements in the understanding of adhesion and blade wear mechanisms, better quality thermal measurements are essential, as results in this and previous studies suggested that both mechanisms are thermally driven. The installation of the thermal camera on the low-speed rig has a potential for providing high quality temperature data. With an improved understanding of how abradable and blade properties affect formation of adhesions, it will potentially be possible to design the contacts in a way that minimises the probability of adhesion formation and adhesion heights.

- Some of the previous research on AlSi-hBN [48] indicated that cutting occurs in contacts with this type of abradable at medium and high incursion rates (0.2-2μm/pass). In contacts with AlSi-polyester abradable rubbing was found to be dominant at all of the considered incursion conditions. However, some of the results in this study obtained with blades with a variable chord thickness indicated that cutting might have occurred at some parts of a blade, but these results require further investigation to fully understand

why the wear behaviour in those parts of the blades was different to the general trends observed with AlSi-polyester abradable sample at all other testing conditions. These results suggest that further research into the ways abradable microstructure and blade geometry and surface could affect the conditions at which cutting occurs could be of interest.

- The next step in understanding the contacts with NiCrAl-bentonite abradables would be the transition from the qualitative description of the ways different parameters influence abradable fracture effectiveness given in this thesis based on the results in this work and in previous research to the more quantitative description.

- The quantitative analysis can allow to better understand the relative importance of each parameter. Additionally, with statistical analysis it will be possible to establish if there are any interactions between different parameters. For example, from the results in this work it is expected that an increase in blade stiffness and addition of a blade tip angle to less stiff blades will have an interaction (a change in one of these two parameters influences the importance of the other one) in their effect on abradable fracture. This will also aid in further exploration of whether a unified map for different types of abradables could be created.

Bibliography

[1] European Comission. Flightpath 2050, europe's vision for aviation. Technical report, High Level Group on Aviation Research, 2011.

[2] IATA. Carbon offsetting for internationalaviation. Technical report, 2020.

[3] Richard Avellán. *On the Design of Energy Efficient Aero Engines Some Recent Innovations*. PhD thesis, Chalmers University of Technology, 2011.

[4] J. A. Storer and N. A. Cumpsty. Tip leakage flow in axial compressors. *Journal of Turbomachinery*, 113(2):252–259, Apr. 1991.

[5] Scott Wilson. Thermally sprayed abradable coating technology for sealingin gas turbines. Technical report, Oerlikon Metco, 2012.

[6] Michael Watson. *Modifications of blade tips in abradable contacts*. PhD thesis, The University of Sheffield, 2017.

[7] Oerlikon Metco. Material product data sheet, nickel chromium aluminum / bentonite abradable powders, dsm-0231.0 – NiCrAl / bentonite abradable powders.

[8] M. Watson, N. Fois, and M.B. Marshall. Effects of blade surface treatments in tip–shroud abradable contacts. *Wear*, 338-339:268–281, Sep. 2015.

[9] Z Wang, A Kulkarni, S Deshpande, T Nakamura, and H Herman. Effects of pores and interfaces on effective properties of plasma sprayed zirconia coatings. *Acta Materialia*, 51(18):5319–5334, Oct. 2003.

[10] H.I. Faraoun, J.L. Seichepine, C. Coddet, H. Aourag, J. Zwick, N. Hopkins, D. Sporer, and M. Hertter. Modelling route for abradable coatings. *Surface and Coatings Technology*, 200(22-23):6578–6582, Jun. 2006.

[11] H.I. Faraoun, T. Grosdidier, J.-L. Seichepine, D. Goran, H. Aourag, C. Coddet, J. Zwick, and N. Hopkins. Improvement of thermally sprayed abradable coating by microstructure control. *Surface and Coatings Technology*, 201(6):2303–2312, Dec. 2006.

[12] Rodolphe Bolot, Jean-Louis Seichepine, Jiang Hao Qiao, and Christian Coddet. Predicting the thermal conductivity of AlSi/polyester abradable coatings: Effects of the numerical method. *Journal of Thermal Spray Technology*, 20(1-2):39–47, Nov. 2010.

[13] Rodolphe Bolot, Delphine Aussavy, and Ghislain Montavon. Application of FEM to estimate thermo-mechanical properties of plasma sprayed composite coatings. *Coatings*, 7(7):91, Jun. 2017.

[14] Michael Watson and Matthew Marshall. A novel image segmentation approach for microstructure modelling. *Coatings*, 7(10):166, Oct. 2017.

[15] Xiao Ma and Allan Matthews. Evaluation of abradable seal coating mechanical properties. *Wear*, 267(9-10):1501–1510, Sep. 2009.

[16] Yi Maozhong, Huang Baiyun, and He Jiawen. Erosion wear behaviour and model of abradable seal coating. *Wear*, 252(1-2):9–15, Jan. 2002.

[17] S. Skiba, L. Faure, S. Philippon, and J. Papasidero. Experimental investigation of the mechanical behavior of an AlSi-PE abradable coating at high strain rates for a large range of temperatures. *Journal of Dynamic Behavior of Materials*, 6(2):213–223, Mar. 2020.

[18] S. Skiba, B. Chevrier, L. Faure, and S. Philippon. Thermoelastoviscoplastic bilinear compressive constitutive law of an AlSi-PE abradable material based on experimental investigations. *Journal of Dynamic Behavior of Materials*, 7(3):499–508, Mar. 2021.

[19] Maozhong Yi, Jiawen He, Baiyun Huang, and Huijiu Zhou. Friction and wear behaviour and abradability of abradable seal coating. *Wear*, 231(1):47–53, Jun. 1999.

[20] Xiao Ma and Allan Matthews. Investigation of abradable seal coating performance using scratch testing. *Surface and Coatings Technology*, 202(4-7):1214–1220, Dec. 2007.

[21] Jiaguangyi Xiao, Yong Chen, Dawei Chen, Jie Tian, Hua Ouyang, and Anjenq Wang. Interactions between blades and abradable coatings: A numerical approach considering geometrical nonlinearity. *International Journal of Mechanical Sciences*, 191:106052, Feb. 2021.

[22] E. Delhez, F. Nyssen, J.-C. Golinval, and A. Batailly. Reduced order modeling of blades with geometric nonlinearities and contact interactions. *Journal of Sound and Vibration*, 500:116037, May 2021.

[23] Bérenger Berthoul, Alain Batailly, Mathias Legrand, Laurent Stainier, and Patrice Cartraud. Abradable coating removal in turbomachines: A macroscopic approach accounting for several wear mechanisms. In *Volume 7B: Structures and Dynamics*. American Society of Mechanical Engineers, Jun. 2015.

[24] Hougong Wang. Criteria for analysis of abradable coatings. *Surface and Coatings Technology*, 79(1-3):71–75, Feb. 1996.

[25] M.O. Borel, A.R. Nicoll, H.W. Schlapfer, and R.K. Schmid. The wear mechanisms occurring in abradable seals of gas turbines. *Surface and Coatings Technology*, 39-40:117–126, Dec. 1989.

[26] Alain Batailly, Mathias Legrand, Antoine Millecamps, and François Garcin. Numerical-experimental comparison in the simulation of rotor/stator interaction through blade-tip/abradable coating contact. *Journal of Engineering for Gas Turbines and Power*, 134(8), Jun. 2012.

[27] Mathias Legrand, Alain Batailly, Benoît Magnain, Patrice Cartraud, and Christophe Pierre. Full three-dimensional investigation of structural contact interactions in turbomachines. *Journal of Sound and Vibration*, 331(11):2578–2601, May 2012.

[28] Alain Batailly and Mathias Legrand. Unilateral contact induced blade/casing vibratory interactions in impellers: Analysis for flexible casings with friction and abradable coating. *Journal of Sound and Vibration*, 348:344–364, Jul. 2015.

[29] Alain Batailly, Quentin Agrapart, Antoine Millecamps, and Jean-François Brunel. Experimental and numerical simulation of a rotor/stator interaction event localized on a single blade within an industrial high-pressure compressor. *Journal of Sound and Vibration*, 375:308–331, Aug. 2016.

[30] Florence Nyssen and Alain Batailly. Sensitivity analysis of rotor/stator interactions accounting for wear and thermal effects within low- and high-pressure compressor stages. *Coatings*, 10(1):74, Jan. 2020.

[31] Schmid, Richard Karl. *New high temperature abradables for gas turbines*. PhD thesis, 1997.

[32] Sarah Baïz, Jacky Fabis, Xavier Boidin, and Yannick Desplanques. Experimental investigation of the blade/seal interaction. *Proceedings of the Institution of Mechanical Engineers, Part J: Journal of Engineering Tribology*, 227(9):980–995, Feb. 2013.

[33] Romain Mandard, Jean-François Witz, Xavier Boidin, Jacky Fabis, Yannick Desplanques, and Jean Meriaux. Interacting force estimation during blade/seal rubs. *Tribology International*, 82:504–513, Feb. 2015.

[34] F. Ghasripoor, R.K. Schmid, M.R. Dorfman, and L. Russo. A review of clearance control wear mechanisms for low temperature aluminium silicon alloys. In Christian Coddet, editor, *Thermal Spray 1998: Proceedings from the International Thermal Spray Conference*. ASM International, May 1998.

[35] Oerlikon Metco. Solutions flash, improve efficiency and reduce emissions with high pressureturbine abradable coatings for industrial gas turbines. Technical report, Oerlikon Metco, 2014.

[36] A. Dadouche, M. J. Conlon, W. Dmochowski, B. Liko, and J.-P. Bedard. Experimental evaluation of abradable seal performance at high temperature. In *Volume 5: Structures and Dynamics, Parts A and B*. ASMEDC, Jan. 2008.

[37] E. Irissou, A. Dadouche, and R. S. Lima. Tribological characterization of plasma-sprayed CoNiCrAlY-BN abradable coatings. *Journal of Thermal Spray Technology*, 23(1-2):252–261, Oct. 2013.

[38] Na Zhang, Jie Shen, Haijun Xuan, Yanqi Hu, and Weirong Hong. Evaluation of an AlSi-polyester abradable seal coating performance using high-temperature and high-velocity abrasion tests. *Proceedings of the Institution of Mechanical Engineers, Part J: Journal of Engineering Tribology*, 230(7):842–851, Dec. 2015.

[39] Haijun Xuan, Na Zjang, Bin Lu, Lijun Cheng, and Weirong Hong. Investigation of high-speed abrasion behavior of an abradable seal rubber in aero-engine fan application. *Chinese Journal of Aeronautics*, 30(4):1615–1623, Aug. 2017.

[40] J. Stringer and M.B. Marshall. High speed wear testing of an abradable coating. *Wear*, 294-295:257–263, Jul. 2012.

[41] N. Fois, J. Stringer, and M.B. Marshall. Adhesive transfer in aero-engine abradable linings contact. *Wear*, 304(1-2):202–210, Jul. 2013.

[42] N Fois, M Watson, and MB Marshall. The influence of material properties on the wear of abradable materials. *Proceedings of the Institution of Mechanical Engineers, Part J: Journal of Engineering Tribology*, 231(2):240–253, Aug. 2016.

[43] W.H. Xue, S.Y. Gao, D.L. Duan, Y. Liu, and S. Li. Material transfer behaviour between a Ti6Al4V blade and an aluminium hexagonal boron nitride abradable coating during high-speed rubbing. *Wear*, 322-323:76–90, Jan. 2015.

[44] Weihai Xue, Siyang Gao, Deli Duan, Jiaping Zhang, Yang Liu, and Shu Li. Effects of blade material characteristics on the high-speed rubbing behavior between al-hBN abradable seal coatings and blades. *Wear*, 410-411:25–33, Sep. 2018.

[45] S. Nitschke, T. Wollmann, C. Ebert, T. Behnisch, A. Langkamp, T. Lang, E. Johann, and M. Gude. An advanced experimental method and test rig concept for investigating the dynamic blade-tip/casing interactions under engine-like mechanical conditions. *Wear*, 422-423:161–166, Mar. 2019.

[46] M. Bounazef, S. Guessasma, and B. Ait Saadi. The wear, deterioration and transformation phenomena of abradable coating BN–SiAl–bounding organic element, caused by the friction between the blades and the turbine casing. *Materials Letters*, 58(27-28):3375–3380, Nov. 2004.

[47] N Fois, M Watson, J Stringer, and MB Marshall. An investigation of the relationship between wear and contact force for abradable materials. *Proceedings of the Institution of Mechanical Engineers, Part J: Journal of Engineering Tribology*, 229(2):136–150, Jul. 2014.

[48] Nicola Fois. *Investigation And Characterisation Of The Wear Mechanics Of Abradable Compressor Linings*. PhD thesis, The University of Sheffield, 2015.

[49] Weihai Xue, Siyang Gao, Deli Duan, Jiaping Zhang, Yang Liu, and Shu Li. Ti6al4v blade wear behavior during high-speed rubbing with NiAl-hBN abradable seal coating. *Journal of Thermal Spray Technology*, 26(3):539–553, Dec. 2016.

[50] Weihai Xue, Siyang Gao, Deli Duan, Hailiang Zheng, and Shu Li. Investigation and simulation of the shear lip phenomenon observed in a high-speed abradable seal for use in aero-engines. *Wear*, 386-387:195–203, Sep. 2017.

[51] Michael Watson and Matthew Marshall. Wear mechanisms at the blade tip seal interface. *Wear*, 404-405:176–193, Jun. 2018.

[52] Andreas Hadjisoteriou. *Investigation of material removal mechanism and thermal response of compressor abradable materials*. PhD thesis, The University of Sheffield, 2021.

[53] T.A. Taylor, B.W. Thompson, and W. Aton. High speed rub wear mechanism in IN-718 vs. NiCrAl–bentonite. *Surface and Coatings Technology*, 202(4-7):698–703, Dec. 2007.

[54] Rolls-Royce plc. Private communication - NiCrAl-bentonite age-hardening behaviour, 2019.

[55] Marco Curreli. Drawings for the new containment for the high-speed rig, 2019.

[56] Micro-Epsilon. Operating instructions thermometer ctl. Technical report.

[57] Eldar Rahimov, Michael Watson, Andreas Hadjisoteriou, and Matthew Marshall. Investigation of wear mechanisms in AlSi-polyester abradable - Ti(6Al4V) blade contacts using stroboscopic imaging. *Wear*, 494-495:204207, Apr. 2022.

[58] J.R Barber. The conduction of heat from sliding solids. *International Journal of Heat and Mass Transfer*, 13(5):857–869, May 1970.

[59] H. Blok. The flash temperature concept. *Wear*, 6(6):483–494, Nov. 1963.

[60] Rolls-Royce plc. Private communication, 2022.